# FLEXIBILITY OF ROBOTS: DESIGN, MODELING AND CONTROL

**A Thesis Submitted to**
**the Graduated School of**
**İzmir Institute of Technology**
**in Partial Fulfillment of the Requirements for the Degree of**

**DOCTOR OF PHILOSOPHY**

**in Mechanical Engineering**

**by**
**İbrahimcan GÖRGÜLÜ**

**December 2024**
**İZMİR**

We approve the thesis of **İbrahimcan GÖRGÜLÜ**

**Examining Committee Members:**

**Prof. Dr. Mehmet İsmet Can DEDE**
Department of Mechanical Engineering, İzmir Institute of Technology

**Prof. Dr. Gökhan KİPER**
Department of Mechanical Engineering, İzmir Institute of Technology

**Prof. Dr. Enver TATLICIOĞLU**
Department of Electrical and Electronics Engineering, Ege University

**Assoc. Prof. Dr. Erkin GEZGİN**
Department of Mechatronics Engineering, İzmir Kâtip Çelebi University

**Assist. Prof. Dr. Halil TETİK**
Department of Mechatronics Engineering, İzmir Institute of Technology

**9 December 2024**

**Prof. Dr. Mehmet İsmet Can DEDE**
Supervisor,
Mechanical Engineering
İzmir Institute of Technology

**Prof. Dr. Mehmet İsmet Can DEDE**
Head of the Department of
Mechanical Engineering

**Prof. Dr. Mehtap EANES**
Dean of the Graduate School

# ACKNOWLEDGMENTS

I would like to express my deepest gratitude to my thesis supervisor, Prof. Dr. Mehmet İsmet Can DEDE, for his invaluable guidance, encouragement, and support throughout my research journey. Your expertise and insights have been a cornerstone of my work, and I am deeply appreciative of the time and effort you have dedicated to helping me grow as a researcher.

I also extend my sincere thanks to the members of my thesis monitoring committee, Prof. Dr. Gökhan KİPER and Prof. Dr. Enver TATLICIOĞLU, for their constructive feedback, thoughtful questions, and unwavering support. Your input has been instrumental in shaping my dissertation and pushing me to achieve my best.

To the members of the jury, thank you for taking the time to evaluate my work and for your insightful comments and suggestions. Your feedback has helped me refine and strengthen my research, and I am honored to have had the opportunity to present my work to such a distinguished panel.

To my colleagues and peers, Dr. Orhan AYİT, Mr. Hüseyin Tuğcan DİNÇ, Mr. Erdi SAYAR, Mr. Fırat KARA and Mr. Erkan PAKSOY. I extend my heartfelt appreciation for the camaraderie, collaboration, and support that have made this journey so memorable. Your encouragement and shared passion for research have been a source of motivation, and I am truly grateful to have worked alongside such talented individuals.

I would like to acknowledge the financial support provided by The Scientific and Technological Research Council of Turkey (TUBITAK) through the project 'Methodologies for Increasing the Positioning Accuracy of High-Acceleration Parallel Robots Used in Industrial Applications' with the grant number of 116M272 for Chapter 2. I thank Dr. Emre Uzunoğlu, Ms. Merve Özkahya, and Mr. Erkan Paksoy, for contribution to the design of the experimental test setup for the project.

I would like to acknowledge the financial support provided by The Scientific and Technological Research Council of Turkey (TUBITAK) through the project 'Design of an Inherently Balanced Robotic Manipulator with Remote Center of Motion to be used as an Endoscope Holder for Endonasal Skull Base Surgery (BalanScope)' with the grant number of 219M483 for Chapters 3 and 4. I thank Mr. Ateş Akşit for his contributions for conducting the experiments in chapter 3.

# ABSTRACT


## FLEXIBILITY OF ROBOTS: DESIGN, MODELING AND CONTROL

All of the materials exhibit some flexibility. Consequently, a robot manipulator constructed from any material inherits this structural flexibility. Typically, flexible robots have lower positioning accuracy. However, flexibility can also be advantageous, as it contributes to a controlled mechanical impedance and enhanced safety in physical human-robot interactions.

The primary challenge is enhancing the input/output performance of a flexible robot. This performance largely relies on three key components: the robot's mechanical structure, its controller, and the accuracy of the mathematical model employed by the controller. Any alterations or adjustments made to these components impact the overall input/output performance. This dissertation encompasses these three key components: model, design, and control.

The first section is dedicated to devising a stiffness model of an over-constrained parallel robot manipulator to estimate the vibrations during operation. Adjusting the desired trajectory (or input) based on these estimations makes it possible to mitigate the vibration effects on the output.

The second part develops a flexible joint for the desired mechanical impedance. This joint exhibits no compliant deflection under small loads but deflects with a softening behavior as interaction loads increase. The joint maintains the robot's positioning performance at low torsion levels while ensuring safe physical human-robot interactions.

Finally, a controller framework is designed for the flexible robot that contains the designed flexible joint. The controller is capable of stable transitions between the mechanical states of the robot (rigid and flexible) and achieving the desired tasks (trajectory tracking, displaying the desired impedance, force/position tracking, and ensuring safety).

# ÖZET

## ROBOTLARIN ESNEKLİĞİ: TASARIM, MODELLEME ve KONTROL

Tüm malzemeler bir miktar esneklik sergiler. Sonuç olarak, herhangi bir malzemeden yapılmış bir robot manipülatörü bu yapısal esnekliği miras alır. Tipik olarak esnek robotların konumlandırma doğruluğu daha düşüktür. Bununla birlikte esneklik, kontrollü bir mekanik empedansa ve fiziksel insan-robot etkileşimlerinde artırılmış güvenliğe katkıda bulunduğundan avantajlı da olabilir.

Temel zorluk esnek bir robotun giriş/çıkış performansını arttırmaktır. Bu performans büyük ölçüde üç temel bileşene dayanır: robotun mekanik yapısı, denetleyicisi ve denetleyici tarafından kullanılan matematiksel modelin doğruluğu. Bu bileşenlerde yapılan herhangi bir değişiklik veya ayarlama, genel giriş/çıkış performansını etkiler. Bu tez şu üç temel bileşeni kapsamaktadır: model, tasarım ve kontrol.

İlk bölüm, çalışma sırasındaki titreşimleri tahmin etmek için aşırı kısıtlanmış bir paralel robot manipülatörünün direngenlik modelinin tasarlanmasına ayrılmıştır. İstenilen yörüngenin (veya girdinin) bu tahminlere göre ayarlanması, çıktı üzerindeki titreşim etkilerinin azaltılmasını mümkün kılar.

İkinci kısım da istenilen mekanik empedans için esnek bir mafsal geliştirilir. Bu mafsal, küçük yükler altında esneklik göstermez, ancak etkileşim yükleri arttıkça yumuşayan davranışla esner. Mafsal, güvenli fiziksel insan-robot etkileşimlerini sağlarken robotun konumlandırma performansını düşük burulma seviyelerinde korur.

Son olarak esnek robot için tasarlanan esnek mafsalı içeren bir denetleyici çerçevesi tasarlanmıştır. Kontrolcü, robotun mekanik durumları (sert ve esnek) arasında istikrarlı geçişler yapma ve istenen görevleri gerçekleştirme (yörünge izleme, istenen empedansı görüntüleme, kuvvet/konum izleme ve güvenliği sağlama) yeteneğine sahiptir.

*Death is worth living for. Love is worth waiting for.*

# TABLE OF CONTENTS

LIST OF FIGURES ..... x

LIST OF TABLES ..... xiii

CHAPTER 1. INTRODUCTION ..... 1
1.1. Problem Definition ..... 4
1.2. On Industrial Robots' Vibration Suppression ..... 5
1.3. On Safe Flexible Robot Design ..... 8
1.4. On Flexible Robot Control for pHRI ..... 11
1.5. Aims of the Dissertation ..... 14
1.5.1. Obtaining an industrial robots' stiffness model for vibration suppression ..... 14
1.5.2. Designing a flexible joint for an inherently safe robot ..... 15
1.5.3. Developing a controller for an RLFJ robot manipulator ..... 16
1.6. Contributions ..... 17

CHAPTER 2. STIFFNESS MODELING OF A 2-DOF OVER-CONSTRAINED PLANAR PARALLEL MECHANISM ..... 19
2.1. Introduction ..... 19
2.2. Stiffness Modeling via the Virtual Joint Method ..... 23
2.3. Case study: Modified 6R Over-Constrained Parallel Mechanism ..... 25
2.3.1. The Mechanism's Insight ..... 25
2.3.2. Stiffness Modeling Objectives ..... 28
2.3.3. Stiffness Model of the Parallelogram Loops ..... 29
2.3.3.1. Stiffness of an Active Parallelogram Loop ..... 31
2.3.3.2. Stiffness of a Passive Parallelogram Loop ..... 34
2.3.4. Stiffness Model of the Manipulator ..... 35
2.3.5. The Displacement of the Mobile Platform due to Compliant Deflections of Flexible Links ..... 38
2.3.6. Summary of Stiffness Modelling ..... 40
2.4. Simulation, Results, and Discussion ..... 41

2.5. Experimental Procedure for Model Parameter Update ..... 46
2.5.1. Processing the Experiment Data ..... 50
2.5.2. Experimental Results and Discussion ..... 52
2.6. Conclusion and Discussion ..... 57

CHAPTER 3. A NEW SAFE FLEXIBLE TORSION JOINT DESIGN WITH SOFTENING STIFFNESS CHARACTERISTICS ..... 59
3.1. Introduction ..... 59
3.2. Working Principle of Torsion Flexible Joint ..... 64
3.2.1. Linear Flexible Joint Analogy ..... 65
3.2.2. Torsion Flexible Joint ..... 68
3.2.3. Series Torsion Flexible Joint ..... 70
3.2.4. Parallel Torsion Flexible Joint ..... 73
3.2.5. Stiffness of a Spiral Torsion Spring ..... 74
3.2.6. System Model ..... 76
3.3. Mechanical Design and Prototyping ..... 76
3.4. Experimental Validation and Procedures ..... 79
3.4.1. Stiffness identification test setup and procedure ..... 79
3.4.2. System identification test setup and procedure ..... 80
3.5. Results and Discussion ..... 82
3.5.1. Stiffness Identification Test Results ..... 82
3.5.2. System Identification Test Results ..... 83
3.6. Conclusion ..... 84

CHAPTER 4. CONTROL OF A RIGID LINK FLEXIBLE JOINT ROBOT FOR SAFE HUMAN ROBOT INTERACTION ..... 86
4.1. Introduction ..... 86
4.2. System Model and Preliminaries ..... 91
4.2.1. Kinematic, Dynamic and Stiffness Models ..... 91
4.2.2. Preliminaries ..... 92
4.3. Control Objective, Controller and Observer Design ..... 94
4.3.1. The Controller for Rigid Mode ..... 94
4.3.2. The Controller for Flexible Mode ..... 97
4.3.2.1. Impedance Controller ..... 98

4.3.2.2. Force/Position Controller ..... 101
4.3.3. Switch Designs ..... 106
4.3.3.1. Trajectory Tracking - Impedance Controller Switch ..... 107
4.3.3.2. Trajectory Tracking - Hybrid Controller Switch ..... 108
4.3.3.3. Safety Switch ..... 109
4.4. Simulation, Experiment, Results and Discussions ..... 109
4.4.1. Simulation and Experiment Preliminaries ..... 109
4.4.2. Trajectory Tracking Controller Results ..... 112
4.4.3. Impedance Controller Results ..... 114
4.4.4. Hybrid Controller Results ..... 117
4.5. Conclusion ..... 121

CHAPTER 5. CONCLUSION ..... 125

REFERENCES ..... 127

APPENDICES ..... 141

APPENDIX A. STIFFNESS PARAMETERS AND SIMULATION RESULTS ..... 141

# LIST OF FIGURES

**Figure** **Page**


Figure 1.1 S-Curve profiles. ..... 6
Figure 1.2 Input shaping method. ..... 7
Figure 1.3 Trajectory filtering. ..... 7
Figure 1.4 Trajectory modification with the help of stiffness model. (The triangular trajectory is followed in a counter-clockwise direction.) ..... 8
Figure 1.5 Illustration of a series elastic actuator. ("A series elastic actuator," image generated by OpenAI's DALL·E, November 5, 2024.) ..... 10
Figure 1.6 Required stiffness characteristics of flexible joint. ..... 16
Figure 2.1 a) CAD sketch and link types of the manipulator, b) the manipulator. ... 27
Figure 2.2 Four types of links. ..... 27
Figure 2.3 Kinematic sketch of modified 6R manipulator and its components. ..... 28
Figure 2.4 Stiffness loops of the frames where "$\rightarrow$" and "$+$" show the serial and parallel connections, respectively. ..... 30
Figure 2.5 Stiffness model sketches. a) Actual the VJM sketch of the parallelogram b) Resultant the VJM equivalent of the parallelogram. Superscripts and subscripts $(ij)$, and $(j)$ denote the $j^{\text{th}}$ joint frame in $i^{\text{th}}$ limb for $i, j = 1, 2$, and $'$ represents the virtual joint frame. ..... 31
Figure 2.6 Stiffness model illustrations of the frames: a) $\mathcal{F}(B)$ b) $\mathcal{F}(E)$ c) $\mathcal{F}(A)$. ..... 37
Figure 2.7 Computation chart to obtain the deflections in frame $\mathcal{F}(E)$. ..... 41
Figure 2.8 Illustration of test points (TP) and their corresponding active joint angles. ..... 43
Figure 2.9 a) Illustration of measurements from the apparatus, b) $-y$-axis view of the manipulator. ..... 50
Figure 2.10 a) Measurement of linear deflection via CMM for force load, b) applied torsion with a moment arm, c) load applied on the manipulator. ..... 51
Figure 2.11 Linear deflections for loads along $F_x$. ..... 55
Figure 2.12 Linear deflections for loads along $F_y$. ..... 56
Figure 2.13 Angular deflections about $x$- and $y$- axes. ..... 57
Figure 3.1 Flexible joint analogy ..... 63

**Figure** **Page**

Figure 3.2 Illustration of bidirectional usage of extension spring. ..... 66
Figure 3.3 Series connection setup of linear springs. a) Rigid region, b) stiff region and c) soft region. ..... 67
Figure 3.4 Parallel connection of the linear springs. ..... 68
Figure 3.5 CW and CCW assembly modes of the spiral springs. ..... 69
Figure 3.6 Flexible torsion joint of clock spring in CW mode, a) Exploded view, b) Assembled joint unit and side view, c) Load transmission on part for the CW loading, d) Load transmission on part for the CW loading. ..... 69
Figure 3.7 Spring unit with mechanical limits. a) 1st Rigid region achieved with initial tensions. b) 2nd Rigid region achieved with mechanical limits. ... 71
Figure 3.8 Series connection of flexible joint units. ..... 71
Figure 3.9 Torque/Angular deflection relation of series connected joint units with mechanical limits. (Dashed: Joint unit with stiffness $k_{\theta 1}$, Dotted: Joint unit with stiffness $k_{\theta 2}$, Solid: Series connected joint) ..... 72
Figure 3.10 Parallel flexible joint setup. 1) Parallel Assembly, 2) Parallel Mode 1, 3) Parallel Mode 2 ..... 74
Figure 3.11 Connection setups of springs. ..... 74
Figure 3.12 Spiral springs. a) Regular spiral spring, b) Clock spring inside a retainer, c) Clock spring removed from retainer. ..... 75
Figure 3.13 PVS joint. a) Exploded view of one of the flexible joint units. b) Series connection of two flexible joint units. ..... 77
Figure 3.14 Actuation options. a) Sandwich option where the output is in between the actuator and flexible joint, b) Standard option. ..... 78
Figure 3.15 Compact series spring design. a) Assembled view, b) Section cut view, c) and d) Exploded views, e) Front view. ..... 78
Figure 3.16 Prototypes of proposed PVS joint. ..... 79
Figure 3.17 Experimental setup for stiffness identification. ..... 80
Figure 3.18 Experimental setup for system identification. ..... 82
Figure 3.19 Stiffness identification experiment results. ..... 83
Figure 3.20 Bode plots of system identification results. ..... 85
Figure 4.1 a) Desired tasks at each stiffness region, b) ISO/TS 15066 2016 safe contact force profile. ..... 90
Figure 4.2 Trajectory tracking control block diagram. ..... 98

**Figure** **Page**

Figure 4.3 Impedance controller block diagram. ..... 101
Figure 4.4 Hybrid force/position controller block diagram. ..... 107
Figure 4.5 RLFJ robot controller framework. ..... 110
Figure 4.6 Five-bar RLFJ robot manipulator and experiment setup. ..... 111
Figure 4.7 Robot's kinematic and inertia properties. ..... 111
Figure 4.8 Moment vs compliant deflection of flexible joints. ..... 112
Figure 4.9 Trajectory tracking control simulation results. ..... 113
Figure 4.10 Trajectory tracking control experiment results. ..... 114
Figure 4.11 Impedance controller simulation results. ..... 116
Figure 4.12 Impedance controller simulation results with high switch gain ($\alpha_4 = 1000$). ..... 117
Figure 4.13 Impedance controller experiment results. ..... 118
Figure 4.14 Hybrid control results on a flat surface (Simulation). ..... 120
Figure 4.15 Hybrid control results on a bumpy surface (Simulation). ..... 121
Figure 4.16 Hybrid control results on a flat surface (Experiment). ..... 122
Figure 4.17 Hybrid control results on a flat surface (Experiment for $F_d = [-0.1, 0]^T$ and $\zeta_{e_{xd}} = 50(mm)$). ..... 123
Figure 4.18 Hybrid control results on a flat surface (Experiment for $F_d = [-0.1, 0]^T$ and $\zeta_{e_{xd}} = 30(mm)$). ..... 124

# LIST OF TABLES


**Table** **Page**

Table 1.1 Comparison of Flexible and Rigid Robots ..... 3

Table 1.2 Stiffness modeling methods. ..... 9

Table 1.3 Control approaches used in flexible robots. ..... 13

Table 2.1 The FEA setup details of ANSYS Workbench. ..... 44

Table 2.2 Summarized deflection results for the FEA and the VJM. ..... 45

Table 2.3 Average RMS error of model output and experimental data with updated and non-updated stiffness model parameters at loading conditions. ..... 53

Table 2.4 Average absolute error between the model and experimental data for all loading conditions. The same upper index symbol indicates the symmetric test points. ..... 54

Table A.1 Optimized modification matrix and virtual moment arms parameters. (N $\cdot$ m/m and N/rad units are simplified to N) ..... 141

Table A.2 Finite Element Analysis (FEA) and Virtual Joint Method (VJM). The compliant deflection unit is $\mu m$. Sub-indices E, A, and B indicate the force is applied from the frames $\mathcal{F}(E)$, $\mathcal{F}(A)$, and $\mathcal{F}(B)$. ..... 142

# CHAPTER 1

# INTRODUCTION

Is it possible for a robot manipulator to be perfectly rigid? The scientific answer to this question is 'No,' but the engineering aspect suggests that a robot manipulator can be considered rigid depending on the loading states on the robot manipulator. Traditionally, robot manipulators are designed to be as stiff as possible to be assumed rigid. However, this assumption may no longer hold true if certain conditions are not met. Thus, the question is not whether they are rigid but when they are. To give an answer, first, the loading states and material properties of the robot manipulator should be known.

A robot manipulator can be programmed to achieve several tasks, including pick-and-place, tracking a desired trajectory, applying force/torque, etc. Robot manipulators that will conduct these operations, especially commercial ones, are typically made with stiff materials for high-precision. They come with several specifications, such as positioning resolution (or positioning error), accuracy, precision, acceleration limits, maximum payload. If a robot manipulator operates within the acceleration and payload limits while maintaining positioning accuracy and resolution, it can be considered rigid. If the positioning accuracy is violated due to the excessive external load and if the positioning error is beyond the foreseen resolution limits, then the manipulator is no longer rigid but flexible, even if its components are highly stiff. In conclusion, the flexible/rigid state of the robot manipulator depends on its material, actuation system, task, and joint types.

At first glance, having a flexible robot seems unfavorable. This might be true for high-precision applications because the rigidity assumption facilitates accurate modeling and precise control development. Nevertheless, flexible robots are still desired for certain tasks. In fact, recent developments focus on making the robots deliberately flexible to enable them to gain new abilities such as energy efficiency, safety, compensating uncertainties (in other words, adaptability), compliance with the environment, and more. When transitioning to a flexible robot, a price needs to be paid in terms of precision, stability, bandwidth, and simplicity. The greatest trade-off might be increasing the structural intricacy of the robot manipulator, which escalates the complexity of the model and leads to arduous control development.

To understand the conflicting alliance between robot softness and control, one should gain in-depth awareness of the nature of flexible robot manipulators. The conditions that make a robot flexible or what makes it flexible can be categorized into two, albeit this number can be exploited from different aspects, such as obtaining a compliant robot through an impedance controller.

The first one is the inherently flexible robot category. In a basic sense, a robot can be considered flexible if it incorporates flexible elements such as elastic links, elastic joints, series elastic actuators, or soft actuators like pneumatic actuators. As a result of these elements, they show compliance when external wrenches are applied. Since these elements are deliberately included in the design of the robot manipulator, flexibility is a 'necessary' property in this category.

These robots excel when adaptability, energy efficiency, and safety are needed. In the case of an operation in an unstructured environment, flexible robots show high adaptability to the changing dynamics of their environment. Especially if there is a human in the workspace of the robot, a collision between the robot and the human has a reduced risk of injury. This makes them suitable for physical human-robot interaction (pHRI). Since elastic elements are reliable components for storing mechanical energy, flexible robots have the capability to convert kinetic energy to potential energy or vice-versa. This leads to less energy consumption for the robot.

The second category is when the robot becomes flexible due to the defined task. In a scenario where high acceleration and high precision are desired, a robot manipulator needs to be designed with lightweight links for low inertia but with stiff materials for resisting bending. However, less weight costs the strength of robot links. Thus, bending phenomena occur at high acceleration levels and result in vibrations. Therefore, this robot becomes flexible even though it is made of stiff materials. Because this flexibility is not desired, it can be considered an 'unwanted' property. If left unchecked, vibrations reduce the accuracy, speed, and stability. Consequently, robots' performance is reduced, and potentially, parts lead to wear or damage over time.

To clarify the differences of flexible robots with their rigid counterparts, a comparison is given in Table 1.1.

If one accepts the advantages and disadvantages of flexible robots and design a flexible robot, the next stage is to control it. At this point, the nature of flexible robots makes control design arduous for engineers for the following reasons.

Table 1.1. Comparison of Flexible and Rigid Robots

| Feature | Flexible Robots | Rigid Robots |
|---|---|---|
| **Structure** | Compliant and adaptable, with components such as flexible joints and soft links that absorb shock (Qaddoori Fenjan and Fatholahi Dehkordi, 2024). | Stiff and inflexible, typically made from metals and composite materials, providing predictable motion (Liu et al., 2022). |
| **Control Complexity** | High due to the compliance dynamics being non-linear. Needs advanced control techniques (Sayahkarajy et al., 2016). | Low, as rigid robots have predictable motion. Traditional controllers are sufficient (Abdallah et al., 1991). |
| **Safety** | Inherently safer for pHRI and has reduced collision impact (Das and Nabi, 2019). | Requires additional safety measures through control, sensors, and emergency stops (Lasota et al., 2017). |
| **Precision** | Limited; flexible elements introduce delays and deflections (Pratt and Williamson, 1995). | Preferred for high precision and repeatability for tasks like assembly, pick-and-place, and welding, especially in controlled environments (Shiakolas et al., 2002). |
| **Energy Efficiency** | High, as compliant components store and release energy, lowering energy consumption (Kashiri et al., 2018). | Lower, as all movements require direct motor power, resulting in higher energy usage (Kashiri et al., 2018). |
| **Applications** | Suitable for pHRI and surgery where safety is prioritized (Rodrigue and Kim, 2024). | Ideal for industrial automation and high precision applications (Hägele et al., 2016). |
| **Maintenance Cost** | Depending on the application, it is generally lower since low precision parts are used (Lee et al., 2017). | Depending on the application, it is typically higher since parts require high quality and precision (Parker and Draper, 1998). |
| **Durability** | May wear over time since elastic materials show lower strength (Lee et al., 2017). | Durable, designed to withstand high loads for many cycles (Kampa, 2018). |

- Flexible robots exhibit highly nonlinear dynamics. Due to their flexible components, they twist, stretch, and bend. This increases the degree of freedom (DoF) of the robot, and forward kinematics computations become less reliable. Consequently, the dynamic calculations become more unpredictable (Li et al., 2024).

- It is difficult to acquire an accurate and reliable stiffness model that is used to compute the compliant position deflections of the robot (Li et al., 2024).

- Vibrations and oscillations may arise when the robot is in motion. Damping out them can be tricky since real-time control adjustments might place significant demands on computing resources. Therefore, there is always a trade-off when gener-

ating a stiffness model that is more accurate but slower to compute or less reliable but faster to calculate (Efafi et al., 2022).

- Robot's stiffness parameters may vary depending on elapsed time, change in temperature, and loading condition (Yang et al., 2018).
- Sensing the precise state of flexible elements can be difficult. Regular encoders may not capture the compliant deformations, or sensors may not be colocated. Additional sensors like force/torque sensors, optic sensors, or acceleration sensors might be needed. This brings the problem of dealing with a redundant number of sensors, which requires complex algorithms and computation power to filter out meaningful data. (Sincak et al., 2024).
- Since flexible robots are compliant, they are prone to be affected by external disturbances like contact forces and internal uncertainties like friction and stiction. Those may cause significant deviations in the robot's behavior, leading to instabilities (Zhang et al., 2021).
- Flexible elements can store energy. If not treated well, the energy of the robot may keep increasing, violating the passivity of the system and resulting in instability (Albu-Schäffer et al., 2007).

Sometimes, flexibility in robots becomes a nice-to-have ability when increasing energy efficiency and compliance with the environment. Sometimes, flexible robots are a must-to-have for ensuring the safety of human-robot interaction. Some other times, however, flexibility is unfortunate-to-have for tasks needing high positioning accuracy. No matter how, if flexibility exists, or rather, if the flexibility of the robot manipulator cannot be neglected, then some precautions should be taken to success desired tasks.

## 1.1. Problem Definition

Three problems arose from two research projects supported by the Scientific and Technological Research Council of Turkey, and the first project is 'Methodologies for Increasing the Positioning Accuracy of High-Acceleration Parallel Robots Used in Industrial Applications' with the grant number of 116M272.

In this project, a parallel robot with an over-constrained kinematic structure has been developed. The robot's links are constructed using lightweight composite materials to achieve a high acceleration level of 5g. The problem is that vibrations occur due to high acceleration and high-frequency tasks. The first solution seems to implement a controller to suppress the vibrations, but industrial robots are unable to run custom control algorithms. Additively, there is no external sensor that directly measures the mobile platform's position or internal sensor that measures acceleration to evaluate the vibrations, not to mention that encoders at the actuator cannot capture them either. Also, no mechanical modification is allowed. So, under these conditions, the primary question is, 'How can vibrations be effectively suppressed for an industrial robot?'

The second project is 'Design of an Inherently Balanced Robotic Manipulator with Remote Center of Motion to be used as an Endoscope Holder for Endonasal Skull Base Surgery (BalanScope)' with the grant number of 219M483.

This project is focused on developing a series of robot manipulators for endonasal skull base surgery, with a particular emphasis on pHRI safety. It is crucial that the robot is inherently flexible to guarantee safety in case of a control failure. Also, preserving the robot's precision is essential if the interaction force is below the safety limit. For this, the robot should be stiff at low force/torque interactions but display higher compliance to higher loadings. These imply that the flexible behavior of the robot should be that of a softening one. In addition, maintaining the robot's remote center of motion is a must. The question is, 'How can an inherently safe and flexible robot be designed?'

The next question is, 'How can a controller be designed for a softening flexible robot?'. The control algorithm should be dexterous enough when assigning different tasks to the different stiffness levels of the robot manipulator. Those tasks mainly cover making the robot track a desired path at high stiffness, ensuring a safe pHRI at decreased stiffness, and guaranteeing safety if the load is increased even further.

The following three sections outline the reasoning and road-map for the studies addressing the problems. Detailed literature surveys follow in each subsequent chapter.

## 1.2. On Industrial Robots' Vibration Suppression

Given the problem of the industrial robot at hand, the input to the robot manipulator is the desired trajectory information. Therefore, the vibration problem needs to be

addressed by modifying the trajectory appropriately.

Trajectory modification is optimizing the motion profiles (path, velocity, acceleration, and jerk) of the robot's motion to minimize excitations that cause vibrations. An adequate trajectory design can decrease the oscillations. Some of the commonly used approaches are S-curve profiles, input shaping, and trajectory filtering.

S-curve profiles are commonly employed in industrial robots for their simplicity and effectiveness against oscillations. S-curve profiles ramp up and ramp down acceleration resulting 'S' shape in the velocity profile as illustrated in Figure 1.1. This altered acceleration profile reduces the jerk and minimizes dynamic forces and vibrations (Fang et al., 2019). This method even can be dated earlier in the form of cam profile designs, which are basically a motion template for a mechanism. These cams are designed so that the mechanism connected to the cam is exposed to low accelerations, hence, low vibrations.

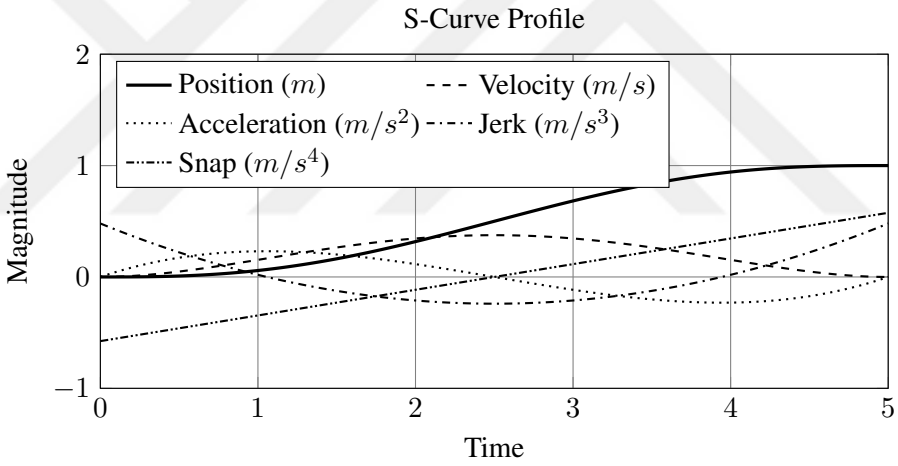



Figure 1.1. S-Curve profiles.

The input/command shaping method is quite renowned in this trajectory optimization (Singer and Seering, 1990; Singhose and Singer, 1996). As its name states, this method shapes the input command to the robot so that it avoids exhibiting its natural frequencies. The method achieves this with timed impulses at specific amplitudes as shown in Figure 1.2. This method has proven effective when vibration suppression is needed (Park et al., 2006; Singhose, 2009). An accurate system model is an essential part of the method for effectiveness.

Trajectory filtering methods analyze the frequency spectrum of the desired trajectory to filter out oscillation-inducing frequencies using low-pass, band-pass, and notch

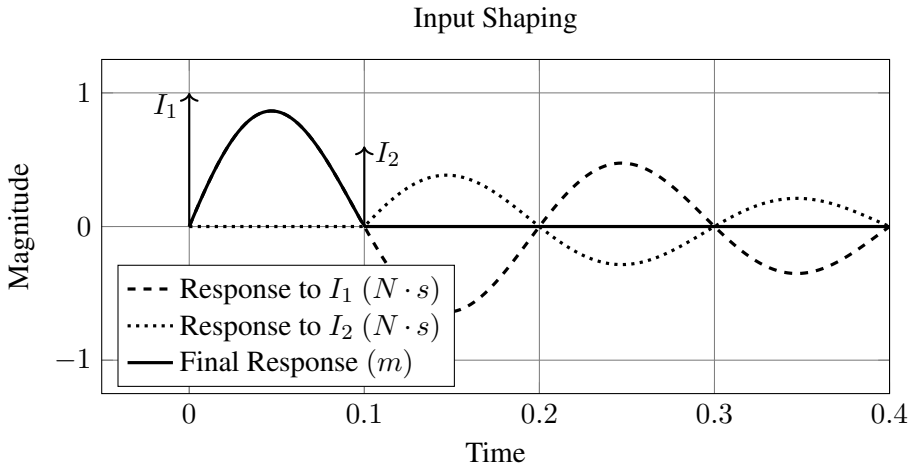



Figure 1.2. Input shaping method.

filters. As shown in Figure 1.3, this is applied when the desired trajectory has high frequency demands. However, filtering can compromise the robot's responsiveness, so a balance between vibration suppression and performance must be considered, requiring model knowledge for optimal filter design. While these methods contribute to vibration suppression, input shaping is likely to surpass them (Singhose and Vaughan, 2010).

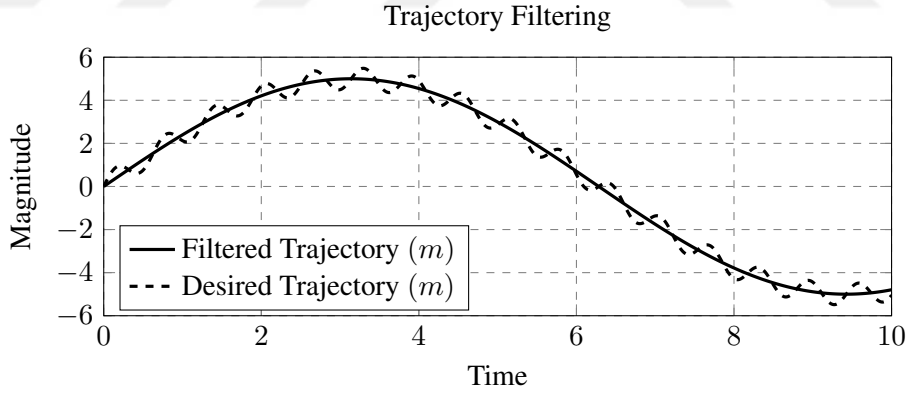



Figure 1.3. Trajectory filtering.

All of these approaches address one common thing, which is acquiring an accurate model of the robotic system. When oscillations are to be dealt with, then it would not be an exaggeration to say that the most crucial element to be known is the stiffness model. The desired trajectory and the inertia of the robot can be used to devise the dynamic loads solely due to the motion, thanks to D'Alambert's principle. The stiffness model can be combined with the loads acting on the robot manipulator to estimate and compensate the flexible deflections effectively (Klimchik, 2011; Tian et al., 2023).

An example is shown in Figure 1.4 for a triangle-shaped desired trajectory. It is apparent that at the corners of this trajectory, high acceleration occurs, hence, high dynamic loads and vibrations. Since the desired trajectory is known, it is possible to estimate the end-effector's final trajectory (desired trajectory + compliant deflections) with an accurate stiffness model. In the same manner, a modified trajectory can be designed in such a way that the final trajectory would become the desired trajectory. The flexibility of a manipulator can be modeled with methods in Table 1.2.

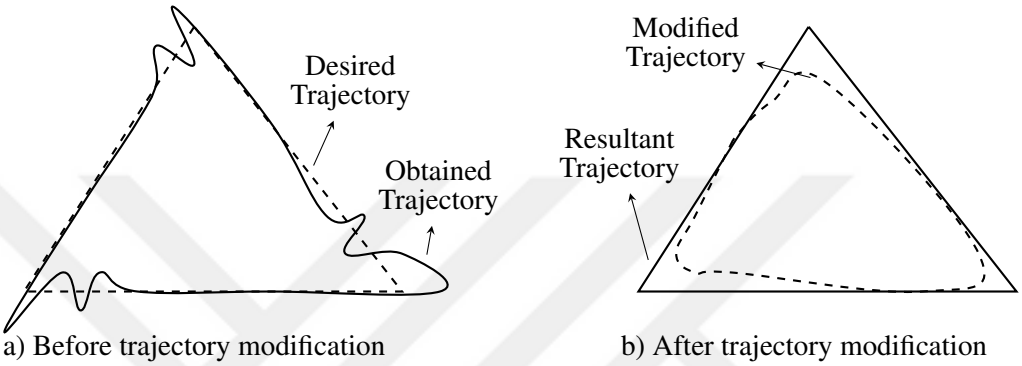



Figure 1.4. Trajectory modification with the help of stiffness model. (The triangular trajectory is followed in a counter-clockwise direction.)

## 1.3. On Safe Flexible Robot Design

A sub-category of flexible robots is soft robots that have highly flexible characteristics (Lee et al., 2017). The main distinction of soft robots is that they are made of elastic materials such as silicone or rubber. These are highly deformable materials. From one aspect, a soft robot arm can be considered a hyper-redundant robot with springs attached to its joints, not actuators. These springs, however, can display compliant deflections in any direction. Therefore, soft robots do not have constrained kinematics.

A soft link deflects in 6-DoF space and is prone to show deflections against loads in any direction. For instance, a rigid five-bar mechanism can only move in its 2-DoF motion space and is resistant to loads applied along their constrained axes. However, a five-bar mechanism made of soft links violates this constraint and gains four more DoF.

A hybrid solution with a robot made of flexible and rigid materials may clarify this problem. There are two types of this hybrid solution: Rigid Link Flexible Joint (RLFJ)

Table 1.2. Stiffness modeling methods.

| **Method** | **Description** | **Advantages and Disadvantages** |
|---|---|---|
| Finite Element Method (FEM) (Dhatt et al., 2012) | Divides the structure into small elements connected at nodes with stiffness, mass, and damping properties. | **(+):** High accuracy for complex geometries. **(-):** Computationally intensive, not suitable for real-time. |
| Virtual Joint Method (VJM) (Pashkevich et al., 2009) | Models flexibility by adding virtual springs or joints, suitable for parallel and serial robots. | **(+):** Computationally efficient, suitable for real-time. **(-):** Limited accuracy for complex compliance. |
| Structural Matrix Analysis (SMA) (Ghali et al., 2017) | Analyzes stiffness using matrix methods to calculate deflections and loads, treating the structure as a series of elements. | **(+):** Efficient for repetitive structures. **(-):** Less accurate for distributed compliance. |
| Modal Analysis (Sun et al., 2018) | Decomposes robot into vibration modes and investigates the vibration in this mode, only. | **(+):** Useful for vibration studies and dynamic analysis. **(-):** Not ideal for static stiffness modeling. |
| Piece-Wise Constant Curvature (PCC) (Renda et al., 2016) | Mainly used for continuum robots, where the robot is approximated as a series of constant curvature segments. | **(+):** Computationally efficient and suitable for real-time control. **(-):** Constant curvatures might be insufficient. |
| Stiffness Mapping Techniques (Mekaouche et al., 2015) | Generates a map across the workspace via the stiffness model and/or experimental data. | **(+):** Effective for workspace specific analysis. **(-):** Requires extensive configuration analysis. |

(Sensinger and Weir, 2006) and Flexible Link Rigid Joint (FLRJ) (Maloisel et al., 2023). Obviously, FLRJ is the case where a five-bar mechanism is made of soft links. Hence, RLFJ is the solution to the problem at hand because flexible joints can only have flexibility along their rotation and/or translation axes. This means that a flexible five-bar mechanism made of flexible joints will only have compliance in its motion space and remain rigid against loads along its constrained axes.

In the next stage, the question of where to place the flexible element in the robot manipulator pops out. In this regard, the Jacobian matrix provides the required answer. A Jacobian matrix linearly maps joint and task spaces' velocities and loads. Therefore, external loads in task space can be mapped to joint space by virtue of the Jacobian matrix. In robot arms, external loads are reflected on the joints where the actuators are connected; in other words, the actuators carry the loads. Hence, if a flexible joint is placed, it should be placed between the actuators and the robot's links. This setup of an actuator coupled with

a flexible joint form a series elastic actuator, as shown in Figure 1.5 (Pratt and Williamson, 1995). The preferred joint type is a revolute joint because revolute joints are known to be more back drivable compared to prismatic joints. The reason is that prismatic joints relatively have more friction compared to revolute joints. Thus, having a rotary series elastic actuator rather than a prismatic one is safer in pHRI (Hong et al., 2017).

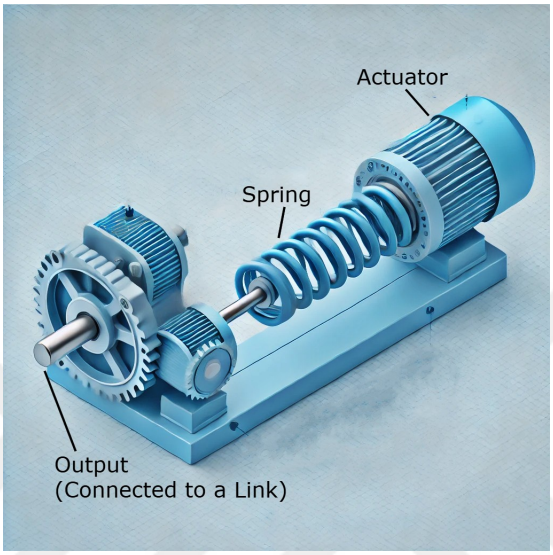



Figure 1.5. Illustration of a series elastic actuator. ("A series elastic actuator," image generated by OpenAI's DALL·E, November 5, 2024.)

Designing a rotary series elastic actuator does not necessarily require torsion spring to build it. A revolute flexible joint can be created with compression/tension springs as well (Zhao et al., 2024). The critical prerequisite is that the output of the flexible joint should be revolute (Vanderborght et al., 2013). Converting the compression/tension force to torque requires an additional mechanism (Liu et al., 2021).

The mechanism that enables this conversion generally comes with non-linear kinematics. Hence, the stiffness of the compression/tension spring is mapped non-linearly. This indicates that as the spring compresses displayed stiffness at the output changes depending on the kinematic relation of the mechanism, giving birth to a variable stiffness phenomenon, either softening or hardening. If this variable behavior is controlled externally by changing the configuration of the stiffness of the mechanism, then the flexible joint becomes an *active variable stiffness* joint. If not, then it is a *passive variable stiffness* joint (Vanderborght et al., 2013).

For ensuring the safety in case of power-related issues or malfunctions in the ac-

tuation system, an inherently flexible robot is needed. Hence, a passive variable stiffness joint with softening characteristics is required. The variable property of this flexible joint can be arranged in such a way that it is highly stiff at low torque levels but gets softer as the deflection increases. This behavior is better for precise tasks at low-level torque and safer as the torque increases.

## 1.4. On Flexible Robot Control for pHRI

The control theory has a long-standing history. A chronological review can be carried out to understand the logic and reasoning behind today's control strategies. There are so many systems to control and so many tasks to achieve. Diving into the sea of control in reverse order and trying to understand the current state of control on flexible robots might bestow a quicker insight to ascertain the borders of the study. Soft robots show extreme flexibility. Such extreme systems require cutting-edge control methods. So, a quick review on this subject is a good start.

In (Best et al., 2016), model predictive control (MPC) is used for pneumatically actuated soft robots. The controller showed better performance over PID in precision, repeatability, and disturbance handling. Yet, control accuracy remained limited due to simplifications in the model. Bruder et al. (2019) addresses this limitation by imbuing a Koopman operator to MPC to outperform linear MPC. Ataka et al. (2020) follows a traditional approach and constructs their inflatable eversion robot's model with an adaptive Euler-Bernoulli beam theory. Another model-based control in (Della Santina et al., 2020) uses Piece-wise Constant Curvature (PCC) for modeling and adopts an impedance control for interactions. However, PCC simplifications limit the performance.

Zheng et al. (2020) investigates using artificial neural networks (ANN) to model and control a soft robot made of silicone and cable driven. ANN-based control outperforms the PID controller in terms of precision and robustness. However, reacting to time-varying disturbances remains a nuisance, and the method needs extensive training. Tang et al. (2021) combines iterative learning control (ILC) with an MPC for regulating a soft robotic glove. Another learning approach used in (Zhang et al., 2017) incorporates reinforcement learning (RL) in closed-loop control, though the controller is limited by hardware capacity. Bern et al. (2020) approaches to control problems by enhancing the accuracy of the robots' ANN model with real-world training for long duration. Thieffry

et al. (2018) and Chenevier et al. (2018) focus on creating reduced order model (ROM) from finite element models of soft robots to resolve the computational cost. Yet, the problem remains as a trade-off between accuracy and computational cost, meaning cost on real-time performance.

When these studies are investigated, two conclusions can be obtained: an accurate model is essential, and feedback is necessary, which are also apparent in recent studies (Della Santina et al., 2023), thus focusing on modeling methods of flexible manipulators (Lee and Alandoli, 2020). Under these conclusions (and also getting inspiration from (Spong, 2022)), the following not-so-bold claim is made: '*The finest achievements in autonomous robotics arise not from artificial intelligence but from the mastery of superior modeling and the art of impeccable feedback control*.' This is logical because what matters is the input/output performance of the closed-loop system. What happens in between does not really matter as long as the stability and robustness are ensured for pHRI safety. Therefore, the performance of the closed-loop system is intrinsically tied to model and feedback control.

Another critical issue is that ANN-based controllers are black-box systems or gray-box at best. We know they work, but how they work may need to be clarified. If pHRI safety is entailed, then robustness and safety in the control stage should be ensured, as well. Although there are some studies to prove ANN-based control's safety by establishing hybrid models, there are several points remaining elusive (Ivanov et al., 2019, 2020; Wei and Liu, 2022). Hence, a model-based robust controller draws more curiosity for safe pHRI. Luckily, the RLFJ robot manipulators' model can be obtained relatively accurately (Spong, 1987), abolishing the necessity of a costly approach like MPC.

An RLFJ robot is actually a nonlinear under-actuated system, having more generalized coordinates variables than control inputs. Being an under-actuated system means that the desired trajectory, or rather a task, cannot be defined arbitrarily. Non-linearity, on the other hand, can be linearized by feedback linearization. If an inner loop feedback linearization is achieved, along with a proper desired task and accurate system parameters, an outer loop controller can be designed. In Table 1.3, some of the flexible robot controllers, their strengths, and weaknesses in terms of flexible robot control are presented.

This list summarizes that none of the controllers are omnipotent, each having its own flaw. For selecting suitable controller, the properties of the robotic systems, tasks to be defined, and available sensors should be known. Only then can one decide on a suitable controller.

Table 1.3. Control approaches used in flexible robots.

| **Control Method** | **Advantages** | **Disadvantages** |
|---|---|---|
| PID Control (Alandoli and Lee, 2020) | Simple, easy to design, computationally efficient | Limited in dealing with flexible systems |
| Linear Quadratic Regulator (LQR) (Alandoli and Lee, 2020) | Optimum and stable control for systems with linearizable dynamics | Less effective for flexible and nonlinear systems |
| Impedance Control (Sharifi et al., 2021) | Adjusts virtual stiffness and damping, stable and robust | Requires careful tuning for desired performance |
| Admittance Control (Li et al., 2018) | Adjusts robot's motion to make it compliant for interactions, stable | Might become unstable when the robot interacts with rigid environments, requires a force sensor |
| Sliding Mode Control (SMC) (Alandoli and Lee, 2020) | Robust to uncertainties and effective for trajectory tracking | Has chattering and causes a toll on actuators |
| $\mu$-Synthesis Control (Alandoli and Lee, 2020) | Provides robust control, responsive to uncertainties and vibrations | Complicated design and arduous implementation. Computationally demanding |
| $H_\infty$ Control (Alandoli and Lee, 2020) | Can handle nonlinear systems, robust, suitable for vibration attenuation | Complex to design and compute |
| Adaptive Control (Bar-Kana and Kaufman, 1993; Jin et al., 2016) | Updates parameters in real-time, adapting to changes in dynamics | Needs significant sensory input. Has intense computations and potential stability issues |
| Back-stepping Control (Lim et al., 1995) | Highly capable when dealing with nonlinear systems and providing accuracy in trajectory tracking | Complex to implement |
| Hybrid Control | Combines various controllers, can exploit advantages of flexible systems | Complex to implement and synchronize, having the risk of going unstable |

Among them, however, impedance and admittance controllers are favored in pHRI tasks because they are originally meant to control the robot's interactions with the environment. The admittance controller is deemed as a safer option in pHRI compared to impedance controller (Sharkawy and Koustoumpardis, 2022). This claim is valid but incomplete.

In admittance control, the robot's motion is regulated in accordance with the applied external force to its end-effector. An admittance controller is a good choice only if the robot is rigid and interacts with a soft environment, such as humans because a rigid robot's motion control can be achieved with high accuracy. If admittance controller is implemented in flexible robot control, some complications would be inevitable since flexible

robot motion control is challenging.

In impedance controller, on the other hand, robots' impedance is adjusted with respect to motion input to the robot's end-effector. This controller is usually preferred in rigid robot control if the environment is also rigid because impedance control adds virtual flexibility to the robot, making it compliant and safer. Since a flexible robot is inherently compliant, considering impedance control for flexible robots in pHRI might be a better choice.

## 1.5. Aims of the Dissertation

This dissertation aims to realize the solutions of three problems given in Section 1.1. Each issue holds specific requirements and limitations. Given these constraints and objectives, some solutions are devised as a result of the preliminary literature survey, which cleared out a road map. The aims to make these solutions available and criteria are presented in this section. Each problem is addressed separately, and a thorough analysis is given in seven steps.

### 1.5.1. Obtaining an industrial robots' stiffness model for vibration suppression

(1) **Problem:** High acceleration in industrial parallel robots results in vibrations.

(2) **Analysis:** The robot is composed of lightweight hollow materials to reduce the moving mass for reaching desired acceleration levels. Hollow materials have less strength. According to D'Alambert's principle, high acceleration causes high dynamic loads. Under these conditions, the robot displays compliant deflections, thus vibrating.

(3) **Question:** How can vibrations be effectively suppressed for an industrial robot?

(4) **Limitations/Requirements on Solution:**

- Custom controller cannot be embedded in the robot.
- Only the desired trajectory information can be fed to the robot.

- Additional sensors (accelerometer) or mechanical modification are not feasible in terms of cost and imposed acceleration limitation due to inertia.

(5) **Solution:** If we obtain a stiffness model of the robot, we can estimate the resulting flexible movements using dynamic loads calculated from inertia and the desired trajectory. We can then create a new adjusted trajectory using the stiffness model to match the resulting trajectory with the desired one.

(6) **Aim:** Developing an accurate stiffness model.

(7) **Criteria:** The model should;

- be developed for an over-constrained mechanism.
- consider internal stress' effect on stiffness.
- consider the effect of auxiliary loads on the end-effector's deflection.
- keep up with real-time computations.

### 1.5.2. Designing a flexible joint for an inherently safe robot

(1) **Problem:** High force output from the end-effector of a robot may lead to injuries for humans in pHRI.

(2) **Analysis:** Stability and safety of a robot used in pHRI depend on the seamless working of several components of the robot such as the control algorithm, the computer that runs the controller, sensors, data acquisition boards, power supply, drivers and actuators. Failure in one of these components may cause high force output at the end-effector of the robot, hence injuring the human operator.

(3) **Question:** How can an inherently safe and flexible robot be designed?

(4) **Limitations/Requirements on Solution:**

- The robot must preserve its kinematic constraints.
- The robot requires softening stiffness characteristics as shown in Figure 1.6.
- The robot should be rigid at low torque levels for operations that require precise positioning.

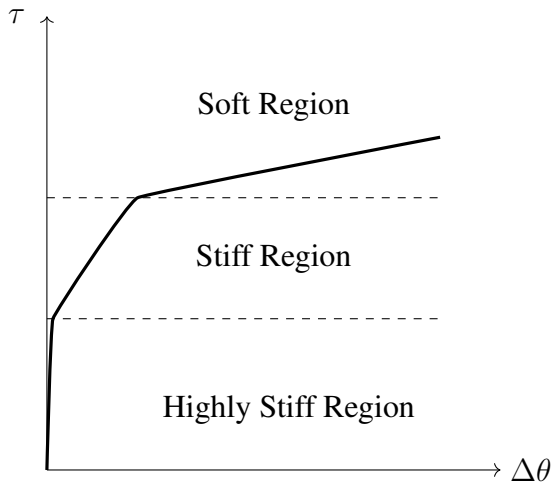



Figure 1.6. Required stiffness characteristics of flexible joint.

(5) **Solution:** Implementing a flexible element in between actuators and the robot's link makes the robot flexible and compliant to excessive loads. As a result, robots become inherently safe.

(6) **Aim:** Developing a flexible rotary joint.

(7) **Criteria:** The flexible joint should;

- be a passive variable stiffness joint for inherent safety.
- comprise at least two springs in series for softening.
- change its stiffness as a function of torque on it (no clutch mechanism).

### 1.5.3. Developing a controller for an RLFJ robot manipulator

(1) **Problem:** Designing a stable and versatile controller for an inherently flexible robot with variable stiffness is challenging when interactions with humans/environment are considered.

(2) **Analysis:** The variable stiffness profile in Figure 1.6 addresses a discontinuous stiffness model. Each stiffness region results in a different dynamic model of the robot, meaning the robot's parameters switch. Moreover, the purpose of different stiffness regions is to achieve different tasks. That also requires switching between different controllers. If not adjusted properly, the controller may cause instability in closed-loop control.

(3) **Question:** How can a controller be designed for a softening flexible robot?

(4) **Limitations/Requirements on Solution:**

- The closed loop system must be stable.
- The robot should follow a desired trajectory at a highly stiff (or can be assumed rigid) region.
- The robot should conduct soft interactions with humans and the relatively stiffer environment.
- The robot should initiate safety precautions in the soft region.

(5) **Proposed Solution:** A hybrid controller, composed of the necessary controller for each desired task, may solve the control problem.

(6) **Aim:** Designing a hybrid controller for achieving desired tasks.

(7) **Criteria:** The controller should;

- track the trajectory in highly stiff region.
- compensate for the lack of velocity information of actuators and robot link angles.
- handle with pHRI and force/position tracking.
- remain stable against disturbances.
- have stable switching between controllers.
- initiate safety precautions at the soft region in accordance with ISO/TS 15066 (de Normalización, 2016).

## 1.6. Contributions

1. A **new stiffness modeling method** is introduced for an industrial over-constrained robot mechanism operating at high acceleration and frequency. The model can consider auxiliary forces on other bodies while calculating the compliant deflection of the end-effector. The model's parameters are optimized to comply with the experiment data. The RMS error between the model and experiment is 5.9 μm. The model estimates the compliant deflections in 6-DoF space at high accuracy and can run at 10 kHz.

2. A **novel flexible revolute joint design** is proposed. This flexible joint's stiffness passively varies depending on its torque. The most notable property, however, is that it has an assembly mode that displays a softening stiffness characteristic for guaranteeing inherently safe robots for human-robot interaction. There is a distinct transition in stiffness regions. This softening behavior of flexible joints forms three stiffness regions: rigid, stiff, and soft. Later, it was used as a series elastic actuator in a five-bar robot mechanism.

3. An **innovative hybrid control framework solution** has been proposed. Hybrid controllers consist of Lyapunov-based trajectory tracking control, impedance control, and force/position control to exploit the virtues of the flexible five-bar robot's rigid, stiff, and soft regions. The rigid region is mainly preserved for trajectory tracking. An impedance controller for human-robot collaboration and a hybrid force/position controller algorithms are run in the stiff regions. A set of appropriate velocity and torque observers are designed. The control structure tracks the torque on the rotary flexible element and adjusts the gain scheduling for a smooth transition between the controllers. A stabilizer algorithm is automatically activated if an unexpected case occurs; in other words, instability arises. On top of everything, a set of safety measures is designed as a safeguard if a robot enters the soft region due to excessive forces. This safeguard pulls the robot manipulator to a stable state and ceases all other activities until safety is ensured. This whole control structure was simulated in MATLAB Simulink and tested on the five-bar flexible robot setup.

# CHAPTER 2

# STIFFNESS MODELING OF A 2-DOF OVER-CONSTRAINED PLANAR PARALLEL MECHANISM[1]

Stiffness model acquisition of over-constrained parallel mechanisms is relatively difficult since they have more than necessary kinematic loops. In this study, a stiffness modeling solution for over-constrained parallel mechanisms is proposed while considering the computational cost efficiency. Three contributions of the chapter are: (1) Presenting the stiffness modeling procedure for serially connected closed-loop structures by using the Virtual Joint Method (2) Considering the effect of dynamic auxiliary forces and dynamic external forces on the mobile platform's deflection and achieving a direct solution by using superposition principle (3) A model fitting procedure for modifying the stiffness coefficients to comply with the experimental data. A 2 degrees-of-freedom over-constrained parallel mechanism is investigated as a case study. However, the proposed stiffness model is 6-DoF since compliant deflections occur in any direction. A finite element analysis and an experimental study verify the model's results.

## 2.1. Introduction

Linkages with high stiffness are desired in the construction of industrial mechanisms to minimize compliant deflections for maintaining accuracy and precision. Stiff linkages result in bulky structures. In return, the system's inertia, power requirements, and electricity cost increase. On the other hand, low-power actuators limit the acceleration of the mechanism and increase the operation time. A solution is to utilize lightweight linkages and address the compliance problem by incorporating the stiffness characteristics of the mechanism in the control system. This work explores the possibility of using a

[1]Görgülü I., Dede M.I.C., Kiper G., "Stiffness modeling of a 2-DoF over-constrained planar parallel mechanism", Mechanism and Machine Theory, Volume 185, 2023.

stiffness model within the control system in real time.

Researchers have focused on three stiffness analysis methods of mechanisms. These are the finite element analysis (FEA), the structural matrix analysis (SMA), and the virtual joint method (VJM). The FEA is the most accurate method due to its higher number of meshes and iterative computation methodology. However, the FEA is computationally intensive and not applicable in a real-time control loop. In addition, each linkage must be re-meshed in every configuration change (Huang et al., 2002). The SMA is a faster method with fewer meshes and nodes (Ghali et al., 2014). A simple beam can be modeled with nodes represented by a $12 \times 12$ stiffness matrix. A higher number of nodes and several limbs of a parallel manipulator may result in higher dimensional matrices which are challenging in analytical computations (Klimchik et al., 2014; Pashkevich et al., 2009).

The VJM locates a single node on each link resulting in a $6 \times 6$ stiffness matrix per link. Therefore, it is also called lumped method approach. The stiffness properties are lumped on a 6 degrees-of-freedom (DoF) virtual joint (or virtual spring) (Salisbury and Craig, 1982; Gosselin, 1990, 2002; Pashkevich et al., 2009; Wu et al., 2014; Hoevenaars et al., 2016). The smaller size of local stiffness matrices and fewer variables make the VJM the simplest and the fastest method. It is also easier to obtain an analytic stiffness model. This way, a small force-to-deflection ratio can be computed in one computation step. Both the SMA and the VJM generally adopt coordinate transformations; however, strain energy with Castigliano's theorem is used to avoid these transformations. The loss in the computation accuracy with the VJM and the SMA versus the FEA is about 1%, as reported in (Görgülü et al., 2020; Yang et al., 2019, 2018). The gain in computation efficiency for 1% of accuracy loss is about 99.998% as reported in (Görgülü et al., 2020) in which the VJM is used to compute the deflections in 0.5 ms. Similarly, a solution of the SMA is obtained in 10 ms in (Klimchik et al., 2019a).

Stiffness modeling methods have been well-established for serial manipulators which have a single kinematic chain. On the other hand, parallel manipulators have internal stresses, passive joints, and several closed kinematic loops. These increase the complexity of the problem because the contribution of each limb to the stiffness must be considered simultaneously (Pashkevich et al., 2011, 2009; Klimchik et al., 2013). In addition, auxiliary wrenches on each link should be distributed throughout the bodies of the manipulator that are solved by iterative computations (Klimchik et al., 2014). Nonetheless, parallel mechanisms are known to possess high positioning accuracy compared to

serial mechanisms (Merlet, 2006; Briot and Bonev, 2007). Over-constrained parallel mechanisms (OCPM) are usually preferred over simply-constrained parallel mechanisms (SCPM) for their higher stiffness (Romdhane et al., 2002; Pashkevich et al., 2009; Harib et al., 2012). It is also reported that OCPMs have good repeatability (Kiper et al., 2015). OCPMs have more joints/links than required, which may increase the number of closed kinematic loops, internal stresses, and the number of joints when compared to SCPMs. Also, the manipulator becomes statically indeterminate, which makes it challenging to compute the distribution of the external load on the links; thus, the compliant deflections.

In (Hu and Huang, 2016), Hu and Huang obtained the stiffness model of a 2RPU-UPR (U=universal joint, P=prismatic joint, R=revolute joint) OCPMs. Stiffness analysis for a class of OCPMs with US (S=spherical joint) and UPS limbs is formulated in (Vertechy and Parenti-Castelli, 2007). Ding et al. (2018) analyzed the accuracy of an over-constrained Stewart platform with actuation stiffness. Yang et al. (2018, 2019) obtained the stiffness model of 2UPR-RPU and 2PUR-PSR OCPMs via strain energy computation by achieving 0.8% and 1.3% accuracy loss compared to the FEA. Cao et al. (2017); Cao and Ding (2018) obtained the stiffness model of OCPMs by using an energy method with less than 3% accuracy loss. Cao et al. (2019) extended the approach considering the weights of the links in which the weight of each limb is distributed between the mobile platform frame and the base.

The manipulators in the studies above have serial kinematic structures in their limbs. Differently, Sun et al. (2016) acquired the stiffness model of a 2-DoF rotational parallel mechanism in which each limb has a closed-loop kinematic chain considering the external wrenches and link weights. Cammarata (2016) included the joint flexibility and pre-loading at joints for the manipulators with closed-loop chains such as parallelograms in their limbs resulting in 3% accuracy loss. Pashkevich et al. (2009) derived the stiffness model of the 3-DoF Orthoglide parallel manipulator in which each limb has a single parallelogram. Nonetheless, the case for consecutive connections of closed-loop chains is not investigated. Later, auxiliary forces on each link are considered, and the effect of each force on the mobile platform's compliant deflection is determined via an iterative solution since the interaction between the limbs must be considered (Klimchik et al., 2014). Finally, Klimchik et al. (2019b) derived the stiffness model of NAVARO II. In (Klimchik et al., 2019b), the connection method of multiple closed-loop chains is illustrated for an external wrench on the mobile platform via SMA; however, the dimensions of the matrices to be computed were relatively high. The fundamentals of the SMA methodology are

given in (Klimchik et al., 2019a).

This chapter focuses on the stiffness formulation of a 2-DoF planar OCPM by using the VJM. However, the stiffness model is 6-DoF since the compliance may occur in any direction. The novelty and the contribution of this work to the literature on mechanisms and machine science are explained as follows:

(1) The inspected mechanism contains a serial connection of closed loops at its limbs, namely, the serial connection of two parallelograms. In the current literature, the VJM is applied for a parallelogram loop connected to a distal link at one node, but a serial connection of two parallelograms in which the connection occurs at two nodes is not studied. This proposed stiffness modeling solution method constructs the basis for the serial connection of closed-loop sub-chains.

(2) In the literature, external wrenches at the mobile platform and auxiliary forces on the links are assumed to be caused by the payload/physical interaction and the weight of the links, respectively. In this study, auxiliary loads due to the acceleration of bodies are considered. In (Klimchik et al., 2014), weights of the links are considered which can be extended for the dynamic cases. However, the solution relies on iterative computations to converge an equal deflection of all limbs at the mobile platform frame. Without iteration, there is no way to conclude how the weight of a limb affects the other limbs' deflection. In the proposed method, a stiffness model is constructed for each auxiliary frame and computed their deflections. Since the joint space deflections are directly obtained, the deflection of all limbs and mobile platform frame are directly computed. Finally, the superposition principle is adopted to compute the resultant deflection. In addition, deflections caused by gravity generally refer to a static case problem. The aim is to use the stiffness model in a control loop to enhance the deflection performance caused by non-gravitational acceleration. Hence, developing a computationally efficient model is necessary. It is also shown how to lump the masses directly on the loading frames. In the case study, 11 moving bodies' masses are lumped on two auxiliary and one mobile platform frame.

(3) A model fitting procedure to comply with the experimental load/deflection tests is introduced. Several unknown correction gain parameters are defined for model fitting, in which their values are determined via an optimization process. These gain parameters are formed so that the configuration and non-configuration-dependent values of the stiffness matrix elements can be captured.

This work aims to acquire a compliance model of OCPMs that is computationally

efficient and can be used in a real-time control loop. The application of the proposed methodology is straightforward once the initially required matrices and vectors are defined. The procedure avoids defining a specific stiffness matrix for each link depending on its DoF and constraints. The results of the FEA and the VJM are compared to validate the stiffness model and to evaluate the computation time performance. Finally, the stiffness model parameters are updated via an experimental procedure. The results indicate a good model fit for the mechanism's stiffness characteristics.

## 2.2. Stiffness Modeling via the Virtual Joint Method

This section gives brief information for the stiffness modeling of parallel mechanisms via the VJM as explained in detail in (Pashkevich et al., 2011) and a glossary given in below. This generic formulation may be adapted to the exceptional cases of the problem at hand. These are highlighted in the case study in Section 2.3.

In the VJM, compliant deflections are small enough to assume $\Delta\bar{X}_i \approx \boldsymbol{J}_i\Delta\bar{Q}_i$ where $\Delta\bar{X}_i$ is the change in position vector of the inspected frame, $\Delta\bar{Q}_i$ is the change in joint space variables, and $\boldsymbol{J}_i$ is the Jacobian matrix of the $i^{\text{th}}$ limb in a parallel manipulator. Bar notations indicate the column matrix format. The compliant deflection, applied load, and passive joint's zero-stiffness-effect for the $i^{\text{th}}$ limb are constructed in the following block matrix format:

$$\begin{bmatrix} (\boldsymbol{J}_{\theta i}\boldsymbol{K}_{\theta i}^{-1}\boldsymbol{J}_{\theta i}^{T}) & \boldsymbol{J}_{pi} \\ \boldsymbol{J}_{pi}^{T} & \mathbf{0} \end{bmatrix} \begin{bmatrix} \bar{F}_{i,ext} \\ \Delta\bar{q}_{pi} \end{bmatrix} = \begin{bmatrix} \Delta\bar{X}_i \\ \bar{0} \end{bmatrix} \tag{2.1}$$

where $\boldsymbol{J}_{\theta i}$, and $\boldsymbol{J}_{pi}$ are the Jacobian matrices that are obtained by taking the partial derivative of the forward kinematic with respect to virtual, and passive joint variables. Accordingly, $\theta$ and $p$ subscripts reflect the relation for virtual, and passive joint variables. $[\boldsymbol{K}_{\theta i}]_{6n\times 6n}$ denotes the non-diagonal structural stiffness matrix belonging to the $i^{\text{th}}$ limb that has $n$ links each defined in their respective link's frame. $[\bar{F}_{i,ext}]_{6\times 1}$ is the external force/torque vector carried by the $i^{\text{th}}$ limb. The bar symbol on top of the variable denotes that the variable is a column matrix. $\bar{q}_{pi}$ contains passive joint variables. $\mathbf{0}$ in the left-hand side matrix contributes the zero-stiffness effect of passive joints.

The matrix at the left-hand side of Equation 2.1 is a compliance matrix of the

virtual and passive joints, namely $\boldsymbol{C}_i$. Taking the inverse of this matrix produces a stiffness matrix including the combined characteristics of the virtual and passive joints. A sub-matrix is extracted from the inverted $\boldsymbol{C}_i$ matrix which is a rank-deficient structural stiffness matrix, $\boldsymbol{K}_i$. This rank deficiency is a result of passive joints' zero-stiffness effect. The inversion is shown as follows:

$$\boldsymbol{C}_i = \begin{bmatrix} (\boldsymbol{J}_{\theta i}\boldsymbol{K}_{\theta i}^{-1}\boldsymbol{J}_{\theta i}^{T}) & \boldsymbol{J}_{pi} \\ \boldsymbol{J}_{pi}^{T} & \mathbf{0} \end{bmatrix} \qquad \Rightarrow \boldsymbol{C}_i^{-1} = \left[\begin{array}{c:c} [\boldsymbol{K}_i]_{6\times 6} & \sim \\ \hdashline [\boldsymbol{K}_{pi}] & \sim \end{array}\right] \tag{2.2}$$

where upper-left $6 \times 6$ sub-part of the above inversion contains the desired Cartesian stiffness matrix, $\boldsymbol{K}_i$. $\boldsymbol{K}_{pi}$ gives the relation between the compliant deflections and passive joint motion. The compliance matrix is a function of joint variables. If the manipulator is not in a singular configuration or does not go into a singular pose after a compliant deflection, $\boldsymbol{C}_i$ is always invertible. The latter can occur in an iterative solution process.

In parallel mechanisms, limbs are represented as a 6-DoF spring. Parallel connected springs are directly summed up to compute the equivalent spring model as shown in Equation 2.3. It is assumed that external force $\bar{F}_{ext}$ is known but the distribution of this force on the limbs is yet to be determined. Since all the limbs are connected at one node, the deflections are all equal. After solving Equation 2.4 for $\Delta\bar{X}$, loads carried by each limb are computed as shown in Equation 2.5.

$$\boldsymbol{K} = \sum_{i=1}^{n} \boldsymbol{K}_i, \quad \bar{F}_{ext} = \sum_{i=1}^{n} \bar{F}_{i,ext}, \quad \Delta\bar{X} = \Delta\bar{X}_1 = \Delta\bar{X}_2 = ... = \Delta\bar{X}_n \tag{2.3}$$

$$\bar{F}_{ext} = \boldsymbol{K}\Delta\bar{X} \tag{2.4}$$

$$\bar{F}_{i,ext} = \boldsymbol{K}_i\Delta\bar{X} \tag{2.5}$$

where $\bar{F}_{ext}$ external wrench applied on the mobile platform. $\boldsymbol{K}$ is the structural stiffness matrix of the manipulator.

Note that the matrix $\boldsymbol{C}_i$ is expressed symbolically. Computers may not handle this inversion operation. To obtain a quick solution, a numeric recursive computation is required.

The initial computation step of virtual joint variable column matrix, $\bar{\theta}_i = \bar{0}$ in $\boldsymbol{J}_{\theta i}$.

This first assignment gives a solution in which the external force/torque is distributed on the flexible bodies with respect to the undeflected states of the links. As the manipulator experiences a compliant displacement, the force/torque distribution changes accordingly. A back-substitution of the virtual and passive joint variables is required to consider this effect.

Once the compliant deflection, $\Delta\bar{X}$, is computed, Equation 2.5 can be used. Solution of Equation 2.6 gives the new $\bar{\theta}_i^{(k+1)}$ where $k$ is the iteration number for $k = 0, 1, ....$ Superscript $(0)$ denotes the state when there is no load on the manipulator. Finally, Equation 2.7 gives the relaxation of passive joints.

$$\boldsymbol{K}_{\theta i}(\bar{\theta}_i^{(k)}, \bar{q}_{ai}^{(0)}, \bar{q}_{pi}^{(k)})[\bar{\theta}_i^{(k+1)} - \bar{\theta}_i^{(0)}] = [\boldsymbol{J}_i^T(\bar{\theta}_i^{(k)}, \bar{q}_{ai}^{(0)}, \bar{q}_{pi}^{(k)})]\bar{F}_{i,ext}^{(k)} \tag{2.6}$$

$$\bar{q}_{pi}^{(k+1)} - \bar{q}_{pi}^{(0)} = \boldsymbol{K}_{(pi)}(\bar{\theta}_i^{(k)}, \bar{q}_{ai}^{(0)}, \bar{q}_{pi}^{(k)})\bar{X}_i^{(k)} \tag{2.7}$$

where $\bar{q}_{ai}$ is a column matrix that contains active joint variables. Generally, it has only one element for parallel manipulators with a single actuator at each limb.

In a static loading case on the mobile platform, an iterative solution is obtained within 3 to 5 iterations (Pashkevich et al., 2009). However, this accuracy improvement is limited for simply-constrained and over-constrained parallel manipulators. Hence, direct computation is preferred.

## 2.3. Case study: Modified 6R Over-Constrained Parallel Mechanism

The over-constrained structure makes the stiffness modeling process more challenging due to several kinematic loop closures. Hence, a systematic modeling approach needs to be developed. Before the modeling process, some simplifications and assumptions must be made.

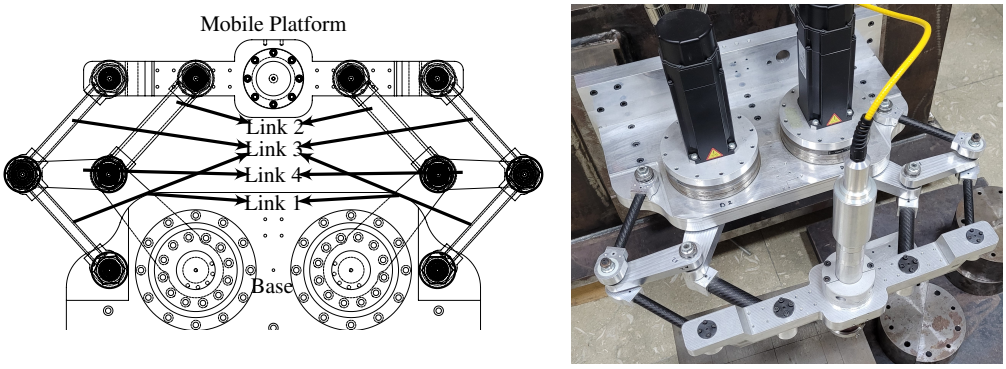
### 2.3.1. The Mechanism's Insight

A drawing of the mechanism is given in Figure 2.1. There are 4 different types of links as shown in the Figure 2.2. While Link 1 and Link 4 are made of aluminium alloy,

Link 2 and Link 3 are combinations of aluminium parts and carbon fiber tubes to have a lighter manipulator. The tubes and aluminium parts are attached via pins and industrial glues. Bearings and retaining rings are made of stainless steel and assembled to Links 2 and 3. Multiple bearings are used on both sides of the aluminium parts for these links to minimize joint clearances. Thus, the following simplifications and assumptions are made in the stiffness model computations:

- The base and the mobile platform are made of thick aluminium alloy. Therefore, they are assumed to be rigid.
- Link 4 is made of aluminium and exposed to tension/compression forces. Therefore, it is assumed to be rigid since the part is highly stiff against these force types. It should be noted that this is not a general case for all parallelogram loops. If there is an assembly arrangement such as the one presented in (Klimchik et al., 2019a), then all the links of a parallelogram may be considered as flexible.
- Links 2 and 3 are flexible due to thin carbon fiber tubes and the glue used for fixing the tubes and the aluminium parts.
- The bearing/retaining rings are stiffened stainless steel. Therefore, these parts are assumed to be rigid.
- The manipulator is over-constrained. Therefore, the joint clearances are assumed to be negligible.
- Link 1 is the actuated link. However, this link is considerably thicker in the link group. Hence, it is relatively rigid. Nonetheless, the link is considered flexible to preserve the generality of the formulation. Its rigidity is achieved by assigning a high stiffness value which did not result in an observable effect in computations.
- The main focus in this chapter is the structural stiffness modeling of this mechanism. In a wider aspect, the stiffness of the actuation, bearings, balancing springs, and series elastic actuators can be considered. Those can be the subject of another research as a future study.

Next, the forces/torques are classified and considered to compute compliant deflections. Since the manipulator has no force/torque interaction with an external object, effective force/torques are caused by dynamic effects and gravity. These are related to inertia. Hence, the followings are considered for mass and mass moment of inertia distribution:




a) b)

Figure 2.1. a) CAD sketch and link types of the manipulator, b) the manipulator.

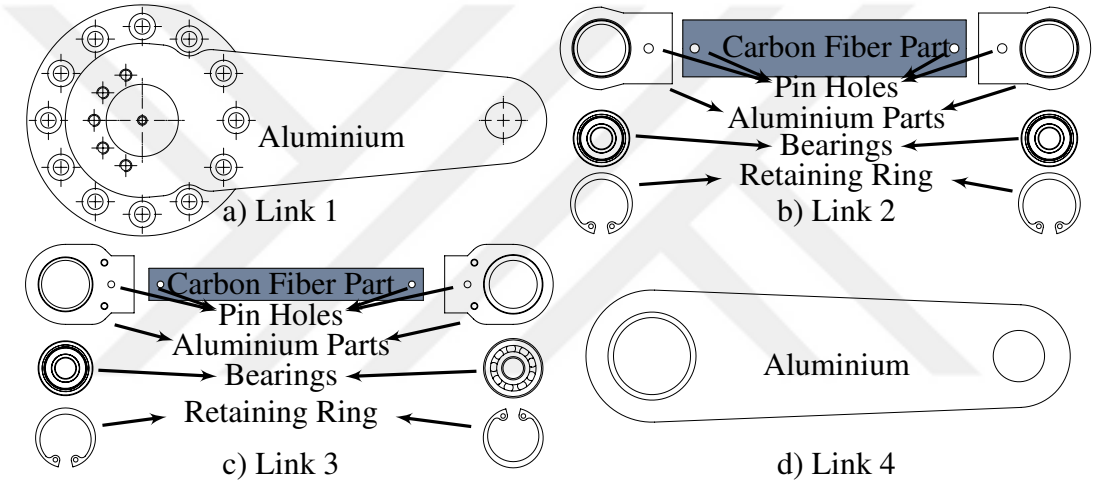



Figure 2.2. Four types of links.

- Accelerations at the mobile platform are up to 5g. Since dynamic effects are dominant, gravitational effects are excluded.
- Carbon fiber tubes of Links 2 and 3 are lightweight compared to their aluminium parts and bearings. Therefore, it can be assumed that the masses are accumulated at the proximal and distal ends of the links instead of the geometric center of the link. As a result, dynamic and gravitational forces/moments are generated at the connection nodes/joints of these links.
- Accumulated masses have a limited rotation, but linear accelerations of these masses are dominant. So, the inertial effects due to rotational motion can be neglected.
- The mobile platform is assumed to have no rotation since the joint clearances are relatively small.

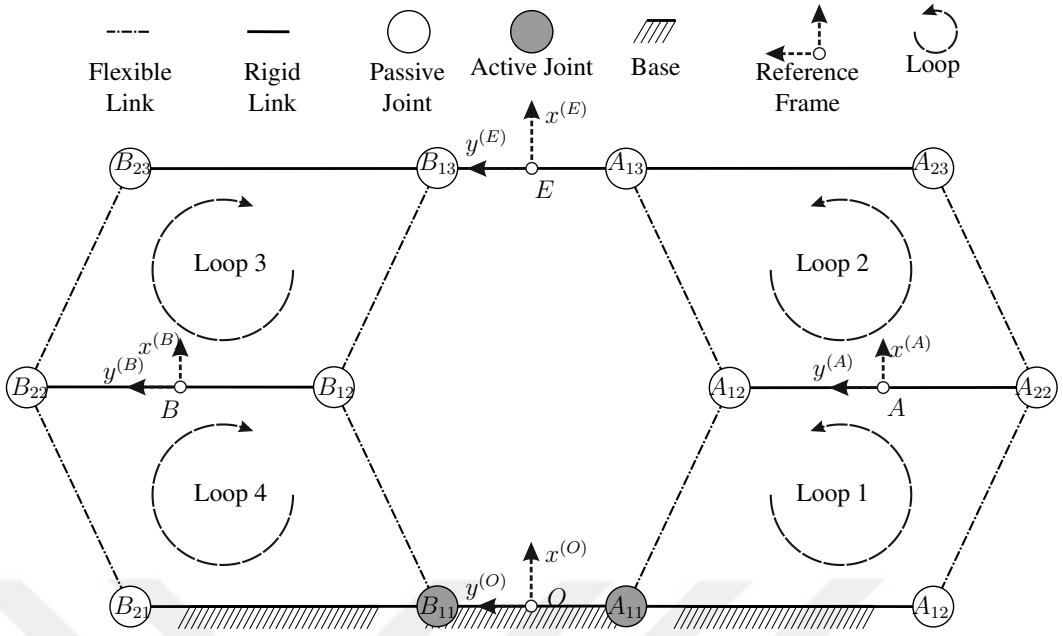



Figure 2.3. Kinematic sketch of modified 6R manipulator and its components.

- Link 4 is assumed to have no rotation, and its mass is equally distributed on the connection nodes/joints.
- Compared to force/moment on the distal end of Link 1 that is caused by the motion of the mobile platform, dynamic forces/moments of Link 1, due to its inertial properties, are negligible.
- The kinematic motion of the manipulator is planar. Consequently, only two components of the resulting dynamic forces acting on the plane and the moment about the normal of this plane can be considered.

### 2.3.2. Stiffness Modeling Objectives

After all these analyses, it is possible to construct a simplified sketch of the manipulator for stiffness model computations as shown in Figure 2.3. The main objective is to compute the compliant deflection of the mobile platform frame, $\mathcal{F}(E)$.

Note that the masses of the links are accumulated on the joints. The masses at the joints $B_{21}$, and $A_{21}$ are not considered since they are at the base. Masses on $B_{22}$-$B_{12}$, and $A_{12}$-$A_{22}$ pairs are rigidly connected to each other. In addition to the mobile platform mass, distributed mass groups of the links at $B_{23}$, $B_{13}$, $A_{13}$, and $B_{23}$ joints are rigidly

connected. The mass centers and also the geometric centers of these connections are located at the origins of frames $\mathcal{F}(E)$, $\mathcal{F}(B)$, and $\mathcal{F}(A)$ as shown in Figure 2.3. These frames are the frames where the external forces/torques are generated due to the dynamic motion and the gravity. Even if there is only one force/torque on one of these frames, not only this frame's location, but also the other frame locations are affected since all links are connected. To compute this effect, there should be 3 stiffness models for all 3 frames. To compute these 3 stiffness models, a solution approach may adopt the divide-and-conquer strategy to overcome the modeling difficulties.

Considering the smallest sub-structures in Figure 2.3, there are 4 sub-loops that are composed of parallelograms. Loops 1 and 4 are active loops that are connected to actuators. Loops 2 and 3 are the passive loops. Loop pair 1-4, and loop pair 2-3 have the same stiffness properties. If the stiffness model of each loop is obtained by connecting them first serially and then parallel to each other, it is possible to get stiffness matrices of the frames $\mathcal{F}(E)$, $\mathcal{F}(B)$, and $\mathcal{F}(A)$.

Let us name the stiffness matrices of the loops 1, 2, 3, and 4 as $\boldsymbol{K}_{L1}$, $\boldsymbol{K}_{L2}$, $\boldsymbol{K}_{L3}$, and $\boldsymbol{K}_{L4}$, respectively. Also, the resulting stiffness matrices for the frames $\mathcal{F}(E)$, $\mathcal{F}(B)$, and $\mathcal{F}(A)$ are called $\boldsymbol{K}_E$, $\boldsymbol{K}_B$, and $\boldsymbol{K}_A$, respectively. By considering the serial/parallel connections of the loops, desired stiffness models are represented in Figure 2.4.

In summary, the sub-tasks that should be completed to obtain stiffness models can be listed as follows:

- Divide the mechanism into smaller parallelogram sub-loops.
- Obtain the stiffness model of each sub-loop. (Parallelogram loop level stiffness model)
- Obtain the stiffness model of each serial limb made up of serial connection of these sub-loops.
- Obtain the stiffness model of the entire mechanism by composing the stiffness models of each serial limb. (6R loop level stiffness model)

### 2.3.3. Stiffness Model of the Parallelogram Loops

The first sub-task is to obtain stiffness matrices of both passive and active parallelograms. Figure 2.5 shows a generic sketch of a parallelogram. Figure 2.5 a) shows

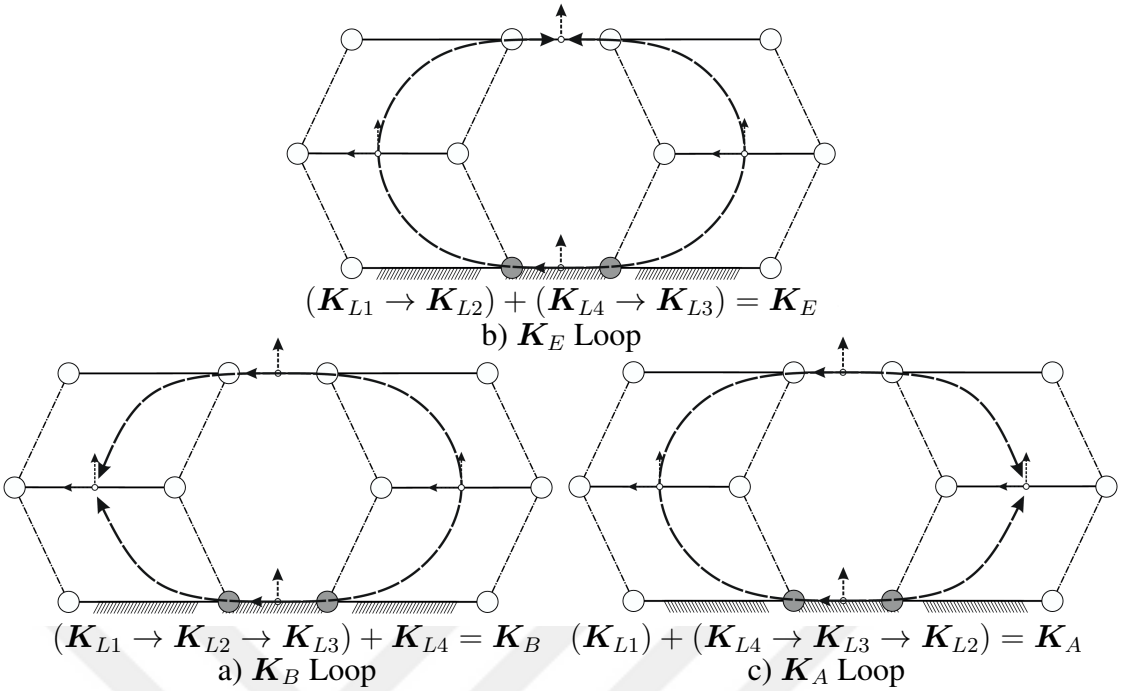



Figure 2.4. Stiffness loops of the frames where "$\rightarrow$" and "$+$" show the serial and parallel connections, respectively.

the actual VJM representation while b) shows the equivalent VJM stiffness model. One important thing that should be noticed is the connection sequence of the joints and virtual joints (or virtual springs). As shown in Figure 2.5 a), the virtual joints/springs are always located at the distal end of the link, but before the regular joint even-though both are coincident. However, these virtual joints do not contain any kinematic information, which means their stiffness information is given with respect to the local frames of the links. A stiffness model combined with the kinematic model is obtained when the stiffness model of the parallelogram is formulated relative to the fixed frame. Then, it can be represented as a single 6-DoF spring as shown in Figure 2.5 b). Note that this is a virtual kinematic chain representing the stiffness properties as the actual one.

The compliant kinematics of parallelogram is formulated by Equations 2.8 and 2.9. Equation 2.10 shows the compliant kinematic model equivalent of the parallelogram. In Equation 2.11, kinematic constraints are given.

$$\boldsymbol{H}_1 = \boldsymbol{T}_y(d/2)\boldsymbol{R}_z(\varphi_{11})\boldsymbol{T}_x(l_1)\boldsymbol{H}_v(\bar{\theta}_{11'})\boldsymbol{R}_z(\varphi_{12})\boldsymbol{T}_y(-d/2) \tag{2.8}$$

$$\boldsymbol{H}_2 = \boldsymbol{T}_y(-d/2)\boldsymbol{R}_z(\varphi_{21})\boldsymbol{T}_x(l_1)\boldsymbol{H}_v(\bar{\theta}_{21'})\boldsymbol{R}_z(\varphi_{22})\boldsymbol{T}_y(d/2) \tag{2.9}$$

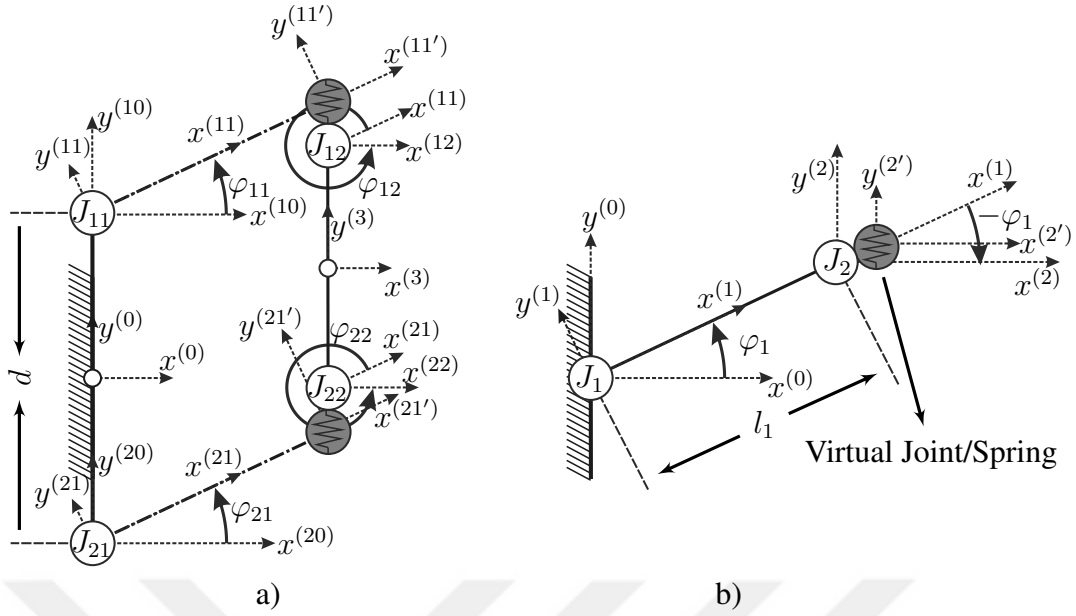



Figure 2.5. Stiffness model sketches. a) Actual the VJM sketch of the parallelogram b) Resultant the VJM equivalent of the parallelogram. Superscripts and subscripts $(ij)$, and $(j)$ denote the $j^{\text{th}}$ joint frame in $i^{\text{th}}$ limb for $i, j = 1, 2$, and $'$ represents the virtual joint frame.

$$\boldsymbol{H}_{Eq} = \boldsymbol{R}_z(\varphi_1)\boldsymbol{T}_x(l_1)\boldsymbol{R}_z(-\varphi_1)\boldsymbol{H}_v(\bar{\theta}_{2'}) \tag{2.10}$$

$$\varphi_{11} = \varphi_{21}, \;\; \varphi_{12} = \varphi_{22}, \;\; \varphi_{11} + \varphi_{12} = \varphi_{21} + \varphi_{22} = 2\pi k \;\; \text{for} \;\; k = 1, 2, ... \tag{2.11}$$

where $\boldsymbol{H}_1$, $\boldsymbol{H}_2$, and $\boldsymbol{H}_{Eq}$ are the compliant kinematic models of upper, and lower limbs and parallelogram's equivalent. $\boldsymbol{R}_{x,y,z}$ and $\boldsymbol{T}_{x,y,z}$ denote the pure rotation and translation homogeneous transformation matrices about/along $x, y, z$ axes. $d$ is the distance between the joints $J_{11}$ and $J_{21}$, while $l_1$ is the link length. $\varphi_{11}$, $\varphi_{12}$, $\varphi_{21}$, and $\varphi_{22}$ are the joint variables. Depending on the computed parallelogram loop, $\varphi_{11}$ and/or $\varphi_{21}$ might be active or passive joints. $\bar{\theta}_{11'}$, $\bar{\theta}_{21'}$, and $\bar{\theta}_{2'}$ denote the column matrices of 6 virtual joint variables in their respective limbs. Due to the rigid connections at the connection frame $\mathcal{F}(3)$ in Figure 2.5 a), $\boldsymbol{H}_1 = \boldsymbol{H}_2 = \boldsymbol{H}_{Eq}$ and also, compliant displacements of these frames for both limbs are the same, $\Delta\boldsymbol{H}_1 = \Delta\boldsymbol{H}_2 = \Delta\boldsymbol{H}_{Eq}$.

The stiffness model computations differ depending on whether there are active and/or passive joints, or not. In the following sections, the formulations are given.

### 2.3.3.1. Stiffness of an Active Parallelogram Loop

In this section, the stiffness model of the active parallelogram loop, $\boldsymbol{K}_{Eq(active)}$, is given. This matrix corresponds to $\boldsymbol{K}_{L1}$ and $\boldsymbol{K}_{L4}$ loops' stiffness matrices. The joint $J_{11}$ is taken as the active joint. Given this statement, the joint variables are re-organized in column matrix form as follows:

$$\bar{Q}_1 = \begin{bmatrix} \bar{\theta}_{11'}^T & q_{a1} & q_{p1} \end{bmatrix}_{8\times1}^T, \quad q_{a1} = \begin{bmatrix} \varphi_{11} \end{bmatrix}_{1\times1}, \quad q_{p1} = \begin{bmatrix} \varphi_{12} \end{bmatrix}_{1\times1} \tag{2.12}$$

$$\bar{Q}_2 = \begin{bmatrix} \bar{\theta}_{21'}^T & \bar{q}_{p2} \end{bmatrix}_{8\times1}^T, \quad \bar{q}_{p2} = \begin{bmatrix} \varphi_{21} & \varphi_{22} \end{bmatrix}_{2\times1}^T \tag{2.13}$$

$$\bar{Q}_{Eq} = \begin{bmatrix} \bar{\theta}_{2'}^T & \varphi_1 \end{bmatrix}_{7\times1}^T \tag{2.14}$$

Next, Jacobian matrices $\boldsymbol{J}_{\theta1}$, $\boldsymbol{J}_{\theta2}$, $\boldsymbol{J}_{\theta Eq}$, $\bar{J}_{a1}$, $\bar{J}_{p1}$, $\boldsymbol{J}_{p2}$, $\bar{J}_{aEq}$, $\boldsymbol{J}_1$, $\boldsymbol{J}_2$, and $\bar{J}_{Eq}$ are computed considering the forward kinematics equation given in Equations 2.8 to 2.10, and joint variables presented Equations 2.12 to 2.14.

Active, passive, and virtual joint-related Jacobian matrices of the upper chain and equivalent model of the parallelogram are presented in Equation 2.15, assuming that $\bar{\theta}_{11'} = \bar{0}$. Considering $\bar{\theta}_{2'} = \bar{0}$, $\bar{J}_{\theta Eq}$ is computed as $6 \times 6$ identity matrix meaning that it emulates the DoF of its equivalent spring. This is logical since the equivalent model merely represents the actual one.

$$\boldsymbol{J}_{\theta1} = \begin{bmatrix} c_{a1} & -s_{a1} & 0 & 0 & 0 & \frac{d}{2} \\ s_{a1} & c_{a1} & 0 & 0 & 0 & 0 \\ 0 & 0 & 1 & \frac{-dc_{a1}}{2} & \frac{ds_{a1}}{2} & 0 \\ 0 & 0 & 0 & c_{a1} & -s_{a1} & 0 \\ 0 & 0 & 0 & s_{a1} & c_{a1} & 0 \\ 0 & 0 & 0 & 0 & 0 & 1 \end{bmatrix} \tag{2.15}$$

$$\begin{bmatrix} \bar{J}_{a1} & \bar{J}_{p1} \end{bmatrix} = \begin{bmatrix} \frac{d}{2} - l_1 s_{a1} & \frac{-d}{2} \\ l_1 c_{a1} & 0 \\ 0 & 0 \\ 0 & 0 \\ 0 & 0 \\ 1 & -1 \end{bmatrix}, \quad \bar{J}_{aEq} = \begin{bmatrix} -l_1 \sin(\varphi_1) \\ l_1 \cos(\varphi_1) \\ 0 \\ 0 \\ 0 \\ 0 \end{bmatrix} \tag{2.16}$$

In Equation 2.15, $c_{a1}$ and $s_{a1}$ denote the cosine($\varphi_{11}$) and sine($\varphi_{11}$) functions, respectively. $\boldsymbol{J}_{\theta 2}$ and $\boldsymbol{J}_{p2}$ are similar to $\boldsymbol{J}_{\theta 1}$ and $\begin{bmatrix} \bar{J}_{a1} & \bar{J}_{p1} \end{bmatrix}$ matrices but $d$ and $\varphi_{11}$ are replaced with $-d$ and $\varphi_{21}$, respectively. $\bar{J}_{aEq}$ indicates that the distal end of the single link equivalence has no rotational property but linear displacements in $xy$-plane, only. This means that the equivalent model only positions the virtual spring at the distal end.

Inversion operation in Equation 2.2 for both upper and lower limbs is carried out to obtain the stiffness matrices $\boldsymbol{K}_1$ and $\boldsymbol{K}_2$. When the lower limb is individually considered with its kinematic constraints, it has 1 DoF that is uncontrollable due to the passive joints. This generates a zero-resistance direction. Hence, it can freely move when a force is applied that is tangent to its path. Therefore, the rank of $\boldsymbol{K}_2$ is 5. However, $\boldsymbol{K}_1$ is full rank. Finally, $\boldsymbol{K}_1$ and $\boldsymbol{K}_2$ stiffness matrices are summed to obtain $\boldsymbol{K}_{Eq(active)}$ according to Equation 2.3 and given as follows:

$$\boldsymbol{K}_{Eq(active)} = \boldsymbol{K}_1 + \boldsymbol{K}_2 \tag{2.17}$$

Equivalent stiffness matrices of upper and lower limbs, $\boldsymbol{K}_1$ and $\boldsymbol{K}_2$, can be procured experimentally or by performing finite element analysis. A parametric definition of these matrices is possible, but the inversion operation in Equation 2.2 may not be succeeded. Yet, it is still possible to obtain an inversion for $\bar{\theta}_{11'} = \bar{0}$, $\bar{\theta}_{21'} = \bar{0}$ and a specific set of values for the angles $\varphi_{11}$ and $\varphi_{21}$. For $\varphi_{11} = 0$, the stiffness of the upper limb, $\boldsymbol{K}_1$, is represented in Equation 2.18 where the $k$ terms are the elements of $\boldsymbol{K}_1$. The stiffness matrix $\boldsymbol{K}_2$ is similar to $\boldsymbol{K}_1$ but the variable $d$ is replaced with $-d$, and the element in 2nd row-2nd column is zero, and elements $k$ are updated according to the stiffness of the lower limb.

$$\boldsymbol{K}_1 = \begin{bmatrix} k_{11}^{(1)} & 0 & 0 & 0 & 0 & -\frac{d}{2}k_{11}^{(1)} \\ 0 & k_{22}^{(1)} - \dfrac{(k_{26}^{(1)})^2}{k_{66}^{(1)}} & 0 & 0 & 0 & 0 \\ 0 & 0 & k_{33}^{(1)} & \dfrac{d}{2}k_{33}^{(1)} & k_{35}^{(1)} & 0 \\ 0 & 0 & \dfrac{d}{2}k_{33}^{(1)} & \dfrac{d^2}{4}k_{33}^{(1)} + k_{44}^{(1)} & \dfrac{d}{2}k_{35}^{(1)} & 0 \\ 0 & 0 & k_{35}^{(1)} & \dfrac{d}{2}k_{35}^{(1)} & k_{55}^{(1)} & 0 \\ -\dfrac{d}{2}k_{11}^{(1)} & 0 & 0 & 0 & 0 & \dfrac{d^2}{4}k_{11}^{(1)} \end{bmatrix} \tag{2.18}$$

#### 2.3.3.2. Stiffness of a Passive Parallelogram Loop

In this section, the stiffness model of the passive parallelogram loop, $\boldsymbol{K}_{Eq(passive)}$, is given. This matrix corresponds to $\boldsymbol{K}_{L2}$ and $\boldsymbol{K}_{L3}$ loops' stiffness matrices. Compared to the active parallelogram, the computation of the stiffness of a passive parallelogram changes only by taking $J_{11}$ as a passive joint. The corresponding joint variables are updated as follows:

$$\bar{Q}_1 = \begin{bmatrix} \bar{\theta}_{11'}^T & \bar{q}_{p1}^T \end{bmatrix}_{8\times1}^T, \quad \bar{q}_{p1} = \begin{bmatrix} \varphi_{11} & \varphi_{12} \end{bmatrix}_{2\times1}^T \tag{2.19}$$

Calculations of Equations 2.2 and 2.3 are straightforward for generating stiffness matrix for passive parallelogram $\boldsymbol{K}_{Eq(passive)}$. This matrix is a rank-deficient matrix with a rank of $5$.

While computing the stiffness of the parallelograms, stiffness matrices of the links are treated as joint space stiffness matrices since the links are the sub-structures of the parallelograms. Similarly, parallelograms are the sub-loops of the whole manipulator. Hence, their stiffness matrices are treated as joint space stiffness matrices of the manipulator. If the stiffness matrices of parallelograms have full rank, the computation in Equation 2.2 would be applicable. However, this computation for passive sub-loops is not possible since they are rank deficient. To overcome this problem, a fictitious stiffness element can be included for the component of $\boldsymbol{K}_{Eq(passive)}$ to deal with the rank deficiency. Another approach is to reduce the virtual joint DoF from 6 to 5 for the passive manipulators' equivalent model. Both methods require manual modification in stiffness and Jacobian matrix elements. This process can be tedious if there are several passive loops as sub-loops. To preserve the straightforward methodology, $J_{11}$ and $J_{21}$ are both considered as active joints to obtain a full rank stiffness matrix of $\boldsymbol{K}_{Eq(passive)}$. The passive joint effect is later viewed in the stiffness model computation of the whole manipulator when connecting the loops (Pashkevich et al., 2009). Consequently, the following joint variable set is constructed:

$$\bar{Q}_1 = \begin{bmatrix} \bar{\theta}_{11'}^T & q_{a1} & q_{p1} \end{bmatrix}_{8\times1}^T, \quad q_{a1} = \begin{bmatrix} \varphi_{11} \end{bmatrix}_{1\times1}, \quad q_{p1} = \begin{bmatrix} \varphi_{12} \end{bmatrix}_{1\times1} \tag{2.20}$$

$$\bar{Q}_2 = \begin{bmatrix} \bar{\theta}_{21'}^T & q_{a2} & q_{p2} \end{bmatrix}_{8\times1}^T, \quad q_{a2} = \begin{bmatrix} \varphi_{21} \end{bmatrix}_{1\times1}, \quad q_{p2} = \begin{bmatrix} \varphi_{22} \end{bmatrix}_{1\times1} \tag{2.21}$$

Next, the new stiffness matrix, $\boldsymbol{K}_{Eq(passive)}$, is computed assuming both upper and lower limbs have active first joints $J_{11}$ and $J_{21}$. The new stiffness matrix, $\boldsymbol{K}_2$, is similar to $\boldsymbol{K}_1$ in Equation 2.18 except the variable $d$ is replaced with $-d$. If both the upper and lower links have the same link designs, $\boldsymbol{K}_{Eq(passive)} = \boldsymbol{K}_1 + \boldsymbol{K}_2$ summation results in $2\boldsymbol{K}_1$ but the parameters with $d$ vanishes due to $\pm$ signs and the elements without $d$ and with $d^2$ are doubled. In the case study, this is not necessary since upper and lower limbs have different designs.

### 2.3.4. Stiffness Model of the Manipulator

In this section, it is shown how $\boldsymbol{K}_{Eq(active)}$ and $\boldsymbol{K}_{Eq(passive)}$ matrices are correlated with each other to obtain the stiffness model of the manipulator. The stiffness matrices belonging to the frames $\mathcal{F}(E)$, $\mathcal{F}(B)$, and $\mathcal{F}(A)$ are presented. These matrices are $\boldsymbol{K}_E$, $\boldsymbol{K}_B$, and $\boldsymbol{K}_A$ matrices, respectively. Using the equivalent stiffness model of the parallelograms, the compliant kinematics of these frames are illustrated in Figure 2.6. The steps are listed below, and a flow chart is shown in Figure 2.7..

1. In Equations 2.22-2.28, the compliant forward kinematics are constructed. $\boldsymbol{H}$ is the kinematic model. Sub-indices $A, B, E$ indicate the belonging frames of the kinematic models. Sub-indices $1, 2$ denote the right and left limbs up to these frames, respectively.

2. In Equations 2.29-2.34, the joint variable column matrices are defined, and passive/active joint variables are grouped.

3. The forward kinematic models and grouped joint variables are used to obtain the required Jacobian matrices. These Jacobian matrices are $\boldsymbol{J}_{\theta B1}$, $\boldsymbol{J}_{\theta B2}$, $\boldsymbol{J}_{\theta A1}$, $\boldsymbol{J}_{\theta A2}$, $\boldsymbol{J}_{\theta E1}$, $\boldsymbol{J}_{\theta E2}$, $\bar{J}_{aB1}$, $\bar{J}_{aB2}$, $\bar{J}_{aA1}$, $\bar{J}_{aA2}$, $\bar{J}_{aE1}$, $\bar{J}_{aE2}$, $\boldsymbol{J}_{pB1}$, $\bar{J}_{pE1}$, $\bar{J}_{pE2}$, and $\boldsymbol{J}_{pA2}$ are obtained. Again, sub-indices $\theta, a, p$ denote that the Jacobian matrix is derived with respect to the virtual, active, and passive joint variables. Here, $\bar{q}_p$ column matrices are used to obtain $\bar{J}_p$ Jacobian matrices. These Jacobian matrices consider the

passive joints' zero stiffness effect in the further computation steps. Therefore, the mathematical manipulation of $\boldsymbol{K}_{Eq(passive)}$ being full rank is corrected.

4. In Equations 2.35-2.40, stiffness matrices of $\boldsymbol{K}_{Eq(active)}$ and $\boldsymbol{K}_{Eq(passive)}$ are used to obtain the joint space stiffness matrices of the limbs. Since each parallelogram is reduced to a single link representation, each limb's joint space stiffness matrix contains a number of these $\boldsymbol{K}_{Eq(active)}$ and $\boldsymbol{K}_{Eq(passive)}$ matrices. $\boldsymbol{K}_{\theta}$ denotes that the matrix is the joint space stiffness matrix, and the remaining sub-indices show the belonging frame and followed limb route.

5. Now, the inversion operation in Equation 2.2 can be held by relating the Jacobian matrices in step 3 and Joint space stiffness matrices in Equations 2.35-2.40. This inversion produces $\boldsymbol{K}_{A1}$, $\boldsymbol{K}_{A2}$, $\boldsymbol{K}_{B1}$, $\boldsymbol{K}_{B2}$, $\boldsymbol{K}_{E1}$, and $\boldsymbol{K}_{E2}$ stiffness matrices of each limb in Cartesian space. Finally, by connecting each limb at its respective frame, in Equation 2.41, the Cartesian space stiffness matrix of each frame $\boldsymbol{K}_{A}$, $\boldsymbol{K}_{B}$, and $\boldsymbol{K}_{E}$ are obtained.

Note that the serial connection of parallelogram loops is mathematically represented by Equation 2.2. This equation provides the mathematical basis for connecting the $\mathcal{F}(3)$ frame of the proximal loop to $\mathcal{F}(0)$ frame of the distal loop in Figure 2.5 a). In other words, the coupler link of the proximal loop becomes coincident with the base link of the distal loop at $\mathcal{F}(0) - \mathcal{F}(3)$ frames.

$$\begin{aligned}\boldsymbol{H}_{B1} = \boldsymbol{T}_y(-d/2)\boldsymbol{R}_z(-\varphi_{11})\boldsymbol{T}_x(l_1)\boldsymbol{R}_z(\varphi_{11})\boldsymbol{H}_v(\bar{\theta}_{12'})\boldsymbol{R}_z(\varphi_{12})\boldsymbol{T}_x(l_1) \\ \boldsymbol{R}_z(-\varphi_{12})\boldsymbol{H}_v(\bar{\theta}_{15'})\boldsymbol{T}_y(d)\boldsymbol{R}_z(\varphi_{13})\boldsymbol{T}_x(l_1)\boldsymbol{R}_z(-\varphi_{13})\boldsymbol{H}_v(\bar{\theta}_{18'})\end{aligned} \tag{2.22}$$

$$\boldsymbol{H}_{B2} = \boldsymbol{T}_y(d/2)\boldsymbol{R}_z(\varphi_{21})\boldsymbol{T}_x(l_1)\boldsymbol{R}_z(-\varphi_{21})\boldsymbol{H}_v(\bar{\theta}_{22'}) \tag{2.23}$$

$$\begin{aligned}\boldsymbol{H}_{E1} = \boldsymbol{T}_y(-d/2)\boldsymbol{R}_z(-\varphi_{11})\boldsymbol{T}_x(l_1)\boldsymbol{R}_z(\varphi_{11})\boldsymbol{H}_v(\bar{\theta}_{12'})\boldsymbol{R}_z(\varphi_{12})\boldsymbol{T}_x(l_1) \\ \boldsymbol{R}_z(-\varphi_{12})\boldsymbol{H}_v(\bar{\theta}_{15'})\boldsymbol{T}_y(d/2)\end{aligned} \tag{2.24}$$

$$\begin{aligned}\boldsymbol{H}_{E2} = \boldsymbol{T}_y(d/2)\boldsymbol{R}_z(\varphi_{21})\boldsymbol{T}_x(l_1)\boldsymbol{R}_z(-\varphi_{21})\boldsymbol{H}_v(\bar{\theta}_{22'})\boldsymbol{R}_z(-\varphi_{22})\boldsymbol{T}_x(l_1) \\ \boldsymbol{R}_z(\varphi_{22})\boldsymbol{H}_v(\bar{\theta}_{25'})\boldsymbol{T}_y(-d/2)\end{aligned} \tag{2.25}$$

$$\boldsymbol{H}_{A1} = \boldsymbol{T}_y(-d/2)\boldsymbol{R}_z(-\varphi_{11})\boldsymbol{T}_x(l_1)\boldsymbol{R}_z(\varphi_{11})\boldsymbol{H}_v(\bar{\theta}_{12'}) \tag{2.26}$$

$$\begin{aligned}\boldsymbol{H}_{A2} = \boldsymbol{T}_y(d/2)\boldsymbol{R}_z(\varphi_{21})\boldsymbol{T}_x(l_1)\boldsymbol{R}_z(-\varphi_{21})\boldsymbol{H}_v(\bar{\theta}_{22'})\boldsymbol{R}_z(-\varphi_{22})\boldsymbol{T}_x(l_1) \\ \boldsymbol{R}_z(\varphi_{22})\boldsymbol{H}_v(\bar{\theta}_{25'})\boldsymbol{T}_y(-d)\boldsymbol{R}_z(-\varphi_{23})\boldsymbol{T}_x(l_1)\boldsymbol{R}_z(\varphi_{23})\boldsymbol{H}_v(\bar{\theta}_{28'})\end{aligned} \tag{2.27}$$

$$\boldsymbol{H}_{B1} = \boldsymbol{H}_{B2}, \quad \boldsymbol{H}_{E1} = \boldsymbol{H}_{E2}, \quad \boldsymbol{H}_{A1} = \boldsymbol{H}_{A2}, \tag{2.28}$$

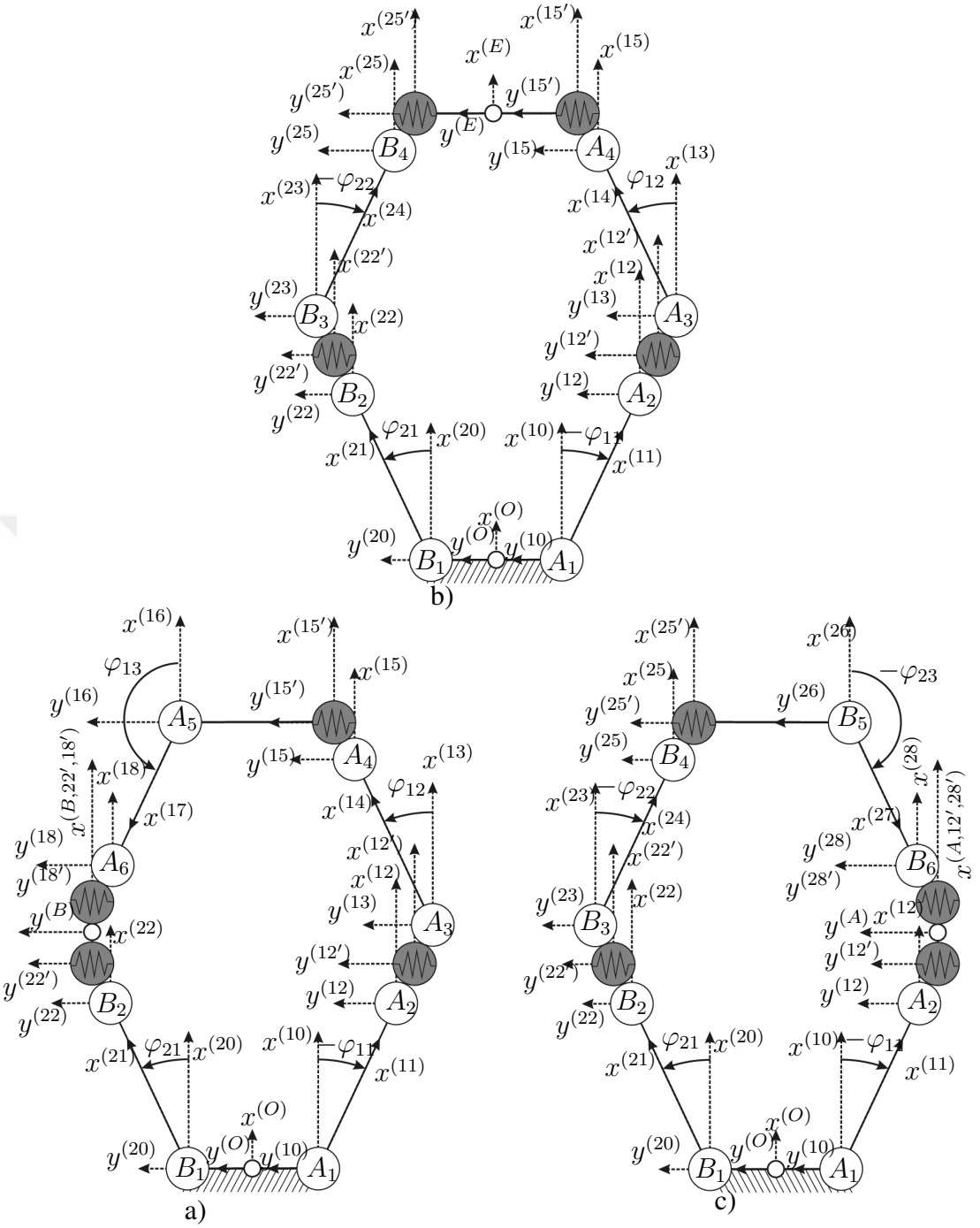



Figure 2.6. Stiffness model illustrations of the frames: a) $\mathcal{F}(B)$ b) $\mathcal{F}(E)$ c) $\mathcal{F}(A)$.

$$\varphi_{21} = \varphi_{12}, \quad \varphi_{11} = \varphi_{22}, \quad \varphi_{13} + \varphi_{11} = \varphi_{23} + \varphi_{21} = \pi$$

$$\bar{Q}_{B1} = \begin{bmatrix} \bar{\theta}_{B1}^T & q_{aB1} & \bar{q}_{pB1}^T \end{bmatrix}_{21\times 1}^T, \quad q_{aB1} = \varphi_{11}, \quad \bar{q}_{pB1}^T = \begin{bmatrix} \varphi_{12} & \varphi_{13} \end{bmatrix}^T \tag{2.29}$$

$$\bar{\theta}_{B1} = \begin{bmatrix} \bar{\theta}_{12'}^T & \bar{\theta}_{15'}^T & \bar{\theta}_{18'}^T \end{bmatrix}_{18\times 1}^T$$

$$\bar{Q}_{B2} = \begin{bmatrix} \bar{\theta}_{B2}^T & q_{aB2} \end{bmatrix}_{7\times 1}^T, \quad q_{aB2} = \varphi_{21}, \quad \bar{\theta}_{B2} = \bar{\theta}_{22'} \tag{2.30}$$

$$\bar{Q}_{E1} = \begin{bmatrix} \bar{\theta}_{E1}^T & q_{aE1} & q_{pE1} \end{bmatrix}_{14\times1}^T, \quad q_{aE1} = \varphi_{11}, \quad q_{pE1} = \varphi_{12}, \tag{2.31}$$

$$\bar{\theta}_{E1} = \begin{bmatrix} \bar{\theta}_{12'}^T & \bar{\theta}_{15'}^T \end{bmatrix}_{12\times1}^T$$

$$\bar{Q}_{E2} = \begin{bmatrix} \bar{\theta}_{E2}^T & q_{aE2} & q_{pE2} \end{bmatrix}_{14\times1}^T, \quad q_{aE2} = \varphi_{21}, \quad q_{pE2} = \varphi_{22}, \tag{2.32}$$

$$\bar{\theta}_{E2} = \begin{bmatrix} \bar{\theta}_{22'}^T & \bar{\theta}_{25'}^T \end{bmatrix}_{12\times1}^T$$

$$\bar{Q}_{A1} = \begin{bmatrix} \bar{\theta}_{A1}^T & q_{aA1} \end{bmatrix}_{7\times1}^T, \quad q_{aA1} = \varphi_{11}, \quad \bar{\theta}_{A1} = \bar{\theta}_{12'} \tag{2.33}$$

$$\bar{Q}_{A2} = \begin{bmatrix} \bar{\theta}_{A2}^T & q_{aA2} & \bar{q}_{pA2}^T \end{bmatrix}_{21\times1}^T, \quad q_{aA2} = \varphi_{21}, \quad \bar{q}_{pA2}^T = \begin{bmatrix} \varphi_{22} & \varphi_{23} \end{bmatrix}^T, \tag{2.34}$$

$$\bar{\theta}_{A2} = \begin{bmatrix} \bar{\theta}_{22'}^T & \bar{\theta}_{25'}^T & \bar{\theta}_{28'}^T \end{bmatrix}_{18\times1}^T$$

$$\boldsymbol{K}_{\theta B1} = diag\left(\boldsymbol{K}_{Eq(active)}, \boldsymbol{K}_{Eq(passive)}, \boldsymbol{K}_{Eq(passive)}\right)_{18\times18} \tag{2.35}$$

$$\boldsymbol{K}_{\theta B2} = diag\left(\boldsymbol{K}_{Eq(active)}\right)_{6\times6} \tag{2.36}$$

$$\boldsymbol{K}_{\theta E1} = diag\left(\boldsymbol{K}_{Eq(active)}, \boldsymbol{K}_{Eq(passive)}\right)_{12\times12} \tag{2.37}$$

$$\boldsymbol{K}_{\theta E2} = diag\left(\boldsymbol{K}_{Eq(active)}, \boldsymbol{K}_{Eq(passive)}\right)_{12\times12} \tag{2.38}$$

$$\boldsymbol{K}_{\theta A1} = diag\left(\boldsymbol{K}_{Eq(active)}\right)_{6\times6} \tag{2.39}$$

$$\boldsymbol{K}_{\theta A2} = diag\left(\boldsymbol{K}_{Eq(active)}, \boldsymbol{K}_{Eq(passive)}, \boldsymbol{K}_{Eq(passive)}\right)_{18\times18} \tag{2.40}$$

$$\boldsymbol{K}_B = \boldsymbol{K}_{B1} + \boldsymbol{K}_{B2}, \quad \boldsymbol{K}_E = \boldsymbol{K}_{E1} + \boldsymbol{K}_{E2}, \quad \boldsymbol{K}_A = \boldsymbol{K}_{A1} + \boldsymbol{K}_{A2} \tag{2.41}$$

### 2.3.5. The Displacement of the Mobile Platform due to Compliant Deflections of Flexible Links

The deflection of the coordinate frame of the mobile platform $\mathcal{F}(E)$, that is caused by the forces acting on this frame, $\bar{F}_E$, is defined as $\Delta\bar{X}_E^{(E)}$. The lower index indicates the frame where the deflections occur, and the upper index shows the location of the force causing this deflection. In this regard, loads acting on $\mathcal{F}(A)$ and $\mathcal{F}(B)$ frames cause $\Delta\bar{X}_E^{(A)}$ and $\Delta\bar{X}_E^{(B)}$ deflections in the $\mathcal{F}(E)$ frame.

To compute the deflection contribution of the forces acting on $\mathcal{F}(A)$ and $\mathcal{F}(B)$ to the frame $\mathcal{F}(E)$, first, the deflections in joint space (virtual and passive) are computed. The virtual and passive joint variables are $[\bar{\theta}_{B1}, \bar{q}_{pB1}]$ for $\mathcal{F}(B)$ and $[\bar{\theta}_{A2}\bar{q}_{pA2}]$ for $\mathcal{F}(A)$ frames.

The resulting total deflection in $\mathcal{F}(E)$ is computed by superposing all these deflections as follows:

$$\Delta\bar{X}_E = \Delta\bar{X}_E^{(E)} + \Delta\bar{X}_E^{(B)} + \Delta\bar{X}_E^{(A)} \tag{2.42}$$

The computation of each element is listed as follows:

1. $\Delta\bar{X}_E^{(E)}$ is computed as shown in Equation 2.43.
2. Equation 2.44 shows the deflection of the frame $\mathcal{F}(A)$ that is caused by the forces acting on this frame. The frame $\mathcal{F}(E)$ is included in the 2nd limb of $\mathcal{F}(A)$. Therefore, compliant kinematics of this limb is used.
3. Equation 2.45 shows the deflections in 2nd limb's passive joints, $\Delta\bar{q}_{pA2}$, of $\mathcal{F}(A)$. Here, $\boldsymbol{K}_{pA2}$ is computed via Equation 2.2.
4. In Equation 2.46, $\boldsymbol{K}_{A2}\Delta\bar{X}_A$ represents the distributed force of $\bar{F}_A$ on 2nd limb. By multiplying this force with $\boldsymbol{J}_{\theta A2}^T$, it is transformed into joint space indicated as $\boldsymbol{J}_{\theta A2}^T\boldsymbol{K}_{A2}\Delta\bar{X}_A$. Then, change in virtual joints, $\Delta\bar{\theta}_{A2}$, are computed by multiplying the joint space force with $\boldsymbol{K}_{\theta A2}^{-1}$.
5. After obtaining both passive and virtual joint values of 2nd limb, they are used in compliant forward kinematics to acquire the deflection in $\mathcal{F}(E)$ caused by the forces acting on $\mathcal{F}(A)$.
6. However, $\bar{\theta}_{A2}$ has 18 virtual joint variables and $\bar{q}_{pA2}$ has 2 passive joint variables. To conduct the computation, variables in $\bar{\theta}_{A2}$ and $\bar{q}_{pA2}$ should be chosen that corresponds to 2nd limb. The first 12 variables of $\bar{\theta}_{A2}$ are selected and shown as $\bar{\theta}_{A2,1-12}$. Similarly, the first element of $\bar{q}_{pA2}$ is shown by $\bar{q}_{pA2}(1)$.
7. Finally, the deflection, $\Delta\bar{X}_E^{(A)}$, is calculated in Equation 2.47. $\boldsymbol{J}_{E2}$ is the Jacobian matrix of 2nd limb that is defined up to $\mathcal{F}(E)$ which includes 12 virtual joints and 1 passive joint.
8. Computations for $\Delta\bar{X}_E^{(B)}$ are given in Equations 2.48-2.51.

$$\Delta\bar{X}_E^{(E)} = \boldsymbol{K}_E^{-1}\bar{F}_E \tag{2.43}$$

$$\Delta \bar{X}_A^{(A)} = \boldsymbol{K}_A^{-1} \bar{F}_A \tag{2.44}$$

$$\Delta \bar{q}_{pA2} = \boldsymbol{K}_{pA2} \Delta \bar{X}_A \tag{2.45}$$

$$\Delta \bar{\theta}_{A2} = \boldsymbol{K}_{\theta A2}^{-1} \boldsymbol{J}_{\theta A2}^T \boldsymbol{K}_{A2} \Delta \bar{X}_A \tag{2.46}$$

$$\Delta \bar{X}_E^{(A)} = \boldsymbol{J}_{E2} \Delta \bar{\theta}_{A2,1-12} + \boldsymbol{J}_{pE2} \Delta \bar{q}_{pA2,1} \tag{2.47}$$

$$\Delta \bar{X}_B^{(B)} = \boldsymbol{K}_B^{-1} \bar{F}_B \tag{2.48}$$

$$\Delta \bar{q}_{pB1} = \boldsymbol{K}_{pB1} \Delta \bar{X}_B \tag{2.49}$$

$$\Delta \bar{\theta}_{B1} = \boldsymbol{K}_{\theta B1}^{-1} \boldsymbol{J}_{\theta B1}^T \boldsymbol{K}_{B1} \Delta \bar{X}_B \tag{2.50}$$

$$\Delta \bar{X}_E^{(B)} = \boldsymbol{J}_{E1} \Delta \bar{\theta}_{B1,1-12} + \boldsymbol{J}_{pE1} \Delta \bar{q}_{pB1,1} \tag{2.51}$$

### 2.3.6. Summary of Stiffness Modelling

A brief summary of the computation steps is given as follows:

1. Determine the active and the passive sub-loops. Active loops are attached to the base frame, and passive loops are located between the active loops and the mobile platform.

2. Calculate the stiffness matrices of active and passive loops as described in Sections 2.3.3.1 and 2.3.3.2. Now, the parallelograms are reduced to a single-link representation.

3. Determine the frames at which loads are applied. There are two auxiliary frames $\mathcal{F}(A)$ and $\mathcal{F}(B)$, and one mobile platform frame $\mathcal{F}(E)$ as shown in Figure 2.6.

4. Perform a serial connection representation of an active and a number of passive loops until these frames. It is a serial connection of an active and a passive loop for the mobile platform frame for both limbs. For auxiliary frames, an active loop is followed by two passive loops at one limb, while the other limb only consists of a single active loop. Serial connection is denoted by "$\rightarrow$" in Figs. 2.4 and 2.7.

5. For each limb, construct the forward kinematics of reduced parallelograms up to these frames as given in Equations 2.22 to 2.28 including the active, passive, and virtual joints of reduced parallelograms. Two forward kinematics formulations are

needed for each loading frame since each frame has 2 limbs. In total, 6 forward kinematic models are acquired. Next, construct the Jacobian matrices of these forward kinematic models of each limb.

6. Construct the diagonal stiffness matrix model of serially connected reduced parallelograms as given in Equations 2.35 to 2.40.

7. Connect each limb parallel to the other. This is a simple summation of stiffness models obtained in the previous step and shown in Equation 2.41. Now, $\boldsymbol{K}_E$, $\boldsymbol{K}_A$, and $\boldsymbol{K}_B$ are obtained. This parallel connection is denoted by "+" in Figs. 2.4 and 2.7. The first column in Figure 2.7 summarizes all the computations including this step.

8. Compute the compliant deflection of each loading frame as shown in the second column of Figure 2.7.

9. Perform the computations in Section 2.3.5 to obtain the compliant deflection of the mobile platform caused by the loads applied at the loading frames. This is the final column of Figure 2.7.

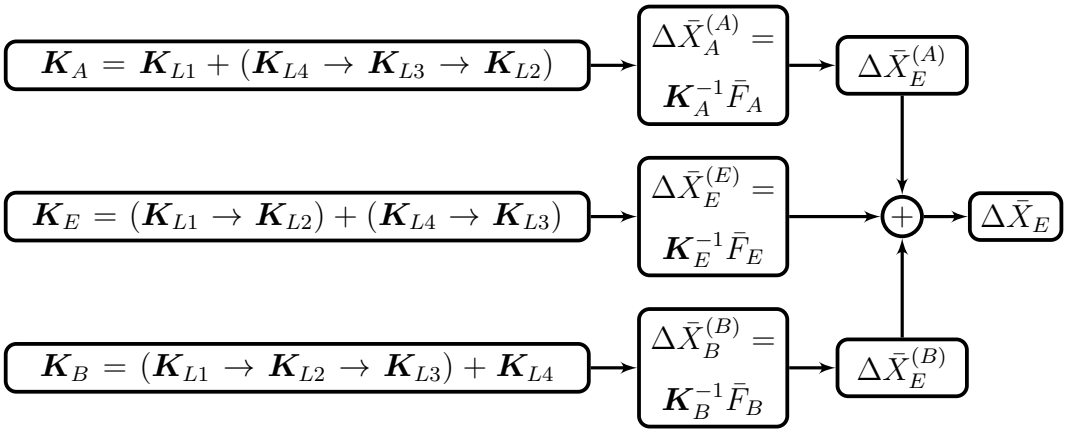



Figure 2.7. Computation chart to obtain the deflections in frame $\mathcal{F}(E)$.

## 2.4. Simulation, Results, and Discussion

The procured stiffness model is coded in MATLAB Simulink, and simulation tests are conducted. Then, the obtained results are compared with the finite element analy-

sis (FEA) results considering the results obtained via ANSYS Workbench. This section presents the results of this verification via comparison.

The stiffness parameters of the links (shown in Figure 2.2) are determined via experiments by applying loads and measuring the compliant deflections with a coordinate measuring machine (CMM) FARO Prime Arm 1.2. Forcing combinations along 3-axes are applied to generate deflections at the distal ends of each link. Complaint deflections at distal ends are captured via CMM (see Figure 2.10 a) and b)). Deflections in Link 1 are smaller than the tolerance range of the CMM ($\pm 0.023$ mm); hence, a high stiffness value is assigned to this link's stiffness matrix, $\boldsymbol{K}_{\theta 1}$. Also, it is considered as a rigid body in the FEM. Based on the experimental data, the local stiffness matrices of Link 2, $\boldsymbol{K}_{\theta 2}$, and Link 3, $\boldsymbol{K}_{\theta 3}$, are computed as given below by relating the deflections to the forcing. The computation is achieved by minimizing $\Delta\bar{F} - \boldsymbol{K}\Delta\bar{X}$ for each test data. Since the format of $\boldsymbol{K}$ is known, optimization for 8 elements of $\boldsymbol{K}$ was sufficient. The units of the stiffness matrix components for upper left-right and lower left-right $3 \times 3$ sub-matrices are N/m, N/rad, N $\cdot$ m/m, and N $\cdot$ m/rad, respectively.

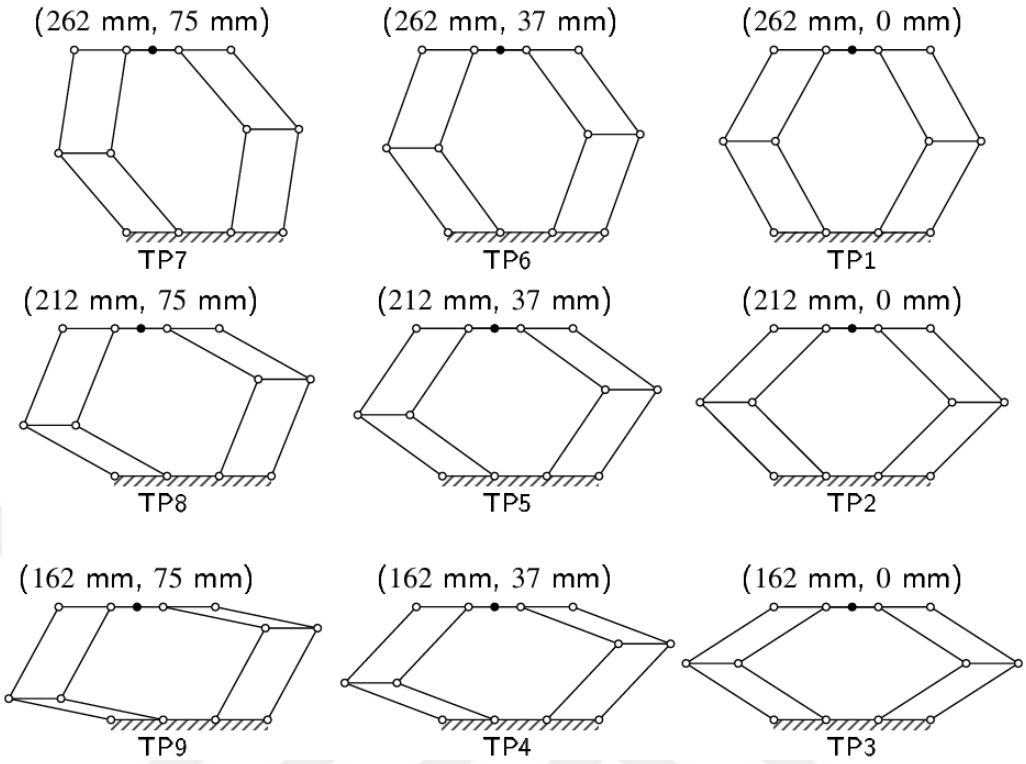
$$\boldsymbol{K}_{\theta 2} = \begin{bmatrix} 92317585 & 0 & 0 & 0 & 0 & 0 \\ 0 & 418506 & 0 & 0 & 0 & -31388 \\ 0 & 0 & 418506 & 0 & 31388 & 0 \\ 0 & 0 & 0 & 604 & 0 & 0 \\ 0 & 0 & 31388 & 0 & 3139 & 0 \\ 0 & -31388 & 0 & 0 & 0 & 3139 \end{bmatrix} \tag{2.52}$$

$$\boldsymbol{K}_{\theta 3} = \begin{bmatrix} 17040334 & 0 & 0 & 0 & 0 & 0 \\ 0 & 77250 & 0 & 0 & 0 & -5794 \\ 0 & 0 & 77250 & 0 & 5794 & 0 \\ 0 & 0 & 0 & 111 & 0 & 0 \\ 0 & 0 & 5794 & 0 & 579 & 0 \\ 0 & -5794 & 0 & 0 & 0 & 579 \end{bmatrix} \tag{2.53}$$

$$\boldsymbol{K}_{\theta 1} = 10^6 \cdot \boldsymbol{K}_{\theta 2} \tag{2.54}$$

The manipulator's stiffness model is analyzed at 9 test points. Since the manipulator has a symmetric behaviour about the $x$-axis, the test points are chosen at one side of the workspace, namely, along the positive $y$-axis (see Figure 2.3). The workspace dimensions are $100$ mm $\times$ $150$ mm along $x$-$y$ axes. The home position of the workspace is located at (212.3 mm, 0 mm) with respect to $\mathcal{F}(O)$ which corresponds to the $\varphi_{21} = 45^\circ, \varphi_{11} = -45^\circ$

of the active joint angles. The test points and the joint angles are given in Figure 2.8.




| TP | 1 | 2 | 3 | 4 | 5 | 6 | 7 | 8 | 9 |
|---|---|---|---|---|---|---|---|---|---|
| $\varphi_{11}(^\circ)$ | -29 | -45 | -57.3 | -43.3 | -34.1 | -19.9 | -8.7 | -22 | -28.6 |
| $\varphi_{21}(^\circ)$ | 29 | 45 | 57.3 | 69.3 | 54.1 | 36.1 | 40.6 | 60.9 | 78.3 |
| $x$ (mm) | 262 | 212 | 162 | 162 | 212 | 262 | 262 | 212 | 162 |
| $y$ (mm) | 0 | 0 | 0 | 37 | 37 | 37 | 75 | 75 | 75 |

Figure 2.8. Illustration of test points (TP) and their corresponding active joint angles.

The manipulator is designed to work at $5$g acceleration range. With the laser emitter mounted on the mobile platform, the combined mass is $5$ kg. The mass of the Link 4 group is $1$ kg. By taking the gravitational acceleration $g = 10 m/s^2$ as numerical simplification, the maximum external forces on the bodies are $250$ N for the mobile platform and $25$ N for the intermediate link group. The values of force assignments are insignificant for comparing the FEA and the VJM results. The aim is to analyze the stiffness model at an instant in which the maximum dynamic forces occur by making use of D'Alembert's principle. Analyses are conducted for dynamic forces acting on 2 intermediate ($\mathcal{F}_{(A)}$, $\mathcal{F}_{(B)}$) and 1 mobile platform ($\mathcal{F}_{(E)}$) terminals on $xy$-plane, simultaneously. These 3 force vectors are parallel to each other. The forces are applied in 6 different directions. These vectors start along the $x$-axis and divide a half rotation into 6 parts. Hence, between each

Table 2.1. The FEA setup details of ANSYS Workbench.

| **Mesh Properties** | |
|---|---|
| Size Function | Curvature |
| Relevance Center | Fine |
| Transition | Slow |
| Span Angle Center | Fine |
| Curvature Normal Angle | $18^\circ$ |
| Min Size | 2mm |
| Max Face Size | 4mm |
| Max Tet Size | 5mm |
| Growth Rate | Default |
| Remaining Parameters | Default |
| Element Type | Quad4 |
| | SHELL181 |

| **Analysis Settings** | |
|---|---|
| Solver Target | Mechanical APDL |
| Solver Type | Iterative |
| Weak Springs | On |
| Spring Stiffness | Program Controlled |
| Solver Pivot Check | Program Controlled |
| Large Deflection | On |
| Newton-Raphson | Program Controlled |
| Force Convergence | On |
| Moment Convergence | On |
| Displacement Convergence | On |
| Rotation Convergence | On |
| Tolerance | $0.05\%$ |
| Minimum Reference | 0.001N, 0.001Nm, 0m, $0^\circ$ |

consecutive force vector, there is $30^\circ$ difference.

The FEA was conducted in the "Static Structural" tool of ANSYS Workbench. To match the experimentally identified stiffness matrices $\boldsymbol{K}_{\theta 2}$, and $\boldsymbol{K}_{\theta 3}$ a new material was defined via assigning Young's modulus value in ANSYS Workbench. Another option could have been to change the link designs to comply with the stiffness values. The base, mobile platform, Link 4, and Link 1 are defined as rigid bodies under the "Geometry" section of "Static Structural", while the remaining bodies were elastic. At each link's distal and proximal ends, "Remote Point" was defined. These nodes were fixed to meshes at the distal and proximal ends. This helps us to track the compliant deflections of distal and proximal ends of each link in 6-DoF. The connection of the links was utilized over the remote points by defining the "Revolute" joint option. To use the FEA in its highest accuracy, the "Iterative" solver option was selected, and "Large Deflections" were activated. Further details are given in Table 2.1.

The compliant deflections calculated via the FEA for forces acting on $\mathcal{F}_{(A)}$, $\mathcal{F}_{(B)}$, and $\mathcal{F}_{(E)}$ are grouped under $\text{FEA}_{\text{EAB}}$ label, and compliant deflections calculated via the VJM are labeled as $\text{VJM}_{\text{EAB}}$. In addition, $\text{VJM}_{\text{E}}$ is considered a force acting on $\mathcal{F}_{(E)}$ only. By comparing these three compliant deflection results, the performance of the proposed superposition methodology, $\text{VJM}_{\text{EAB}}$, can be evaluated over the traditional one, $\text{VJM}_{\text{E}}$. The results are given in Appendix Table A1. To evaluate the performance more practically, the results are further summarized by averaging the magnitudes of the compliant deflections for all force directions. The summarized results are given in Table 2.2. A per-

cent error term is defined below to determine if the superposition methodology, $\text{VJM}_{\text{EAB}}$, is superior with respect to $\text{VJM}_{\text{E}}$, or not.

$$e_E = (|FEA_{\text{EAB}} - VJM_{\text{E}}|/FEA_{\text{EAB}}) \times 100 \tag{2.55}$$

$$e_{EAB} = (|FEA_{\text{EAB}} - VJM_{\text{EAB}}|/FEA_{\text{EAB}}) \times 100 \tag{2.56}$$

Table 2.2. Summarized deflection results for the FEA and the VJM.

| **Test Point** | **$\text{FEA}_{\text{EAB}}$** $\Delta x(\mu m)$ | **$\text{VJM}_{\text{E}}$** $\Delta x(\mu m)$ | **$\text{VJM}_{\text{EAB}}$** $\Delta x(\mu m)$ | $e_{xE}$ **%** | $e_{xEAB}$ **%** | **$\text{FEA}_{\text{EAB}}$** $\Delta y(\mu m)$ | **$\text{VJM}_{\text{E}}$** $\Delta y(\mu m)$ | **$\text{VJM}_{\text{EAB}}$** $\Delta y(\mu m)$ | $e_{yE}$ **%** | $e_{yEAB}$ **%** |
|---|---|---|---|---|---|---|---|---|---|---|
| 1 | 1.1 | 1 | 1.2 | 4.7 | 14.1 | 41.6 | 41.7 | 41.7 | 0.2 | 0.2 |
| 2 | 1.6 | 1.5 | 1.8 | 5.2 | 10.3 | 20.8 | 20.9 | 20.9 | 0.3 | 0.3 |
| 3 | 2.8 | 2.7 | 3.1 | 3.6 | 12.1 | 14.7 | 14.7 | 14.7 | 0.1 | 0.1 |
| 4 | 15.8 | 16.2 | 16 | 2.5 | 1.2 | 19.1 | 19.7 | 19.1 | 3.2 | 0.1 |
| 5 | 7.5 | 7.5 | 7.5 | 0.2 | 0.7 | 23.1 | 23.2 | 23.1 | 0.7 | 0.1 |
| 6 | 8.7 | 8.7 | 8.7 | 0.0 | 0.4 | 48.6 | 48.8 | 48.7 | 0.3 | 0.2 |
| 7 | 20.7 | 20.8 | 20.8 | 0.2 | 0.2 | 61.1 | 61.3 | 61.3 | 0.4 | 0.2 |
| 8 | 17.6 | 17.9 | 17.7 | 1.6 | 0.8 | 26.6 | 27.1 | 26.6 | 2.1 | 0.2 |
| 9 | 71 | 72.4 | 68.6 | 2.0 | 3.4 | 35.5 | 36.6 | 34.8 | 2.9 | 2.2 |

It can be observed in Table 2.2 that overall accuracy for the calculation of $y$-axis deflections via $\text{VJM}_{\text{EAB}}$ compared to $\text{VJM}_{\text{E}}$ is better while $x$-axis deflection estimation accuracy of $\text{VJM}_{\text{EAB}}$ is relatively worse. Specifically, $x$-axis performance of $\text{VJM}_{\text{EAB}}$ is lower at test points 1, 2, 3, and 9. The first three points are located along the symmetry axis, and the $9^{\text{th}}$ point is positioned at a corner of the workspace. A point on the symmetry axis corresponds to a special configuration, and a corner point is closer to the singular configuration of the manipulator. Hence, extreme performance increments/decrements or no contribution might be expected at these points. Compared to $\text{VJM}_{\text{E}}$, $\text{VJM}_{\text{EAB}}$ did not improve further the error term at test points 5, 6, 7 for $x$-axis and 1, 2, 3 for $y$-axis. Finally, $x$-axis performance at test points 4, 8, and $y$-axis performance at test points 4 to 9 are increased when the proposed methodology is used. In short, when the new method ($\text{VJM}_{\text{EAB}}$) was used, performance increased in eight conditions, remained the same in six conditions, and got worse in four conditions among the nine $x$ and nine $y$-axis deflections conditions. It is possible to use the superposition methodology for $y$-axis deflections and the regular methodology ($\text{VJM}_{\text{E}}$) for $x$-axis deflection computation. Note that the stiffness model computation of serially connected parallelograms presented in this chapter are still

used in both cases. The computation cost for running the stiffness model for one node (i.e. $\mathcal{F}_{(E)}$) is examined. It is measured that it can run at 10kHz on a computer with Dual Intel Xeon E5-2600 processor and 16GB ECC RDIMM Memory at running at 1600MHz.

Note that the manipulator operates in a 2-DoF motion space (2 translations). However, the actual manipulator has loop assemblies at different heights (see Figure 2.1 b) and 2.9 b)). The height difference between the distal and proximal parallelograms are not considered in this part. Nonetheless, the presented calculation procedure and acquired stiffness model via the VJM are developed using 6-DoF virtual joints. Since the VJM and the FEA models are developed with this procedure, their results validate each other.

## 2.5. Experimental Procedure for Model Parameter Update

In the experimental study, the mobile platform is subjected to external static loads to generate compliant deflections. Only the static forces acting at the end-effector are considered; hence, no dynamic loads acts on the manipulator resulting in auxiliary forces at A and B nodes. Consequently, $\text{VJM}_\text{E}$ model is found to be suitable for tuning its parameters via this experimental study since it excludes the other A and B nodes and superposition methodology. In the actuator system, Kollmorgen AKM33E brushless servo motors with built-in brake and Sumitomo Fine Cyclo F1C-A15 gearbox are used. Built-in brakes of the servo motor are used to lock the mechanism. At the loading conditions, the brakes of the actuator are on and actuation stiffness is not considered. Next, measurements are taken via FARO Prime Arm 1.2 model CMM. Then, the stiffness parameters are optimized to minimize the error between the model and experiment data. The mobile platform location has pre-load and post-load conditions. Pre-load condition is formulated as shown below:

$$\bar{X}_M^{(1)} = \bar{X}_R^{(1)} + \bar{X}_G^{(1)} + \bar{X}_I^{(1)} + \bar{X}_J^{(1)} \tag{2.57}$$

where $\bar{X}_M^{(1)}$ is the position vector of the mobile platform frame with respect to the base frame. This vector is computed via CMM measurements, and it can be decomposed into a set of vector summations. $\bar{X}_R^{(1)}$ is the position vector computed by rigid body forward kinematics. $\bar{X}_G^{(1)}$ is the deflection caused by gravity. $\bar{X}_I^{(1)}$ is the compliant deflection contribution of internal stresses due to the over-constrained structure. $\bar{X}_J^{(1)}$ is the joint

clearance contributions. The upper index 1 indicates the initial state, i.e., pre-load state.

When the load is applied on the mobile platform, the mechanism switches from state 1 to state 2 which can be expressed as follows:

$$\bar{X}_M^{(2)} = \bar{X}_R^{(2)} + \bar{X}_G^{(2)} + \bar{X}_I^{(2)} + \bar{X}_J^{(2)} + \bar{X}_E^{(2)} \tag{2.58}$$

$$\Delta\bar{X}_M = \bar{X}_M^{(2)} - \bar{X}_M^{(1)} \tag{2.59}$$

$\bar{X}_E$ is deflection caused by external force applied on the mobile platform. Superscript 2 indicates the post-load state. $\Delta\bar{X}_M$ suggests the change in position between the states. $\bar{X}_R$ is calculated by using the encoder data connected to the actuator. Since the actuators are locked, $\Delta\bar{X}_R = \bar{0}$. It is known that parallel mechanisms reduce the adverse effect of joint clearances; hence, $\Delta\bar{X}_J = \bar{0}$ is assumed. The most significant drawback of an over-constrained mechanism is its high internal stresses. These internal stresses are caused by the geometrical errors of the manufactured parts. The mechanism was produced with high production precision. In addition, special hinge construction is used to tolerate a possible geometric error, and a particular assembling procedure is followed when fastening the connection screws. Although these precautions help reduce internal stresses, they cannot be fully neglected. Hence, $\Delta\bar{X}_I \neq \bar{0}$. Due to the compliant kinematic state change, the compliant deflection caused by gravity differs in the first and second position states. Since the applied load on the mobile platform is much greater than the change in gravitational loading from the first to second position state, $\Delta\bar{X}_G = \bar{0}$ can be assumed. As a result, the first and second position states are simplified,and a force/compliant deflection equation is written as follows:

$$\bar{F} = \boldsymbol{K}_C \Delta\bar{X}_M = \boldsymbol{K}_C(\Delta\bar{X}_I + \bar{X}_E) \tag{2.60}$$

Stiffness model $\boldsymbol{K}_C$ is a function of the local stiffness matrices $\boldsymbol{K}_{\theta 1}$, $\boldsymbol{K}_{\theta 2}$, and $\boldsymbol{K}_{\theta 3}$, and the joint variables $\varphi_{11}$ and $\varphi_{21}$. $\varphi_{11}, \varphi_{21}$ variables are determined by the controller for the desired trajectory. The parameters of these local stiffness matrices need to be updated in accordance with the compliant deflection of the mobile platform. This update is achieved by adding a symmetric modification matrix to the local stiffness ma-

trices, which has 21 parameters to be determined. The modification matrix can also be considered a measure of deviation from the original stiffness values of the link. This deviation can be caused by the contribution of the shaft, bearing, bolt, fastening torque of the screws, and internal stresses. As mentioned earlier, $\boldsymbol{K}_{\theta 1}$ is assumed to be highly stiff. Therefore, a total of 42 parameters must be determined for $\boldsymbol{K}_{\theta 2}$, and $\boldsymbol{K}_{\theta 3}$. The parameter update is defined as follows:

$$\boldsymbol{K}'_{\theta 2} = \boldsymbol{K}_{\theta 2} + \begin{bmatrix} k_1 & k_7 & k_{12} & k_{16} & k_{19} & k_{21} \\ k_7 & k_2 & k_8 & k_{13} & k_{17} & k_{20} \\ k_{12} & k_8 & k_3 & k_9 & k_{14} & k_{18} \\ k_{16} & k_{13} & k_9 & k_4 & k_{10} & k_{15} \\ k_{19} & k_{17} & k_{14} & k_{10} & k_5 & k_{11} \\ k_{21} & k_{20} & k_{18} & k_{15} & k_{11} & k_6 \end{bmatrix} \tag{2.61}$$

$$\boldsymbol{K}'_{\theta 3} = \boldsymbol{K}_{\theta 3} + \begin{bmatrix} k_{22} & k_{28} & k_{33} & k_{37} & k_{40} & k_{42} \\ k_{28} & k_{23} & k_{29} & k_{34} & k_{38} & k_{41} \\ k_{33} & k_{29} & k_{24} & k_{30} & k_{35} & k_{39} \\ k_{37} & k_{34} & k_{30} & k_{25} & k_{31} & k_{36} \\ k_{40} & k_{38} & k_{35} & k_{31} & k_{26} & k_{32} \\ k_{42} & k_{41} & k_{39} & k_{36} & k_{32} & k_{27} \end{bmatrix} \tag{2.62}$$

where superscript $'$ denotes the updated stiffness matrices. The units of the modification matrix components for upper left-right and lower left-right $3 \times 3$ sub-matrices are N/m, N/rad, $\mathrm{N} \cdot \mathrm{m/m}$, and $\mathrm{N} \cdot \mathrm{m/rad}$, respectively. The links of the manipulator are located at different positions along the $z$-axis, as shown in Figure 2.9 b). These position differences are not considered in the modeling. Since the position along $z$-axis is constant for all parts, connection shafts along the $z$-axis make a constant contribution to local stiffness matrices and they are not a function of joint variables. The effect of this continious contribution of $z$-axis offset can be carried out by the modification matrices necessary to comply with the experiment data. Hence, the existing model can be used.

Another contribution of the modification matrices is acquiring the internal stress-related stiffness model. Internal stress behaves like a compressed/stretched spring that depends on the kinematic states of the manipulator. In addition, applied external force contributes to the internal stresses by further compression/tension. Therefore, $\boldsymbol{K}_C$ in Equation 2.60 can be updated to contain internal stiffness parameters, $\boldsymbol{K}_I$, as follows:

$$\boldsymbol{K}'_C = \boldsymbol{K}_C + \boldsymbol{K}_I \tag{2.63}$$

Acquisition of $\boldsymbol{K}_I$ requires an additional stiffness model for internal stresses as a function of kinematics which is a tedious process. Instead, the stiffness model $\boldsymbol{K}_I$ is separated into two parts. The first part, $\boldsymbol{K}_{Iv}$, is the variable part that changes with the mechanism's configuration. $\boldsymbol{K}_{Ic}$ is the constant part, and $\boldsymbol{K}_I = \boldsymbol{K}_{Iv} + \boldsymbol{K}_{Ic}$. $\boldsymbol{K}_{Iv}$ part is already infused in $\boldsymbol{K}'_{\theta 2}$ and $\boldsymbol{K}'_{\theta 3}$ while determining the modification matrix. For the constant $\boldsymbol{K}_{Ic}$ part, a new symmetric set of stiffness coefficients with 21 elements are defined. These coefficients are specified in the optimization process along with modification matrices.

$$\boldsymbol{K}'_C = \boldsymbol{K}_C(\boldsymbol{K}_{\theta 1}, \boldsymbol{K}'_{\theta 2}, \boldsymbol{K}'_{\theta 3}) + \boldsymbol{K}_{Ic}, \quad \boldsymbol{K}_{Ic} = \begin{bmatrix} k_{43} & k_{49} & k_{54} & k_{58} & k_{61} & k_{63} \\ k_{49} & k_{44} & k_{50} & k_{55} & k_{59} & k_{62} \\ k_{54} & k_{50} & k_{45} & k_{51} & k_{56} & k_{60} \\ k_{58} & k_{55} & k_{51} & k_{46} & k_{52} & k_{57} \\ k_{61} & k_{59} & k_{56} & k_{52} & k_{47} & k_{53} \\ k_{63} & k_{62} & k_{60} & k_{57} & k_{53} & k_{48} \end{bmatrix} \tag{2.64}$$

A final modification is issued for the external force applied on the mobile platform. Since there is a positional difference along the $z$-axis between the links, as shown in Figure 2.9 b), external force, $\bar{F}$, generates a moment on the links. The planar stiffness model cannot capture this effect. Nonetheless, the external force can be adapted for the stiffness model by introducing virtual vertical moment arms that will generate the same torsional effect on the links. Hence, the external force is updated as follows:

$$\bar{F} = \begin{bmatrix} F_x & F_y & 0 & 0 & 0 & 0 \end{bmatrix}^T \quad \rightarrow \bar{F}' = \begin{bmatrix} F_x & F_y & 0 & h_1 F_y & h_2 F_x & 0 \end{bmatrix}^T \tag{2.65}$$

where $\bar{F}$ is the actual external force applied on the mobile platform, and $\bar{F}'$ is the modified force. $h_1$ and $h_2$ are the moment arms in m determined in the model fitting process along with modification matrices. Including the stiffness matrix coefficients and moment arms, there are 65 parameters to be determined by the model-fitting algorithm. The objective function to fit the model to the experimental data is defined as follows:

$$\bar{e} = \boldsymbol{K}'^{-1}_C \bar{F}' - \Delta \bar{X}_{\text{Measured}}, \quad E = \|\bar{e}_{1-5}\|, \quad E_{net} = \sum_{1}^{45} E \tag{2.66}$$

where $\bar{e}$ is the error vector between the modeled and measured deflection. $E$ is the norm of the error vector's first 5 elements. The final element for $z$-axis rotation is excluded since it is not possible to measure the rotation of this axis with the measurement points in Figure 2.9 b) which are aligned along the $z$-axis. Note that this introduces redundancy to the optimization, which searches for a suitable parameter set for the 5-DoF system using the 6-DoF stiffness model. Hence, the obtained result may not be unique. $E_{net}$ is the objective function to be minimized, which is the summation of error norms through 45 measurements. The solution of the objective function is achieved via MATLAB by using *fmincon* and *fminsearch* functions. Initial values for parameters are defined between 0-1 randomly.

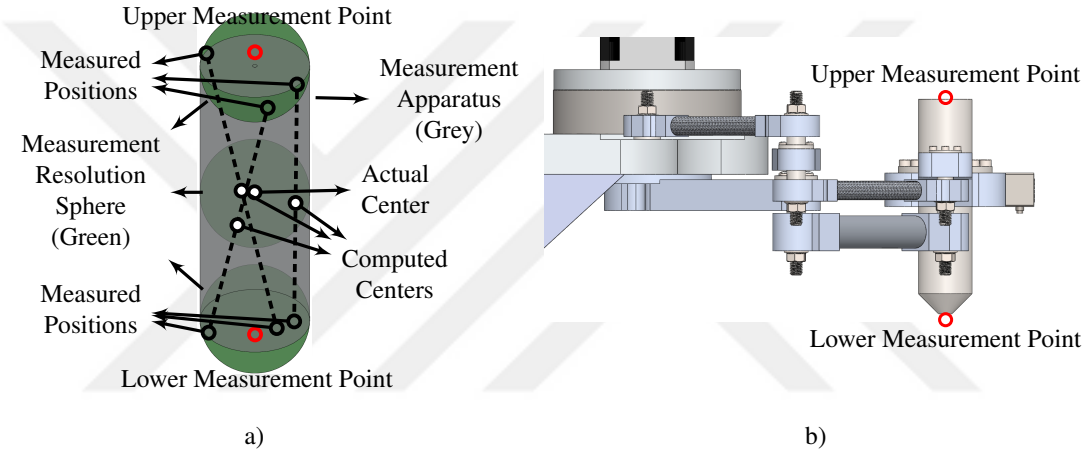
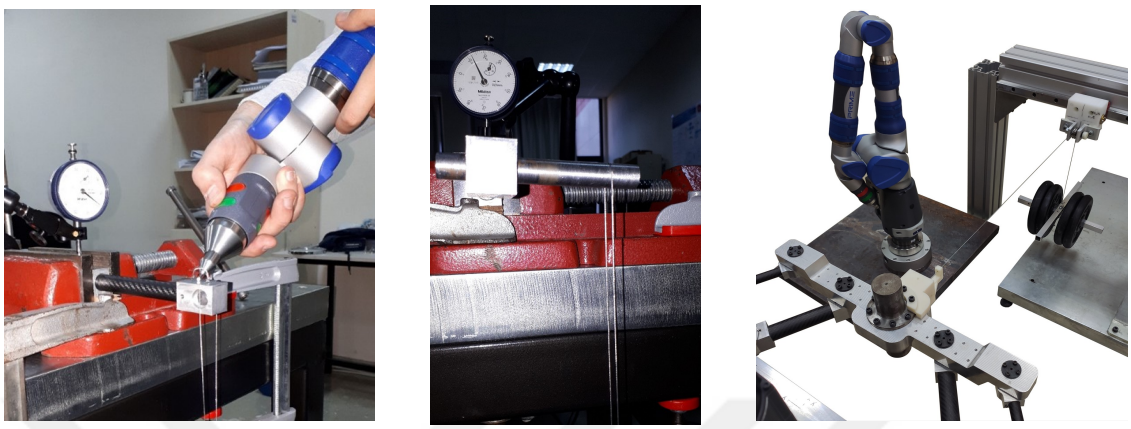



Figure 2.9. a) Illustration of measurements from the apparatus, b) $-y$-axis view of the manipulator.

### 2.5.1. Processing the Experiment Data

Experiment measurements need to be collected from the mobile platform frame origin, but it is impossible to reach this point with the CMM tip (ceramic spherical measuring tip). Therefore, a measurement apparatus was designed as a dummy tool for the mobile platform. There are upper and lower measurement points on the apparatus. With the location data collected from these points, the position of the mobile platform frame can be calculated. The resolution of the FARO Prime Arm 1.2 CMM, on which the test measurements were made, is $\pm 0.023$ mm. This means that the actual location of a point measured in space can be anywhere within a sphere with a radius of 0.023 mm. So when

calculating the position of the mobile platform frame, this calculation has a margin of error of $\pm 0.023$ mm. The actual center of the mobile platform and the calculated centers are visualized in Figure 2.9 a).



a) b) c)

Figure 2.10. a) Measurement of linear deflection via CMM for force load, b) applied torsion with a moment arm, c) load applied on the manipulator.
(Source: Paksoy et al. (2021))

15 test points are determined in the workspace. Blocks with 5, 10, 15, 20, and 25 kg masses are used for loading and applied separately along $x$- and $y$-axes. These masses generate 49.05, 98.1, 147.15, 196.2, and 245.25 N loads, respectively. The coordinates of the mobile platform frame are measured via CMM once at each test point and for each loading case. Including the no-load case measurement, 6 measurements are recorded at each test point. By subtracting the measured coordinates of the dummy tool during the loaded case from measurements during the no-load case, 5 compliant deflection values are obtained for 5 to 25 kg loading cases. Thus, 75 deflection data are obtained for each $x$- and $y$-axes loading case. The experiment setup is shown in Figure 2.10 and details are described in (Paksoy et al., 2021).

The stiffness model of this manipulator has the same absolute eigenvalues about the $x$-axis at the symmetric positions. For example, the absolute eigenvalue is the same at the (220 mm, -50 mm) and (220 mm, 50 mm) positions, meaning the same amount of compliant deflection should be observed for the same loading from the mobile platform frame. Nevertheless, the experimental data do not show a symmetrical feature. This is because the measurement accuracy of the CMM is not high enough. If a post-processing procedure is carried out to make the data obtained around the $x$-axis symmetrical, it is

seen that the most significant error between the symmetric data set and the actual data set is smaller than $\pm 0.023$ mm. The amount of correction required for this process is defined as:

$$W = \left( ||V_{\text{Measured,Left}}| - |V_{\text{Measured,Right}}| \right) /2 \tag{2.67}$$

$$V_{\text{Measured,Left}} \pm W = V_{\text{Measured,Right}} \mp W \tag{2.68}$$

Here $W$ is the symmetry correction value, and $V$ is the measured data. Measurements made on the right and left sides of the $x$-axis are compared with each other's kinematic symmetry, and new symmetrical values are obtained. When this correction is applied, the most considerable modification required to make the data obtained in the $x$-axis deflection experiments symmetrical is 0.0098 mm and 0.0217 mm for the $y$-axis. The largest change in angular deflections is $0.005^\circ$ for $x$-axis rotation and $0.0085^\circ$ for $y$-axis rotation. Therefore, it can be concluded that the cause of the symmetry error is due to the low resolution of the CMM. The symmetrical data set significantly facilitates fitting the model to the data. There are two reasons for this. The first is that the symmetrical state is closer to the ideal state, thus more mathematically suitable for calculations. The second is that about half of the data required to update the model parameters is sufficient, thanks to symmetry. Therefore, it is possible to obtain a faster solution.

### 2.5.2. Experimental Results and Discussion

The optimized modification matrix parameters are presented in Appendix Table A2. If these parameters are closer to zero, less modification is required, and the initial guess is accurate. As described in Equation 2.65, the loading conditions from the mobile platform frame have zero components for $z$-axis force and moment. It means 3$^{\text{rd}}$ and 6$^{\text{th}}$ columns of the inverse of the stiffness matrix $\boldsymbol{K}_C'$ are multiplied with zero values during optimization of the modification matrix. This introduces redundancy in optimizing the modification matrix; hence, this set of parameters is not unique. Furthermore, this redundancy fits the model to the experimental data as if it is reserved for fine adjustment. In this regard, the computed modification matrix is a solution of a Pareto-front optimal set.

Table 2.3. Average RMS error of model output and experimental data with updated and non-updated stiffness model parameters at loading conditions.

| | **Updated Model - $F_x$ Load** | | | | **Updated Model - $F_y$ Load** | | | |
|---|---|---|---|---|---|---|---|---|
| **Load (N)** | $\Delta x$ $(\mu m)$ | $\Delta y$ $(\mu m)$ | $\Delta z$ $(\mu m)$ | $\Delta\theta_y$ $(^\circ)$ | $\Delta x$ $(\mu m)$ | $\Delta y$ $(\mu m)$ | $\Delta z$ $(\mu m)$ | $\Delta\theta_x$ $(^\circ)$ |
| 49.05 | 4.2 | 4.6 | 8.6 | $2\times10^{-3}$ | 5.1 | 5.7 | 5.0 | $3\times10^{-3}$ |
| 98.1 | 4.0 | 3.7 | 5.7 | $2\times10^{-3}$ | 5.5 | 2.2 | 10.3 | $2\times10^{-3}$ |
| 147.15 | 5.7 | 8.1 | 8.6 | $2\times10^{-3}$ | 7.6 | 5.2 | 11.2 | $2\times10^{-3}$ |
| 196.2 | 7.1 | 10.0 | 6.8 | $1\times10^{-3}$ | 8.1 | 5.5 | 11.5 | $2\times10^{-3}$ |
| 245.25 | 8.3 | 10.7 | 5.6 | $2\times10^{-3}$ | 10.7 | 5.9 | 13.6 | $2\times10^{-3}$ |

| | **Non-Updated Model - $F_x$ Load** | | | | **Non-Updated Model - $F_y$ Load** | | | |
|---|---|---|---|---|---|---|---|---|
| **Load (N)** | $\Delta x$ $(\mu m)$ | $\Delta y$ $(\mu m)$ | $\Delta z$ $(\mu m)$ | $\Delta\theta_y$ $(^\circ)$ | $\Delta x$ $(\mu m)$ | $\Delta y$ $(\mu m)$ | $\Delta z$ $(\mu m)$ | $\Delta\theta_x$ $(^\circ)$ |
| 49.05 | 42.3 | 39.0 | 18.8 | $20\times10^{-3}$ | 39.6 | 172.7 | 4.9 | $10\times10^{-3}$ |
| 98.1 | 86.4 | 77.5 | 33.6 | $30\times10^{-3}$ | 78.9 | 351.4 | 10.6 | $20\times10^{-3}$ |
| 147.15 | 130.8 | 118.3 | 50.6 | $50\times10^{-3}$ | 121.6 | 526.4 | 11.7 | $20\times10^{-3}$ |
| 196.2 | 175.3 | 151.6 | 66.9 | $70\times10^{-3}$ | 159.5 | 699.8 | 11.9 | $30\times10^{-3}$ |
| 245.25 | 217.7 | 188.9 | 83.8 | $80\times10^{-3}$ | 201.0 | 879.5 | 13.8 | $40\times10^{-3}$ |

Table 2.3 presents the average root-mean-square (RMS) of the errors between the model and experimental data with updated and non-updated stiffness matrix parameters for all loads. The effectiveness of parameter update can be easily seen by comparing the $F_y/\Delta y$ load/deflection relation at 25 kg of mass loading condition for updated and non-updated results. A reduction from 879.5 μm RMS error to 5.9 μm RMS error is achieved. The error set of $F_y/\Delta y$ shows the best performance enhancement and has the minimum error set after the parameter update, even though other loads/deflection sets have lower errors before the parameter update. The reason for this behavior lies in the definition of the objective function in Equation 2.66. Since the large loads and large deflections are related to the stiffness parameters, a slight modification in these parameters is amplified by the large load/deflection relation, which results in a greater error achieved from the model. Therefore, the optimization algorithm prioritizes reducing the large deflection errors by adjusting their related stiffness parameters. It can be said that large load/deflection relation defines a weight on the objective function. As a result, small load/deflection relations become less critical. It can be proved by comparing $F_y/\Delta z$ RMS errors before and after the parameter updates. The error remains the same because $F_y/\Delta z$ has the minimum load/deflection values as shown in Table 2.3.

Table 2.4. Average absolute error between the model and experimental data for all loading conditions. The same upper index symbol indicates the symmetric test points.

| | | | $F_x$ Load | | | | $F_y$ Load | | | |
|---|---|---|---|---|---|---|---|---|---|---|
| Test Point | $\varphi_{11}(^\circ)$ | $\varphi_{21}(^\circ)$ | $e_x(\mu m)$ | $e_y(\mu m)$ | $e_z(\mu m)$ | $e_{\theta y}(^\circ)$ | $e_x(\mu m)$ | $e_y(\mu m)$ | $e_z(\mu m)$ | $e_{\theta x}(^\circ)$ |
| $1^\dagger$ | -27.7 | 74.8 | 1.37 | 5.43 | 4.45 | $2\times10^{-3}$ | 2.45 | 5.38 | 15.24 | $1\times10^{-3}$ |
| $2^\star$ | -19.9 | 57.3 | 6.71 | 4.15 | 1.18 | $1\times10^{-3}$ | 7.30 | 2.48 | 12.26 | $2\times10^{-3}$ |
| $3^\bullet$ | -4.4 | 35.2 | 3.59 | 4.59 | 2.94 | $1\times10^{-3}$ | 6.56 | 2.78 | 8.12 | $3\times10^{-3}$ |
| $4^\otimes$ | -15.9 | 31.6 | 1.64 | 2.44 | 3.11 | $1\times10^{-3}$ | 7.41 | 3.85 | 8.37 | $3\times10^{-3}$ |
| $5^\triangle$ | -31.7 | 50.9 | 4.22 | 13.69 | 12.89 | $3\times10^{-3}$ | 3.52 | 1.67 | 5.75 | $2\times10^{-3}$ |
| $6^\diamond$ | -41.7 | 66.3 | 2.44 | 7.11 | 1.76 | $1\times10^{-3}$ | 3.52 | 2.67 | 6.40 | $1\times10^{-3}$ |
| 7 | -55.0 | 55.0 | 7.81 | 0.86 | 5.43 | $1\times10^{-3}$ | 13.12 | 8.56 | 6.46 | $1\times10^{-3}$ |
| 8 | -42.2 | 42.2 | 12.09 | 0.69 | 6.48 | $1\times10^{-3}$ | 2.81 | 6.34 | 9.09 | $2\times10^{-3}$ |
| 9 | -24.9 | 24.9 | 5.04 | 0.46 | 4.31 | $2\times10^{-3}$ | 8.10 | 5.54 | 10.21 | $3\times10^{-3}$ |
| $10^\diamond$ | -66.3 | 41.7 | 2.59 | 7.45 | 1.86 | $1\times10^{-3}$ | 7.36 | 2.91 | 5.14 | $1\times10^{-3}$ |
| $11^\triangle$ | -50.9 | 31.7 | 4.38 | 14.69 | 16.62 | $3\times10^{-3}$ | 3.40 | 1.45 | 5.70 | $2\times10^{-3}$ |
| $12^\otimes$ | -31.6 | 15.9 | 1.65 | 2.38 | 3.06 | $1\times10^{-3}$ | 5.49 | 3.79 | 6.28 | $3\times10^{-3}$ |
| $13^\bullet$ | -35.2 | 4.4 | 5.03 | 4.52 | 3.07 | $1\times10^{-3}$ | 9.59 | 3.86 | 11.67 | $3\times10^{-3}$ |
| $14^\star$ | -57.3 | 19.9 | 7.30 | 4.51 | 1.78 | $1\times10^{-3}$ | 5.71 | 1.48 | 12.17 | $2\times10^{-3}$ |
| $15^\dagger$ | -74.8 | 27.7 | 1.24 | 5.27 | 5.36 | $2\times10^{-3}$ | 2.25 | 3.24 | 15.68 | $1\times10^{-3}$ |

Table 2.4 shows absolute deflection errors between the model and the experimental data. The presented results are the average errors considering all loading conditions from 49.05 N to 245.25 N at each test point. The same upper index symbol indicates symmetric test points. $x$-axis deflections for $F_x$ load and $y$-axis deflections for $F_y$ load show smaller average error than 10 $\mu m$, but only in one occurrence for $F_x/\Delta x$ load/deflection relation at test point 8 the error surpasses 10 $\mu m$. $F_x/\Delta y$ and $F_y/\Delta x$ load/deflection relations also present a smaller error performance than 10 $\mu m$ except at three occurrences at test points 5, 11, and 6.

In Figure 2.11, 2.12, and 2.13, measured deflections and the model's output, which is updated by the modification matrix, are illustrated. When the obtained model is compared with the experimental data, a good overlap is observed even for large deflection values. If the joint clearances were more significant than anticipated or the internal stresses were higher than predicted, the stiffness problem would take on a much more non-linear mathematical nature. In this case, the obtained model and the designed parameters would be insufficient to solve the problem. After its parameters are updated correctly, the stiff-

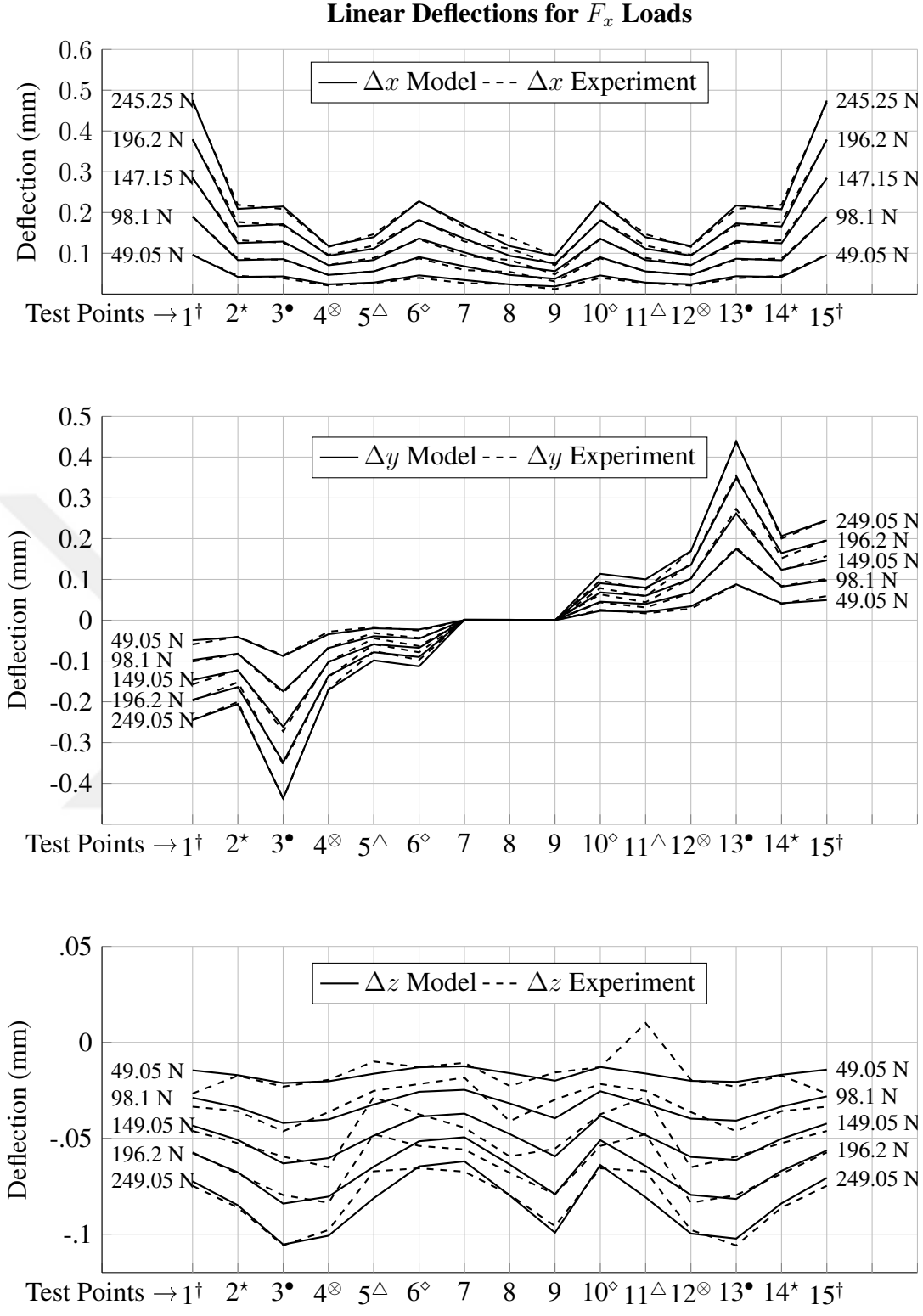



Figure 2.11. Linear deflections for loads along $F_x$.

ness model captures the manipulator's general characteristics. In Figure 2.11 and 2.12, $x$-axis deflections for $F_x$ load and $y$-axis deflections for $F_y$ load display the greatest deflection values. 0.5 mm and 1.7 mm maximum deflections are recorded for $F_x/\Delta x$ and

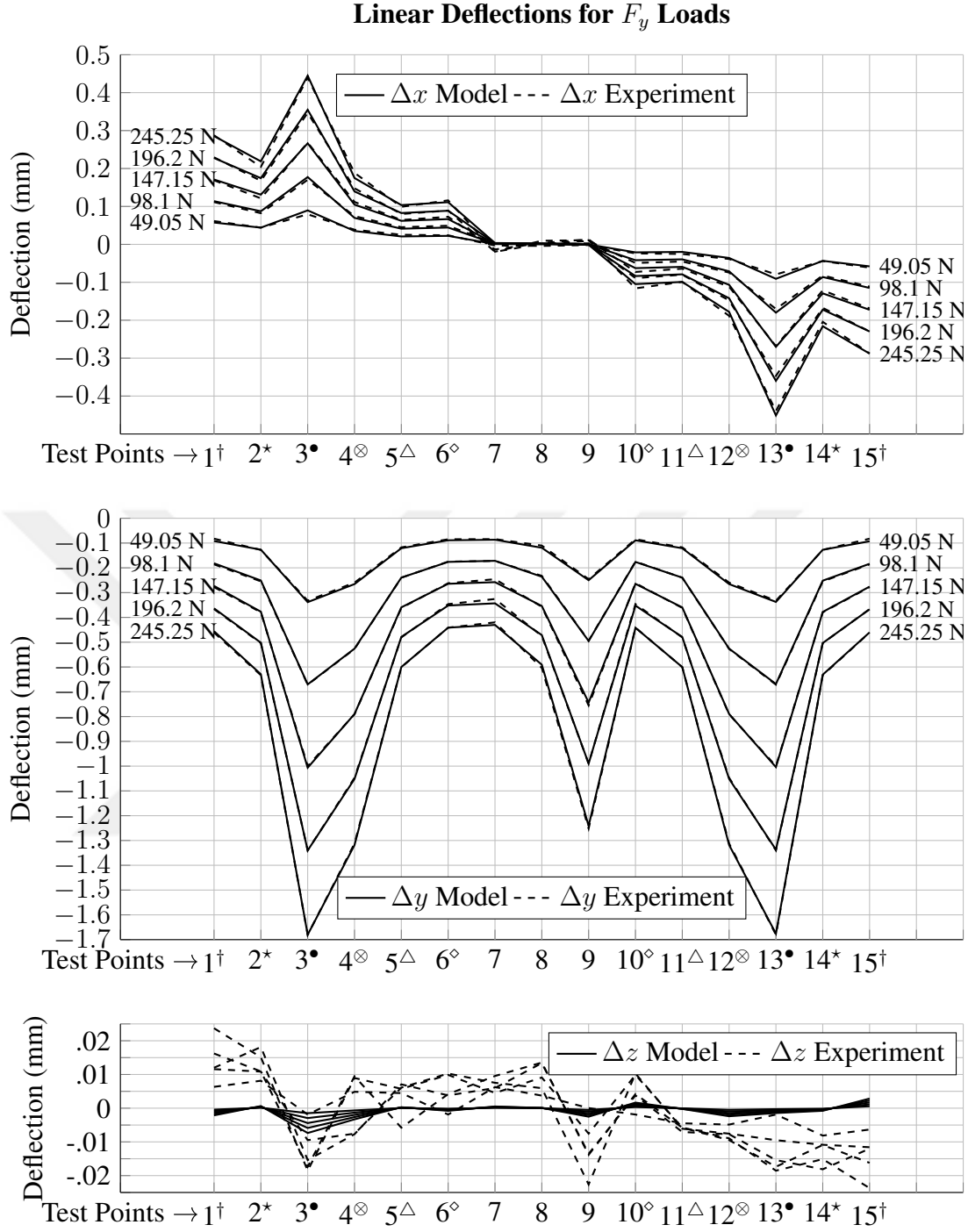



Figure 2.12. Linear deflections for loads along $F_y$.

$F_y/\Delta y$ load/deflection relations, respectively. Since there is no force component along $z$-axis, minimal deflection values are recorded along this axis. When the model's performance for angular deflections is examined, it provides a good match for the angular deflections about $y$- and $x$-axes. Maximum angular deflections are smaller than 1.6° for $y$-axis rotation under $F_x$ load and 1° for $x$-axis rotation under $F_y$ load.

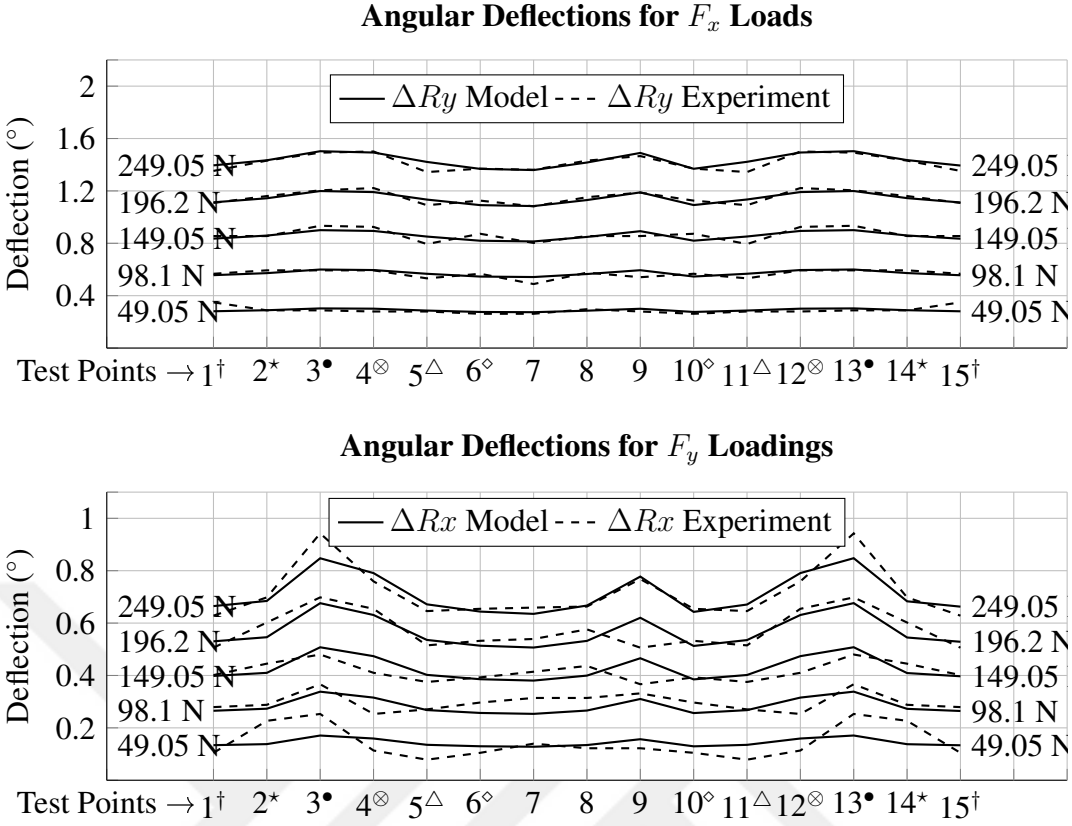



Figure 2.13. Angular deflections about $x$- and $y$- axes.

In this part, a model fitting process was applied to the existing stiffness model from the previous section. It is possible to update the model considering the height difference between the distal and proximal parallelograms. In that case, distal parallelograms would experience only forces since their links are at the same height level with the mobile platform. However, the proximal parallelograms would experience both force and moment due to the height difference. This moment can be computed considering the load distribution in the joint space. This computation is explained in Equation 2.65. This modified force and moment vector is computed using the virtual moment arm parameters obtained during the model fitting process to comply with the experiment results.

## 2.6. Conclusion and Discussion

This chapter uses a case study to present stiffness model acquisition via the VJM of parallel manipulators with serially connected sub-loops in their limbs. Auxiliary force effects on the end-effector's compliant deflection are considered via the superposition

principle. In order to investigate the performance of the auxiliary force consideration method, two VJM models of the manipulator are acquired in which one is only subjected to forces at the end-effector, and the other one is subjected to auxiliary forces and end-effector forces. Auxiliary forces are calculated to be one-tenth of the end-effector forces; hence, minimal differences between the two models are expected. The outputs are compared with a finite element model subjected to auxiliary and end-effector forces. Nine test points are determined within the manipulator's workspace, and compliant deflections are obtained for each $x$- and $y$-axes in the simulation environment. 18 simulation test results are obtained with the proposed methodology. Among these results, (1) in 8 tests, the proposed method produced better results compared to the case where only the forces at the end-effector are considered, (2) in 6 tests, both methods produced the same results and (3) in 4 tests, the proposed method produced relatively worse results. The proposed method ($\text{VJM}_{\text{EAB}}$) may output better results if an iterative method is adopted. Nevertheless, both VJM models have captured the configuration-dependent stiffness characteristics of the manipulator. Hence, it can be concluded that the proposed VJM model acquisition procedure for parallel manipulators that have serially connected sub-loops is applicable. Also, the proposed superposition methodology works when considering the auxiliary forces; however, this feature calls for further investigation. In addition, the 6-DoF VJM model runs at 10 kHz in a Matlab environment and can even run faster if the size of the stiffness matrix is made smaller by discarding the columns and rows of unneeded deflection axes.

The VJM model accuracy and performance are also compared with the experimental results obtained from the actual manipulator. 49.05 N to 245.25 N loads are applied to the real manipulator along $x$- and $y$-axes, and compliant deflection results are obtained. Next, a modification matrix is proposed to update the VJM model parameters using experimental data. It was able to capture configuration-dependent and configuration-independent gain values for enhancing the accuracy of the stiffness model. Then, the VJM model output is compared with the experiment results. The maximum average RMS error of 879.5 μm is reduced to 5.9 μm. Hence, the ability of the proposed VJM method to represent the configuration-dependent stiffness behavior of the manipulator is experimentally verified. This proves the soundness of the proposed stiffness modeling solution of having serially connected sub-loops at the limbs of parallel manipulators and the vitality of the modification matrix for the stiffness parameter update process.

# CHAPTER 3

# A NEW SAFE FLEXIBLE TORSION JOINT DESIGN WITH SOFTENING STIFFNESS CHARACTERISTICS

This chapter introduces a novel flexible joint design that enhances mechanical versatility. The design shows how to obtain bidirectional deflections from a unidirectional spring. It enables the parallel and serial connections of springs. It features multiple stiffness regions determined by applied load levels, eliminating the need for a clutch mechanism. Mechanical limits can be added to customize stiffness, offering more hardening or softening regions. The design also allows for connecting multiple flexible joint units in series. In a case study, the series flexible joint design is developed with two flexible joint units, providing a softening stiffness characteristic. The joint has rigid, stiff, and soft regions. When used as a series elastic actuator in a robot manipulator, the rigid region aims to conduct the tasks at low torque levels, i.e., trajectory tracking. The stiff region is preserved for collaborative tasks in human-robot interaction, while the soft region enhances the robot's safety in case of control failure or collision. Static and dynamic test results comply with the ideal model. This flexible joint design improves mechanical performance, safety, and adaptability.

## 3.1. Introduction

In the early years of robot technologies, stiff robots were in demand for high positioning performance because high stiffness meant precision, stability, and larger bandwidth. Now, the expectations from a robot are more complex, such as safe human interaction, compliance with the environment, energy efficiency, and shock absorption. Each subject addresses the regulation of the robot's mechanical impedance. This problem can be handled in mechanical design and control design domains. Compliance controllers developed for stiff robot manipulators have been used to regulate the physical interaction of the robot with its environment. However, these controllers struggle to address all these new expectations. Hence, adjusting the impedance at the mechanical level becomes

a necessity. One of the ways to achieve this is by introducing flexibility to the robot manipulator through constant or variable stiffness joints (Vanderborght et al., 2013).

In recent years, researchers have focused on joints with variable stiffness. Studies are mainly oriented around active variable stiffness (AVS) joints. These joints permit the active change of the stiffness of a joint and give more dexterity to controlling the mechanical impedance. Constant stiffness or passive variable stiffness (PVS) joints, on the other hand, are safer for human-robot and robot-environment interactions. This type of joint makes the robot mechanism inherently compliant against external interactions by reducing the risks of a robot harming humans or damaging itself in case of a collision.

This chapter focuses on developing a novel PVS joint mainly aiming at human safety. With this PVS joint, the goal is to adapt to different operation conditions. This joint can also be coupled with an actuator to obtain a series elastic actuator (SEA). The proposed design approach can be applied to torsion and linear springs. The proposed joint design addresses many design problems of flexible joints. Below, flexible joint design approaches are investigated from a broader perspective to highlight their design problems clearly.

Implementing elastic elements into a robot mechanism gave birth to various design methods. Ham et al. (2009) categorized flexible joint design approaches as equilibrium, antagonistic, structure, and mechanical methods. The equilibrium method is locating a spring between the input and output, resulting in force/torque equilibrium. An early example was developed by Pratt and Williamson (1995) in the middle of the 1990s as a SEA. In the mechanical method, the spring stiffness is adjusted with an additional mechanism (Morita and Sugano, 1995). In an antagonistic setup, the springs are assembled antagonistically, like muscle/joint connection systems. They can also be considered parallel connections of two separate SEAs on a joint (Migliore et al., 2005). As the last type of design method, structural methods focus on selecting a material with the desired Young's modulus, designing their moment of inertia, and defining effective beam lengths (Stienen et al., 2009). These methods can be employed independently or fused and used simultaneously.

Examples of designs with the structural methods using torsion springs are shown in (Dos Santos et al., 2017; Stienen et al., 2009; Sergi et al., 2012; Hou and Lan, 2013; Lagoda et al., 2010). The parameters that affect the stiffness of the spring are adjusted via finite element simulations, resulting in intricate designs. They are generally unidirectional springs (Dos Santos et al., 2017; Hou and Lan, 2013). Thus, they have different stiffness

for clockwise (CW) and counterclockwise (CCW) deflections (Stienen et al., 2009). Kong et al. (2009) used a single torsion spring for both direction deflection. However, this design shows different stiffness characteristics at $-25^\circ$ and $+25^\circ$ of deflections. Sergi et al. (2012) designed a symmetric structural torsion spring to address this problem. Yet, it still suffers from a limited deflection range. Their intricate design makes their production costly. Since they are primarily prototypes, their long-term fatigue performances have yet to be discovered.

Some examples of antagonistic flexible joint/actuator design were presented in (Migliore et al., 2005; Li et al., 2022; Celebi et al., 2013; Agarwal and Deshpande, 2017). They generally use linear spring elements that have non-linear spring characteristics. Migliore et al. (2005) adjusts the tension on springs and Li et al. (2022) modifies the joint assembly mode for desired stiffness. Celebi et al. (2013) and Agarwal and Deshpande (2017) use Bowden cables with antagonistic setup to remotely actuate the joints. Also, Agarwal and Deshpande (2017) introduce a pair of torsion springs to their system as an alternative to linear springs. Typically, a torsion antagonistic flexible joint deflects about an equilibrium point. The actuator can be used to adjust the initial location of the equilibrium point. Due to the constructional limits, the initial location is limited within a $\pm 180^\circ$ range.

AVS joints that use mechanism designs are investigated in (Kim and Song, 2010; Jafari et al., 2012; Sun et al., 2018). Among them, Kim and Song (2010) and Jafari et al. (2012) adopt the lever arm/moment arm mechanism. By adjusting the arm's length, they actively regulate the output stiffness. Sun et al. (2018) used the Archimedean spiral cam mechanism to adjust the lever arm actively. Liu et al. (2021), on the other hand, combined slider-crank and four-bar mechanisms for stiffness mapping. Wolf and Hirzinger (2008) used a linear spring attached to a roller and a cam disk. The roller slides on the cam disk when torque is applied to the joint. The profile of the cam disk establishes the relationship between the spring stiffness and applied torque. These designs adopt a linear spring for rotary motion. This leads to complex designs, increasing the cost, the number of parts, and weight. Another reason that leads to these problems stems from the unidirectional characteristic of the springs. Because of this, a minimum of two springs (one for each direction) are used (Jin et al., 2018; Wyeth, 2008; Awad et al., 2016; Li et al., 2017). An alternative solution is presented by Sariyildiz et al. (2023) and Xu et al. (2021), which combine structural and mechanical methods.

Flexible joints developed using the equilibrium approach are relatively better at

energy storage and shock absorption. In (Verstraten et al., 2016), it is stated that a SEA can reduce energy consumption up to 78%. Therefore, equilibrium design is essential in mobile robots (Curran and Orin, 2008) or exoskeleton designs (Kong et al., 2009) where the system is not fixed to the ground and batteries are used. Another example is the SEA developed by Paine et al. (2013). In their design, a spring element is located between the load and base. Thus, the spring element stores all the energy of the external load. This design was later used in (Shao et al., 2021).

To understand the difference between these design methods, let's assume a spring mechanism shown in Figure 3.1. The four design methods can be generalized in the following equation:

$$\boldsymbol{K}_C = \boldsymbol{J}^{-T}\boldsymbol{K}_\theta\boldsymbol{J}^{-1} \tag{3.1}$$

$$\boldsymbol{J} = \boldsymbol{J}(l_1, l_2, \theta) \tag{3.2}$$

where $\boldsymbol{K}_\theta$ is the stiffness matrix of the spring element/s, $\boldsymbol{K}_C$ is the effective stiffness matrix displayed at the output shaft of the joint, $\boldsymbol{J}$ is the Jacobian matrix related to the mechanism adjusting the output stiffness. Structural methods deal with the design of $\boldsymbol{K}_\theta$. Mechanical methods are used for designing $\boldsymbol{J}$ for a desired $\boldsymbol{K}_C$. Here, $l_1$ is the crank length, $l_2$ is the natural length of the spring, and $\theta$ is the crank angle. The joint is equilibrium-controlled if $\boldsymbol{J}$ is a constant matrix which refers to $\theta = 0°$. $180° > \theta > 0°$ refers to a PVS joint, and output stiffness $\boldsymbol{K}_C$ operates according to predefined kinematic relation. If the angle $\theta$ is controlled by an actuator, the joint is called an AVS joint. The antagonistic method deals with the serial/parallel combination of stiffness adjusting mechanisms ($\boldsymbol{K}_C$) and/or elastic components ($\boldsymbol{K}_\theta$). The proposed equation only gives a better idea of the composition of flexible joints. The spring systems with non-continuous stiffness models (stiff and soft modes) or those accommodating a clutch mechanism would require additions/modifications to this equation (Liu et al., 2018; Plooij et al., 2017).

Independent of the method chosen for designing a variable stiffness joint, in a human-robot or robot-environment interaction, the desired joint behavior is achieving high stiffness at low interaction forces for precision and low stiffness at high interaction forces for safety. There have been various designs to achieve this softening behavior for a robot mechanism. Park et al. (2008) and López-Martínez et al. (2015) proposed a link

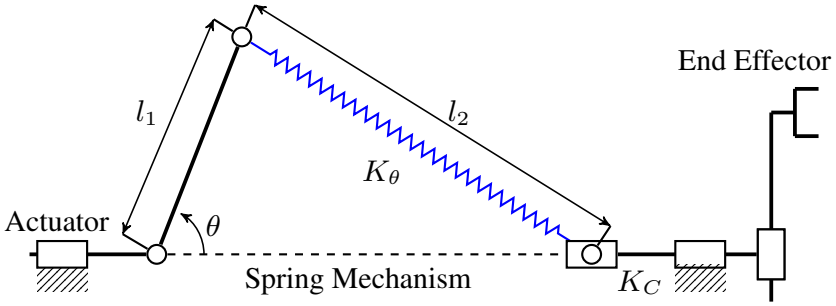



Figure 3.1. Flexible joint analogy

design. The link was divided into two segments that were assembled by the use of a spring in between. When an external force is applied to the link, enough to overcome the pretension force on the spring, the link enters the soft state and ensures the interaction safety. However, this poses a critical problem by introducing an additional DoF to the system. For instance, a remote center of motion (RCM) mechanism is designed to strictly move about a point. To conserve this kinematic constraint, any flexible links are to be avoided. Zebardast et al. (2013) and Zheng et al. (2021) proposed a flexible revolute joint aiming safety. They use a similar idea to drive-click torque wrenches. They assemble two sides of the revolute joints (one side has engraved slots on it) by using springs. In these four studies, proposed designs operate like on/off systems. They only adjust the safe interaction limits. On the other hand, Hyun et al. (2010), Kim et al. (2010), and Wang et al. (2015) inspired from cam disk design of Wolf and Hirzinger (2008). They added a slot on the cam disk to achieve a high-stiffness region. While these joints perform similar to on/off system designs below the safe limits, they display a desired stiffness behavior when the load is beyond the safe limits. In Kim et al. (2010) and Park et al. (2008), on the other hand, used a slider-crank mechanism in their flexible revolute joint design for the same purpose.

In this work, a PVS joint is proposed. The joint brings several novelties to both torsion- and linear-type flexible joints. A case study has been developed for the proposed torsion-type PVS joint. Henceforth, the comments on the design are mainly given for revolute flexible joints. The novelties of this work are listed below:

- Adopting the relative motion aspect makes it possible to use a unidirectional spring for bidirectional deflections, thus reducing the required number of springs by half.
- The design permits parallel/serial connection of torsion springs, including the an-

tagonistic assembly mode.

- The design enables having multiple stiffness regions by employing serial connections of torsion springs and adjusting their initial tensions.
- The transition between stiffness regions depends on the load passing on the flexible joint. Therefore, there is no need for a clutch mechanism.
- There is no fixed equilibrium point for the deflection. Compliant deflection can occur at any joint angle unbounded by the number of rounds.
- Each revolute PVS joint unit can have a deflection for full cycle rotation. The series connection of these joints increases the number of total round deflections by the number of used units.
- It is scalable for stiffer/softer and larger/smaller systems.
- The design is simple and cheap, can be constructed using off-the-shelf components and is easy to manufacture.

Last but not least, when investigated from the safe joint aspect, the series flexible joint design with two flexible joint units provides a softening stiffness characteristic, unlike the cam disk design in (Wolf and Hirzinger, 2008), which is a hardening spring design. The proposed design has rigid, stiff, and soft regions. Here, rigid region refers to the region where no elastic component is deflected. If the flexible joint is deflected to its maximum limit, it again shows rigid behaviour. In addition, mechanical limits can be added to these two flexible joint units for acquiring more hardening or softening regions. Since each flexible joint unit can have one full round of deflection, the serial connection of an additional flexible joint unit increases this range up to two full rounds of deflection. The selected spring for the revolute PVS joint is a spiral torsion spring, also known as the clock spring. This kind of spring has space efficiency, the ability to produce constant stiffness, longevity, and cost-effectiveness. The stiffness of this spring is adjusted at the design stage. However, it also permits small adjustments after manufacturing by changing its outer diameter or shortening its length. Combining the design solution and selected spring, the proposed revolute PVS joint provides a solution that is one of the softest and has the largest deflection range among the flexible joints. Finally, the design permits the connection of many flexible joint units in series, thus forming as many stiffness regions as desired.

## 3.2. Working Principle of Torsion Flexible Joint

This section describes the simplified design of the novel torsion PVS joint to explain its working principle. Initially, the PVS joint mechanism's working principles are explained using a linear spring analogy. Then, the principles are extended to torsion flexible joints by providing a conceptual design.

### 3.2.1. Linear Flexible Joint Analogy

Springs can be categorized as compression springs and extension springs. Compression springs' length decreases under the load, while extension springs' length increases in the direction of applied force. They are both unidirectional springs. Extension springs are used in the following linear spring analogy.

The flexible joint setup for bidirectional deflection is shown in Figure 3.2. This flexible joint unit comprises a spring, two red caps, and moving/fixed parts. The caps are in contact with the moving/fixed parts thanks to restoring force on the spring. When there is no force, or the force is below the initial tension force on the spring, the setup is in rigid mode as shown in Figure 3.2a. As the force increases, one of the caps detaches from the fixed body, complies with the load, and enters the soft mode as shown in Figure 3.2b. Note that the moving and fixed-end concepts are interchangeable, as well as the direction of the force, hence the deflection direction. In this setup, the important feature is the relative motion of the parts. Therefore, both ends can be assigned as either input or output ends. When considering this setup for a part of the flexible joint structure, one end is connected to the actuator's output shaft while the other one is connected to the driven link (e.g. link of a robot arm).

$k_1$ is the stiffness coefficient of the spring. $x_1$ is the initial tension (i.e. pretension) length of the spring. The spring is undeflected when $x_1 = 0$. Assuming the stiffness is constant, the force/deflection model is given below:

$$\Delta x = \begin{cases} 0 & , |F| < F_1 \\ (F - \mathrm{sgn}(F)F_1)/k_1 & , |F| \geq F_1 \end{cases} \tag{3.3}$$

where $F_1 = k_1 x_1$ is the initial tension force. $|F| < F_1$ case addresses the rigid region of the joint while $|F| \geq F_1$ is required condition to enter the soft mode.

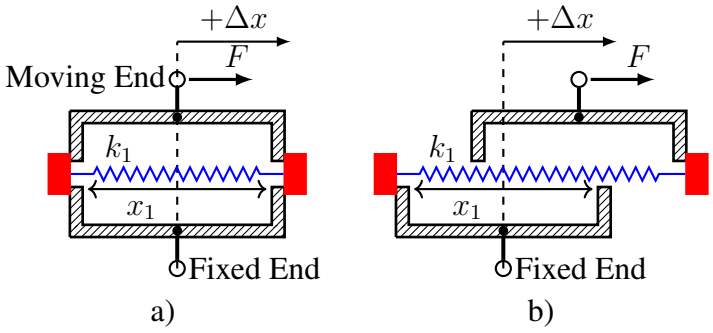



Figure 3.2. Illustration of bidirectional usage of extension spring.

The series of spring connections for flexible joint setup is shown in Figure 3.3. In this setup, a secondary flexible joint unit is attached to the moving end of the first joint unit. This constructs the series connection of the springs. Note that the force is a through variable, and applied force is transmitted through all springs in a series connection. Therefore, if the applied force is below the initial tension force on springs 1 and 2 (having stiffness of $k_1$ and $k_2$), the rigid state in Figure 3.3a is observed. If the initial tension on spring 2 is greater than spring 1, spring 1 becomes the first spring that shows compliant displacement under the increased load as shown in Figure 3.3b. When the force is increased further, spring 2 succumbs to loading and, as a result, starts to deflect as shown in Figure 3.3c. The stiffness modes of these consecutive cases are identified as rigid, stiff, and soft regions, respectively. The force/deflection relation of this softening flexible joint is given as follows:

$$\Delta x = \begin{cases} 0 & , F_1 > |F| \\ (F - \mathrm{sgn}(F)F_1)/k_1 & , F_2 > |F| \geq F_1 \\ (F - \mathrm{sgn}(F)F_2)\frac{(k_1+k_2)}{(k_1 k_2)} + \mathrm{sgn}(F)(F_2 - F_1)\frac{1}{k_1} & , |F| \geq F_2 \end{cases} \tag{3.4}$$

where the region with 0 deflection is the rigid region. $F_1 = k_1 x_1$ and $F_2 = k_2 x_2$ are the initial tension force of the springs. $F_2 > |F| \geq F_1$ defines the stiff region with stiffness $k_1$. Finally, $|F| \geq F_2$ addresses the soft region having a stiffness of $(k_1 k_2)/(k_1 + k_2)$ due to the series connection of springs. The term $(F_2 - F_1)/k_1$ refers to the maximum

deflection limit in the stiff region.

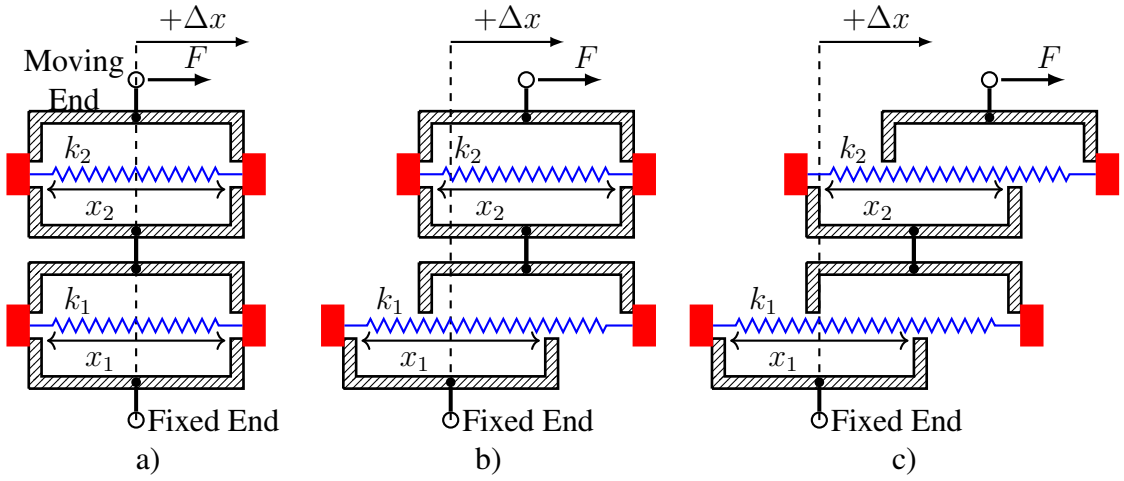



Figure 3.3. Series connection setup of linear springs. a) Rigid region, b) stiff region and c) soft region.

Another joint setup employs a parallel spring connection. There are two assembly modes for a flexible joint with a parallel spring connection. The first parallel mode, parallel mode 1, is shown in Figure 3.4a. The initial tension of the joint can be adjusted by generating tension on one or both of the springs so that rigid and soft stiffness regions are obtained. Hence, $x_2$ can be zero while $x_1$ might be deflected for tension. The stiffness of the soft region does not depend on which one of the springs is given initial tension if the stiffness coefficient of both springs is constant. However, springs with non-linear stiffness affect the flexible joint's overall stiffness in the soft region. The force/deflection model is given as follows:

$$\Delta x = \begin{cases} 0 & , F_1 + F_2 > |F| \\ (F - \text{sgn}(F)(F_1 + F_2))/(k_1 + k_2) & , |F| \geq F_1 + F_2 \end{cases} \tag{3.5}$$

The second mode, parallel mode 2, is a well-known antagonistic connection setup shown in 3.4b. Here, adjusting the initial tensions on springs does not generate a rigid region. However, this setup proves useful when springs with non-linear stiffness are combined because it makes it possible to adjust the output stiffness at the handle. This output stiffness can be set or manipulated actively via initial tension force/length on the springs.

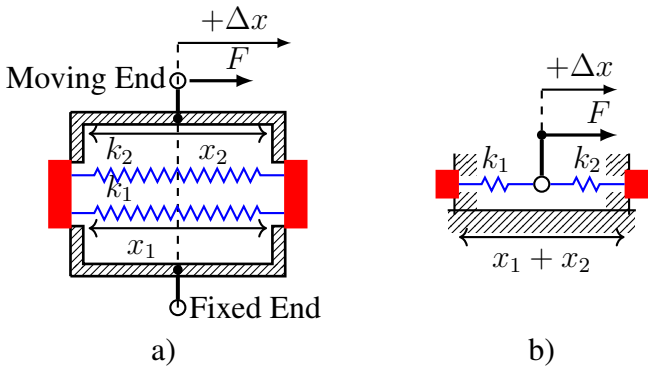



Figure 3.4. Parallel connection of the linear springs.

The downside of this setup is that its operation range is limited to the total initial tension length of the springs. As a side note, it is possible to realize this setup using parallel mode 1 by replacing one of the springs with a compression spring. This mode's force/deflection model for non-linear stiffness springs is formulated as follows:

$$F = a(x_1 + \Delta x)^{n+1} - b(x_2 - \Delta x)^{s+1}, \quad , k_1 = ax^n \quad k_2 = bx^s \tag{3.6}$$

where $x$ is the deflection length of the spring.

### 3.2.2. Torsion Flexible Joint

Figure 3.5 shows a spiral torsion spring and its housing. It can be seen that there are two assembly modes, CW and CCW. In CW assembly mode, the spring can only deflect in the CW direction when torsion is applied to the Inner End of the spring. Similar rule applies to the spring in CCW mode. The flexible joint design is mainly explained by using CW mode without the loss of generality.

As can be observed from Figure 3.2, a linear spring's proximal end moves in the negative direction under a negative force, and the distal end moves in the positive direction under a positive force. Bidirectional usage of the CW spring relies on the same logic of linear spring solution. The objective is to construct a mechanism that directs the CW and CCW loads to the inner and outer ends, respectively. This mechanism's simplified CAD model is shown in Figure 3.6a and b. It consists of two Input/Output Parts, an Inner End

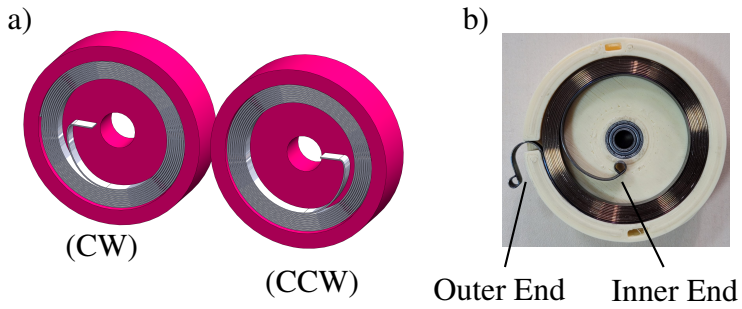



Figure 3.5. CW and CCW assembly modes of the spiral springs.

Clutch, an Outer End Clutch (also serves as a Housing for the spring), and a clock spring used in CW mode shown in Figure 3.6a. The bodies are aligned along a rotation axis. If the flexible joint unit has no net torque acting on it, all bodies are free to rotate.

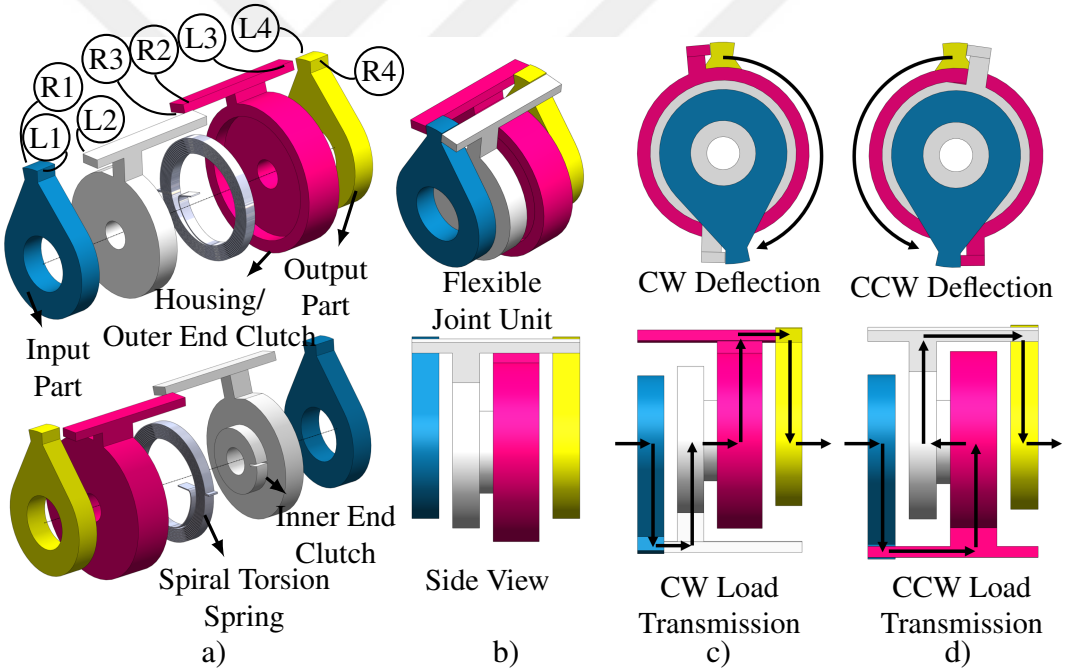



Figure 3.6. Flexible torsion joint of clock spring in CW mode, a) Exploded view, b) Assembled joint unit and side view, c) Load transmission on part for the CW loading, d) Load transmission on part for the CW loading.

Input and Output Parts are responsible for receiving and transmitting the torque. As indicated earlier, the concept of being input or output is interchangeable. Therefore, an actuator can be coupled either with the Input or Output Part, while the other end might be connected to a link of a robot mechanism. The important thing is the assembly of the

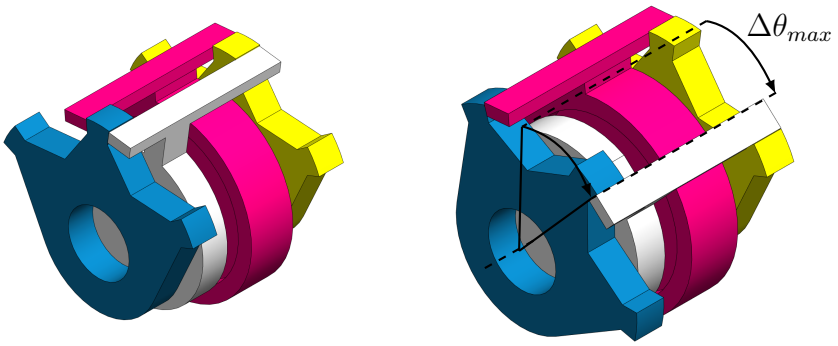
flexible unit and the correct adjustment of contact surfaces. These surfaces are shown in Figure 3.6a. When there is no net torque on the unit, L1-L2, L3-L4, R1-R2, and R3-R4 surface pairs should be in contact to prevent joint clearance. The assembled system is shown in Figure 3.6b. It should be noted that L2 and R3 are on the same surface of the same body (Inner End Clutch), and R2 and L3 are on the same surface of the same body (Outer End Clutch).

In Figure 3.6c and d, to visualize compliant deflections of the flexible torsion joint in CW and CCW directions, an input load is applied to the Input Part when the Output Part is fixed. In CW deflection (Left Rotation), the Input Part establishes contact with the Inner End Clutch part on L1-L2 surfaces. The Inner End Clutch part transmits the load to the Inner End of the spring. The load passes through the spring and reaches the Outer End of the spring. Then, the load reaches the Output Part through the Outer End Clutch and Output Part's contact surface, namely L3-L4 surfaces. In CCW deflection (Right Rotation), the Input Part couples with the Outer End Clutch over R1-R2 contact surfaces. It transmits the load to the Outer End of the spring. The load reaches its Inner End after passing through the spring. Then, through the Inner End Clutch, this load is transmitted to the Output Part thanks to the contact of R3-R4 surfaces.

If desired, it is possible to limit the angular deflection range of flexible joint unit by adding a mechanical limit as shown in Figure 3.7. This setup forms two rigid regions, first one is achieved with the initial tensions on the spring while the second one is the result of mechanical limits. In between, there is a flexible region. The torque/angular deflection model of this unit is given as follows:

$$\Delta\theta = \begin{cases} 0 & , \tau_{min} > |\tau| \\ (\tau - \mathrm{sgn}(\tau)\tau_{min})/k_\theta & , \tau_{max} > |\tau| \geq \tau_{min} \\ \mathrm{sgn}(\tau)(\tau_{max} - \tau_{min})/k_\theta & , |\tau| \geq \tau_{max} \end{cases} \tag{3.7}$$

where $\Delta\theta$ is the angular deflection. $\tau$ is the input torque. $k_\theta$ denotes the stiffness of the torsion spring. $\tau_{min} = \theta_{min} k_\theta$ is the initial tension torque on the spring where $\theta_{min}$ stands for the initial tension angle. $\tau_{min}$ is also the minimum required torque to overcome 1$^{st}$ rigid region. $\tau_{max}$ is the maximum torque that can be displayed by the flexible region. $\Delta\theta_{max} = (\tau_{max} - \tau_{min})/k_\theta$ is the range of the flexible region, thus, the flexible joint unit.




a) 1st Rigid Mode b) 2nd Rigid Mode

Figure 3.7. Spring unit with mechanical limits. a) 1st Rigid region achieved with initial tensions. b) 2nd Rigid region achieved with mechanical limits.

### 3.2.3. Series Torsion Flexible Joint

Series assembly of the flexible joint units is shown in Figure 3.8a. Coupling the Input Part and Output Part of two flexible joint units using a Connection Part is sufficient to establish a series of flexible joint setups. Due to the interchangeability property of the design, input/input or output/output couplings are also possible. Now, let's assume flexible joint 1 has an initial tension. When a load is applied from the Input Part of

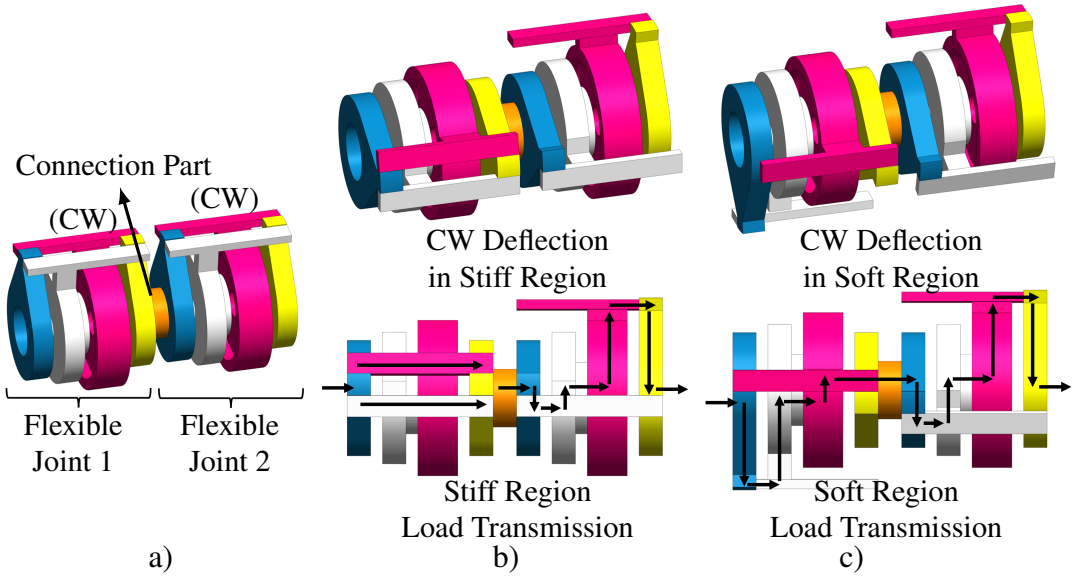



Figure 3.8. Series connection of flexible joint units.

the flexible joint 1, the flexible joint 2 unit becomes the first unit that shows compliant displacement as shown in Figure 3.8b. The compliant deflection on flexible joint 1 is observed when the load at the Input Part becomes greater than the initial tension acting on this joint. This case is shown in Figure 3.8c. If different initial tensions are defined on both flexible joint units, then it is possible to obtain rigid-stiff-soft stiffness behavior using the series of flexible joints.

When two joint units with mechanical limits (Unit 1 and Unit 2) are used for series assembly, it is possible to obtain five different stiffness regions. Depending on the initial tension levels of joint units, these regions might come in the form of Rigid-Stiff$_1$-

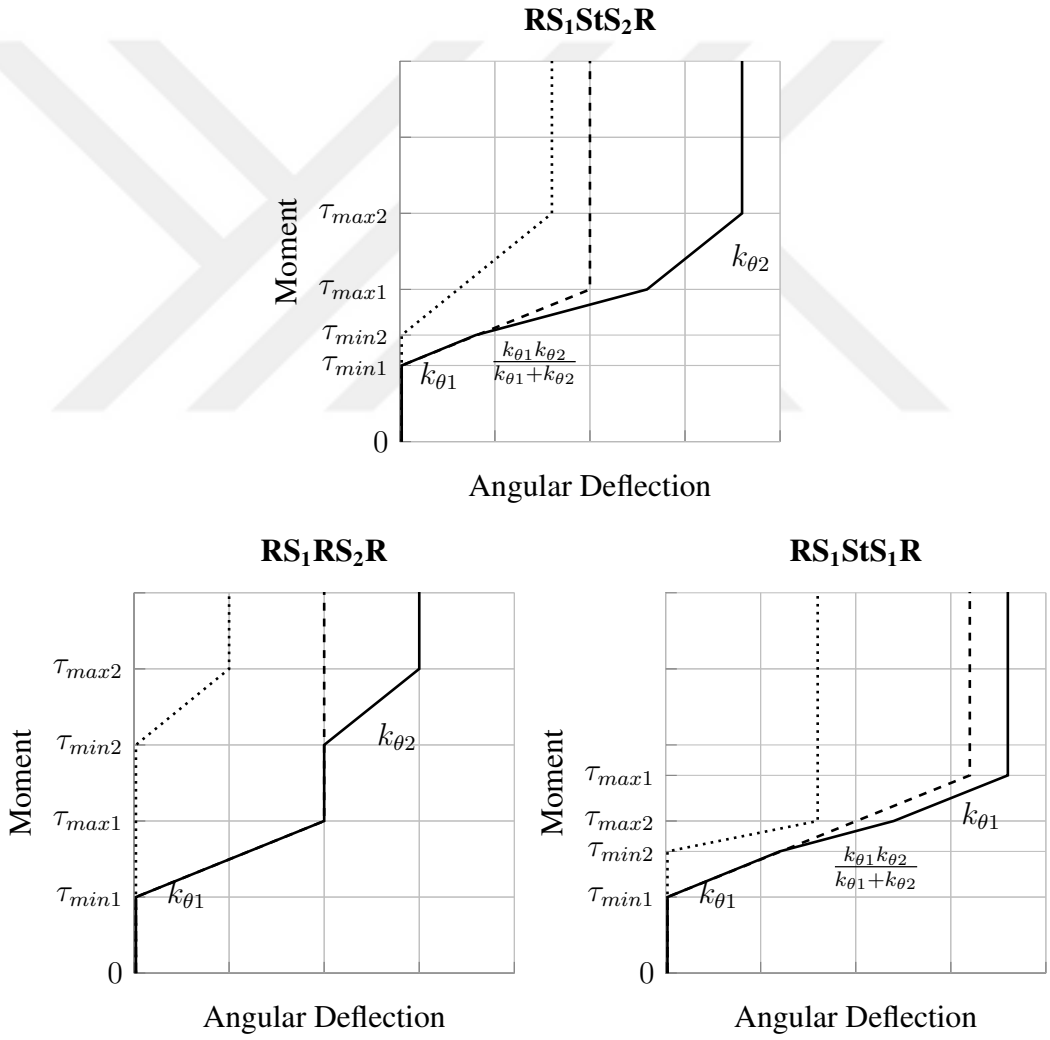



Figure 3.9. Torque/Angular deflection relation of series connected joint units with mechanical limits. (Dashed: Joint unit with stiffness $k_{\theta 1}$, Dotted: Joint unit with stiffness $k_{\theta 2}$, Solid: Series connected joint)

Rigid-Stiff$_2$-Rigid (RS$_1$RS$_2$R), Rigid-Stiff$_1$-Soft-Stiff$_2$-Rigid (RS$_1$StS$_2$R), or Rigid-Stiff$_1$-Soft-Stiff$_1$-Rigid (RS$_1$StS$_1$R). Here, subscripts 1 and 2 indicate the deflecting joint unit in stiff mode. Both springs exhibit deflection in soft mode, while rigid mode addresses no deflection change. Required conditions for each mode are listed as follows:

- RS$_1$RS$_2$R: $\tau_{min1} < \tau_{max1} < \tau_{min2} < \tau_{max2}$
- RS$_1$StS$_2$R: $\tau_{min1} < \tau_{min2} < \tau_{max1} < \tau_{max2}$
- RS$_1$StS$_1$R: $\tau_{min1} < \tau_{min2} < \tau_{max2} < \tau_{max1}$

where $\tau_{min}$ is the initial tension torque levels of their respective joint unit while $\tau_{max}$ is the maximum torque that can be displayed by the joint unit. Deflection of each unit are denoted as $\Delta\theta_1$ and $\Delta\theta_2$ which are computed from Equation 3.7 and torque/angular deflection plots of three modes are shown in Figure 3.9.

### 3.2.4. Parallel Torsion Flexible Joint

Parallel connection setup for the springs is given in Figure 3.10a1. The parallel connection is established by coupling the Outer End to Outer End and Inner End to Inner End of two torsion springs. Parallel mode 1 can be realized using two CW torsion springs. Required initial tensions can be set by generating the illustrated deflection shown in Figure 3.10a2 so that a1 can be realized. According to Figure 3.10, the transition from a2 to a1 causes a collision among the parts because the illustration is kept simple to avoid over-crowding the drawing. This, however, can be solved by constructing the bodies through sub-assemblies, as shown in Figure 3.13 a), where contact surfaces are assembled on the clutch parts via screws. Parallel mode 2 (antagonistic mode) uses both CW and CCW springs. As shown in Figure 3.10a3, an initial tension must be defined for this flexible joint setup. Since the initial tension of CW and CCW are defined in opposite directions, Inner End Clutches should be designed as two separate parts for a two-part parallel mode. After the initial tension, they are attached together. The total initial tension length of both springs determines the total operation range of the flexible joint in parallel mode 2.

The load transmission through the parts of both parallel modes is shown in Figure 3.10b and c for CCW and CW deflections, respectively. First, the CCW load from the Input Part is transferred to the Outer End Clutch. After passing through the springs, the load reaches the Inner End Clutch and Output Part. For CW deflection, the Inner End Clutch receive the input load from the Input Part. Then, the load follows the spring,

Outer End Clutch, and Output Part pathway. A family of alternative connection setups of flexible joints are shown in Figure 3.11.

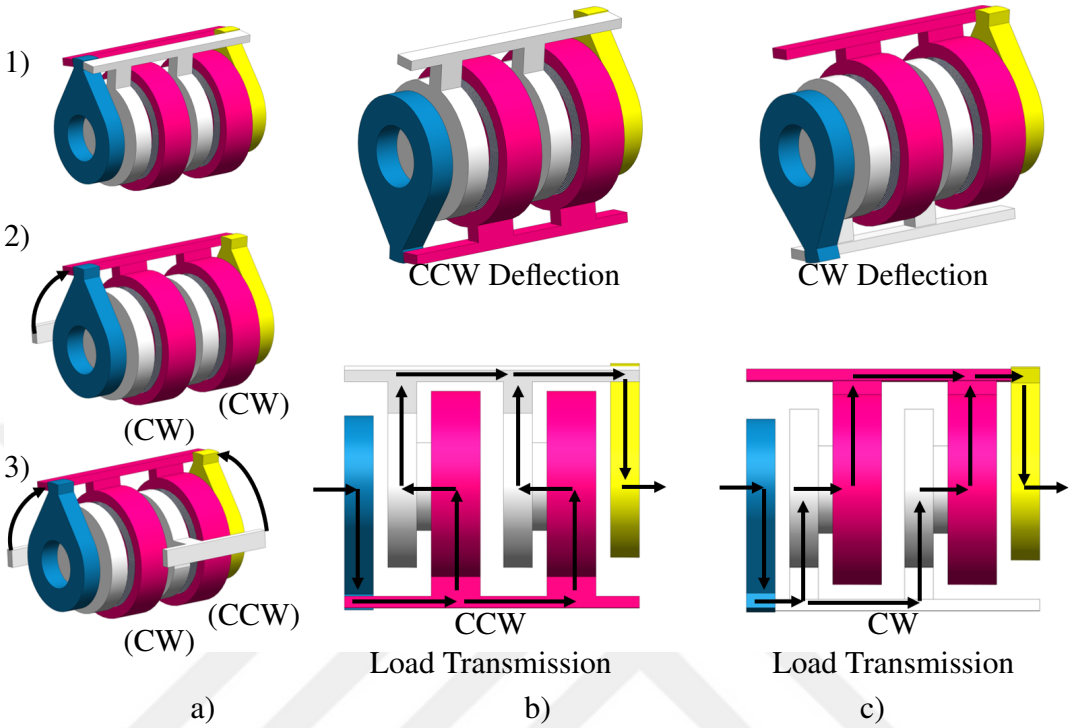



Figure 3.10. Parallel flexible joint setup. 1) Parallel Assembly, 2) Parallel Mode 1, 3) Parallel Mode 2

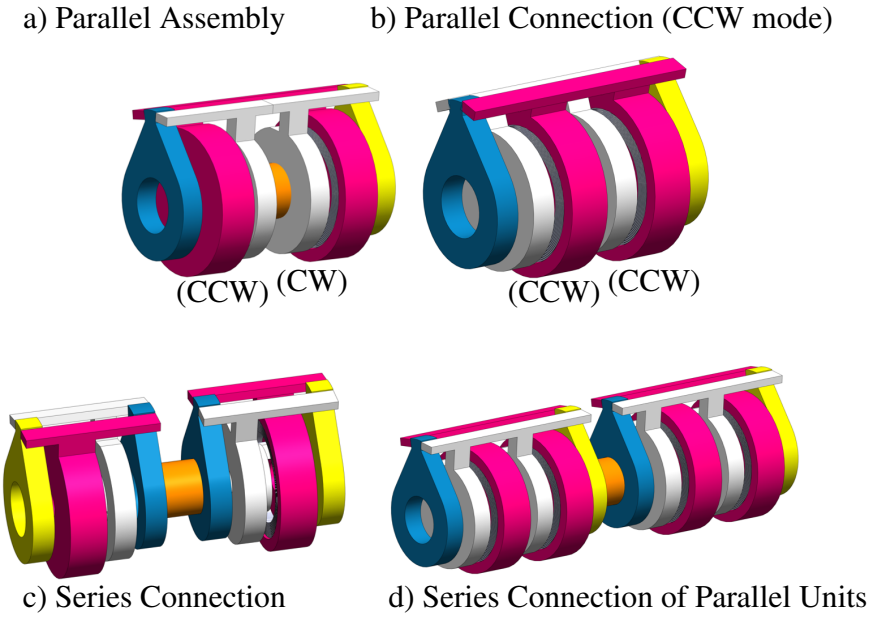
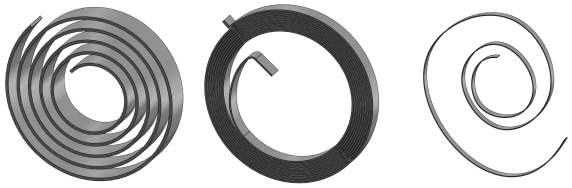



Figure 3.11. Connection setups of springs.

### 3.2.5. Stiffness of a Spiral Torsion Spring

There are various spiral spring types such as motor-power-clock springs, constant force springs, hairspring, brush springs, constant torque springs, and pre-stressed power springs (Carlson, 1978). The names may vary depending on its usage or manufacturer.



a) b) c)

Figure 3.12. Spiral springs. a) Regular spiral spring, b) Clock spring inside a retainer, c) Clock spring removed from retainer.

In this study, the clock spring was chosen. A comparative illustration of regular and clock spiral springs is shown in Figure 3.12. Regular spiral springs are designed and produced at their free lengths as given in Figure 3.12a. Therefore, their stiffness can be computed with high accuracy. However, clock springs have different shapes and forms when they are in their retainer and removed from their retainer, as shown in Figure 3.12b and c, respectively. As a result, it is not possible to formulate the stiffness of a clock spring with great accuracy (Carlson, 1978). Finite element analysis can be used to determine the relation between the stiffness and dimension of the spring. Nonetheless, this form of clock spring brings forth two possibilities for regulating their stiffness 1) reducing the length of the spring and 2) changing the housing diameter of its container. First, consider the stiffness formula for a regular spiral spring given below:

$$k = \frac{Ebt^3}{12l} \tag{3.8}$$

where $k$ is the stiffness, $E$ elastic modulus, $b$ is the material width, $t$ is the thickness, and $l$ is the total length of the spring. This formula can be used as a basis for the stiffness of the clock spring. It is clear that reducing the length of the spring increases the output stiffness. The housing diameter of the container is inversely proportional to the stiffness. Reducing the diameter means compressing the spring in a tighter place, thus

increasing the stiffness. Apart from finite element analysis and custom manufacturing of the spring, desired stiffness can be adjusted through experiments on several off-the-shelf clock springs from various companies.

### 3.2.6. System Model

The torsion flexible joint unit can be assumed to have a second-order mechanical system behavior. The stiffness remains the same for CW and CCW rotations. The effective inertia, however, differs due to the design of inner/outer end parts. Therefore, the model of the system is represented by a piece-wise function. Let's assume that the flexible joint is a rigid coupling between the actuator and the link up to a certain acting torque on the joint. For such a flexible joint, actuator torque can be defined based on the following equations for different conditions:

$$\begin{cases} \tau = (I_{Link} + I_{Output} + I_{Housing} + I_{Clutch} + I_{Input} + I_{Actuator})\ddot{q}_i & , \Delta q = 0 \end{cases} \tag{3.9}$$

$$\begin{cases} 0 = (I_{Link} + I_{Output} + I_{Clutch})\ddot{q}_o + b\Delta\dot{q} + k\Delta q + \tau_1 \\ \tau = (I_{Input} + I_{Actuator} + I_{Housing})\ddot{q}_i - b\Delta\dot{q} - k\Delta q - \tau_1 \end{cases} , \Delta q > 0 \tag{3.10}$$

$$\begin{cases} 0 = (I_{Link} + I_{Output} + I_{Housing})\ddot{q}_o + b\Delta\dot{q} + k\Delta q - \tau_1 \\ \tau = (I_{Input} + I_{Actuator} + I_{Clutch})\ddot{q}_i - b\Delta\dot{q} - k\Delta q + \tau_1 \end{cases} , \Delta q < 0 \tag{3.11}$$

$$\Delta q = q_o - q_i \tag{3.12}$$

where $q_o$ and $q_i$ are output and input angle variables, respectively. $\tau$ is the actuator torque and $\tau_1$ is the magnitude of initial tension torque. $I$ terms denote the inertia term of the respective parts. $b$ is the damping coefficient of rotating parts in the flexible joint unit. $k$ indicates the stiffness of the spring.

## 3.3. Mechanical Design and Prototyping

Two different constructional designs of the proposed flexible joint concept are proposed. The first one has the capability to adjust the initial tension on the springs. This

first design is manufactured for initial tests. The second design is relatively more compact but does not allow altering the initial tension.

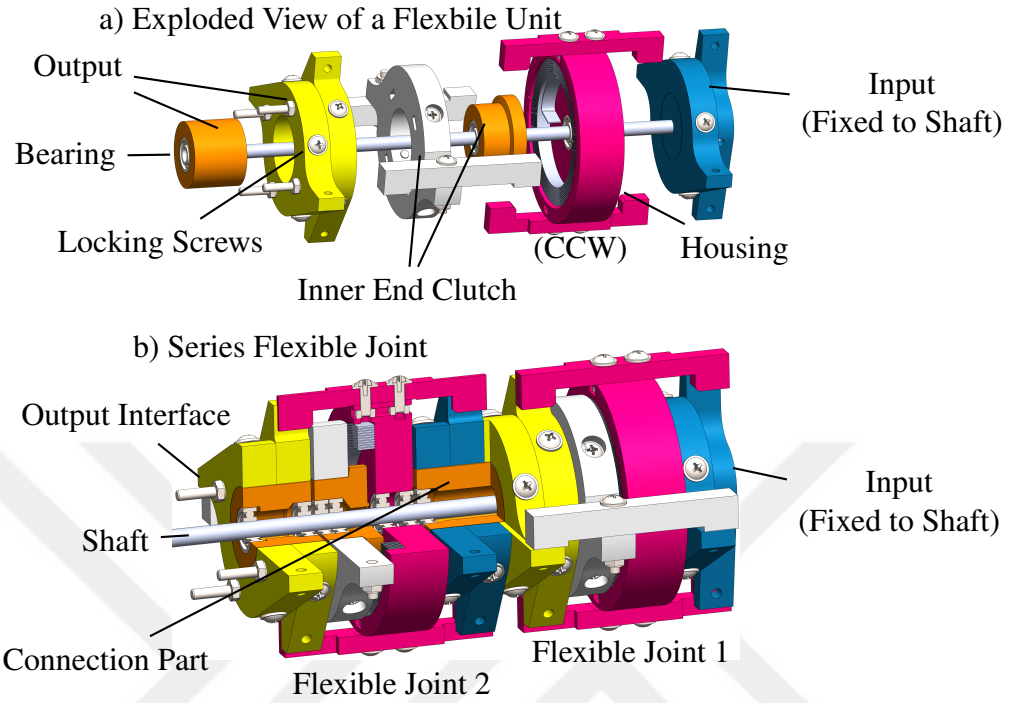



Figure 3.13. PVS joint. a) Exploded view of one of the flexible joint units. b) Series connection of two flexible joint units.

The constructional design of the adjustable flexible joint unit is depicted in Figure 3.13a. The design consists of Input/Output Parts, Springs, Outer/Inner End Clutches, Bearings, a Shaft, and Screws/Nuts. Input and Output Parts are designed to be adjustable to regulate the initial tension on the springs. After the initial tension adjustment, parts are locked on the parts via screws. Similarly, the Inner End Clutch has two separate pieces for correct alignment of the angles, which are later mounted on each other.

A secondary flexible unit's input is coupled with the Output Part of the first flexible unit via a Connection Part, as shown in Figure 3.13b. The Shaft part is mainly used to make the parts rotate about the same axis. Bearings are located between the parts and shaft to enable the free rotation of the parts with respect to the shaft having low frictional resistance. Only the Input Part is fixed to the Shaft. In this design, the actuator can be directly coupled to the Input Part without the Shaft coupling to the actuator or the Input Part. Coupling the Input Part to the Shaft provides another actuator-flexible joint-link assembly option, as shown in Figure 3.14.

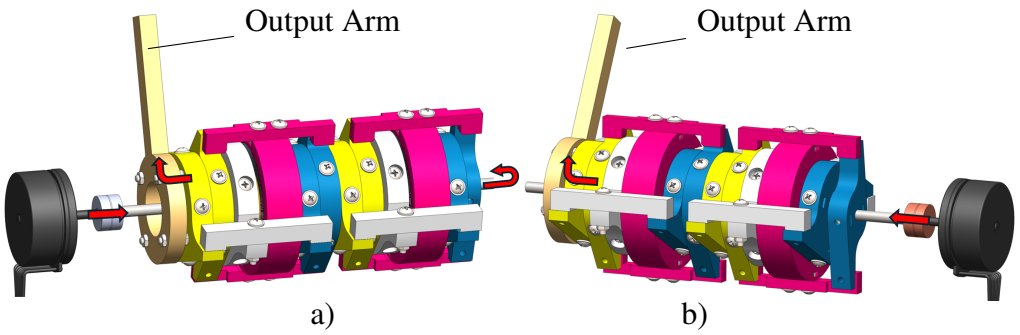



Figure 3.14. Actuation options. a) Sandwich option where the output is in between the actuator and flexible joint, b) Standard option.

Input/Output Parts and Inner/Outer End Clutches are designed to be symmetric to increase the contact surface by 2 folds. This ensures the equal distribution of the load on the contact surfaces. Covering these surfaces with a thin rubber membrane for a smoother transition between the rigid-stiff-soft regions is possible.

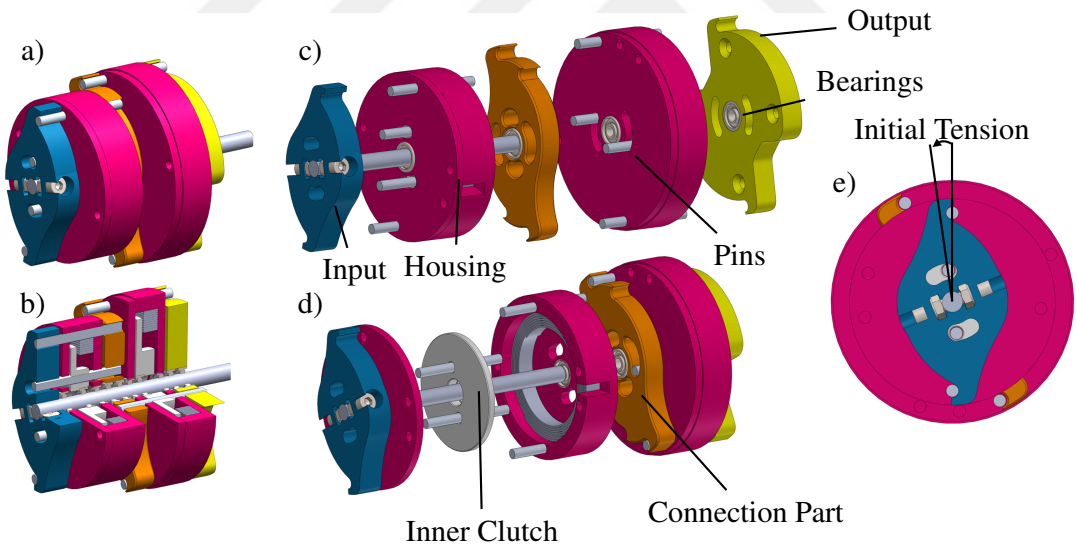



Figure 3.15. Compact series spring design. a) Assembled view, b) Section cut view, c) and d) Exploded views, e) Front view.

The compact version of the series flexible joint is shown in Figure 3.15. The Inner End Clutch is hidden inside of the Outer End Clutch. The load transmission occurs through the pins. Each flexible unit uses four pins, two for the Inner End Clutch and two for the Outer End Clutch. The initial tension of the springs is determined at the design stage by the angle difference of the Inner and Outer Pins as shown in Figure 3.15e.

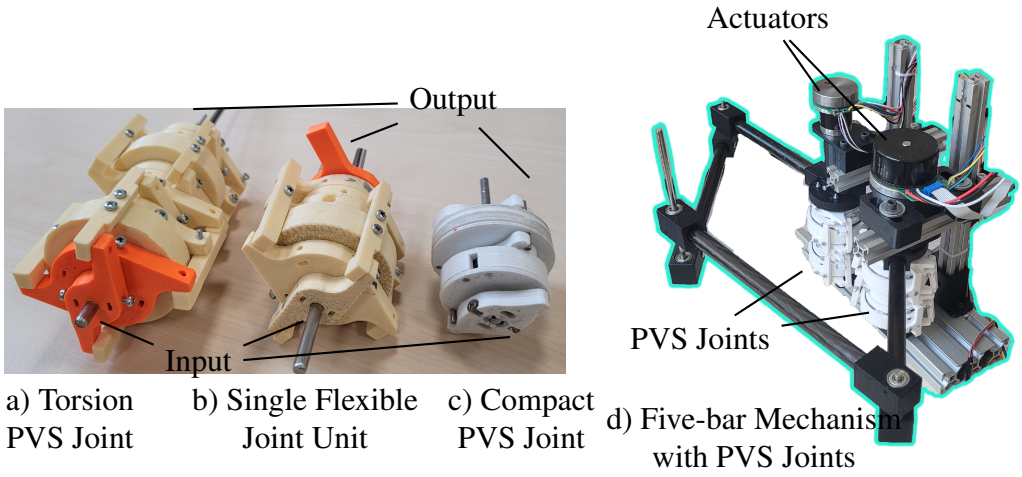



Figure 3.16. Prototypes of proposed PVS joint.

The parts beside the springs, the shaft and the fasteners are manufactured by using a 3D printer. Note that the stiffness of 3D printed parts is much greater than the stiffness of the springs. The prototypes are shown in Figure 3.16. All of the prototypes use a spring with 5 mm thickness. Nonetheless, each spring has a different stiffness due to the material, length, and diameter of its housing. The prototypes have total lengths of 120 mm and 60 mm, as shown in Figure 3.16a and c, respectively. Finally, an example of SEA assembled to a five-bar mechanism is shown in Figure 3.16d.

## 3.4. Experimental Validation and Procedures

There are two test setups; one aims for stiffness identification, and the other is designed for system identification.

### 3.4.1. Stiffness identification test setup and procedure

The stiffness identification test setup is shown in Figure 3.17. A DC motor with a reduction and an embedded encoder is coupled to the input of the torsion PVS joint. A moment arm part is attached to the output. The moment arm converts the moment generated by the DC motor to force so that this force can be measured by the load cell.

The stiffness identification experiment aims to prove the concept of a unidirec-

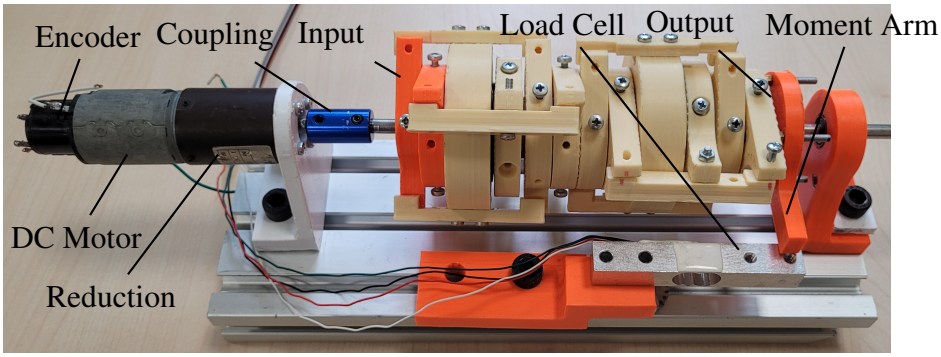



Figure 3.17. Experimental setup for stiffness identification.

tional softening flexible joint unit and verify the rigid-stiff-soft stiffness region transition. During the experiment; first, the actuator is driven at low speed in the CW direction and then in the CCW direction after relocating the load cell. Simultaneously, the encoder and the load cell data are recorded. Since the length of the moment arm and the reduction ratio of the actuator are known, a relation is established for the moment and angular deflection on the torsion PVS joint.

### 3.4.2. System identification test setup and procedure

Figure 3.18 shows the test setup for the system identification. The PVS joint in this setup has different stiffness characteristics compared to the previous PVS joint used in the stiffness identification tests. This time, a Maxon EC motor is used because the actuator dynamics of this motor are well-known and allow accurate torque delivery. A gear-head and built-in encoder are coupled to the EC motor.

The system identification experiment is designed to determine the system characteristics when the torsion PVS joint is used as a SEA. The output of the flexible joint is locked to the base so that SEA could show compliant deflection. The encoder is used to record the position data of the motor shaft. Torque and position data are the input and output of the system. Hence, these two data sets are used for estimating the system parameters of the PVS joint, gearbox, and motor.

In this test, the excitation to the PVS joint can be achieved by sinusoidal torque inputs by sweeping the frequencies or by sending random inputs. In both cases, input (actuator torque) and output (compliant deflection) are recorded for evaluation. The random

input method requires a Fast Fourier Transform (FFT) analysis. Independent of the input signal type, the results contain the response of every component in the test setup, and it might be challenging to isolate the behavior of the PVS joint. However, by sweeping the frequencies, it is possible to filter out the response of unwanted components on the test setup.

The system model of the flexible joint differs depending on the deflection direction and rigid-stiff-soft stiffness regions. Hence, a system identification test should be conducted on each of the stiffness regions for each direction. The main focus of this experiment is determining dynamic behavior in the complaint modes. Therefore, a rigid region investigation was not conducted. In order to generate oscillation in stiff and soft regions, a suitable constant torque ($\tau_c$) can be applied to the flexible joint so that the torsion PVS joint enters and remains in the desired region. After that, the sinusoidal signal can be fed to the system on top of the constant torque signal as shown in Equation 3.13 where $f_{in}$ and $t$ are input frequency and time, respectively. The range of the sinusoidal signal should be small enough to avoid changing the stiffness region, which is adjusted by the gain $B$. In this experiment, the torque levels of the torsion PVS joint were slightly modified for each test case so that more compliant displacement would improve the measurement quality. First, the rigid region torque level was reduced, and the stiff region's operational torque range was increased for stiff region experiments. For the soft region tests, the torque level to enter the soft region was reduced to relieve the load on the actuator.

$$\tau(t) = B \sin(2\pi f_{in} t) + \tau_c \tag{3.13}$$

The evaluation of the input/output relation was carried out by calculating the change in the mechanical impedance. First, recorded position data was fit to a generic sinusoidal function ($p$) in Equation 3.14 to acquire output amplitude ($A$) and the frequency ($f_{out}$). Then, the derivative of the function with respect to time ($v$) was used for calculating the compliant deflection rates as given in Equation 3.15. The magnitude of impedance at the inspected frequency is computed by the ratio of output to input as shown in Equation 3.16.

$$p(t) = A \sin(2\pi f_{out} t) \tag{3.14}$$

$$v(t) = 2A\pi f_{out} \cos\left(2\pi f_{out} t\right) \tag{3.15}$$

$$M(f_{out}) = 20 \log_{10} \frac{2A\pi f_{out}}{B} \tag{3.16}$$

The scanned frequency ranges from 0.1 Hz to 1 Hz with a 0.1 Hz increment and from 1 Hz to 10 Hz with an increment of 1 Hz.

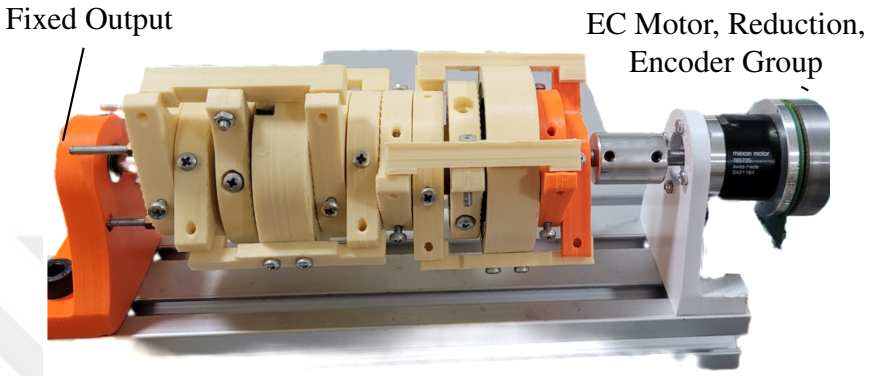



Figure 3.18. Experimental setup for system identification.

## 3.5. Results and Discussion

The results obtained from both tests are given and discussed in this section.

### 3.5.1. Stiffness Identification Test Results

The results of five repeated experiments for the stiffness identification test are given in Figure 3.19. In this figure, the red parts indicate the experimental data and the black lines indicate the fitted lines to these data. The rigid region is defined on the first flexible joint unit by assigning an initial tension of $\sim 95\ N \cdot mm$. Hence, no deflection was observed up to $\sim \pm 95\ N \cdot mm$ torque level. As the magnitude of deflection increases, the PVS joint enters the first flexible region, which is the stiff region. The stiffness of this region was computed as $\sim 3.45\ N \cdot mm/^{\circ}$, which complies with the stiffness of the first flexible joint unit. The second flexible joint unit accommodating a spring with $\sim 1.25$ $N \cdot mm/^{\circ}$ stiffness was loaded with $\sim 170\ N \cdot mm$ initial tension. Thus, the PVS joint enters the soft region when the torque level surpasses $\sim 170\ N \cdot mm$ or, in other words,

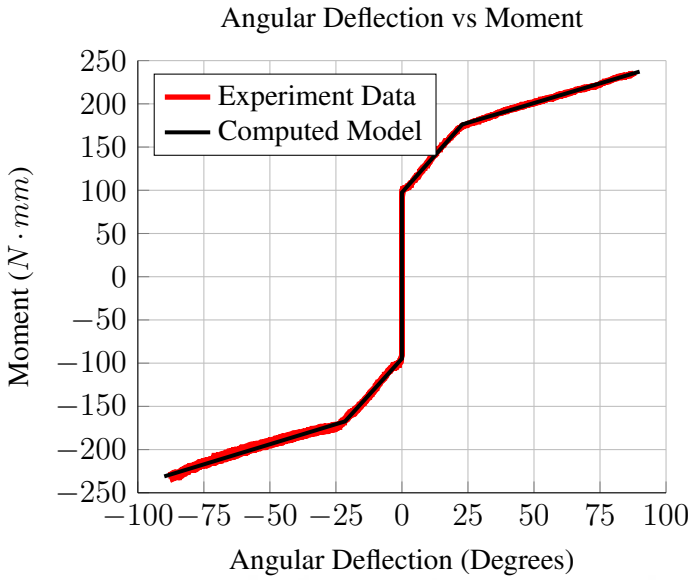



Figure 3.19. Stiffness identification experiment results.

compliant deflection exceeds $\sim 22°$. The computed stiffness of the soft region is $\sim 0.92$ $N \cdot mm/°$. The relation of compliant deflection and torque was computed as follows:

$$\Delta\theta = \begin{cases} (\tau + 167.4)/0.93 - 21.6 & , -250.0 < \tau \leq -167.4 \\ (\tau + 94.74)/3.37 & , -167.4 < \tau \leq -94.7 \\ 0 & , -94.7 < \tau \leq 97.5 \\ (\tau - 97.5)/3.44 & , 97.5 < \tau \leq 176.2 \\ (\tau - 176.2)/0.91 + 22.9 & , 176.2 < \tau \leq 250.0 \end{cases} \tag{3.17}$$

where $\Delta\theta$ (°) is compliant deflection and $\tau$ ($N \cdot mm$) is the torque load on PVS joint.

The proposed joint mechanism does not have a switch to change the stiffness but relies on initial tensions on flexible joint units. The results in Figure 3.19 clearly show the continuous change in compliant deflection under a continuous torque load. The continuity on both positive and negative loading directions proves the unidirectional motion capacity of the PVS joint.

### 3.5.2. System Identification Test Results

Dynamic test results for system identification are presented in Figure 3.20 along with their 2nd order system models printed in solid black lines. As an initial observation,

results show no significant difference in impedance characteristics depending on rotation directions. This mainly indicates that the change in inertia depending on the direction of the deflection is negligible since the components rotating in each direction are designed to have compatible physical properties (i.e. inertia).

The transfer functions of stiff and soft states of the PVS joint are determined as follows:

$$TF = \frac{s}{ms^2 + bs + k} \tag{3.18}$$

$$\begin{bmatrix} m_{\text{stiff}} & b_{\text{stiff}} & k_{\text{stiff}} \end{bmatrix} = \begin{bmatrix} 0.0944 & 0.1980 & 0.6190 \end{bmatrix} \times 10^{-3} \tag{3.19}$$

$$\begin{bmatrix} m_{\text{soft}} & b_{\text{soft}} & k_{\text{soft}} \end{bmatrix} = \begin{bmatrix} 0.1019 & 0.1335 & 0.3616 \end{bmatrix} \times 10^{-3} \tag{3.20}$$

where $m$, $b$, and $k$ are the mass moment of inertia, damping, and stiffness coefficients with the units of $kg \cdot m^2$, $kg \cdot m^2/s$, and $kg \cdot m^2/s^2$, respectively. Here, a smaller value of $k_{\text{soft}}$ was observed compared to $k_{\text{stiff}}$, which is expected and furthermore desired. Accordingly, $m_{\text{soft}}$ is greater than $m_{\text{stiff}}$ because the number of rotating bodies is greater in the soft state of the PVS joint. The soft state's damping coefficient, $b_{\text{soft}}$, is relatively small compared to the stiff state's damping coefficient, which is expected due to the serial connection of the dampers.

## 3.6. Conclusion

The newly developed flexible joint design presents a novel advancement in variable stiffness joints. This design offers enhanced versatility and functionality by enabling a unidirectional spring for bidirectional deflections. The ability to connect springs in both parallel and serial configurations further extends its applicability across various mechanical systems that require flexibility.

One of the most notable features of this design is its multiple stiffness regions, which are determined by the applied load levels. This eliminates the need for a clutch mechanism, simplifying the overall design and reducing potential points of failure. From a safety perspective, the series flexible joint design with two flexible joint units exhibits a softening stiffness characteristic, which can be crucial in human-robot interactions.

Additionally, the incorporation of mechanical limits within the flexible joint units

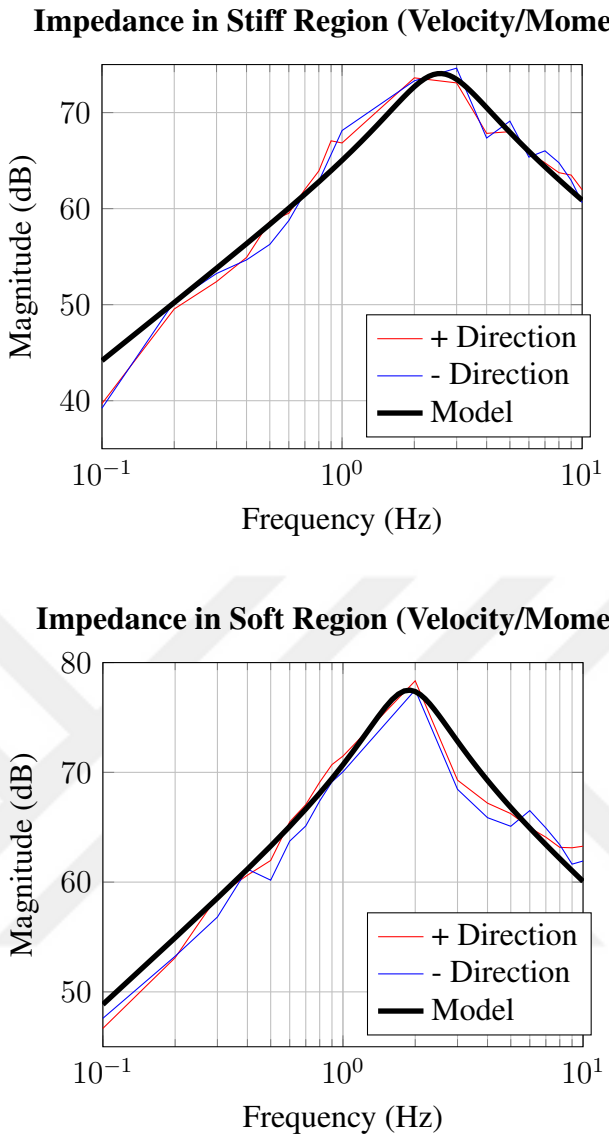



Figure 3.20. Bode plots of system identification results.

allows for the customization of stiffness characteristics, providing either more hardening or softening regions as needed. This adaptability ensures that the joint can be tailored to meet specific requirements, enhancing its utility in a wide range of applications.

The practical implementation of this design has been achieved through 3D printing and off-the-shelf materials. The results from these tests have validated the theoretical advantages, demonstrating the joint's effectiveness. The transition among the rigid, stiff, and soft regions has been proved through the quasi-static experiments. The system identification experiment presents the system characteristics of stiff and soft modes of flexible joints. The case study not only underscores the feasibility of the design, but also highlights its potential for real-world applications.

# CHAPTER 4

# CONTROL OF A RIGID LINK FLEXIBLE JOINT ROBOT FOR SAFE HUMAN ROBOT INTERACTION

Flexible robots are deemed to be safer in the existence of physical human-robot interactions (pHRI). A regular robot manipulator can be made flexible by adding flexible components. Moreover, the stiffness of these flexible components can be determined in a way that the robot ends up with the desired mechanical impedance. However, flexible components might degrade the positioning performance of the robot. Modifying the flexible joints may introduce flexibility for only higher interaction forces. That way, the robot can preserve its positioning performance at small interaction forces while ensuring safety in excessive interaction forces. The control of such a robotic system requires several controllers, each excelling in its own task. Also, a set of stable switch laws is needed for the activation and deactivation of these controllers. This study shows the implementation of desired controllers and switches for a rigid link flexible joint robot manipulator that has rigid and flexible states depending on the interaction force levels. Three main tasks are defined. Trajectory tracking is at the rigid state of the manipulator and displays the desired impedance, and hybrid force/position tracking is at the flexible state of the manipulator. Three controllers also require three velocity observers for links and actuators. The switch law uses sigmoid functions for a smooth transition between the controllers.

## 4.1. Introduction

In human-robot interaction (HRI), safety is a must-have property and has standards stated by the International Organization of Standardization (ISO) in ISO/TS 15066 2016 (de Normalización, 2016). This can be achieved with methods such as control, motion planning, or predicting human intentions and taking necessary precautions (Lasota et al., 2017). Another approach is implementing mechanical level safety that makes the robot manipulator inherently compliant to interactions, namely constructing a soft/flexible robot (Lee et al., 2017; Yang et al., 2018; Blanc et al., 2017). However, soft robots can

have countless degrees of freedom (DoF) if their components are made of soft materials (i.e., rubber), introducing plenty of challenges in modeling and controlling (Das and Nabi, 2019), as well as sensing their states (Sincak et al., 2024). A review study by Bhagat et al. (2019) highlights the necessity of artificial neural networks for modeling and controlling to address this problem, while another review study by Della Santina et al. (2023) shows that recent trends are relying on model-based control.

The difficulty of modeling and, therefore, controlling can be reduced to a more manageable level by introducing flexible components to the rigid structures of robot manipulators by having a hybrid solution. The hybrid solutions are rigid link flexible joint (RLFJ) and flexible link rigid joint (FLRJ) robot manipulators (Kiang et al., 2015; Li et al., 2024). Using flexible links in a robot manipulator increases its DoF by removing the kinematic constraints. As a result, uncontrollable motion axes appear. Although there are many studies on FLRJ robots' modeling and control, they mainly assume small deflections and focus on vibration suppression (Sayahkarajy et al., 2016; Alandoli and Lee, 2020; Lee and Alandoli, 2020). In HRI, however, robot manipulators are expected to show large deflections to be safe, and the aim is to achieve HRI in the existence of flexion, not to suppress it. RLFJ robot manipulators, on the other hand, show flexibility only in the robot's motion space. This property makes them a feasible option since HRI is intended to exist in the robot's motion space. The flexible element in this type of robot is placed in between the actuators and the robot's linkages by forming a so-called series elastic actuator (SEA) (Pratt and Williamson, 1995; Vanderborght et al., 2013).

RLFJ robot manipulators are under-actuated systems and have at least a fourth-order dynamic model, which is relatively simpler compared to soft and FLRJ robots. To deal with the nonlinear system dynamics, Spong proposed a static feedback linearization (Spong, 1987), De Luca et al. (1985) addressed the importance of dynamic feedback linearization, and Khorasani and Spong (1985) used singular perturbation methods. Once the system is linearized, a suitable controller can be selected depending on the desired task. The control of RLFJ robots gained attention around the 1980s, and at that time, the purpose of the control at that time was to reduce vibration by modeling the link's flexibility as a spring at joints and compensate for the error caused by the newly emerging robotic component named harmonic drive. Thus, the desired task was trajectory tracking.

In HRI, however, the main desired task is to control the interaction itself, but it is also expected that the RLFJ robot manipulator should perform another task on its own, such as trajectory tracking. So, the control problem here has two parts: trajectory track-

ing for the robot's self-operation to do work and HRI impedance/admittance adjustment. They can also be called robot-in-charge and human-in-charge modes, respectively (Li et al., 2016).

Regarding the first part, there are several studies that address the problem. If the model is well known, a model-based controller with inverse dynamic or computed torque methods can be developed for trajectory tracking (de Queiroz et al., 1998). PID/LQR-based controllers can also be an option, but they can be impotent in conducting the task properly. Hence, they generally assisted with other methods like input shaping and MPC, or gains of the PID/LQR controller consistently optimized during operation (Zhang et al., 2015; Pedro and Tshabalala, 2015; Annisa et al., 2018; Ahmad and Mohamed, 2009). If the model is not fully known, it might be better to prefer a robust controller like a sliding mode controller (Mamani et al., 2012; Bridges et al., 1994; Song et al., 2022; Xu, 2017), a passivity-based controller (Ott et al., 2008) or adaptive controller for constantly enhancing the performance of the closed-loop system (Dawson et al., 1993; Montoya-Cháirez et al., 2022). As an example, Bridges et al. (1994) developed a Lyapunov-based robust controller for RLFJ robot with redundant actuators. Nasiri et al. (2020) suggested a state-depended Riccati equation-based robust control method under time-varying disturbances. In (Kim et al., 2019), model-free friction observers are proposed for achieving robustness in RLFJ robots with non-negligible frictions.

An RLFJ robot manipulator's nature is similar to a nested structure in which two second-order systems (actuator and manipulator) are connected in series. One of the most suitable controller for dealing with such systems is using the backstepping technique (Khalil, 2002). The drawback of this method is the need to observe higher-order states, dependency on model accuracy, and tuning of controller gains, which, in short, are complex development processes. Yet, it is still an intriguing method that attracts the attention of researchers (Bridges et al., 1995). In this regard, Lim et al. (1995) developed a backstepping-based partial state feedback controller adopting the observer in (Nicosia and Tomei, 1990; Lim et al., 1996), which only requires actuator and link position measurements (Lim et al., 1995). Global output feedback is achieved in (Dixon et al., 1998) with an observer-based backstepping approach. Kim and Lee (2004); Lim et al. (1997) outlined the necessary procedures for developing an adaptive backstepping-based control.

Regarding HRI, both impedance and admittance controllers are developed for applications where interactions between robots and humans/environment occur. Admittance controllers seem to perform better with rigid robots compared to flexible robots (Horibe

et al., 2016), albeit their usage is not limited to rigid robots only (Zhong et al., 2021), but, in this case, admittance-based controllers need to be finely tuned. In addition, an admittance controller requires a force/torque sensor and has to deal with the sensor's noise and delay. On the other hand, an impedance controller can be implemented on a flexible robot even with minimal model knowledge (Spyrakos-Papastavridis and Dai, 2020). In general, however, the stabilization of an RLFJ robot is harder compared to fully rigid robots, and because of this reason, there is a tendency to develop passivity-based controllers.

The most promising studies are presented by Ott et al. in (Ott et al., 2003, 2004, 2008; Albu-Schaffer et al., 2004) clearly outlining the procedure for implementation of impedance control for an RLFJ robot while guaranteeing the passivity. In (Spyrakos-Papastavridis et al., 2019), the way of preserving the passivity in case of the existence of variable impedance is shown. In (Calanca et al., 2017), acceleration-based impedance control was developed within the passivity concept. Although, it provides a greater performance enhancement in closed-loop systems, acquiring clean acceleration information from actual hardware remains a problem.

While the passivity concept ensures stability, it reduces the effective performance of the robot since the stability is guaranteed more conservatively. There are also other ways to avoid the passivity concept and hope for better performance, such as developing adaptive or neural network-assisted impedance/force controllers (Yu et al., 2023; Ding et al., 2021). However, collaborative HRI operations generally occur at low speeds and frequencies; this side effect of passivity should be considered as a manageable loss. Besides, high-speed operations may compromise safety.

When the need for two or more controllers is on the table for any system, there comes the stability question in switching between the controllers. This stability can be ensured with several methods like constructing a common Lyapunov function, smooth/slow transition between the controllers (Lin and Antsaklis, 2009), or dwell time approach (Briat, 2017). The common Lyapunov function method ensures all controllers have a unified stability criterion. A smooth transition gradually blends the control inputs to avoid abrupt changes like chattering. In the dwell time approach, the controlled system can have enough time to settle with the switched controller's dynamics, thus preserving the system's stability. Among these strategies, smooth switching can be implemented effectively in a stable nonlinear system. For instance, using a backstepping control approach, Li et al. (2016) developed an adaptive controller for cases of robot-in-charge and human-in-charge. Although this may address the requirement of two different controllers, the

change here is not in the control but in the desired task. The change in the desired task is adjusted by changing the gain related to the tasks between one and zero with a smooth transition that is a function of the actuator/SEA load. This smooth transition ensures the stability of the switching. They also designed observers to deal with higher-order terms. At its core, they have a desired trajectory for the end-effector (for both trajectory tracking and complying with humans), which results in a required actuator trajectory. The controller is developed to follow this actuator trajectory.

This chapter addresses the control problem of a five-bar parallel RLFJ robot that accompanies flexible joints introduced in the previous chapter. A hybrid control framework has been proposed. A Lyapunov-based trajectory tracking control, an impedance control for HRI, and a force/position control are employed. These controllers are designed to operate in the robot's rigid, stiff, and soft states, and the robot's desired tasks at each stiffness state are shown in Figure 4.1a. In the soft region, a safety precaution is taken to reduce the contact forces in accordance with ISO/TS 15066 2016 (de Normalización, 2016). This standard suggests that forces above the comfort zone can be applied to human operators but cannot remain above it for more than 0.5 seconds, as shown in Figure 4.1b.

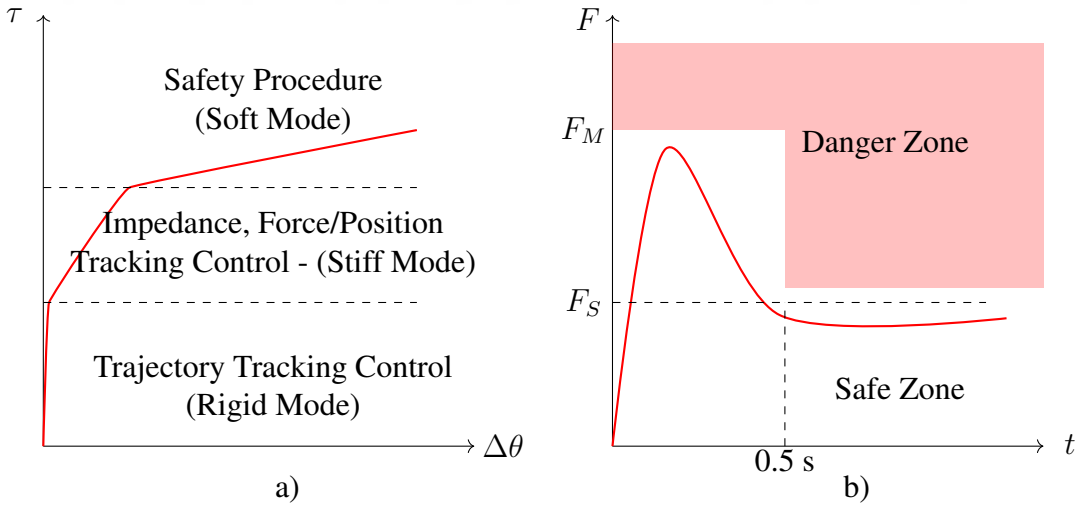



Figure 4.1. a) Desired tasks at each stiffness region, b) ISO/TS 15066 2016 safe contact force profile.

Desired trajectory's maximum speed and acceleration are limited so that the robot does not enter the flexible mode due to the dynamics of the bodies. At flexible region one of the two controllers can be selected for desired task. If HRI is desired, an impedance

controller is activated. Otherwise a force/position task can be assigned. Finally, if the safety procedure is activated, then, the torque on the actuators are reduced to safe levels until safety is ensured. Two velocity observers, one for the actuators and the other one for the robot links, are designed for make the controllers operational. The switch between the controllers achieved smoothly to prevent instability. The state that triggers switches is a function of the torque load on the flexible elements between the actuators and robot's links.

## 4.2. System Model and Preliminaries

This section introduces the dynamic and stiffness models of the robot as well as defines some preliminaries to be used in controller and observer development.

### 4.2.1. Kinematic, Dynamic and Stiffness Models

Kinematics of a robot manipulator is represented as follows:

$$x = f(q), \quad q = f^{-1}(x), \quad \dot{x} = \boldsymbol{J}\dot{q}, \quad \boldsymbol{J} = \frac{\partial f}{\partial q} \tag{4.1}$$

where $q(t) \in \mathbb{R}^n$ is angular position of robot's link, $x(t) \in \mathbb{R}^n$ is the end-effector position in Cartesian space. $f : \mathbb{R}^n \to \mathbb{R}^n$ is the forward kinematics function. $\dot{q}(t) \in \mathbb{R}^n$ is the angular velocity of robot's links, $\dot{x}(t) \in \mathbb{R}^n$ is the end-effector velocity and $\boldsymbol{J}(q) \in \mathbb{R}^{n\times n}$ is the Jacobian matrix.

The RLFJ robot manipulator has two modes: flexible and rigid. The flexible mode's dynamic model is presented as follows (Spong, 1987):

$$\boldsymbol{M}_r(q)\ddot{q} + \boldsymbol{V}_r(q,\dot{q})\dot{q} + \boldsymbol{B}_r\dot{q} + G(q) = \tau_m + \tau_{ext} \tag{4.2}$$

$$\boldsymbol{M}_m\ddot{q}_m + \boldsymbol{B}_m\dot{q}_m + \tau_m = u_m \tag{4.3}$$

$$\tau_{ext} = \boldsymbol{J}^T F_{ext} \tag{4.4}$$

where $q_m(t)$, $\dot{q}_m(t)$, $\ddot{q}_m(t) \in \mathbb{R}^n$ are the actuators' positions, velocities, and accelerations, respectively. $\ddot{q}(t)$ is the angular acceleration of robot's link. $\boldsymbol{M}_r(q) \in \mathbb{R}^{n\times n}$ is robot's inertia matrix, $\boldsymbol{M}_m \in \mathbb{R}^{n\times n}$ is actuators' inertia matrix. $\boldsymbol{B}_r \in \mathbb{R}^{n\times n}$ and $\boldsymbol{B}_m \in \mathbb{R}^{n\times n}$ are friction coefficient matrices for robot and actuators, respectively. $\boldsymbol{V}_r(q,\dot{q}) \in \mathbb{R}^{n\times n}$ is the centripetal-Coriolis matrix. $G(q) \in \mathbb{R}^n$ denotes the gravity vector. $\tau_m(t) \in \mathbb{R}^n$ and $\tau_{ext}(t) \in \mathbb{R}^n$ are the torque on revolute flexible joints and external load resolved in joint space. $u_m(t) \in \mathbb{R}^n$ represents the torque input signal in flexible mode.

The flexible joint's stiffness model describing the behavior of $\tau_m$ is defined for the 2-DoF RLFJ robot manipulator as follows:

$$\tau_m = \begin{bmatrix} \tau_{m1} \\ \tau_{m2} \end{bmatrix} = \boldsymbol{K} z + \nu, \quad z = q_m - q, \quad \boldsymbol{K} = \begin{bmatrix} k_1 & 0 \\ 0 & k_2 \end{bmatrix}, \quad \nu = \begin{bmatrix} \nu_1 \\ \nu_2 \end{bmatrix} \tag{4.5}$$

$$k_i = \begin{cases} k_{\text{stiff}} & , \tau_{\text{stiff}} \leq \tau_{mi} < \tau_{\text{soft}} \\ k_{\text{soft}} & , \tau_{\text{soft}} \leq \tau_{mi} \end{cases}, \quad \nu_i = \begin{cases} \nu_{\text{stiff}} & , \tau_{\text{stiff}} \leq \tau_{mi} < \tau_{\text{soft}} \\ \nu_{\text{soft}} & , \tau_{\text{soft}} \leq \tau_{mi} \end{cases} \tag{4.6}$$

where $z$ denotes the compliant deflection on the flexible joint. $\boldsymbol{K} \in \mathbb{R}^{2\times 2}$ is the diagonal positive definite stiffness coefficient matrix with elements of $k_1$ and $k_2$ which can take values of $k_{\text{stiff}}$ and $k_{\text{soft}}$ depending on the torque load on flexible joint with the magnitude of $\tau_{mi}$ for $i = 1, 2$. Similarly, $\nu$ is the column matrix denoting the pretension torque levels of the springs in the flexible joints. $\nu_1$ and $\nu_2$ are the elements of $\nu$, and they can take values of $\nu_{\text{stiff}}$ and $\nu_{\text{soft}}$ as a function of $\tau_{mi}$ for $i = 1, 2$. Torque magnitudes $\tau_{\text{stiff}}$ and $\tau_{\text{soft}}$ indicates the torque levels at stiffnesses change.

In the rigid model, the angular positions of the robot's link and actuators are the same. By using the angular position $q$ only, the model in the rigid mode of the system is given as follows:

$$\boldsymbol{M}(q)\ddot{q} + \boldsymbol{V}(q,\dot{q})\dot{q} + \boldsymbol{B}\dot{q} + G(q) = u_r \tag{4.7}$$

where $\boldsymbol{M}$, $\boldsymbol{V}$, $\boldsymbol{B} \in \mathbb{R}^{n\times n}$ are the inertia, centripetal-Coriolis, and friction coefficient matrices in the rigid mode, respectively. $u_r(t) \in \mathbb{R}^n$ represents the control input signal in rigid mode.

### 4.2.2. Preliminaries

The desired tasks are stated as desired motion, desired impedance and desired force to be applied to environment. The desired task space motion is determined as $x_d(t)$, $\dot{x}_d(t)$, $\ddot{x}_d(t) \in \mathbb{R}^n$ which are desired task space position, velocity, and acceleration, respectively, and they are sufficiently smooth. The joint space solution of the task space motion is denoted by $q_d(t)$, $\dot{q}_d(t)$, $\ddot{q}_d(t) \in \mathbb{R}^n$ which are desired joint space position, velocity, and acceleration, respectively. The desired impedance parameters are denoted by $\boldsymbol{M}_d$, $\boldsymbol{B}_d$, $\boldsymbol{K}_d$, $\in \mathbb{R}^{n\times n}$. $\boldsymbol{M}_d$ is the apparent inertia matrix. $\boldsymbol{B}_d$ and $\boldsymbol{K}_d$ are the desired friction and stiffness coefficient matrices. $F_d(t) \in \mathbb{R}^n$ is the desired force that is intended to apply to the environment.

Desired inputs and dynamic model terms are bounded by known positive constants, $\zeta$, and presented as follows (Lewis et al., 2003):

$$||x_d|| \leq \zeta_{x_d}, \quad ||\dot{x}_d|| \leq \zeta_{\dot{x}_d}, \quad ||\ddot{x}_d|| \leq \zeta_{\ddot{x}_d}, \quad ||F_d|| \leq \zeta_F \tag{4.8}$$

$$||q_d|| \leq \zeta_{q_d}, \quad ||\dot{q}_d|| \leq \zeta_{\dot{q}_d}, \quad ||\ddot{q}_d|| \leq \zeta_{\ddot{q}_d} \tag{4.9}$$

$$||\boldsymbol{M}_d||_{i2} = \zeta_{\boldsymbol{M}_d}, \quad ||\boldsymbol{B}_d||_{i2} = \zeta_{\boldsymbol{B}_d}, \quad ||\boldsymbol{K}_d||_{i2} = \zeta_{\boldsymbol{K}_d} \tag{4.10}$$

$$\zeta_{\boldsymbol{M},min}\boldsymbol{I} \leq \boldsymbol{M} \leq \zeta_{\boldsymbol{M},max}\boldsymbol{I} = ||\boldsymbol{M}||_{i2}\boldsymbol{I}, \quad ||\boldsymbol{B}||_{i2} = \zeta_{\boldsymbol{B}} \tag{4.11}$$

$$\zeta_{\boldsymbol{M}_r,min}\boldsymbol{I} \leq \boldsymbol{M}_r \leq \zeta_{\boldsymbol{M}_r,max}\boldsymbol{I} = ||\boldsymbol{M}_r||_{i2}\boldsymbol{I}, \quad ||\boldsymbol{B}_r||_{i2} = \zeta_{\boldsymbol{B}_r} \tag{4.12}$$

$$||\boldsymbol{M}_m||_{i2} = \zeta_{\boldsymbol{M}_m}, \quad ||\boldsymbol{B}_m||_{i2} = \zeta_{\boldsymbol{B}_m} \tag{4.13}$$

$$||\boldsymbol{V}(q,a)||_{i\infty} \leq \zeta_{\boldsymbol{V}}||a||, \quad ||\boldsymbol{V}_r(q,a)||_{i\infty} \leq \zeta_{\boldsymbol{V}_r}||a||, \quad \forall a \in \mathbb{R}^n \tag{4.14}$$

$$||\boldsymbol{J}||_{i\infty} \leq \zeta_{\boldsymbol{J}1}, \quad ||\boldsymbol{J}^{-1}||_{i\infty} \leq \zeta_{\boldsymbol{J}2}, \quad ||F_{ext}|| \leq \zeta_{F_{ext}} \tag{4.15}$$

where $||\cdot||$, $||\cdot||_{i2}$ and $||\cdot||_{i\infty}$ denote the Euclidean norm, matrix-induced two-norm, and matrix-induced infinity norm, respectively. $\boldsymbol{I} \in \mathbb{R}^{n\times n}$ is the identity matrix. $\boldsymbol{M}_d$, $\boldsymbol{B}_d$, $\boldsymbol{K}_d$, $\boldsymbol{M}_m$, $\boldsymbol{B}_m$, $\boldsymbol{B}_r$ and $\boldsymbol{B}$ are constant, positive definite and diagonal matrices.

The time derivative of the inverse Jacobian matrix is defined and bounded as follows:

$$\frac{d}{dt}\boldsymbol{J}^{-1}(q) = \boldsymbol{O}(q,\dot{q}) = -\boldsymbol{J}^{-1}(q)\left(\frac{\partial \boldsymbol{J}}{\partial q}\dot{q}\right)\boldsymbol{J}^{-1}(q) \tag{4.16}$$

$$||\boldsymbol{O}(q,\dot{q})||_{i\infty} \leq \zeta_{\boldsymbol{O}}||\dot{q}|| \tag{4.17}$$

Dynamic terms satisfy the following swapping and skew-symmetric properties $\forall a, b \in \mathbb{R}^n$ .

$$\boldsymbol{V}(q,a)b = \boldsymbol{V}(q,b)a \tag{4.18}$$

$$\boldsymbol{V}_r(q,a)b = \boldsymbol{V}_r(q,b)a \tag{4.19}$$

$$\boldsymbol{O}(q,a)b = \boldsymbol{O}(q,b)a \tag{4.20}$$

$$a^T\left(\dot{\boldsymbol{M}} - 2\boldsymbol{V}\right)a = 0 \tag{4.21}$$

$$a^T\left(\dot{\boldsymbol{M}}_r - 2\boldsymbol{V}_r\right)a = 0 \tag{4.22}$$

## 4.3. Control Objective, Controller and Observer Design

This section presents the control objectives, controller developments, and observer designs for both rigid and flexible robot modes.

### 4.3.1. The Controller for Rigid Mode

The aim of the rigid mode is to track a desired trajectory, and there is no desired interaction force, $F_d = 0$. The dimensions of the generalized coordinates for a 2-DoF robot is two, so $n = 2$. A filtered trajectory tracking error is defined as follows:

$$e_1 = q_d - q \tag{4.23}$$

$$\Omega_{r1} = \dot{q}_d + \alpha_1 e_1 \tag{4.24}$$

$$r_1 = \Omega_{r1} - \dot{q} \tag{4.25}$$

where $e_1(t)$ is the positioning error. $r_1(t)$ is the filtered tracking error and $\alpha_1$ is a positive constant gain.

Next, an auxiliary observer error term is defined as follows:

$$\tilde{q}_1 = q - \hat{q}_1 \tag{4.26}$$

$$\Omega_{s1} = -\dot{\hat{q}}_1 + \alpha_1 \tilde{q}_1 \tag{4.27}$$

$$s_1 = \Omega_{s1} + \dot{q} \tag{4.28}$$

where $\tilde{q}_1(t)$ is the observation error. $\hat{q}_1(t)$ and $\dot{\hat{q}}_1(t)$ are the estimated joint position and velocity, respectively. $s_1(t)$ is the auxiliary observation error.

Next, the time derivatives of $r_1$ and $s_1$ are computed and premultiplied by the inertia matrix, $\boldsymbol{M}$, as follows:

$$\begin{aligned} \boldsymbol{M}\dot{r}_1 = G + \alpha_1 \boldsymbol{M}\dot{q}_d + \boldsymbol{M}\ddot{q}_d + (\boldsymbol{B} + \boldsymbol{V}(q, \Omega_{r1}) - \alpha_1 \boldsymbol{M})\Omega_{r1} \\ +(-\boldsymbol{B} - \boldsymbol{V}(q, \Omega_{r1}) + \alpha_1 \boldsymbol{M})r_1 - \boldsymbol{V}r_1 - u_r \end{aligned} \tag{4.29}$$

$$\begin{aligned} \boldsymbol{M}\dot{s}_1 = u_r - G - \boldsymbol{M}\ddot{\hat{q}}_1 - \alpha_1 \boldsymbol{M}\dot{\hat{q}}_1 + (\boldsymbol{B} - \boldsymbol{V}(q, \Omega_{s1}) - \alpha_1 \boldsymbol{M})\Omega_{s1} \\ +(-\boldsymbol{B} + \boldsymbol{V}(q, \Omega_{s1}) + \alpha_1 \boldsymbol{M})s_1 - \boldsymbol{V}s_1 \end{aligned} \tag{4.30}$$

The observed velocity, $\dot{\hat{q}}_1$, is designed as follows (Yih, 2012):

$$\begin{aligned} \dot{p}_1 = \boldsymbol{M}^{-1}[u_r - G + (\boldsymbol{B} - \boldsymbol{V}(q, \Omega_{s1}) - \alpha_1 \boldsymbol{M})\Omega_{s1} + \tilde{q}_1 - \alpha_1 \boldsymbol{M}\dot{\hat{q}}_1] \\ +\alpha_1 w_{s1}\tilde{q}_1 - \alpha_1 w_{r1} e_1 \end{aligned} \tag{4.31}$$

$$\dot{\hat{q}}_1 = p_1 + w_{s1}\tilde{q}_1 - w_{r1}e_1 \tag{4.32}$$

where $w_{s1}$ and $w_{r1}$ are positive constant gains.

Given the observer in Equations 4.31 and 4.32, the controller signal, $u_r$, is designed as follows:

$$\begin{aligned} u_r = G + \boldsymbol{M}(\alpha_1 \dot{q}_d + \ddot{q}_d) + (\boldsymbol{B} + \boldsymbol{V}(q, \Omega_{r1}) - \alpha_1 \boldsymbol{M})\Omega_{r1} \\ +e_1 + w_{r1}\boldsymbol{M}(r_1 + s_1) \end{aligned} \tag{4.33}$$

Note that $r_1$ and $s_1$ cannot be computed individually, but $(r_1 + s_1)$ is an implementable term for the controller.

The stability analysis is conducted for the following scalar Lyapunov candidate function, $V_1$, as follows:

$$V_1 = \frac{1}{2} s_1^T \boldsymbol{M} s_1 + \frac{1}{2} r_1^T \boldsymbol{M} r_1 + \frac{1}{2} \tilde{q}_1^T \tilde{q}_1 + \frac{1}{2} e_1^T e_1 \tag{4.34}$$

$V_1$ is lower and upper bounded as shown:

$$\frac{1}{2} \min(1, \zeta_{\boldsymbol{M},min}) ||\Lambda_1||^2 \leq V_1 \leq \frac{1}{2} \max(1, \zeta_{\boldsymbol{M},max}) ||\Lambda_1||^2 \tag{4.35}$$

$$\Lambda_1 = \begin{bmatrix} e_1^T & \tilde{q}_1^T & r_1^T & s_1^T \end{bmatrix}^T \tag{4.36}$$

Next, the time derivative of $V_1$ is computed. Then, controller, $u_1$, in Equation 4.33 and the time derivative of the velocity observer, $\dot{\hat{q}}_1$ in Equation 4.32 are substituted, and the skew-symmetric property in Equation 4.21 is employed, as a result, obtaining the following equality:

$$\begin{aligned} \dot{V}_1 = s_1^T (\boldsymbol{V}(q, \Omega_{s1}) + \alpha_1 \boldsymbol{M}) s_1 + r_1^T (-\boldsymbol{V}(q, \Omega_{r1}) + \alpha_1 \boldsymbol{M}) r_1 - w_{r1} r_1^T \boldsymbol{M} (r_1 + s_1) \\ - w_{s1} s_1^T \boldsymbol{M} s_1 + w_{r1} s_1^T \boldsymbol{M} r_1 - \alpha_1 e_1^T e_1 - \alpha_1 \tilde{q}_1^T \tilde{q}_1 \end{aligned} \tag{4.37}$$

which can be simplified by using $\Omega_{s1} = s_1 + r_1 - \Omega_{r1}$, and upper bounded as follows:

$$\begin{aligned} \dot{V}_1 \leq ||s_1||^2 \left( \alpha_1 \zeta_{\boldsymbol{M},max} + \zeta_{\boldsymbol{V}} \zeta_{\dot{q}_d} + \alpha_1 \zeta_{\boldsymbol{V}} ||e_1|| + \zeta_{\boldsymbol{V}} ||s_1|| + \zeta_{\boldsymbol{V}} ||r_1|| - w_{s1} \zeta_{\boldsymbol{M},min} \right) \\ + ||r_1||^2 \left( \alpha_1 \zeta_{\boldsymbol{M},max} + \zeta_{\boldsymbol{V}} \zeta_{\dot{q}_d} + \alpha_1 \zeta_{\boldsymbol{V}} ||e_1|| - w_{r1} \zeta_{\boldsymbol{M},min} \right) - \alpha_1 ||e_1||^2 - \alpha_1 ||\tilde{q}_1||^2 \end{aligned} \tag{4.38}$$

The following inequalities are also valid:

$$3\alpha_1 ||\Lambda_1|| \geq ||s_1|| + ||r_1|| + \alpha_1 ||e_1|| \tag{4.39}$$

$$\alpha_1||\Lambda_1|| \geq \alpha_1||e_1|| \tag{4.40}$$

$$||\Lambda_1|| \leq \sqrt{2V_1 \frac{1}{\min(1, \zeta_{\boldsymbol{M},min})}} \tag{4.41}$$

When the initial conditions and $\Lambda_1$ inequalities are substituted, the gains' conditions are computed as follows:

$$w_{s1} \geq \alpha_1 \frac{\zeta_{\boldsymbol{M},max}}{\zeta_{\boldsymbol{M},min}} + \frac{\zeta_{\boldsymbol{V}}}{\zeta_{\boldsymbol{M},min}} \left( \zeta_{\dot{q}_d} + 3\alpha_1 \sqrt{2V_1(0) \frac{1}{\min(1, \zeta_{\boldsymbol{M},min})}} \right) \tag{4.42}$$

$$w_{r1} \geq \alpha_1 \frac{\zeta_{\boldsymbol{M},max}}{\zeta_{\boldsymbol{M},min}} + \frac{\zeta_{\boldsymbol{V}}}{\zeta_{\boldsymbol{M},min}} \left( \zeta_{\dot{q}_d} + \alpha_1 \sqrt{2V_1(0) \frac{1}{\min(1, \zeta_{\boldsymbol{M},min})}} \right) \tag{4.43}$$

An upper bound is described for $V_1(0)$:

$$V_1(0) \leq \frac{1}{2} \max(1, \zeta_{\boldsymbol{M},max}) ||\Lambda_1(0)||^2 \tag{4.44}$$

By introducing this last bound, the final condition of gains are determined as follows:

$$w_{s1} \geq \alpha_1 \frac{\zeta_{\boldsymbol{M},max}}{\zeta_{\boldsymbol{M},min}} + \frac{\zeta_{\boldsymbol{V}}}{\zeta_{\boldsymbol{M},min}} \left( \zeta_{\dot{q}_d} + 3\alpha_1 ||\Lambda_1(0)|| \sqrt{2 \frac{\max(1, \zeta_{\boldsymbol{M},max})}{\min(1, \zeta_{\boldsymbol{M},min})}} \right) \tag{4.45}$$

$$w_{r1} \geq \alpha_1 \frac{\zeta_{\boldsymbol{M},max}}{\zeta_{\boldsymbol{M},min}} + \frac{\zeta_{\boldsymbol{V}}}{\zeta_{\boldsymbol{M},min}} \left( \zeta_{\dot{q}_d} + \alpha_1 ||\Lambda_1(0)|| \sqrt{2 \frac{\max(1, \zeta_{\boldsymbol{M},max})}{\min(1, \zeta_{\boldsymbol{M},min})}} \right) \tag{4.46}$$

According to the above inequalities, the initial condition, $||\Lambda_1(0)||$, is at its maximum value when $t = 0$ and approaches zero as $t \to \infty$. It is also possible to construct a more conservative bound by updating the initial condition, $||\Lambda_1(0)||$, in accordance with the maximum expected errors; for instance, the maximum position error, $e_1(0)$, is upper bounded by the workspace.

The closed-loop system's block diagram is shown in Figure 4.2.

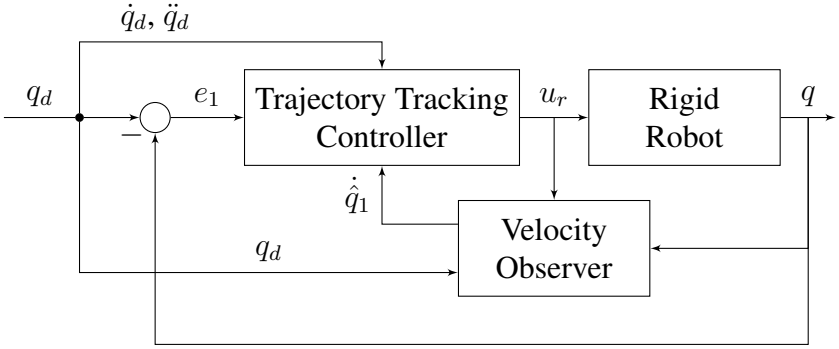



Figure 4.2. Trajectory tracking control block diagram.

### 4.3.2. The Controller for Flexible Mode

This section presents the desired objectives reserved for flexible mode and the controllers for reaching these objectives, along with necessary observers.

#### 4.3.2.1. Impedance Controller

In the flexible mode, one of the aims is to achieve the desired impedance in joint space. In rigid robot manipulators, the stiffness property of the desired impedance is induced by a virtual stiffness gain. The same can be conducted for the RLFJ robot manipulator. However, exploiting the natural impedance of the robot is the main idea in RLFJ robot control.

The desired robot impedance is stated as follows:

$$\boldsymbol{M}_r\ddot{q} + \boldsymbol{V}_r\dot{q} + \boldsymbol{B}_d(\dot{q} - \dot{q}_d) + \boldsymbol{K}_d(q - q_d) + \nu = \tau_{ext} \tag{4.47}$$

The actuator side's control must first be handled to realize the desired impedance. For this, the viscous friction term is compensated, and the apparent rotor inertia is reduced to increase the transparency of control input to the flexible joint as much as possible so that output torque and control input can be assumed equal.

First, an observer for the actuator is designed with the following auxiliary observer error:

$$\tilde{q}_m = q_m - \hat{q}_m \tag{4.48}$$

$$\Omega_{s2} = -\dot{\hat{q}}_m + \alpha_2 \tilde{q}_m \tag{4.49}$$

$$s_2 = \Omega_{s2} + \dot{q}_m \tag{4.50}$$

where $\tilde{q}_m(t)$ is the actuator's observation position error. $\hat{q}_m(t)$ and $\dot{\hat{q}}_m(t)$ are the estimated actuator position and velocity, respectively. $s_2(t)$ is the auxiliary observation error.

The actuator's velocity observer is designed as follows:

$$\dot{p}_2 = \boldsymbol{M}_m^{-1}[u_m - \tau_m - \alpha_2 \boldsymbol{M}_m \dot{\hat{q}}_m - (-\boldsymbol{B}_m + \alpha_2 \boldsymbol{M}_m)\Omega_{s2} + \tilde{q}_m] + \alpha_2 w_{s2} \tilde{q}_m \tag{4.51}$$

$$\dot{\hat{q}}_m = p_2 + w_{s2} \tilde{q}_m \tag{4.52}$$

$w_{s2}$ is a positive constant gain.

The stability of the observer is verified for the following Lyapunov function:

$$V_2 = \frac{1}{2} s_2^T \boldsymbol{M}_m s_2 + \frac{1}{2} \tilde{q}_m^T \tilde{q}_m \tag{4.53}$$

$$\dot{V}_2 = \alpha_2 s_2^T \boldsymbol{M}_m s_2 - w_{s2} s_2^T \boldsymbol{M}_m s_2 \tag{4.54}$$

$$w_{s2} \geq \alpha_2 \tag{4.55}$$

The controller $u_m$ is designed as follows:

$$u_m = \tau_m + \rho \boldsymbol{B}_m \dot{\hat{q}}_m + \boldsymbol{M}_m \boldsymbol{M}_d^{-1}(u_f - \tau_m) \tag{4.56}$$

where $0 \leq \rho < 1$ is friction compensation ratio and $\zeta_{\boldsymbol{M}_d} < \zeta_{\boldsymbol{M}_m}$. $u_f(t)$ is the new control input to be designed. When selecting $\boldsymbol{M}_d$ and $\rho$, the following passivity condition must be met:

$$\int_0^t u_m^T q_m \geq 0 \tag{4.57}$$

With the given control signal, the new closed-loop actuator dynamics is computed

as follows:

$$\boldsymbol{M}_d\ddot{q}_m + \boldsymbol{M}_d\boldsymbol{M}_m^{-1}(\boldsymbol{B}_m\dot{q}_m - \rho\boldsymbol{B}_m\dot{\hat{q}}_m) + \tau_m = u_f \tag{4.58}$$

In this actuator dynamics, if $\boldsymbol{M}_d$ is selected a small value and $\rho$ is selected a close value to $1$, then the following assumption can be made:

$$\tau_m \approx u_f \tag{4.59}$$

which means torque on the flexible joint can be determined with control input $u_f$.

With the new actuator dynamics, the model in Equation 4.2 is updated as follows:

$$\boldsymbol{M_r}(q)\ddot{q} + \boldsymbol{V_r}(q,\dot{q})\dot{q} + \boldsymbol{B_r}\dot{q} + G(q) = u_f + \tau_{ext} \tag{4.60}$$

Now, the control input $u_f$ is designed to achieve the desired robot impedance, as in the following equation:

$$u_f = G + \boldsymbol{B}_r\dot{\hat{q}} + \boldsymbol{B}_d(\dot{q}_d - \dot{\hat{q}}) + \boldsymbol{K}_d(q_d - q) - \nu \tag{4.61}$$

In an RLFJ robot, friction should be limited to a reasonable level to make the flexible joint operate smoothly. Since flexible joints are designed with a specific stiffness, the desired impedance is the natural impedance of the robot itself in RLFJ robots. Also, the controller does not require an observer of the robot's link velocities. Then, the controller is defined as follows:

$$u_f = G + \boldsymbol{B}_r\dot{q}_d + \boldsymbol{K}(q_d - q) - \nu \tag{4.62}$$

When the controller in Equation 4.62 is used, the closed-loop control system sug-

gests that the actuator angles should track the desired link angles to display the natural impedance of the robot perfectly. This can be easily achieved by a simpler controller to drive $q_m \rightarrow q_d$. The impedance controller developed in Equation 4.62, however, allows better versatility on the robot. For instance, increasing/decreasing the apparent impedance, friction compensation, or introducing higher damping is possible with the controller developed here.

The closed-loop impedance controller block diagram is shown in Figure 4.3.

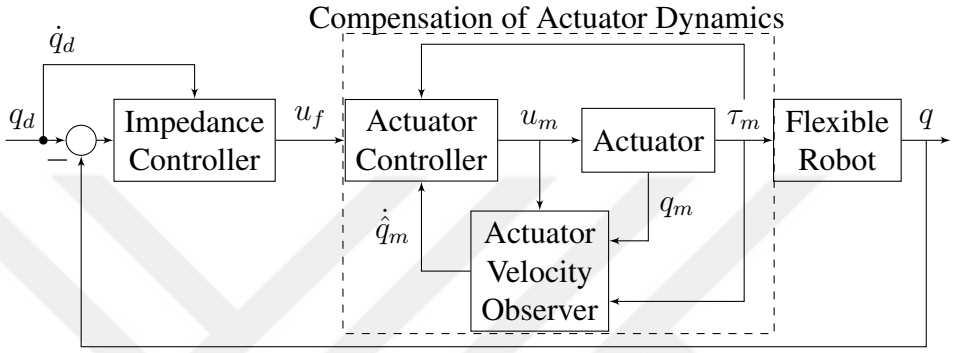



Figure 4.3. Impedance controller block diagram.

### 4.3.2.2. Force/Position Controller

In hybrid force/position control, the desired force and velocity vectors are defined as perpendicular to each other. A decoupling control law needs to be designed in task space to achieve both desires. A selection matrix achieves this decoupling. Force and velocity errors in task space are constructed with the aid of selection matrix as follows:

$$\dot{e}_x = \dot{x}_d - \boldsymbol{D}\dot{x} \tag{4.63}$$

$$e_F = F_d - (\boldsymbol{I} - \boldsymbol{D})F_{ext} \tag{4.64}$$

where $\dot{e}_x(t)$ and $e_F(t)$ are velocity and force errors defined in task space. $\dot{x}(t)$ and $F_{ext}(t)$ are measured velocity and applied force to environment. $\boldsymbol{D}$ is the diagonal selection matrix for isolating measured force/velocity in desired directions.

Both force and velocity measurements require sensors. For the latter, there is

only an encoder. Thus, this issue is to be solved by a velocity observer. The former, however, can be solved by virtue of the stiffness model of flexible joints in the RLFJ robot and encoders. The position difference between the actuator and robot's link provides the compliant deflection on the flexible joints, and combined with the stiffness model, interaction force at the end-effector can be estimated if there is a contact.

There must be an obstacle that is in contact with the end-effector to apply force to the environment. Because of this obstacle, the end-effector cannot move perpendicular to the contact surface, but can move only tangent to it. Thus, there is no motion along the contact surface's normal direction. This introduces a natural constraint. With the aid of selection matrix and the estimation of the torque on the flexible joint, the force applied to the environment by the end-effector is formulated as follows:

$$F_{ext} = (\boldsymbol{I} - \boldsymbol{D})\boldsymbol{J}^{-T}(\tau_m - G) \tag{4.65}$$

where $F_{ext}$ is the external force acting on the environment. $\tau_m$ carries the torque information that generates contact force, motion, and gravity compensation. The term $(\tau_m - G)$ removes the gravity feed-forward term from this information set. $\boldsymbol{J}^{-T}$ maps joint space torque information to task space as force, and $(\boldsymbol{I} - \boldsymbol{D})$ extracts the contact force information only.

The control signal has two parts that are responsible for generating the desired force and motion. Each part is designed separately. Using the natural constraints, partial actuator dynamic compensation in Equation 4.56 and the assumption in Equation 4.59, the dynamic model of the RFLJ robot in Equation 4.60 is dissected as follows:

$$\boldsymbol{M_r}(q)\ddot{q} + \boldsymbol{V_r}(q,\dot{q})\dot{q} + \boldsymbol{B_r}\dot{q} + G(q) = u_{fm} \tag{4.66}$$

$$0 = u_{ff} + \tau_{ext} \tag{4.67}$$

$$u_{ff} + u_{fm} = u_f \tag{4.68}$$

where $u_{ff}(t)$ and $u_{fm}(t)$ are control signals for regulating the contact force and motion, respectively.

The error term, $\dot{e}_x$, is designed in task space. A controller needs to be designed

in task space to drive these errors to zero. However, the transition between joint and task space during controller design might bear singular matrix problems. The singular matrix problem is caused by $\boldsymbol{D}$ being a singular matrix. This issue is resolved in two steps. First, a trajectory tracking control in task space is developed with the necessary velocity observer. Then, the error and desired input vectors in the controller are multiplied with the selection matrix $\boldsymbol{D}$ to prevent the robot from moving in the undesired direction.

A Filtered trajectory tracking error (which is designed in (Cobanoglu et al., 2018)), $r_2(t)$, is shown as follows:

$$e_x = x_d - x \tag{4.69}$$

$$\Omega_{r2} = \dot{x}_d + \alpha_3 e_x \tag{4.70}$$

$$r_2 = \boldsymbol{J}^{-1}\Omega_{r2} - \dot{q} \tag{4.71}$$

where $\alpha_3$ is a constant positive gain.

The auxiliary observation error is defined as follows:

$$\tilde{q}_3 = q - \hat{q}_3 \tag{4.72}$$

$$\Omega_{s3} = -\dot{\hat{q}}_3 + \alpha_3 \tilde{q}_3 \tag{4.73}$$

$$s_3 = \Omega_{s3} + \dot{q} \tag{4.74}$$

where $\tilde{q}_3(t)$ is the observation error. $\hat{q}_3(t)$ and $\dot{\hat{q}}_3(t)$ are the estimated joint position and velocity of the robot, respectively. $s_3(t)$ is the auxiliary observation error.

Next, the time derivative of $r_2$ is computed and pre-multiplied with $\boldsymbol{M}_r$:

$$\begin{aligned}\boldsymbol{M}_r\dot{r}_2 = (\boldsymbol{M}_r\boldsymbol{O}_{\Omega r2}\boldsymbol{J}^{-1} + \boldsymbol{V}_{\Omega r2}\boldsymbol{J}^{-1} + \boldsymbol{B}_r\boldsymbol{J}^{-1})\Omega_{r2} + \boldsymbol{M}_r\boldsymbol{J}^{-1}\ddot{x}_d - \alpha_3^2\boldsymbol{M}_r\boldsymbol{J}^{-1}e_x \\ +(-\boldsymbol{M}_r\boldsymbol{O}_{\Omega r2} + \alpha_3\boldsymbol{M}_r - \boldsymbol{V}_{\Omega r2} - \boldsymbol{B}_r)r_2 + G - \boldsymbol{V}_r r_2 - u_{fm} \qquad (4.75)\end{aligned}$$

$$\boldsymbol{O}_{\Omega r2} = \boldsymbol{O}(q, \boldsymbol{J}^{-1}\Omega_{r2}), \quad \boldsymbol{V}_{\Omega r2} = \boldsymbol{V}_r(q, \boldsymbol{J}^{-1}\Omega_{r2}) \tag{4.76}$$

The controller for these dynamics is designed as follows:

$$u_{fm} = \boldsymbol{M}_r \boldsymbol{J}^{-1} \ddot{x}_d - \alpha_3^2 \boldsymbol{M}_r \boldsymbol{J}^{-1} e_x + G + \boldsymbol{J}^T e_x + \boldsymbol{M}_r w_{r2}(r_2 + s_3)$$
$$+(\boldsymbol{M}_r \boldsymbol{O}_{\Omega r2} \boldsymbol{J}^{-1} + \boldsymbol{V}_{\Omega r2} \boldsymbol{J}^{-1} + \boldsymbol{B}_r \boldsymbol{J}^{-1})\Omega_{r2} \tag{4.77}$$

In order to make the controller operate along the desired velocity direction, the task space error and desired terms are premultiplied by $\boldsymbol{D}$ and $e_x$, $r_2$, $\Omega_{r2}$, $\boldsymbol{O}_{\Omega r2}$, and $\boldsymbol{V}_{\Omega r2}$ are updated as follows:

$$e'_x = \boldsymbol{D} e_x \tag{4.78}$$
$$\Omega'_{r2} = \boldsymbol{D}\dot{x}_d + \alpha_3 e'_x \tag{4.79}$$
$$r'_2 = \boldsymbol{J}^{-1}\Omega'_{r2} - \dot{q} \tag{4.80}$$
$$\boldsymbol{O}_{\Omega' r2} = \boldsymbol{O}(q, \boldsymbol{J}^{-1}\Omega'_{r2}) \tag{4.81}$$
$$\boldsymbol{V}_{\Omega' r2} = \boldsymbol{V}_r(q, \boldsymbol{J}^{-1}\Omega'_{r2}) \tag{4.82}$$
$$u'_{fm} = \boldsymbol{M}_r \boldsymbol{J}^{-1} \boldsymbol{D} \ddot{x}_d - \alpha_3^2 \boldsymbol{M}_r \boldsymbol{J}^{-1} e'_x + G + \boldsymbol{J}^T e'_x + \boldsymbol{M}_r w_{r2}(r'_2 + s_3)$$
$$+(\boldsymbol{M}_r \boldsymbol{O}_{\Omega' r2} \boldsymbol{J}^{-1} + \boldsymbol{V}_{\Omega' r2} \boldsymbol{J}^{-1} + \boldsymbol{B}_r \boldsymbol{J}^{-1})\Omega'_{r2} \tag{4.83}$$

Next, the time derivative of $s_3$ is computed and premultiplied with $\boldsymbol{M}_r$:

$$\boldsymbol{M}_r \dot{s}_3 = u_{fm} - G - \boldsymbol{M}_r \ddot{\hat{q}}_3 - \alpha_3 \boldsymbol{M}_r \dot{\hat{q}}_3 + (\boldsymbol{B}_r - \boldsymbol{V}_r(q, \Omega_{s3}) - \alpha_3 \boldsymbol{M}_r)\Omega_{s3}$$
$$+(-\boldsymbol{B}_r + \boldsymbol{V}_r(q, \Omega_{s3}) + \alpha_3 \boldsymbol{M}_r)s_3 - \boldsymbol{V}_r s_3 \tag{4.84}$$

The observed velocity, $\dot{\hat{q}}_3$, is designed as follows:

$$\dot{p}_3 = \boldsymbol{M}_r^{-1}[u'_{fm} - G + (\boldsymbol{B}_r - \boldsymbol{V}_r(q, \Omega_{s3}) - \alpha_3 \boldsymbol{M}_r)\Omega_{s3} + \tilde{q} - \alpha_3 \boldsymbol{M}_r \dot{\hat{q}}]$$
$$+\alpha_3 w_{s3} \tilde{q}_3 - w_{r2} \boldsymbol{J}^{-1}\Omega'_{r2} \tag{4.85}$$
$$\dot{\hat{q}}_3 = p_3 + w_{s3}\tilde{q}_3 + w_{r2} q \tag{4.86}$$

where $w_{s3}$ and $w_{r2}$ are positive constant gains.

The stability analysis is conducted for the following Lyapunov function that is

upper and lower bounded as shown:

$$V_3 = \frac{1}{2} s_3^T \boldsymbol{M}_r s_3 + \frac{1}{2} r_2'^T \boldsymbol{M}_r r_2' + \frac{1}{2} \tilde{q}_3^T \tilde{q}_3 + \frac{1}{2} e_x'^T e_x' \tag{4.87}$$

$$\frac{1}{2} \min(1, \zeta_{\boldsymbol{M}_{r,min}}) ||\Lambda_2||^2 \leq V_3 \leq \frac{1}{2} \max(1, \zeta_{\boldsymbol{M}_{r,max}}) ||\Lambda_2||^2 \tag{4.88}$$

$$\Lambda_2 = \begin{bmatrix} e_x'^T & \tilde{q}_3^T & r_2^T & s_3^T \end{bmatrix}^T \tag{4.89}$$

By computing the time derivative of the Lyapunov function and adopting the skew-symmetric property in Equation 4.22, the following result is obtained:

$$\begin{aligned} \dot{V}_3 = s_3^T (\boldsymbol{V}_r(q, \Omega_{s3}) + \alpha_3 \boldsymbol{M}_r) s_3 - w_{s3} s_3^T \boldsymbol{M}_r s_3 + w_{r2} s_3^T \boldsymbol{M} r_2' - w_{r2} r_2'^T \boldsymbol{M}_r (r_2' + s_3) \\ + r_2'^T (-\boldsymbol{M}_r \boldsymbol{O}_{\Omega' r2} + \alpha_3 \boldsymbol{M}_r - \boldsymbol{V}_{\Omega' r2}) r_2' - \alpha_3 e_x'^T e_x' - \alpha_3 \tilde{q}_3^T \tilde{q}_3 \end{aligned} \tag{4.90}$$

The norms $||\Omega_{s3}||$ and $||\boldsymbol{J}^{-1}\Omega_{r2}'||$ are bounded as follows:

$$||\Omega_{s3}|| \leq ||s_3|| + ||r_2'|| + \zeta_{\boldsymbol{J}2} \zeta_{\dot{x}_d}' + \zeta_{\boldsymbol{J}2} \alpha_3 ||e_x'|| \tag{4.91}$$

$$||\boldsymbol{J}^{-1}\Omega_{r2}'|| \leq \zeta_{\boldsymbol{J}2} \zeta_{\dot{x}_d}' + \zeta_{\boldsymbol{J}2} \alpha_3 ||e_x'|| \tag{4.92}$$

$$\begin{aligned} \dot{V}_3 \leq ||s_3||^2 \left( \zeta_{V_r} (||s_3|| + ||r_2'|| + \zeta_{\boldsymbol{J}2} \zeta_{\dot{x}_d}' + \zeta_{\boldsymbol{J}2} \alpha_3 ||e_x'||) + \alpha_3 \zeta_{M_{r,max}} - w_{s3} \zeta_{M_{r,min}} \right) \\ + ||r_2||^2 \left( (\zeta_{M_{r,max}} \zeta_O + \zeta_{V_r}) (\zeta_{\boldsymbol{J}2} \zeta_{\dot{x}_d}' + \zeta_{\boldsymbol{J}2} \alpha_3 ||e_x'||) + \alpha_3 \zeta_{M_{r,max}} - w_{r2} \zeta_{M_{r,min}} \right) \\ - \alpha_3 ||e_x'||^2 - \alpha_3 ||\tilde{q}_3||^2 \end{aligned} \tag{4.93}$$

where $\zeta_{\dot{x}_d}' = ||\boldsymbol{D}\dot{x}_d||$.

As a result, the gains' conditions are defined as follows:

$$w_{s3} \geq \frac{\zeta_{V_r} \zeta_{\boldsymbol{J}2} \zeta_{\dot{x}_d}'}{\zeta_{M_{r,min}}} + \alpha_3 \frac{\zeta_{M_{r,max}}}{\zeta_{M_{r,min}}} + \frac{\zeta_{V_r}}{\zeta_{M_{r,min}}} (||s_3|| + ||r_2'|| + \zeta_{\boldsymbol{J}2} \alpha_3 ||e_x'||) \tag{4.94}$$

$$w_{r2} \geq \frac{(\zeta_{M_{r,max}} \zeta_O + \zeta_{V_r})(\zeta_{\boldsymbol{J}2} \zeta_{\dot{x}_d}')}{\zeta_{M_{r,min}}} + \alpha_3 \frac{\zeta_{M_{r,max}}}{\zeta_{M_{r,min}}} + \frac{\zeta_{M_{r,max}} \zeta_O + \zeta_{V_r}}{\zeta_{M_{r,min}}} (\zeta_{\boldsymbol{J}2} \alpha_3 ||e_x'||) \tag{4.95}$$

The following inequalities with the initial conditions are obtained:

$$3\zeta_{\boldsymbol{J}2}\alpha_3||\Lambda_2|| \geq ||s_3|| + ||r_2'|| + \zeta_{\boldsymbol{J}2}\alpha_3||e_x'|| \tag{4.96}$$

$$\zeta_{\boldsymbol{J}2}\alpha_3||\Lambda_2|| \geq \zeta_{\boldsymbol{J}2}\alpha_3||e_x'|| \tag{4.97}$$

$$||\Lambda_2(0)|| \leq \sqrt{2V_3(0)\frac{1}{\min(1,\zeta_{M_{r,min}})}} \tag{4.98}$$

$$V_3(0) \leq \frac{1}{2}\max(1,\zeta_{M_{r,max}})||\Lambda_2(0)||^2 \tag{4.99}$$

Thus, the final gain conditions are set as follows:

$$w_{s3} \geq \frac{\zeta_{V_r}\zeta_{\boldsymbol{J}2}\zeta_{\dot{x}_d}'}{\zeta_{M_{r,min}}} + \alpha_3\frac{\zeta_{M_{r,max}}}{\zeta_{M_{r,min}}} + 3\alpha_3\zeta_{\boldsymbol{J}2}\frac{\zeta_{V_r}}{\zeta_{M_{r,min}}}||\Lambda_2(0)||\sqrt{2\frac{\max(1,\zeta_{\boldsymbol{M}_{r,max}})}{\min(1,\zeta_{\boldsymbol{M}_{r,min}})}} \tag{4.100}$$

$$w_{r2} \geq \frac{(\zeta_{M_{r,max}}\zeta_O + \zeta_{V_r})(\zeta_{\boldsymbol{J}2}\zeta_{\dot{x}_d}')}{\zeta_{M_{r,min}}} + \alpha_3\frac{\zeta_{M_{r,max}}}{\zeta_{M_{r,min}}}$$
$$+\zeta_{\boldsymbol{J}2}\alpha_3\frac{\zeta_{M_{r,max}}\zeta_O + \zeta_{V_r}}{\zeta_{M_{r,min}}}||\Lambda_2(0)||\sqrt{2\frac{\max(1,\zeta_{\boldsymbol{M}_{r,max}})}{\min(1,\zeta_{\boldsymbol{M}_{r,min}})}} \tag{4.101}$$

Now, along the remaining motion axis, a force controller can be developed for driving the error $e_F$ to zero.

$$u_{ff} = \boldsymbol{J}^T\left(F_d + \lambda_F\right) \tag{4.102}$$

$$\lambda_F = \begin{cases} \int_{t_1}^{t}\left[F_d - (\boldsymbol{I}-\boldsymbol{D})\boldsymbol{J}^{-T}(\tau_m - G)\right]d\sigma & \text{, if } e_x^T\boldsymbol{D}^T\boldsymbol{D}e_x < \zeta_{e_{xd}}^2 \\ 0 & \text{, otherwise} \end{cases} \tag{4.103}$$

where $\zeta_{e_{xd}}$ is a constant magnitude that will activate the integrator. The first two terms, $F_d$ and $\lambda_F$, are PI-based control for displaying the desired force.

The closed-loop hybrid controller block diagram is shown in Figure 4.4.

### 4.3.3. Switch Designs

The switching between the controllers needs to be done smoothly to ensure system stability. The smooth transition is achieved with sigmoid functions. The required switch

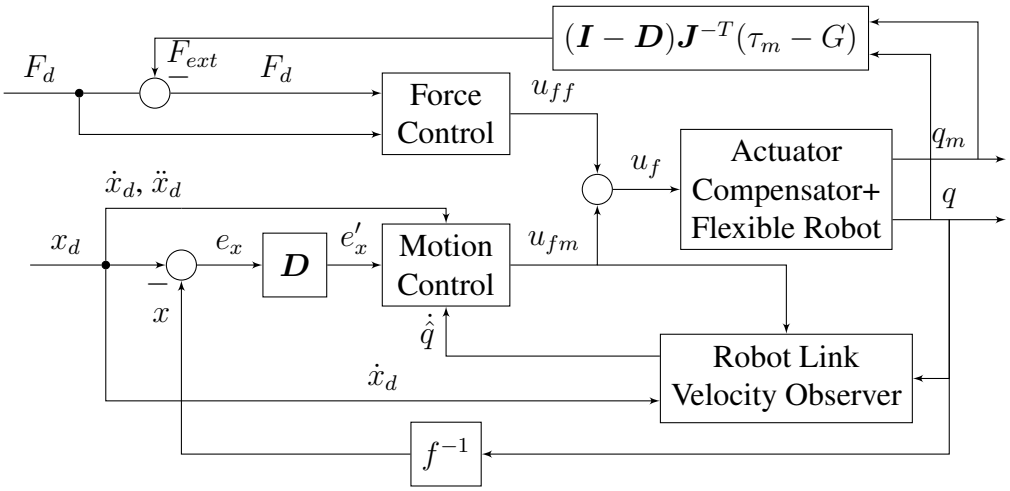



Figure 4.4. Hybrid force/position controller block diagram.

cases are switching between rigid state trajectory tracking control and impedance control, switching between rigid state trajectory tracking control and force/position control, and switch for activating safety procedure for excessive loads.

#### 4.3.3.1. Trajectory Tracking - Impedance Controller Switch

The controller gains of rigid mode's trajectory tracking can be selected as small or large depending on the intended work. Small gains generate smaller torque signals at the actuators, even if the trajectory error is large. Similarly, larger gains lead to higher actuator torque. The latter, however, drives the flexible joints closer to the flexible mode, which raises a switch flag for activating impedance control. From this, it can be concluded that the switch state is a function of torsion on the flexible joints.

Torsion on the flexible joints can be computed via the stiffness model. Yet, there is a problem. The stiffness model is useful only if there is a compliant deflection on the joints. For a stable switch, the impedance controller should be prepared for flexible mode even before the deflections occur. That way, the impedance controller can become partially active at the instant that the compliant deflections are measured. A torque observer can estimate the torsion state on flexible joints.

The torque load on flexible joints is derived from the flexible robot dynamics in Equation 4.2 as follows:

$$\tau_m = (\boldsymbol{I} - \boldsymbol{M}_m\boldsymbol{M}_r^{-1})^{-1}\left[u_m + \boldsymbol{M}_m\boldsymbol{M}_r^{-1}(\boldsymbol{V}_r + \boldsymbol{B}_r)\dot{q} - \boldsymbol{B}_m\dot{q} - \boldsymbol{M}_m\ddot{z} - \boldsymbol{B}_z\dot{z}\right] \quad (4.104)$$

In rigid mode, $\ddot{z} = \dot{z} = 0$. By substituting the velocities with the observed velocity, the torque observer for the switch is acquired as follows:

$$\hat{\tau}_m = (\boldsymbol{I} - \boldsymbol{M}_m \boldsymbol{M}_r^{-1})^{-1} \left[ u_m + \boldsymbol{M}_m \boldsymbol{M}_r^{-1} (\boldsymbol{V}_r(q, \dot{\hat{q}}) + \boldsymbol{B}_r)\dot{\hat{q}} - \boldsymbol{B}_m \dot{\hat{q}} \right] \tag{4.105}$$

The switches are designed as follows:

$$\chi = \begin{cases} |\hat{\tau}_m| & \text{, if } |\hat{\tau}_m| < |\tau_{stiff}| \text{ and } z = 0 \\ |\boldsymbol{K} z + \nu| & \text{, otherwise} \end{cases} \tag{4.106}$$

$$\xi_{flex} = \frac{1}{1 + e^{-\alpha_4(\chi - \tau_{stiff})}} \tag{4.107}$$

$$\xi_{rigid} = \frac{1}{1 + e^{\alpha_4(\chi - \tau_{stiff})}} \tag{4.108}$$

where $\alpha_4$ is a positive smoothness gain. $\xi_{rigid}$ and $\xi_{flex}$ are smooth switches ranging between 0 and 1. $\xi_{rigid}$ and $\xi_{flex}$ are to be multiplied by rigid trajectory tracking control and impedance control signals, respectively.

### 4.3.3.2. Trajectory Tracking - Hybrid Controller Switch

Before activating the force/position controller, the end-effector should first reach close proximity of the desired position. This is achieved by a rigid trajectory tracking controller. In this switch, a positioning error-based switch mechanism is designed as follows:

$$\xi_{tt} = \frac{1}{1 + e^{-\alpha_5(\sqrt{e_x^T \boldsymbol{D}^T \boldsymbol{D} e_x} - \zeta_{e_{xd}})}} \tag{4.109}$$

$$\xi_{hybrid} = \frac{1}{1 + e^{\alpha_5(\sqrt{e_x^T \boldsymbol{D}^T \boldsymbol{D} e_x} - \zeta_{e_{xd}})}} \tag{4.110}$$

where $\alpha_5$ is a positive smoothness gain. $\zeta_{e_{xd}}$ is the magnitude of error reserved for switching. $\xi_{tt}$ and $\xi_{fp}$ are smooth switches ranging between 0 and 1. $\xi_{tt}$ is active until the

end-effector reaches close proximity of the desired position. Then, $\xi_{fp}$ is activated for initializing the hybrid controller.

#### 4.3.3.3. Safety Switch

The safety switch is activated in case of excessive force loads are estimated at the end-effector. Yet, excessive forces can be permitted for 0.5 seconds. Therefore, this switch is a function of time and force. The switch cuts off all the control signals generated by the controller to return safe limits. Then, the controllers reactivated automatically to return to the default operation mode. The safety switch is designed as follows:

$$\chi_F = \sqrt{\tau_m^T \boldsymbol{J}^{-1} \boldsymbol{J}^{-T} \tau_m} \tag{4.111}$$

$$\begin{cases} t_e = t, \text{flag} = 1 & \text{, if } |F_{max}| < \chi_F(t) \text{ and } |F_{max}| < \chi_F(t-0.5) \text{ and flag} = 0 \\ \text{flag} = 0 & \text{, } (t - t_e) \geq 2 \end{cases} \tag{4.112}$$

$$\xi_{safety} = \frac{1}{1 + e^{17.37(t-t_e-0.5)}} + \frac{1}{1 + e^{-17.37(t-t_e-1.5)}} \tag{4.113}$$

where $t_e$ is the time when the event is triggered at the instant the first condition is satisfied. In the first condition, the current force and the force belonging 0.5 seconds earlier are compared with the safe torque level $F_{max}$. This allows momentarily entering above the safe force limits but prevents staying in there any longer. When the condition is satisfied, $t_e$ is updated with the current time. As a result, $\xi_{safety}$ stars an action to reach zero in 1 second and return to 1 in the next second, which takes two seconds in total. $t_e = 2$ when $t = 0$ to make $\xi_{safety} = 1$ at $t = 0$.

Figure 4.5 shows all the connections of controllers and switches. The saturation block limits the generated control signal to prevent the manipulator from entering the flexible mode.

## 4.4. Simulation, Experiment, Results and Discussions

In this section, simulation and experiment conditions are described. The results of both are presented and compared.

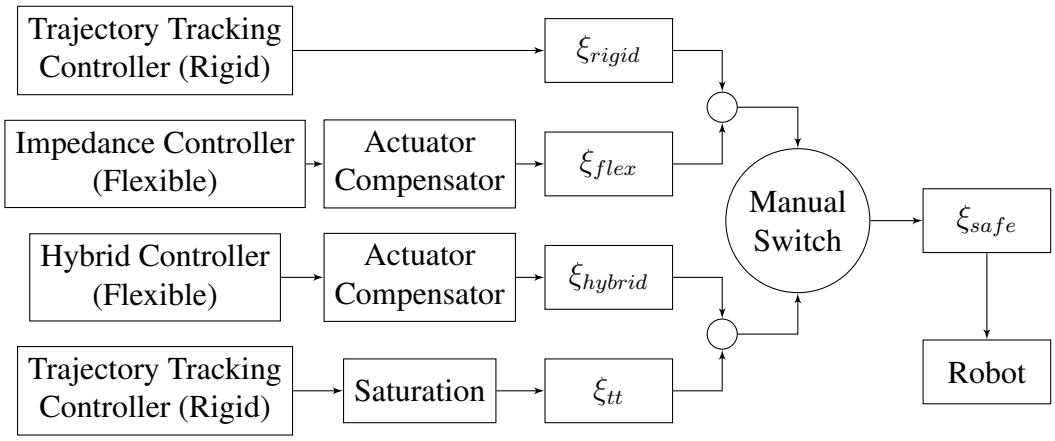



Figure 4.5. RLFJ robot controller framework.

### 4.4.1. Simulation and Experiment Preliminaries

The controllers are tested for a 2-DoF five-bar RLFJ robot manipulator by using MATLAB Simulink to manage the experiment hardware and run the simulation. Both experiment and simulation run at 10 kHz sampling frequency. The robot and the test setup are shown in Figure 4.6. The dimensions and the mass properties of the robot are shown in Figure 4.7. The link lengths are synthesized to have a relatively uniform end-effector force output throughout the workspace. Therefore, the distal links ($l_{12}$ and $l_{22}$) operate in a close range of perpendicular angle to proximal links ($l_{11}$ and $l_{21}$).

System parameters are obtained experimentally. For acquiring dynamics-related parameters (inertia/friction), first, a robust controller makes the end-effector follow a certain trajectory that covers the operational workspace. Meanwhile, input/output data is recorded. The parameters are adjusted through an optimization problem to justify the input/output (torque/velocity) relation. For clarity, the flexible joints' inertia is included in the inertia of the proximal links. The robot manipulator is constrained along the gravity axis. However, due to the joint clearances, a linear gravity term has to be computed. System parameters are presented as follows:

$$\boldsymbol{M}_m = \begin{bmatrix} 6.4 & 0 \\ 0 & 6.4 \end{bmatrix} \times 10^{-5}, \quad \boldsymbol{B}_r = \begin{bmatrix} 7 & 0 \\ 0 & 7 \end{bmatrix} \times 10^{-6}, \quad \boldsymbol{B}_m = \begin{bmatrix} 2 & 0 \\ 0 & 2 \end{bmatrix} \times 10^{-3} \tag{4.114}$$

$$G = \left( \begin{bmatrix} 1.2 & 6.9 \\ 0.99 & 6.8 \end{bmatrix} q + \begin{bmatrix} -8.37 \\ -0.015 \end{bmatrix} \right) \times 10^{-3}, \quad q = \begin{bmatrix} q_1 \\ q_2 \end{bmatrix} \tag{4.115}$$

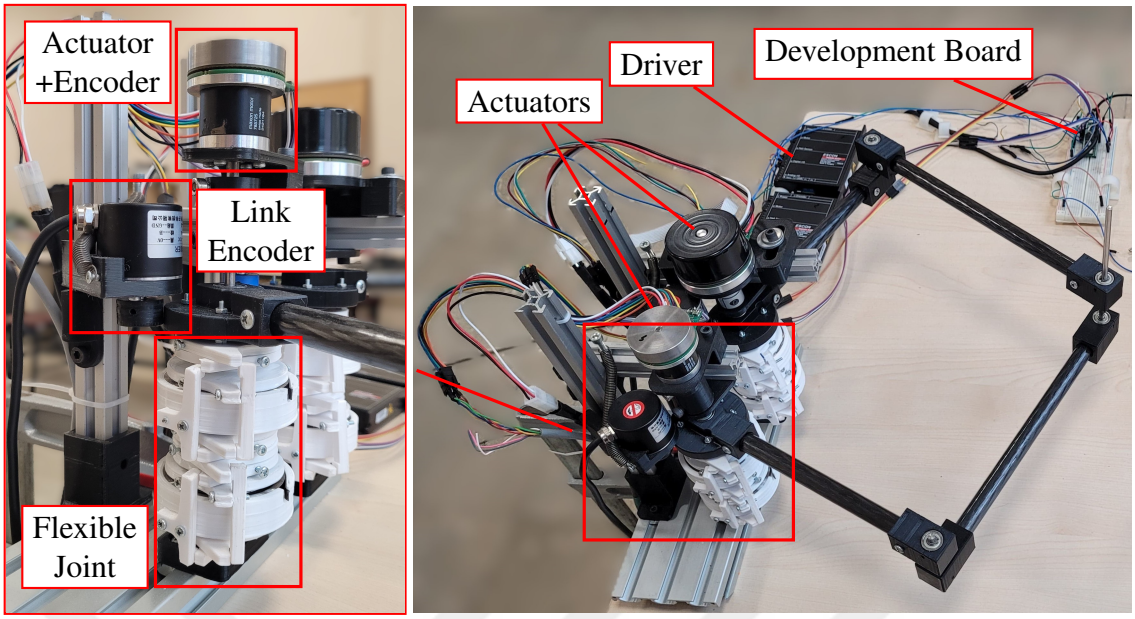



Figure 4.6. Five-bar RLFJ robot manipulator and experiment setup.

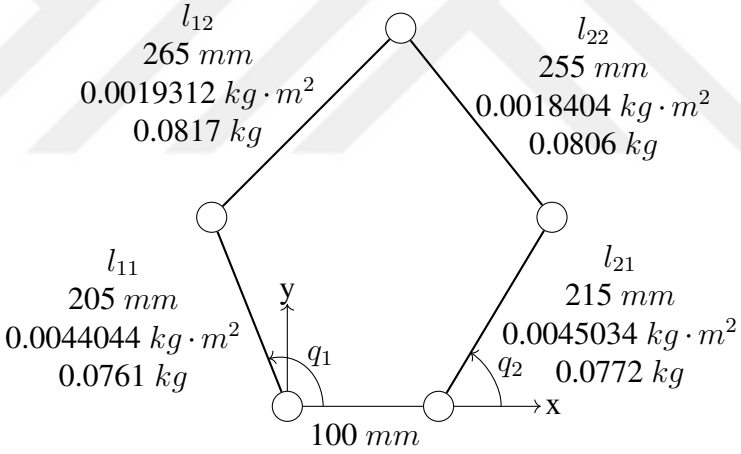



Figure 4.7. Robot's kinematic and inertia properties.

The static properties (stiffness) of the robot are acquired experimentally. Figure 4.8 shows the experimental load/compliant deflection of the flexible joints. As a result, the stiffness parameters of each joint are derived from the measured data as follows:

$$k_1 = \begin{cases} 0.027 & ,0.110 \leq \tau_{m1} < 0.130 \\ 0.015 & ,0.130 \leq \tau_{m1} \end{cases}, \quad \nu_1 = \begin{cases} 0.110 & ,0.110 \leq \tau_{m1} < 0.130 \\ 0.119 & ,0.130 \leq \tau_{m1} \end{cases} \tag{4.116}$$

$$k_2 = \begin{cases} 0.036 & ,0.115 \leq \tau_{m2} < 0.148 \\ 0.020 & ,0.148 \leq \tau_{m2} \end{cases}, \quad \nu_2 = \begin{cases} 0.115 & ,0.115 \leq \tau_{m2} < 0.148 \\ 0.131 & ,0.148 \leq \tau_{m2} \end{cases} \tag{4.117}$$

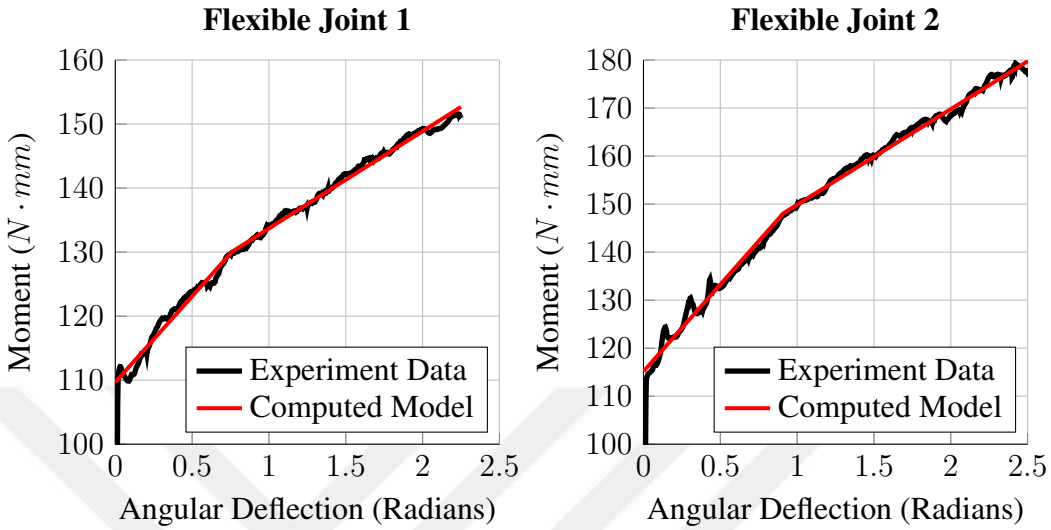



Figure 4.8. Moment vs compliant deflection of flexible joints.

### 4.4.2. Trajectory Tracking Controller Results

In the first evaluation, the rigid mode's trajectory tracking is simulated and experimented with. The desired trajectory and controller/observer gains are defined as follows:

$$x_d = \begin{bmatrix} 100\sin 2t + 50 \\ 75\sin\left(2t + \pi/2\right) + 275 \end{bmatrix} (mm), \quad w_{r1} = 5, \quad w_{s1} = 5, \quad \alpha_1 = 1 \tag{4.118}$$

where $x_d$ defines a circular path in workspace.

Regarding the simulation results, the followed path by the end-effector and the desired path are compared in Figure 4.9a. The initial position of the end-effector is located at $\approx (50, 310)mm$. Since the initial conditions of the manipulator and desired trajectory are not equal, significant errors are recorded at the beginning of the simulation for both end-effector trajectory tracking and link's velocity observer errors as shown in Figure 4.9b and c. However, the tracking and observation errors approach or oscillate around zero, which complies with the stability condition of the closed-loop system. (Note that links'

velocity observer performance is compared over actual and estimated joint positions in Figure 4.9c.) Also, the performance of the observer is evaluated by applying zero-order-hold to joint position sensors in a simulated model with a 100 Hz sampling rate. However, no significant difference is recorded. The controller signal is presented in Figure 4.9d.

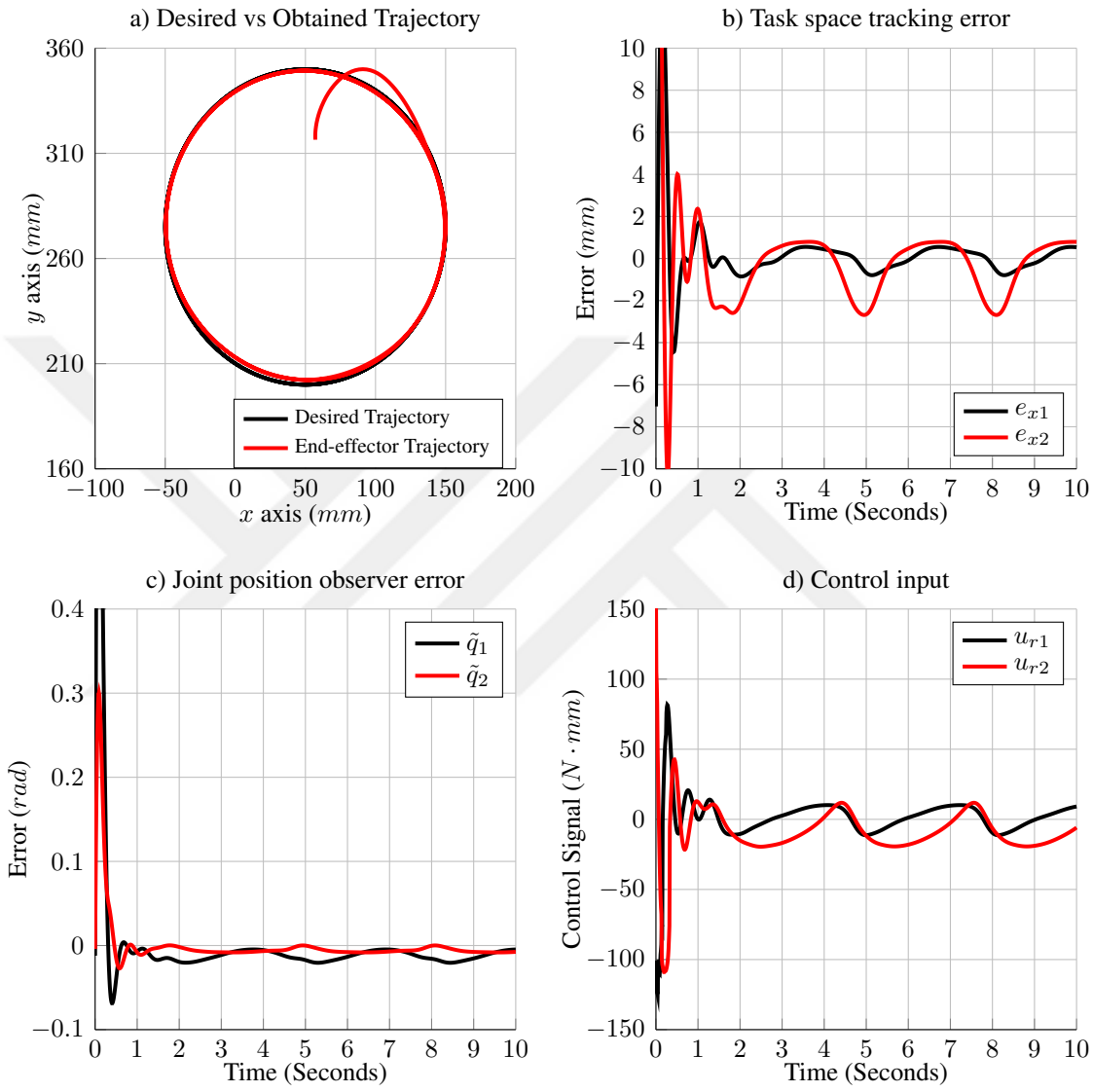



Figure 4.9. Trajectory tracking control simulation results.

The experimental results are presented in Figure 4.10. In order to avoid mechanical failures in the system, the actuators are slowly enabled. Thus, initial high-control signals are alleviated. Hence, the results are presented when they reach a steady state.

It should be noted that the experiment setup may contain impurities due to the manufacturing quality. Hence, the experiment and simulations may only partially validate each other. For instance, in Figure 4.10a, desired and obtained trajectories are presented.

It is evident that there are vibrations at the end-effector when it is close to the actuators (or the origin). These unknown impurities might cause it. It is possible to avoid these vibrations by reducing the controller and observer gains, thus reducing the sensitivity of the closed-loop system to unknowns. This, however, degrades the tracking performance, as well. Besides the vibration, overall tracking performance is satisfactory, which can be understood by low error as shown in Figure 4.10b. Velocity observer also closely tracks the actual link velocity as shown in Figure 4.10c. Finally, control signals are presented in Figure 4.10d, and as expected, the torque levels do not surpass $\approx 100N \cdot mm$ level, which means it does not enter flexible mode during motion.

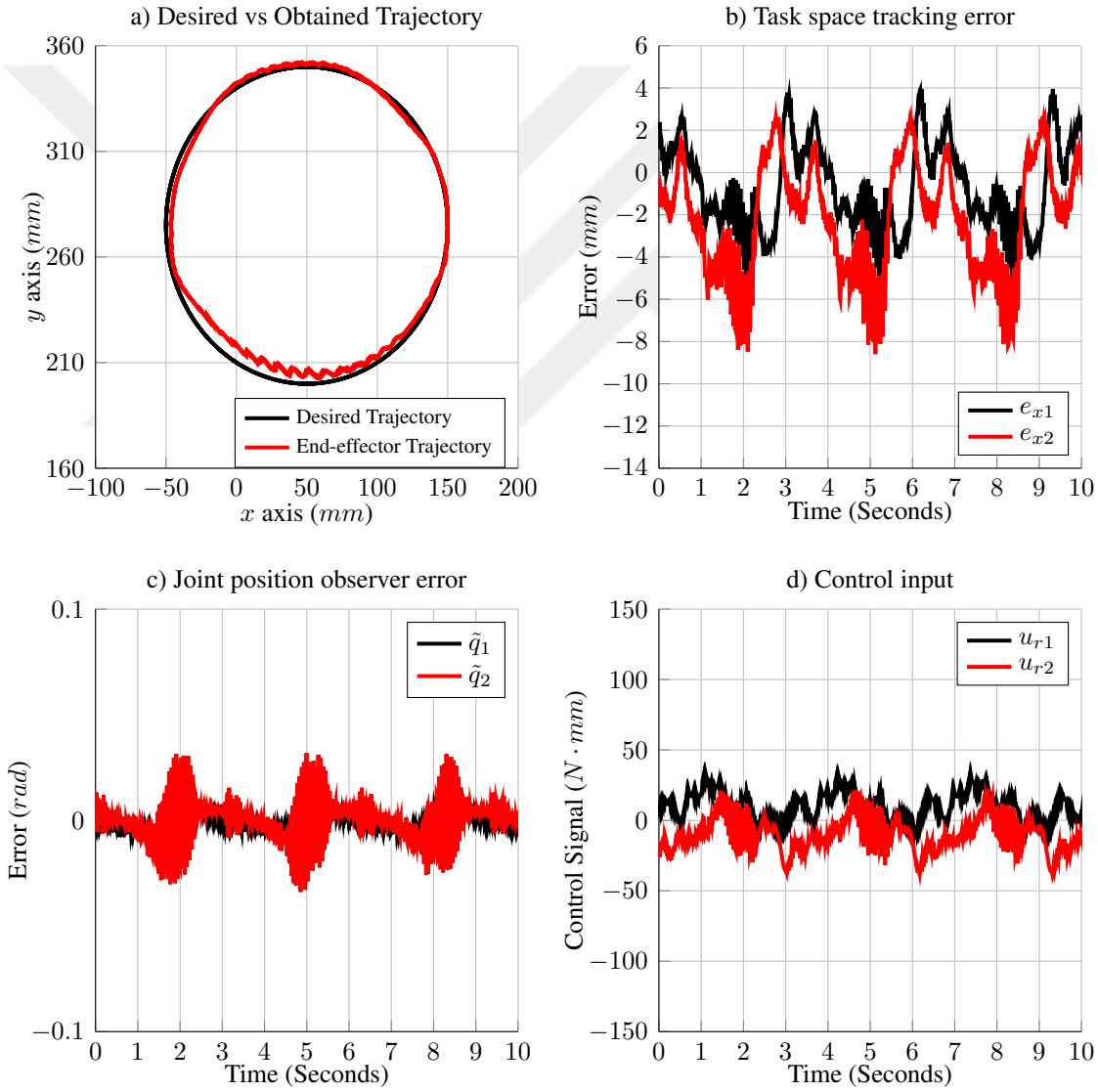



Figure 4.10. Trajectory tracking control experiment results.

### 4.4.3. Impedance Controller Results

The desired trajectory is kept the same as in Equation 4.118. In the simulation, the end-effector is constrained by a spring/damper to generate resistance at the end-effector and make the robot enter flexible mode. Here, the aim is to display the system's natural impedance; hence, the controller in Equation 4.62 is used. The observer gains for actuator velocity estimation and switch gain are selected as follows:

$$w_{s2} = 2, \quad \alpha_2 = 1, \quad \alpha_4 = 100 \tag{4.119}$$

In Figure 4.11a, the desired joint space angles and actuator angles are shown. Figure 4.11b presents the torque observer and control signal. Due to the robot's low speed and the actuators' low inertia, the difference turns out to be small. Hence, even without the $\tau_m \approx u_f$ assumption in Equation 4.59, the dynamics of the actuator might be neglected for low-speed interactions. Nonetheless, actuator linearization enhances the overall performance, albeit slightly. Figure 4.11c shows the actuator position and observed position where no noteworthy difference was recorded. The switching for the actuator with $q_{m1}$ variable is shown in Figure 4.11d. The switches occur at the specified torque levels.

According to the closed-loop system's desired impedance, if the controller perfectly displays the system's natural impedance, then the actuator angle ($q_m$) should closely track the desired angle ($q_d$). Therefore, the performance is evaluated over how close the actuator follows the desired path as shown in Figure 4.11a. It is immediately observed that the obtained performance is not what is expected. Nonetheless, the source of the performance issues is not the designed controller but the smoothness of the controller switch. The switch action for one of the actuators' control signals is shown in Figure 4.11d. For instance, the activation ratio of the trajectory tracking controller is around 10% while the impedance controller is active with 90% of its power in 0-1 seconds time intervals. This 10% partial activation of the trajectory tracking controller contributes more torque than necessary, thus causing a low performance in the desired impedance. The problem can be easily avoided by increasing the smoothness gain $\alpha_4$. In Figure 4.12, the performance of the impedance controller and switch status is shown for $\alpha_4 = 1000$, and this time, the actuator closely follows the desired angles, meaning the controller displays the desired

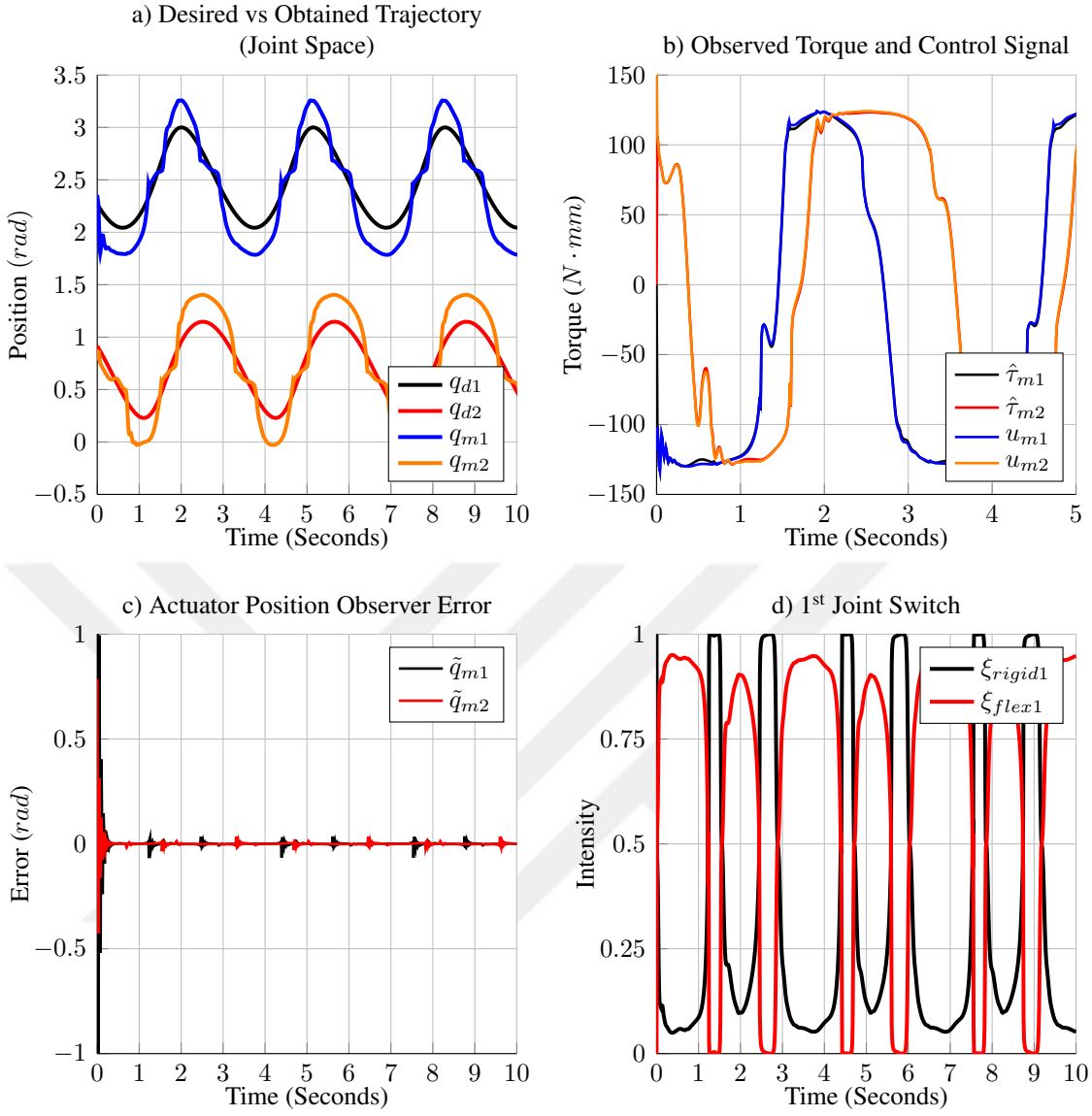



Figure 4.11. Impedance controller simulation results.

impedance.

In the simulation, the selection of high smoothness gain does not introduce any problem. Still, in experiments, this should be avoided for stability concerns because the greater the gain, the quicker the switching and, therefore, the sudden transition between the controllers. Thus, the problem is addressed with a different approach that is slightly modifying the controller in Equation 4.62 as follows:

$$u_f = G + \boldsymbol{B}_r \dot{q}_d + 2\boldsymbol{K}(q_d - q) - n \tag{4.120}$$

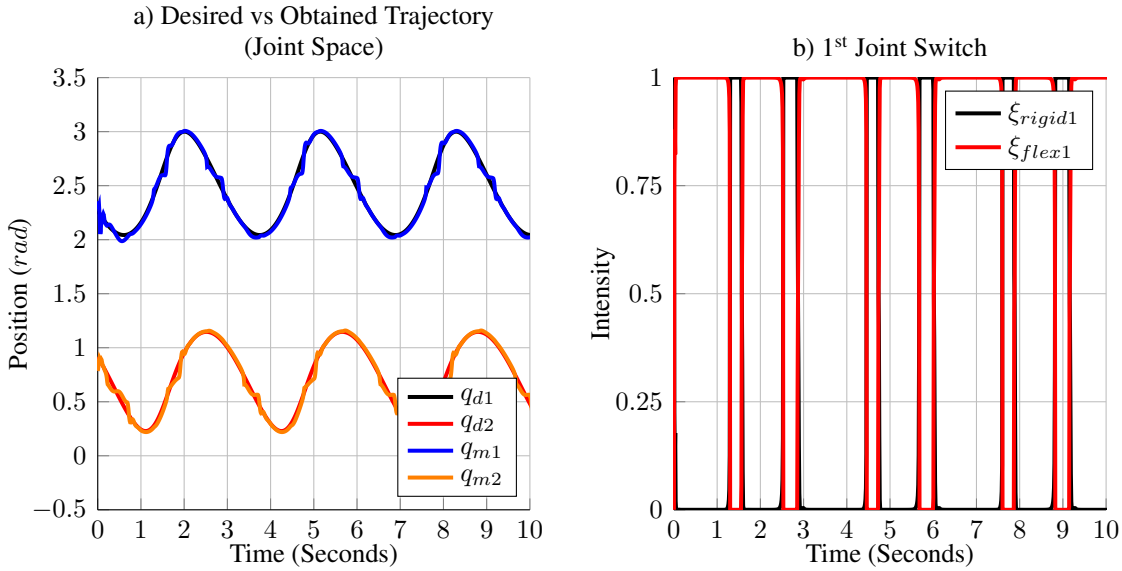



Figure 4.12. Impedance controller simulation results with high switch gain ($\alpha_4 = 1000$).

here, the gain of 2 is added in accordance with the trials and errors on the experiment setup. What it does is increase the intensity of the torque signal generated by the impedance controller. That way, 10% contribution of the trajectory tracking controller and 90% contribution of the impedance controller add up to the required torque for making the actuator follow the desired joint angle. Similar action could also be taken in the trajectory tracking controller by reducing its excessive control signal power instead of increasing the power of the impedance controller. However, this might limit the maximum torque output that can be generated by trajectory tracking, thus permanently blocking the way to reach the torque levels to enter flexible mode and activate the impedance controller. Also, this may lead to lowered tracking performance in rigid mode.

### 4.4.4. Hybrid Controller Results

Next, the hybrid controller is simulated on flat and bumpy surfaces. The assigned task is tracking motion along the y-axis and applying force along the negative x-axis. The desired trajectory, force, and required gains are defined as follows:

$$x_d = \begin{bmatrix} 50 \\ 75\sin(2t + \pi/2) + 275 \end{bmatrix} (mm), \quad F_d = \begin{bmatrix} -1 \\ 0 \end{bmatrix} (N), \quad \boldsymbol{D} = \begin{bmatrix} 0 & 0 \\ 0 & 1 \end{bmatrix} \tag{4.121}$$

$$w_{r2} = 10, \quad w_{s3} = 10, \quad \alpha_3 = 9, \quad \alpha_5 = 100, \quad \zeta_{e_{xd}} = 50(mm) \tag{4.122}$$

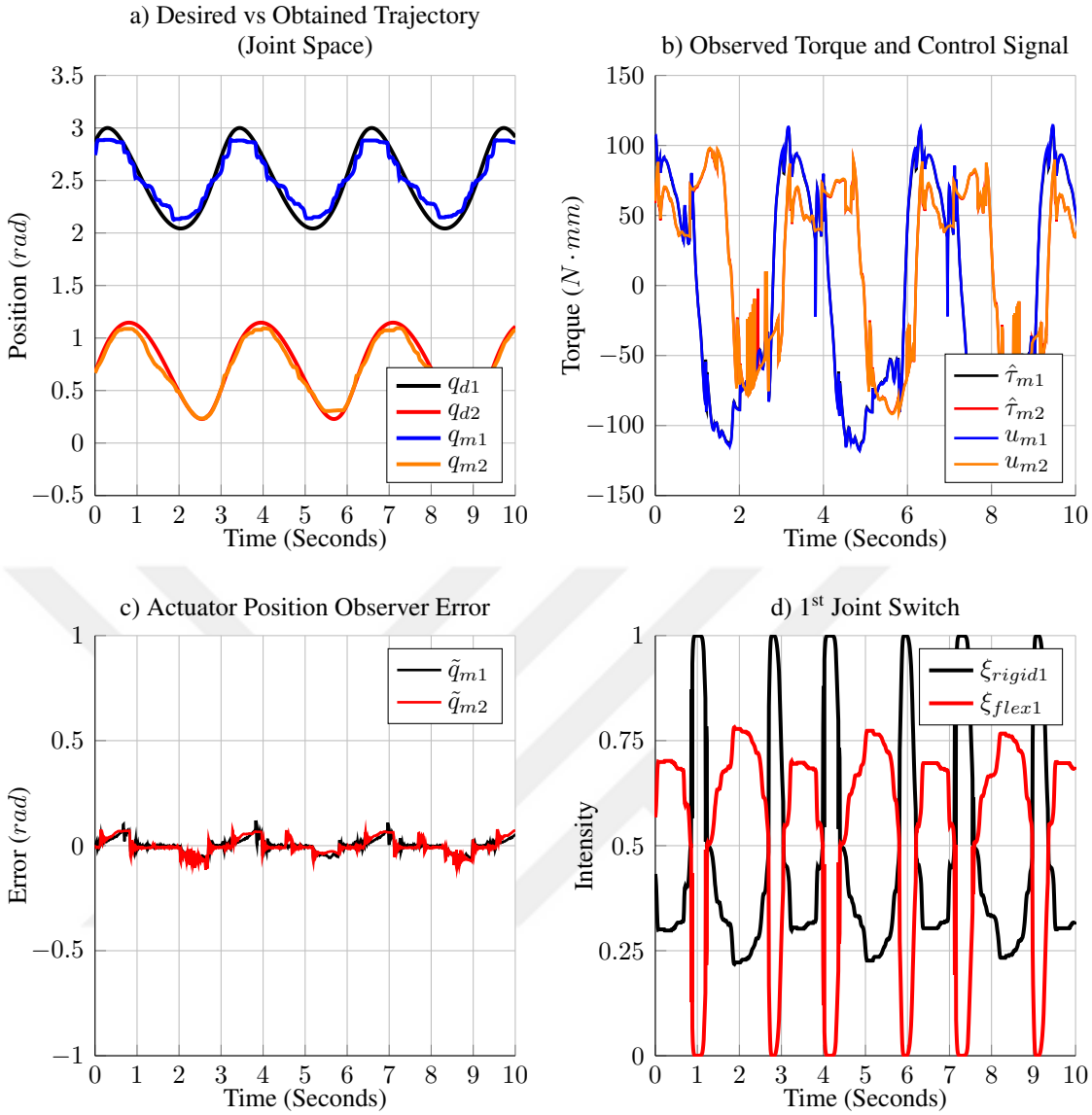



Figure 4.13. Impedance controller experiment results.

The results are shown in Figure 4.14a for flat and Figure 4.15a for bumpy surfaces. Figure 4.14b and Figure 4.15b show the applied force to the environment. Estimated force is computed through the deflections on the flexible joint and stiffness model, while measured force is directly obtained from the interaction surface in simulation. Figure 4.14c and Figure 4.15c present the trajectory tracking error, which is along the y-axis only. Figure 4.14d and Figure 4.15d show the state of the switches.

As expected, it is easier to satisfy the desires of a flat surface for both trajectory tracking and applying force. The initial large errors before reaching the flat surface are caused by the initial conditions of the controller and the simulated model not being met.

However, the steady-state case does not present any irregularity. The motion and force demands are satisfied properly, and the trajectory tracking switch is only active at the beginning of the simulation, meaning during the hybrid operation, the manipulator never fails to follow the desired path at all.

On the other hand, a bumpy surface is itself an obstacle and, therefore, prevents smooth motion and force application. Because of that, the trajectory tracking switch is partially activated for bumpy surfaces. The partial activation of trajectory tracking makes the robot overcome the obstacle because, in trajectory tracking, the desired position contains both x-axis and y-axis components. When both switches (trajectory tracking and hybrid) are partially active, the robot tries to reduce not only the vertical positioning error but also the horizontal positioning error. This leads to an inconsistency in contact force. Nonetheless, it should also be noted that the rigid contact surface design parameters in a simulation environment may also not be the part but the source of this inconsistency.

In force/position controller experiments, the desired trajectory and other gains are updated as follows:

$$x_d = \begin{bmatrix} 0 \\ 50\sin\left(2t + \pi/2\right) + 275 \end{bmatrix} (mm), \quad F_d = \begin{bmatrix} -0.5 \\ 0 \end{bmatrix} (N) \tag{4.123}$$

$$w_{r2} = 8, \quad w_{s3} = 5, \quad \alpha_3 = 6, \quad \alpha_5 = 100, \quad \zeta_{e_{xd}} = 50(mm) \tag{4.124}$$

The results regarding the experiment are shown in Figure 4.16. In Figure 4.16a, desired and obtained end-effector positions are presented. It is quickly evident that the end-effector can follow about half of the desired motion along the y-axis. As the end-effector gets closer to the origin, the error in position increases, as shown in Figure 4.16c. It is estimated that the problem occurs due to friction and stiction effects that are either caused by the surface/end-effector contact or the internal mechanics of the robot. Higher gains were tried but to no avail, since this action led the system to instability. High gains lead to higher torque generation on the actuators. These causes accumulation of energy on the flexible joints. The sudden evacuation of the energy drives the system to an unstable state the instant the stiction is overcome.

Figure 4.16b presents the estimated applied force to an environment that is computed from the deflections of the flexible joints and the forward kinematics. Figure 4.16d shows the switch state. As the tracking error approaches the limit $\zeta_{e_{xd}} = 50(mm)$ as

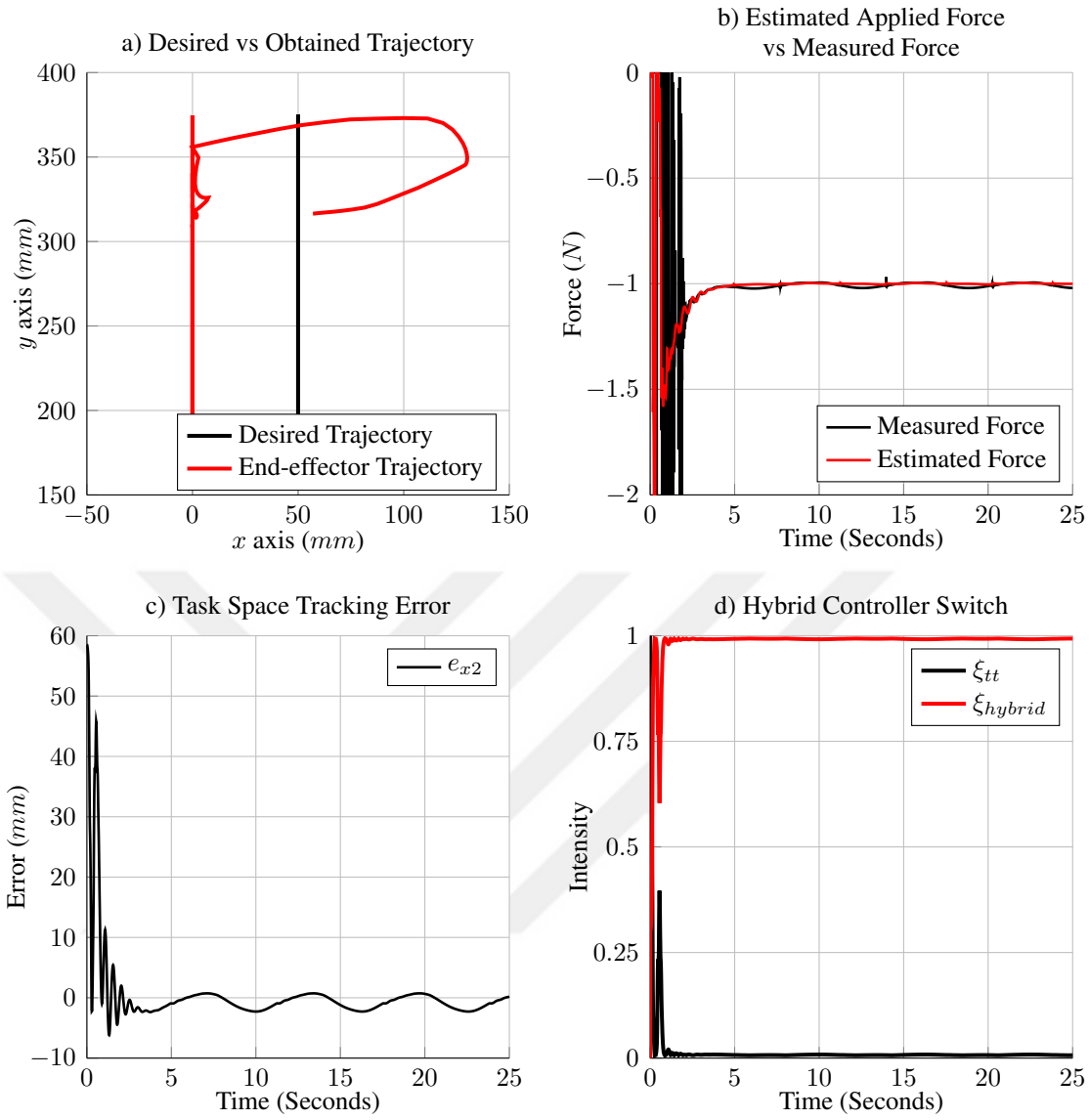



Figure 4.14. Hybrid control results on a flat surface (Simulation).

shown in Figure 4.16c, the switching is partially activated. This leads to a slight reduction in applied force (i.e., around 2.5 seconds) since the trajectory tracking controller is partially activated.

In order to clarify the source of the tracking performance issues, the interaction forces are reduced to $F_d = [-0.1, 0]^T$ and the experiment is carried out again, and the results are presented in Figure 4.17. It is clear that the tracking performance is enhanced, which addresses the fact that the problems in the previous experiment were indeed caused by friction/stiction. The end-effector trajectory is not parallel to the desired trajectory because of the misplacement of the obstacle in task space.

Another experiments is conducted with the update $F_d = [-0.1, 0]^T$ and $\zeta_{e_{xd}} =$

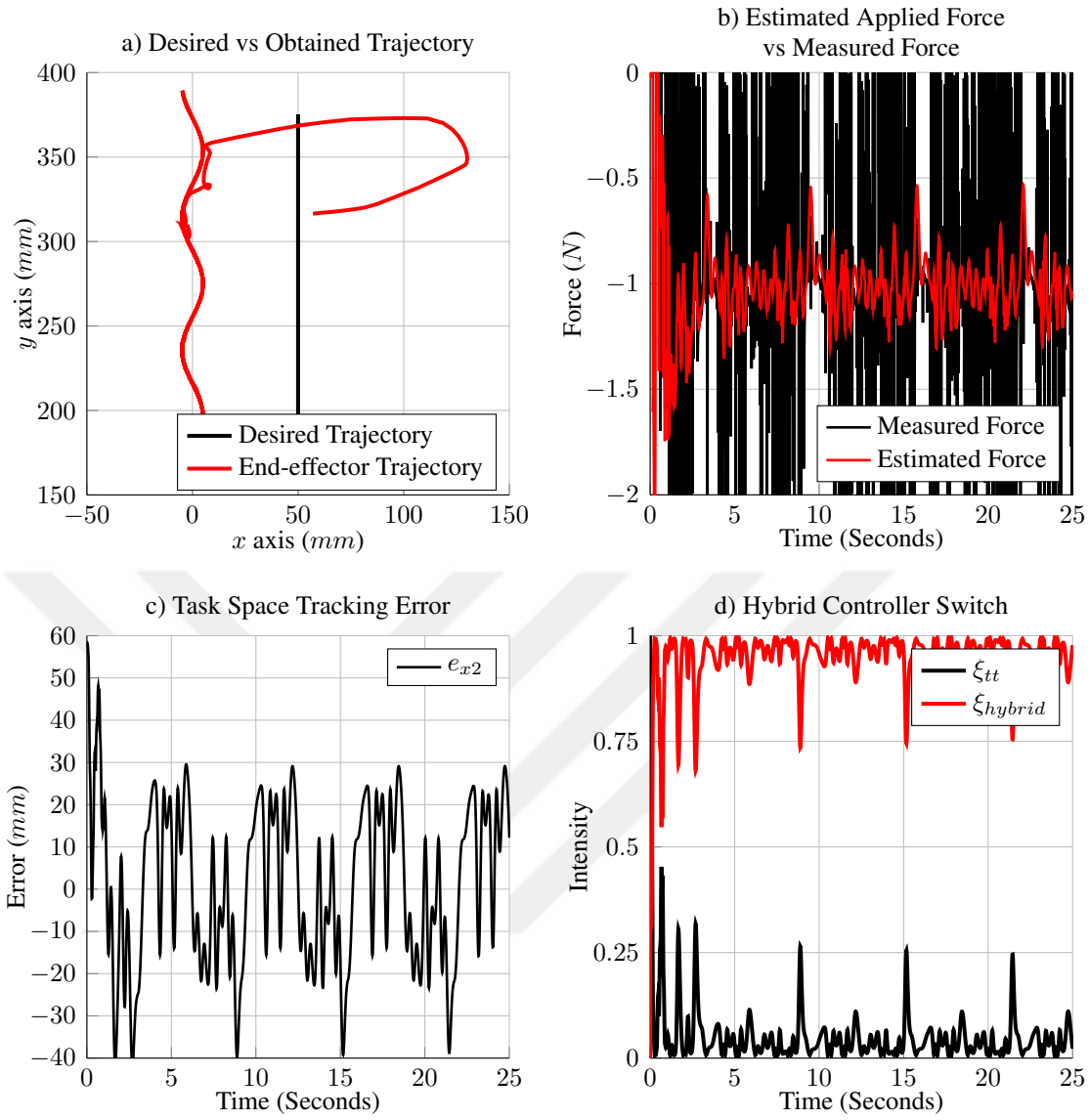



Figure 4.15. Hybrid control results on a bumpy surface (Simulation).

$30(mm)$ for observing the switching performance. The position of the end-effector and switch intensity are shown in Figure 4.18. Since the trajectory tracking error in the previous experiment (shown in Figure 4.17c) is in close range of $\zeta_{e_{xd}} = 30(mm)$, the switching between the hybrid control and trajectory tracking control is partially activated. Because of this partial activation, the end-effector momentarily tries to reach the desired trajectory that is located at x=0 mm. Hence, for short duration of time, the end-effector detaches from the surface and returns after a while when the switch turns in favor of the hybrid controller. Therefore, the followed path by the end-effector exhibits a bumpy path.

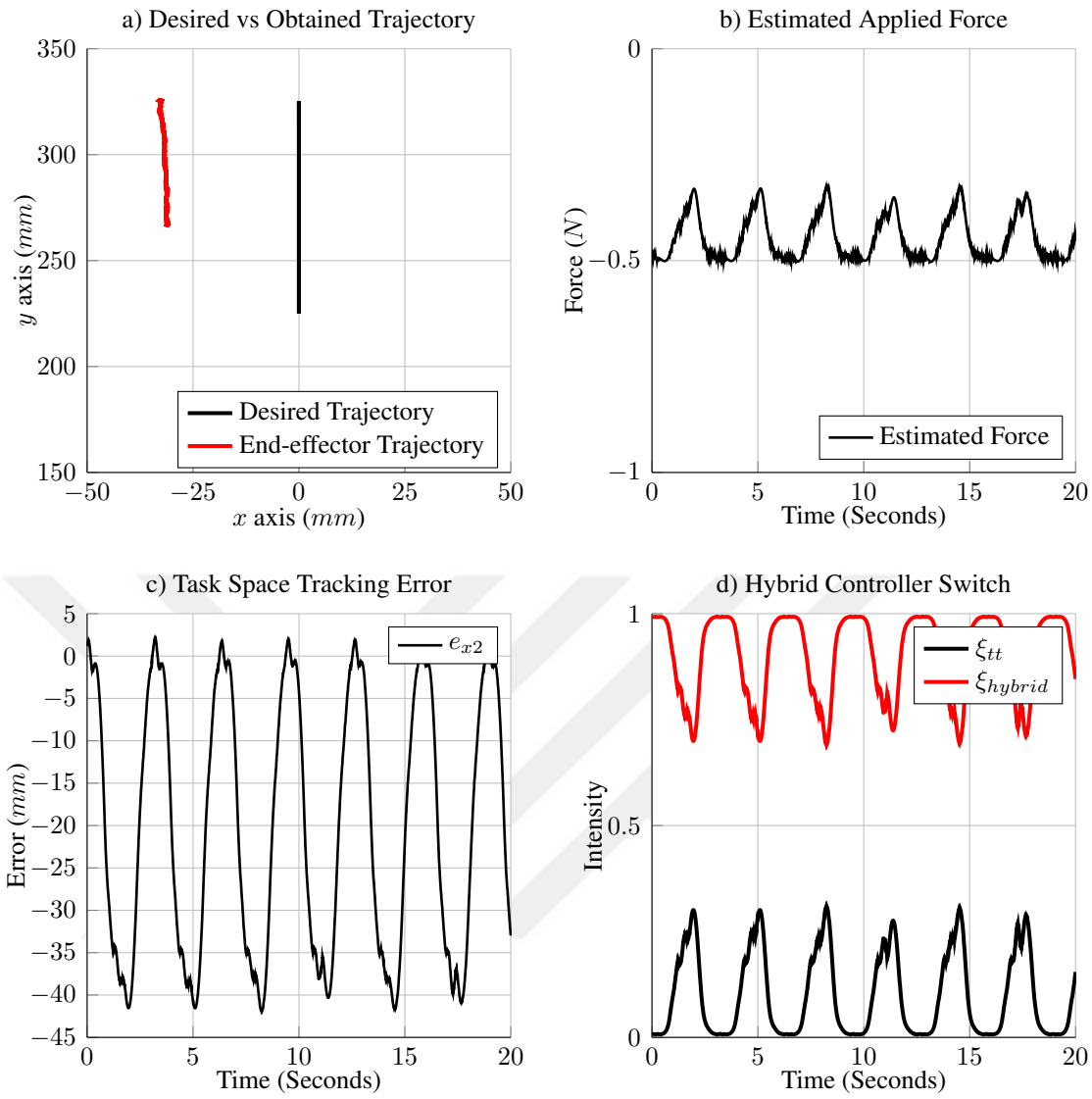



Figure 4.16. Hybrid control results on a flat surface (Experiment).

## 4.5. Conclusion

This study addresses the control problem of a flexible robot that includes a rigid mode. The robot requires two dynamic models: a rigid manipulator model and a flexible manipulator model. The torsion on the joints determines which mode is active. Three separate tasks are assigned to exploit the versatility of each mode. Rigid mode is reserved for trajectory tracking only. A Lyapunov-based controller and a velocity observer are designed to achieve this aim. For flexible mode, an impedance and a hybrid controller are developed. The impedance controller and hybrid controller use the principle of passivity to compensate for the actuator dynamics. Another velocity observer for the actuator is

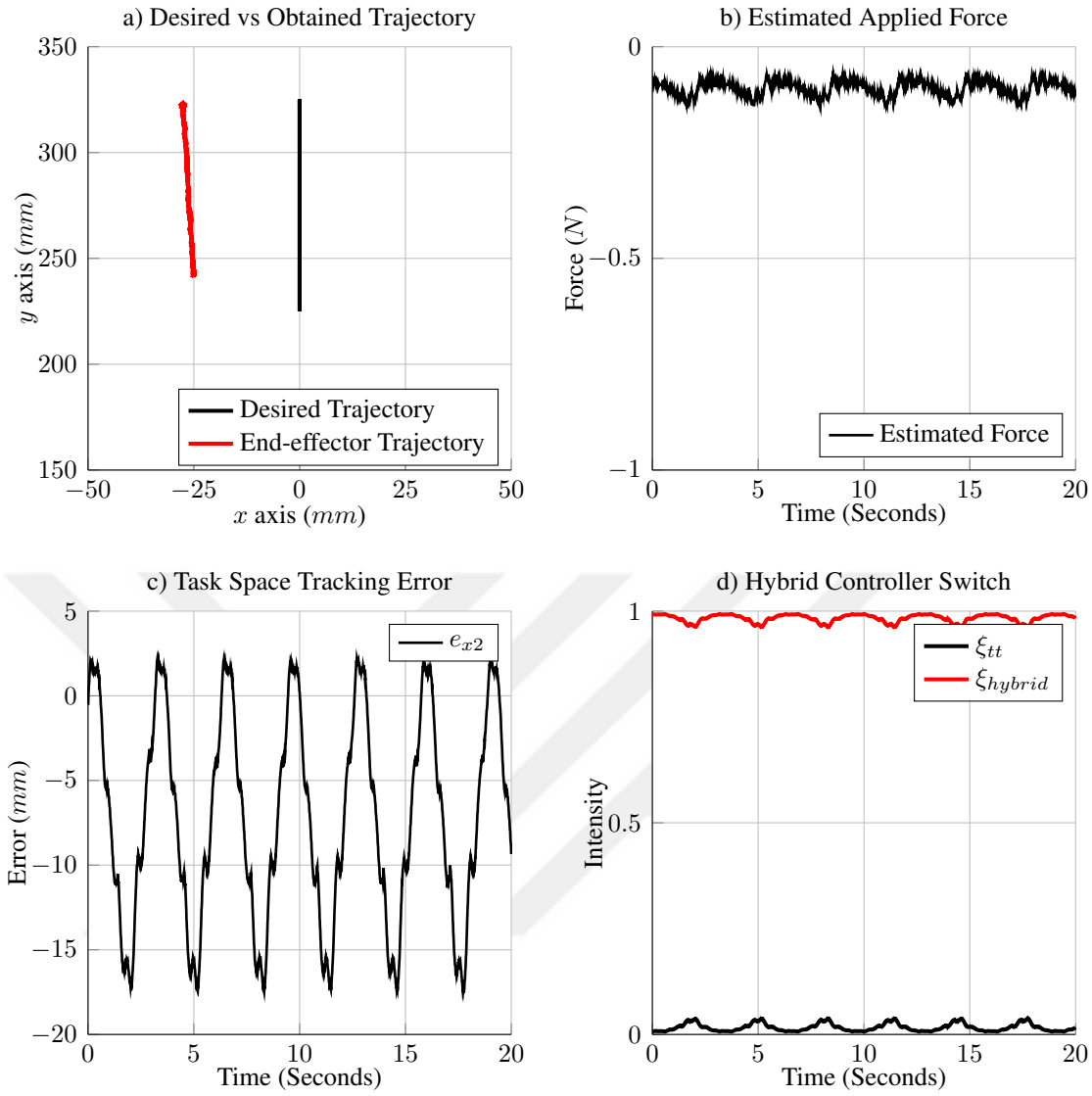



Figure 4.17. Hybrid control results on a flat surface (Experiment for $F_d = [-0.1, 0]^T$ and $\zeta_{e_{xd}} = 50(mm)$).

designed for the partial compensation of viscous friction, which belongs to the actuator dynamics. Since the mass and the friction of the actuators are small, it is concluded that the actuator dynamics can also be neglected. The desired closed-loop impedance is desired to be equal to the robot's impedance because the robot is already manufactured with the desired impedance. This leads to dodging the necessity of a velocity observer of the robot's links, thus improving stability. Finally, the hybrid controller is developed for trajectory tracking in task space and applying the desired force to the environment. Due to the selection matrix's nature, the trajectory tracking controller is designed as if there is no selection matrix, but its rank deficiency effect is implemented in the final controller later

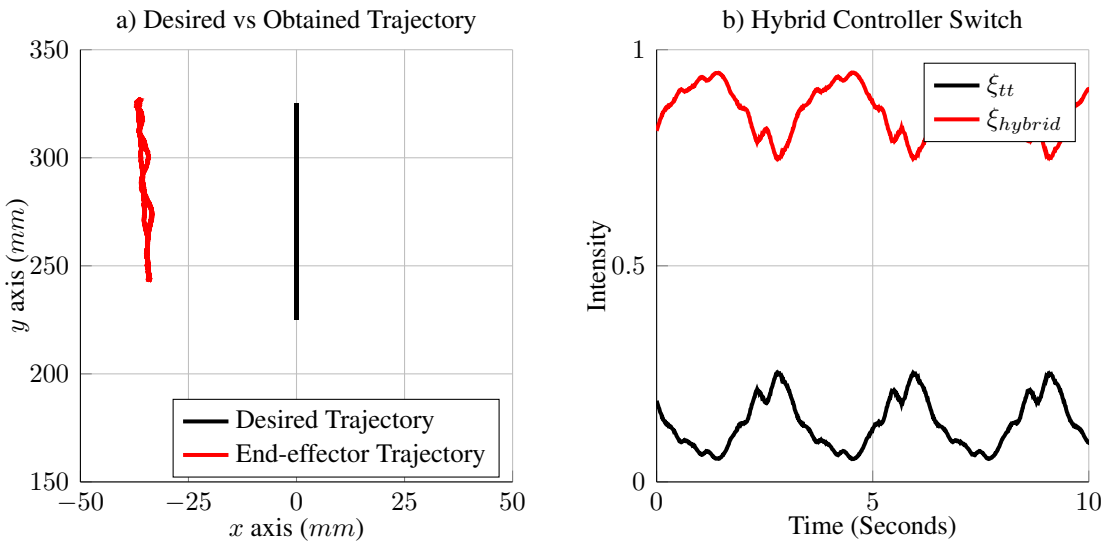



Figure 4.18. Hybrid control results on a flat surface (Experiment for $F_d = [-0.1, 0]^T$ and $\zeta_{e_{xd}} = 30(mm)$).

on. To achieve the desired trajectory, a link velocity observer that runs in flexible mode is designed. A set of smooth switches that are based on sigmoid functions are designed for stable transition between the controllers. All closed loops with different controllers stabilize and conduct their desired tasks. Only the hybrid controller, when interacting with a bumpy surface, suffers some performance issues, but it is mainly an optimization problem of controller and observer gains in the system.

# CHAPTER 5

# CONCLUSION

This dissertation makes contributions to three critical aspects of flexible robots: modeling, control, and design. Each field accompanies unique challenges: vibrations in high acceleration-induced industrial robots, inherently safe flexible joint designs in human-robot interaction, and the control of robots with variable stiffness properties. The dissertation proposes advancements in modeling, mechanical design, and control for specific case studies to address these challenges.

First, a new stiffness modeling method was proposed for an industrial over constrained parallel robot that operates under high acceleration. The stiffness model accurately estimates compliant deflections for given forces. Also, the model is constructed considering the internal stresses. The model enables high-frequency computations at 10 kHz, which makes it suitable for real-time applications. With an adjustment in the input trajectory with the aid of the stiffness model, the vibration effects on positioning accuracy can be minimized effectively.

Second, a novel flexible revolute joint was designed to ensure inherent safety in physical human-robot interactions. The flexible joint passively softens based on applied torque with distinct stiffness regions (rigid, stiff, and soft). The design guarantees the robot's safe operation without compromising free-motion performance at low torque levels. Especially displays compliant deflection under excessive loads, which ensures safety. The flexible joint was successfully implemented as a series elastic actuator in a five-bar mechanism.

Finally, a unifying control framework was devised to control the five-bar mechanism that is made of the proposed novel softening flexible joint. The Lyapunov-based controllers are developed for trajectory tracking, impedance control, and hybrid force/position control. This approach enables the robot to perform various tasks in rigid, stiff, and soft regions. Smooth transitions between controllers guarantee stability and safety. The proposed control framework was validated in simulations and experiments.

In conclusion, this dissertation has successfully combined theoretical approaches and practical solutions to address the challenges of flexible robot manipulators. The stiff-

ness model, flexible joint design, and controllers provide a comprehensive solution for improving positioning performance, ensuring safety, and achieving versatile control. These contributions pave the way for the development of high-performance, safe, and adaptive robotic systems. In particular, for the environments that require precise interaction with humans and complex tasks. Future work may extend these findings to different robotic architectures and further enhance the integration of flexibility in robotic systems.

# REFERENCES


Abdallah, Chaouki, Darren M Dawson, Peter Dorato, and Mohammad Jamshidi 1991. Survey of robust control for rigid robots. *IEEE Control Systems Magazine 11*(2), 24–30.

Agarwal, Priyanshu and Ashish D Deshpande 2017. Series elastic actuators for small-scale robotic applications. *Journal of Mechanisms and Robotics 9*(3), 031016.

Ahmad, Mohd Ashraf and Zaharuddin Mohamed 2009. Techniques of vibration and end-point trajectory control of flexible manipulator. In *2009 6th International Symposium on Mechatronics and its Applications*, pp. 1–6. IEEE.

Alandoli, Esmail Ali and Tian Soon Lee 2020. A critical review of control techniques for flexible and rigid link manipulators. *Robotica 38*(12), 2239–2265.

Albu-Schaffer, Alin, Christian Ott, and Gerd Hirzinger 2004. A passivity based cartesian impedance controller for flexible joint robots-part ii: Full state feedback, impedance design and experiments. In *IEEE International Conference on Robotics and Automation, 2004. Proceedings. ICRA'04. 2004*, Volume 3, pp. 2666–2672. IEEE.

Albu-Schäffer, Alin, Christian Ott, and Gerd Hirzinger 2007. A unified passivity-based control framework for position, torque and impedance control of flexible joint robots. *The international journal of robotics research 26*(1), 23–39.

Annisa, J, IZ Mat Darus, MO Tokhi, and S Mohamaddan 2018. Implementation of pid based controller tuned by evolutionary algorithm for double link flexible robotic manipulator. In *2018 International Conference on Computational Approach in Smart Systems Design and Applications (ICASSDA)*, pp. 1–5. IEEE.

Ataka, Ahmad, Taqi Abrar, Fabrizio Putzu, Hareesh Godaba, and Kaspar Althoefer 2020. Model-based pose control of inflatable eversion robot with variable stiffness. *IEEE Robotics and Automation Letters 5*(2), 3398–3405.

Awad, Mohammad I, Dongming Gan, Marco Cempini, Mario Cortese, Nicola Vitiello, Jorge Dias, Paolo Dario, and Lakmal Seneviratne 2016. Modeling, design & characterization of a novel passive variable stiffness joint (pvsj). In *2016 IEEE/RSJ International Conference on Intelligent Robots and Systems (IROS)*, pp. 323–329. IEEE.

Bar-Kana, Izhak and Howard Kaufman 1993. Simple adaptive control of large flexible space structures. *IEEE Transactions on Aerospace and Electronic Systems 29*(4), 1137–1149.

Bern, James M, Yannick Schnider, Pol Banzet, Nitish Kumar, and Stelian Coros 2020. Soft robot control with a learned differentiable model. In *2020 3rd IEEE International Conference on Soft Robotics (RoboSoft)*, pp. 417–423. IEEE.

Best, Charles M, Morgan T Gillespie, Phillip Hyatt, Levi Rupert, Vallan Sherrod, and

Marc D Killpack 2016. A new soft robot control method: Using model predictive control for a pneumatically actuated humanoid. *IEEE Robotics & Automation Magazine 23*(3), 75–84.

Bhagat, Sarthak, Hritwick Banerjee, Zion Tsz Ho Tse, and Hongliang Ren 2019. Deep reinforcement learning for soft, flexible robots: Brief review with impending challenges. *Robotics 8*(1), 4.

Blanc, Loïc, Alain Delchambre, and Pierre Lambert 2017. Flexible medical devices: Review of controllable stiffness solutions. In *Actuators*, Volume 6, pp. 23. MDPI.

Briat, Corentin 2017. Dwell-time stability and stabilization conditions for linear positive impulsive and switched systems. *Nonlinear Analysis: Hybrid Systems 24*, 198–226.

Bridges, Michael M, Darren M Dawson, and Chaouki T Abdallah 1995. Control of rigid-link, flexible-joint robots: a survey of backstepping approaches. *Journal of Robotic Systems 12*(3), 199–216.

Bridges, Michael M, Darren M Dawson, Zhihua Qu, and Scott C Martindale 1994. Robust control of rigid-link flexible-joint robots with redundant joint actuators. *IEEE transactions on systems, man, and cybernetics 24*(7), 961–970.

Briot, Sébastien and Ilian A Bonev 2007. Are parallel robots more accurate than serial robots? *Transactions of the Canadian Society for Mechanical Engineering 31*(4), 445–455.

Bruder, Daniel, Brent Gillespie, C David Remy, and Ram Vasudevan 2019. Modeling and control of soft robots using the koopman operator and model predictive control. *arXiv preprint arXiv:1902.02827*.

Calanca, Andrea, Riccardo Muradore, and Paolo Fiorini 2017. Impedance control of series elastic actuators: Passivity and acceleration-based control. *Mechatronics 47*, 37–48.

Cammarata, Alessandro 2016. Unified formulation for the stiffness analysis of spatial mechanisms. *Mechanism and Machine Theory 105*, 272–284.

Cao, Wen-ao and Huafeng Ding 2018. A method for stiffness modeling of 3R2T overconstrained parallel robotic mechanisms based on screw theory and strain energy. *Precision Engineering 51*, 10–29.

Cao, Wen-ao, Huafeng Ding, and Donghao Yang 2017. A method for compliance modeling of five degree-of-freedom overconstrained parallel robotic mechanisms with 3T2R output motion. *Journal of Mechanisms and Robotics 9*(1). 011011.

Cao, Wen-ao, Huafeng Ding, and Weiguo Zhu 2019. Stiffness modeling of overconstrained parallel mechanisms under considering gravity and external payloads. *Mechanism and Machine Theory 135*, 1–16.

Carlson, H. 1978. *Spring Designer's Handbook*, pp. 221–239. Dekker Mechanical Engineering. Taylor & Francis.

Celebi, Besir, Mustafa Yalcin, and Volkan Patoglu 2013. Assiston-knee: A self-aligning knee exoskeleton. In *2013 IEEE/RSJ International Conference on Intelligent Robots and Systems*, pp. 996–1002. IEEE.

Chenevier, Jean, David González, J Vicente Aguado, Francisco Chinesta, and Elías Cueto 2018. Reduced-order modeling of soft robots. *PloS one 13*(2), e0192052.

Cobanoglu, Necati, Kamil Cetin, Enver Tatlicioglu, and Erkan Zergeroglu 2018. A dynamic model free observer based output feedback tracking control of robot manipulators in task-space. In *2018 Annual American Control Conference (ACC)*, pp. 2121–2126. IEEE.

Curran, Simon and David E Orin 2008. Evolution of a jump in an articulated leg with series-elastic actuation. In *2008 IEEE International Conference on Robotics and Automation*, pp. 352–358. IEEE.

Das, Apurba and M Nabi 2019. A review on soft robotics: Modeling, control and applications in human-robot interaction. In *2019 International Conference on Computing, Communication, and Intelligent Systems (ICCCIS)*, pp. 306–311. IEEE.

Dawson, Darren M, Zhihua Qu, and MM Bridges 1993. Hybrid adaptive control for tracking of rigid-link flexible-joint robots. In *IEE Proceedings D (Control Theory and Applications)*, Volume 140, pp. 155–159. IET.

De Luca, Alessandro, Alberto Isidori, and Fernando Nicolo 1985. Control of robot arm with elastic joints via nonlinear dynamic feedback. In *1985 24th IEEE conference on decision and control*, pp. 1671–1679. IEEE.

de Normalización, Organización Internacional 2016. *ISO-TS 15066: Robots and robotic devices: Collaborative robots*, pp. 17–19. ISO.

de Queiroz, Marcio S, S Donepudi, T Burg, and Darren M Dawson 1998. Model-based control of rigid-link flexible-joint robots: an experimental evaluation. *Robotica 16*(1), 11–21.

Della Santina, Cosimo, Christian Duriez, and Daniela Rus 2023. Model-based control of soft robots: A survey of the state of the art and open challenges. *IEEE Control Systems Magazine 43*(3), 30–65.

Della Santina, Cosimo, Robert K Katzschmann, Antonio Bicchi, and Daniela Rus 2020. Model-based dynamic feedback control of a planar soft robot: trajectory tracking and interaction with the environment. *The International Journal of Robotics Research 39*(4), 490–513.

Dhatt, Gouri, Emmanuel LefranÃ, and Gilbert Touzot 2012. *Finite element method*. John Wiley & Sons.

Ding, Jianzhong, Chunjie Wang, and Hongyu Wu 2018. Accuracy analysis of redundantly actuated and overconstrained parallel mechanisms with actuation errors. *Journal of Mechanisms and Robotics 10*(6). 061010.

Ding, Shuai, Jinzhu Peng, Hui Zhang, and Yaonan Wang 2021. Neural network-based adaptive hybrid impedance control for electrically driven flexible-joint robotic manipulators with input saturation. *Neurocomputing 458*, 99–111.

Dixon, Warren E, Erkan Zergeroglu, Marcio S de Queiroz, and Darren M Dawson 1998. Global output feedback tracking control for rigid-link flexible-joint robots. In *Proceedings. 1998 IEEE International Conference on Robotics and Automation (Cat. No. 98CH36146)*, Volume 1, pp. 498–503. IEEE.

Dos Santos, Wilian M, Glauco AP Caurin, and Adriano AG Siqueira 2017. Design and control of an active knee orthosis driven by a rotary series elastic actuator. *Control Engineering Practice 58*, 307–318.

Efafi, M, SAA Hosseini, and H Tourajizadeh 2022. Robust control and vibration reduction of a 3d nonlinear flexible robotic arm. *Iranian Journal of Science and Technology, Transactions of Mechanical Engineering 46*(4), 1157–1173.

Fang, Yi, Jie Hu, Wenhai Liu, Quanquan Shao, Jin Qi, and Yinghong Peng 2019. Smooth and time-optimal s-curve trajectory planning for automated robots and machines. *Mechanism and Machine Theory 137*, 127–153.

Ghali, Amin, Adam Neville, and Tom Brown 2017. *Structural analysis: a unified classical and matrix approach*. Crc Press.

Ghali, Amin, Adam Neville, and Tom G Brown 2014. *Structural Analysis: A Unified Classical and Matrix Approach*. CRC Press.

Görgülü, İbrahimcan, Giuseppe Carbone, and Mehmet İsmet Can Dede 2020. Time efficient stiffness model computation for a parallel haptic mechanism via the virtual joint method. *Mechanism and Machine Theory 143*, 103614.

Gosselin, Clement 1990. Stiffness mapping for parallel manipulators. *IEEE Transactions on Robotics and Automation 6*(3), 377–382.

Gosselin, CM 2002. Stiffness analysis of parallel mechanisms using a lumped model. *International Journal of Robotics and Automation. 17*, 17–27.

Hägele, Martin, Klas Nilsson, J Norberto Pires, and Rainer Bischoff 2016. Industrial robotics. *Springer handbook of robotics*, 1385–1422.

Ham, Ronald, Thomas Sugar, Bram Vanderborght, Kevin Hollander, and Dirk Lefeber 2009. Compliant actuator designs. *IEEE Robotics & Automation Magazine 3*(16), 81–94.

Harib, Khalifa H, Kamal AF Moustafa, AMM Sharif Ullah, and Salah Zenieh 2012.

*Parallel, Serial and Hybrid Machine Tools and Robotics Structures: Comparative Study on Optimum Kinematic Designs*. IntechOpen.

Hoevenaars, Antonius GL, Patrice Lambert, and Just L Herder 2016. Jacobian-based stiffness analysis method for parallel manipulators with non-redundant legs. *Proceedings of the Institution of Mechanical Engineers, Part C: Journal of Mechanical Engineering Science 230*(3), 341–352.

Hong, Seonghun, Changhyun Cho, Hyeongcheol Lee, Sungchul Kang, and Woosub Lee 2017. Joint configuration for physically safe human–robot interaction of serial-chain manipulators. *Mechanism and Machine Theory 107*, 246–260.

Horibe, Takamasa, Emma Treadway, and R Brent Gillespie 2016. Comparing series elasticity and admittance control for haptic rendering. In *Haptics: Perception, Devices, Control, and Applications: 10th International Conference, EuroHaptics 2016, London, UK, July 4-7, 2016, Proceedings, Part I 10*, pp. 240–250. Springer.

Hou, Chia-Wen and Chao-Chieh Lan 2013. Functional joint mechanisms with constant-torque outputs. *Mechanism and Machine Theory 62*, 166–181.

Hu, Bo and Zhen Huang 2016. Kinetostatic model of overconstrained lower mobility parallel manipulators. *Nonlinear Dynamics 86*(1), 309–322.

Huang, Tian, Xingyu Zhao, and David J Whitehouse 2002. Stiffness estimation of a tripod-based parallel kinematic machine. *IEEE Transactions on Robotics and Automation 18*(1), 50–58.

Hyun, Dongjun, Hyun Seok Yang, Jungwan Park, and Youngbo Shim 2010. Variable stiffness mechanism for human-friendly robots. *Mechanism and Machine Theory 45*(6), 880–897.

Ivanov, Radoslav, Taylor J Carpenter, James Weimer, Rajeev Alur, George J Pappas, and Insup Lee 2020. Verifying the safety of autonomous systems with neural network controllers. *ACM Transactions on Embedded Computing Systems (TECS) 20*(1), 1–26.

Ivanov, Radoslav, James Weimer, Rajeev Alur, George J Pappas, and Insup Lee 2019. Verisig: verifying safety properties of hybrid systems with neural network controllers. In *Proceedings of the 22nd ACM International Conference on Hybrid Systems: Computation and Control*, pp. 169–178.

Jafari, Amir, Nikos G Tsagarakis, Irene Sardellitti, and Darwin G Caldwell 2012. A new actuator with adjustable stiffness based on a variable ratio lever mechanism. *IEEE/ASME Transactions on Mechatronics 19*(1), 55–63.

Jin, Hongzhe, Decai Yang, Hui Zhang, Zhangxing Liu, and Jie Zhao 2018. Flexible actuator with variable stiffness and its decoupling control algorithm: Principle prototype design and experimental verification. *IEEE/ASME Transactions on Mechatronics 23*(3), 1279–1291.

Jin, Maolin, Jinoh Lee, and Nikolaos G Tsagarakis 2016. Model-free robust adaptive control of humanoid robots with flexible joints. *IEEE Transactions on Industrial Electronics 64*(2), 1706–1715.

Kampa, Adrian 2018. The review of reliability factors related to industrial robots. *Robotics and Automation Engineering Journal 3*(5), 1–5.

Kashiri, Navvab, Andy Abate, Sabrina J Abram, Alin Albu-Schaffer, Patrick J Clary, Monica Daley, Salman Faraji, Raphael Furnemont, Manolo Garabini, Hartmut Geyer, et al. 2018. An overview on principles for energy efficient robot locomotion. *Frontiers in Robotics and AI 5*, 129.

Khalil, H.K. 2002. *Nonlinear Systems*, pp. 589–604. Pearson Education. Prentice Hall.

Khorasani, Khashayar and M Spong 1985. Invariant manifolds and their application to robot manipulators with flexible joints. In *Proceedings. 1985 IEEE International Conference on Robotics and Automation*, Volume 2, pp. 978–983. IEEE.

Kiang, Chang Tai, Andrew Spowage, and Chan Kuan Yoong 2015. Review of control and sensor system of flexible manipulator. *Journal of Intelligent & Robotic Systems 77*, 187–213.

Kim, Byeong-Sang and Jae-Bok Song 2010. Hybrid dual actuator unit: A design of a variable stiffness actuator based on an adjustable moment arm mechanism. In *2010 IEEE International Conference on Robotics and Automation*, pp. 1655–1660. IEEE.

Kim, Hwi-Su, Jung-Jun Park, Jae-Bok Song, and Jin-Ho Kyung 2010. Design of safety mechanism for an industrial manipulator based on passive compliance. *Journal of mechanical science and technology 24*, 2307–2313.

Kim, Min Jun, Fabian Beck, Christian Ott, and Alin Albu-Schäffer 2019. Model-free friction observers for flexible joint robots with torque measurements. *IEEE Transactions on Robotics 35*(6), 1508–1515.

Kim, Min S and Jin S Lee 2004. Adaptive tracking control of flexible-joint manipulators without overparametrization. *Journal of Robotic Systems 21*(7), 369–379.

Kiper, Gökhan, Mehmet İsmet Can Dede, Emre Uzunoğlu, and Ercan Mastar 2015. Use of hidden robot concept for calibration of an over-constrained mechanism. In *14th International Federation for the Promotion of Mechanism and Machine Science World Congress*, Volume 5, pp. 2822–2826. IFToMM.

Klimchik, Alexandr 2011. *Enhanced stiffness modeling of serial and parallel manipulators for robotic-based processing of high performance materials*. Ph. D. thesis, Ecole Centrale de Nantes (ECN); Ecole des Mines de Nantes.

Klimchik, Alexandr, Damien Chablat, and Anatol Pashkevich 2014. Stiffness modeling for perfect and non-perfect parallel manipulators under internal and external loadings. *Mechanism and Machine Theory 79*, 1–28.

Klimchik, Alexandr, Anatol Pashkevich, and Damien Chablat 2019a. Fundamentals of manipulator stiffness modeling using matrix structural analysis. *Mechanism and Machine Theory 133*, 365–394.

Klimchik, A, Anatol Pashkevich, and Damien Chablat 2019b. Stiffness modeling of navaro ii transmission system. *IFAC-PapersOnLine 52*(13), 701–706.

Klimchik, Alexandr, Anatol Pashkevich, Damien Chablat, and Geir Hovland 2013. Compliance error compensation technique for parallel robots composed of non-perfect serial chains. *Robotics and Computer-Integrated Manufacturing 29*(2), 385–393.

Kong, Kyoungchul, Joonbum Bae, and Masayoshi Tomizuka 2009. Control of rotary series elastic actuator for ideal force-mode actuation in human–robot interaction applications. *IEEE/ASME transactions on mechatronics 14*(1), 105–118.

Lagoda, Claude, Alfred C Schouten, Arno HA Stienen, Edsko EG Hekman, and Herman van der Kooij 2010. Design of an electric series elastic actuated joint for robotic gait rehabilitation training. In *2010 3rd IEEE RAS & EMBS international conference on biomedical robotics and biomechatronics*, pp. 21–26. IEEE.

Lasota, Przemyslaw A, Terrence Fong, Julie A Shah, et al. 2017. A survey of methods for safe human-robot interaction. *Foundations and Trends® in Robotics 5*(4), 261–349.

Lee, Chiwon, Myungjoon Kim, Yoon Jae Kim, Nhayoung Hong, Seungwan Ryu, H Jin Kim, and Sungwan Kim 2017. Soft robot review. *International Journal of Control, Automation and Systems 15*, 3–15.

Lee, Tian Soon and Esmail Ali Alandoli 2020. A critical review of modelling methods for flexible and rigid link manipulators. *Journal of the Brazilian Society of Mechanical Sciences and Engineering 42*, 1–14.

Lewis, Frank L, Darren M Dawson, and Chaouki T Abdallah 2003. *Robot manipulator control: theory and practice*, pp. 40–51. CRC Press.

Li, Bai, Xinyuan Li, Hejia Gao, and Fei-Yue Wang 2024. Advances in flexible robotic manipulator systems—part i: Overview and dynamics modeling methods. *IEEE/ASME Transactions on Mechatronics*.

Li, Shuai, Jian Li, Si-qi Li, and Zong-lin Huang 2017. Design and implementation of robot serial integrated rotary joint with safety compliance. *Journal of Central South University 24*(6), 1307–1321.

Li, Xiang, Yongping Pan, Gong Chen, and Haoyong Yu 2016. Adaptive human–robot interaction control for robots driven by series elastic actuators. *IEEE Transactions on Robotics 33*(1), 169–182.

Li, Zhongyi, Weihai Chen, Jianbin Zhang, Qihang Li, Jianhua Wang, Zaojun Fang, and Guilin Yang 2022. A novel cable-driven antagonistic joint designed with variable stiffness mechanisms. *Mechanism and Machine Theory 171*, 104716.

Li, Zhijun, Bo Huang, Zhifeng Ye, Mingdi Deng, and Chenguang Yang 2018. Physical human–robot interaction of a robotic exoskeleton by admittance control. *IEEE Transactions on Industrial Electronics 65*(12), 9614–9624.

Lim, Ser Yong, Darren M Dawson, and K Anderson 1996. Re-examining the nicosia-tomei robot observer-controller from a backstepping perspective. *IEEE Transactions on Control Systems Technology 4*(3), 304–310.

Lim, Ser Yong, Darren M Dawson, Jun Hu, and Marcio S de Queiroz 1997. An adaptive link position tracking controller for rigid-link flexible-joint robots without velocity measurements. *IEEE Transactions on Systems, Man, and Cybernetics, Part B (Cybernetics) 27*(3), 412–427.

Lim, Ser Yong, J Hu, DM Dawson, and M Queiroz 1995. A partial state feedback controller for trajectory tracking of rigid-link flexible-joint robots using an observed backstepping approach. In *Proceedings of 1995 American Control Conference-ACC'95*, Volume 6, pp. 4300–4304. IEEE.

Lin, Hai and Panos J Antsaklis 2009. Stability and stabilizability of switched linear systems: a survey of recent results. *IEEE Transactions on Automatic control 54*(2), 308–322.

Liu, Fei, Mingen Li, Jingpei Lu, Entong Su, and Michael C Yip 2022. Parameter identification and motion control for articulated rigid body robots using differentiable position-based dynamics. *arXiv preprint arXiv:2201.05753*.

Liu, Xin, Anthony Rossi, and Ioannis Poulakakis 2018. A switchable parallel elastic actuator and its application to leg design for running robots. *IEEE/ASME Transactions on Mechatronics 23*(6), 2681–2692.

Liu, Yuwang, Dongqi Wang, Shangkui Yang, Jinguo Liu, and Guangbo Hao 2021. Design and experimental study of a passive power-source-free stiffness-self-adjustable mechanism. *Frontiers of Mechanical Engineering 16*, 32–45.

López-Martínez, Javier, José Luis Blanco-Claraco, Daniel García-Vallejo, and Antonio Giménez-Fernández 2015. Design and analysis of a flexible linkage for robot safe operation in collaborative scenarios. *Mechanism and Machine Theory 92*, 1–16.

Maloisel, Guirec, Espen Knoop, Christian Schumacher, Bernhard Thomaszewski, Moritz Bächer, and Stelian Coros 2023. Optimal design of flexible-link mechanisms with desired load-displacement profiles. *IEEE Robotics and Automation Letters 8*(7), 4203–4210.

Mamani, Gabriela, Jonathan Becedas, and Vicente Feliu 2012. Sliding mode tracking control of a very lightweight single-link flexible robot robust to payload changes and motor friction. *Journal of Vibration and Control 18*(8), 1141–1155.

Mekaouche, Adel, Frédéric Chapelle, and Xavier Balandraud 2015. Fem-based generation of stiffness maps. *IEEE Transactions on Robotics 31*(1), 217–222.

Merlet, Jean-Pierre 2006. *Parallel robots*, Volume 128. Springer Science and Business Media.

Migliore, Shane A, Edgar A Brown, and Stephen P DeWeerth 2005. Biologically inspired joint stiffness control. In *Proceedings of the 2005 IEEE international conference on robotics and automation*, pp. 4508–4513. IEEE.

Montoya-Cháirez, Jorge, Javier Moreno-Valenzuela, Víctor Santibáñez, Ricardo Carelli, Fracisco G Rossomando, and Ricardo Pérez-Alcocer 2022. Combined adaptive neural network and regressor-based trajectory tracking control of flexible joint robots. *IET Control Theory & Applications 16*(1), 31–50.

Morita, Toshio and Shigeki Sugano 1995. Design and development of a new robot joint using a mechanical impedance adjuster. In *Proceedings of 1995 IEEE International Conference on Robotics and Automation*, Volume 3, pp. 2469–2475. IEEE.

Nasiri, Neda, Ahmad Fakharian, and Mohammad Bagher Menhaj 2020. Observer-based robust control for flexible-joint robot manipulators: A state-dependent riccati equation-based approach. *Transactions of the Institute of Measurement and Control 42*(16), 3135–3155.

Nicosia, S and P Tomei 1990. Robot control by using only joint position measurements. *IEEE Transactions on Automatic control 35*(9), 1058–1061.

Ott, Christian, Alin Albu-Schaffer, Andreas Kugi, and Gerd Hirzinger 2003. Decoupling based cartesian impedance control of flexible joint robots. In *2003 IEEE International Conference on Robotics and Automation (Cat. No. 03CH37422)*, Volume 3, pp. 3101–3107. IEEE.

Ott, Christian, Alin Albu-Schaffer, Andreas Kugi, and Gerd Hirzinger 2008. On the passivity-based impedance control of flexible joint robots. *IEEE Transactions on Robotics 24*(2), 416–429.

Ott, Christian, Alin Albu-Schaffer, Andreas Kugi, S Stamigioli, and Gerd Hirzinger 2004. A passivity based cartesian impedance controller for flexible joint robots-part i: Torque feedback and gravity compensation. In *IEEE International Conference on Robotics and Automation, 2004. Proceedings. ICRA'04. 2004*, Volume 3, pp. 2659–2665. IEEE.

Paine, Nicholas, Sehoon Oh, and Luis Sentis 2013. Design and control considerations for high-performance series elastic actuators. *IEEE/ASME Transactions on Mechatronics 19*(3), 1080–1091.

Paksoy, Erkan, Mehmet Ismet Can Dede, and Gökhan Kiper 2021. Experimental compliance matrix derivation for enhancing trajectory tracking of a 2-dof high-accelerated over-constrained mechanism. In *IFToMM Asian conference on Mechanism and Machine Science*, pp. 354–362. Springer.

Park, Juyi, Pyung-Hun Chang, Hyung-Soon Park, and Eunjeong Lee 2006. Design of learning input shaping technique for residual vibration suppression in an industrial

robot. *IEEE/ASME Transactions on Mechatronics 11*(1), 55–65.

Park, Jung-Jun, Byeong-Sang Kim, Jae-Bok Song, and Hong-Seok Kim 2008. Safe link mechanism based on nonlinear stiffness for collision safety. *Mechanism and Machine Theory 43*(10), 1332–1348.

Parker, Lynne E and John V Draper 1998. Robotics applications in maintenance and repair. *Handbook of industrial robotics 2*, 1023–1036.

Pashkevich, Anatol, Damien Chablat, and Philippe Wenger 2009. Stiffness analysis of overconstrained parallel manipulators. *Mechanism and Machine Theory 44*(5), 966–982.

Pashkevich, Anatol, Alexandr Klimchik, and Damien Chablat 2011. Enhanced stiffness modeling of manipulators with passive joints. *Mechanism and Machine Theory 46*(5), 662–679.

Pedro, Jimoh O and Thando Tshabalala 2015. Hybrid nnmpc/pid control of a two-link flexible manipulator with actuator dynamics. In *2015 10th Asian Control Conference (ASCC)*, pp. 1–6. IEEE.

Plooij, Michiel, Wouter Wolfslag, and Martijn Wisse 2017. Clutched elastic actuators. *IEEE/ASME transactions on mechatronics 22*(2), 739–750.

Pratt, Gill A and Matthew M Williamson 1995. Series elastic actuators. In *Proceedings 1995 IEEE/RSJ international conference on intelligent robots and systems. Human robot interaction and cooperative robots*, Volume 1, pp. 399–406. IEEE.

Qaddoori Fenjan, Shakir and Siavash Fathollahi Dehkordi 2024. Soft robotic system with continuum manipulator and compliant gripper: Design, fabrication, and implementation. In *Actuators*, Volume 13, pp. 298. MDPI.

Renda, Federico, Vito Cacucciolo, Jorge Dias, and Lakmal Seneviratne 2016. Discrete cosserat approach for soft robot dynamics: A new piece-wise constant strain model with torsion and shears. In *2016 IEEE/RSJ International Conference on Intelligent Robots and Systems (IROS)*, pp. 5495–5502. IEEE.

Rodrigue, Hugo and Jongwoo Kim 2024. Soft actuators in surgical robotics: a state-of-the-art review. *Intelligent Service Robotics 17*(1), 3–17.

Romdhane, Lotfi, Z Affi, and M Fayet 2002. Design and singularity analysis of a 3-translational-dof in-parallel manipulator. *Journal of Mechanical Design 124*(3), 419–426.

Salisbury, J Kenneth and John J Craig 1982. Articulated hands: Force control and kinematic issues. *The International Journal of Robotics Research 1*(1), 4–17.

Sariyildiz, Emre, Rahim Mutlu, Jon Roberts, Chin-Hsing Kuo, and Barkan Ugurlu 2023. Design and control of a novel variable stiffness series elastic actuator. *IEEE/ASME*

*Transactions on Mechatronics 28*(3), 1534–1545.

Sayahkarajy, Mostafa, Z Mohamed, and Ahmad Athif Mohd Faudzi 2016. Review of modelling and control of flexible-link manipulators. *Proceedings of the Institution of Mechanical Engineers, Part I: Journal of Systems and Control Engineering 230*(8), 861–873.

Sensinger, Jonathon W and Richard F Ff Weir 2006. Improvements to series elastic actuators. In *2006 2nd IEEE/ASME International Conference on Mechatronics and Embedded Systems and Applications*, pp. 1–7. IEEE.

Sergi, Fabrizio, Dino Accoto, Giorgio Carpino, Nevio Luigi Tagliamonte, and Eugenio Guglielmelli 2012. Design and characterization of a compact rotary series elastic actuator for knee assistance during overground walking. In *2012 4th IEEE RAS & EMBS international conference on biomedical robotics and biomechatronics (BioRob)*, pp. 1931–1936. IEEE.

Shao, Yixin, Wuxiang Zhang, Yujie Su, and Xilun Ding 2021. Design and optimisation of load-adaptive actuator with variable stiffness for compact ankle exoskeleton. *Mechanism and Machine Theory 161*, 104323.

Sharifi, Mojtaba, Amir Zakerimanesh, Javad K Mehr, Ali Torabi, Vivian K Mushahwar, and Mahdi Tavakoli 2021. Impedance variation and learning strategies in human–robot interaction. *IEEE Transactions on Cybernetics 52*(7), 6462–6475.

Sharkawy, Abdel-Nasser and Panagiotis N Koustoumpardis 2022. Human–robot interaction: A review and analysis on variable admittance control, safety, and perspectives. *Machines 10*(7), 591.

Shiakolas, PS, KL Conrad, and TC Yih 2002. On the accuracy, repeatability, and degree of influence of kinematics parameters for industrial robots. *International journal of modelling and simulation 22*(4), 245–254.

Sincak, Peter Jan, Erik Prada, L'ubica Miková, Roman Mykhailyshyn, Martin Varga, Tomas Merva, and Ivan Virgala 2024. Sensing of continuum robots: A review. *Sensors 24*(4), 1311.

Singer, N. and W. Seering 1990. Preshaping command inputs to reduce system vibration. pp. 128–147.

Singhose, William 2009. Command shaping for flexible systems: A review of the first 50 years. *International journal of precision engineering and manufacturing 10*, 153–168.

Singhose, William and Joshua Vaughan 2010. Reducing vibration by digital filtering and input shaping. *IEEE Transactions on Control Systems Technology 19*(6), 1410–1420.

Singhose, William E and Neil C Singer 1996. Effects of input shaping on two-dimensional trajectory following. *IEEE Transactions on Robotics and Automa-*

*tion 12*(6), 881–887.

Song, Zhibin, Tianyu Ma, Keke Qi, Emmanouil Spyrakos-Papastavridis, Songyuan Zhang, and Rongjie Kang 2022. A trajectory tracking control based on a terminal sliding mode for a compliant robot with nonlinear stiffness joints. *Micromachines 13*(3), 409.

Spong, Mark W 1987. Modeling and control of elastic joint robots.

Spong, Mark W 2022. An historical perspective on the control of robotic manipulators. *Annual Review of Control, Robotics, and Autonomous Systems 5*(1), 1–31.

Spyrakos-Papastavridis, Emmanouil, Peter RN Childs, and Jian S Dai 2019. Passivity preservation for variable impedance control of compliant robots. *IEEE/ASME Transactions on Mechatronics 25*(5), 2342–2353.

Spyrakos-Papastavridis, Emmanouil and Jian S Dai 2020. Minimally model-based trajectory tracking and variable impedance control of flexible-joint robots. *IEEE Transactions on Industrial Electronics 68*(7), 6031–6041.

Stienen, Arno HA, Edsko EG Hekman, Huub Ter Braak, Arthur MM Aalsma, Frans CT Van Der Helm, and Herman Van Der Kooij 2009. Design of a rotational hydroelastic actuator for a powered exoskeleton for upper limb rehabilitation. *IEEE Transactions on biomedical engineering 57*(3), 728–735.

Sun, Changyin, Hejia Gao, Wei He, and Yao Yu 2018. Fuzzy neural network control of a flexible robotic manipulator using assumed mode method. *IEEE transactions on neural networks and learning systems 29*(11), 5214–5227.

Sun, Jiantao, Zhao Guo, Dingyang Sun, Siyu He, and Xiaohui Xiao 2018. Design, modeling and control of a novel compact, energy-efficient, and rotational serial variable stiffness actuator (svsa-ii). *Mechanism and Machine Theory 130*, 123–136.

Sun, Tao, Binbin Lian, and Yimin Song 2016. Stiffness analysis of a 2-dof overconstrained rpm with an articulated traveling platform. *Mechanism and Machine Theory 96*, 165–178.

Tang, Zhi Qiang, Ho Lam Heung, Kai Yu Tong, and Zheng Li 2021. Model-based online learning and adaptive control for a "human-wearable soft robot" integrated system. *The International Journal of Robotics Research 40*(1), 256–276.

Thieffry, Maxime, Alexandre Kruszewski, Christian Duriez, and Thierry-Marie Guerra 2018. Control design for soft robots based on reduced-order model. *IEEE Robotics and Automation Letters 4*(1), 25–32.

Tian, Yong, Xiang Yue, Lin Wang, and Yan Feng 2023. Vibration suppression of collaborative robot based on modified trajectory planning. *Industrial Robot: the international journal of robotics research and application 50*(1), 45–55.

Vanderborght, Bram, Alin Albu-Schäffer, Antonio Bicchi, Etienne Burdet, Darwin G Caldwell, Raffaella Carloni, Manuel Catalano, Oliver Eiberger, Werner Friedl, Ganesh Ganesh, et al. 2013. Variable impedance actuators: A review. *Robotics and autonomous systems 61*(12), 1601–1614.

Verstraten, Tom, Philipp Beckerle, Raphaël Furnémont, Glenn Mathijssen, Bram Vanderborght, and Dirk Lefeber 2016. Series and parallel elastic actuation: Impact of natural dynamics on power and energy consumption. *Mechanism and Machine Theory 102*, 232–246.

Vertechy, Rocco and Vincenzo Parenti-Castelli 2007. Static and stiffness analyses of a class of over-constrained parallel manipulators with legs of type us and ups. In *Proceedings 2007 IEEE International Conference on Robotics and Automation*, pp. 561–567. IEEE.

Wang, Zerui, Hiu Man Yip, David Navarro-Alarcon, Peng Li, Yun-hui Liu, Dong Sun, Hesheng Wang, and Tak Hong Cheung 2015. Design of a novel compliant safe robot joint with multiple working states. *IEEE/ASME Transactions on Mechatronics 21*(2), 1193–1198.

Wei, Tianhao and Changliu Liu 2022. Safe control with neural network dynamic models. In *Learning for Dynamics and Control Conference*, pp. 739–750. PMLR.

Wolf, Sebastian and Gerd Hirzinger 2008. A new variable stiffness design: Matching requirements of the next robot generation. In *2008 IEEE International Conference on Robotics and Automation*, pp. 1741–1746. IEEE.

Wu, Guanglei, Shaoping Bai, and Jørgen Kepler 2014. Mobile platform center shift in spherical parallel manipulators with flexible limbs. *Mechanism and Machine Theory 75*, 12–26.

Wyeth, Gordon 2008. Demonstrating the safety and performance of a velocity sourced series elastic actuator. In *2008 IEEE International Conference on Robotics and Automation*, pp. 3642–3647. IEEE.

Xu, Bin 2017. Composite learning control of flexible-link manipulator using nn and dob. *IEEE Transactions on Systems, Man, and Cybernetics: Systems 48*(11), 1979–1985.

Xu, Yapeng, Kai Guo, Jie Sun, and Jianfeng Li 2021. Design, modeling and control of a reconfigurable variable stiffness actuator. *Mechanical Systems and Signal Processing 160*, 107883.

Yang, Chao, Qiaohong Chen, Junhua Tong, and Qinchuan Li 2019. Elastostatic stiffness analysis of a 2 p ur-p sr overconstrained parallel mechanism. *International Journal of Precision Engineering and Manufacturing 20*(4), 569–581.

Yang, Chao, Qinchuan Li, Qiaohong Chen, and Lingmin Xu 2018. Elastostatic stiffness modeling of overconstrained parallel manipulators. *Mechanism and Machine Theory 122*, 58–74.

Yang, Yang, Yingtian Li, and Yonghua Chen 2018. Principles and methods for stiffness modulation in soft robot design and development. *Bio-Design and Manufacturing 1*(1), 14–25.

Yih, C.-C. 2012. Extended nicosia–tomei velocity observer-based robot-tracking control. *IET Control Theory and Applications 6*, 51–61.

Yu, Xinbo, Sisi Liu, Shuang Zhang, Wei He, and Haifeng Huang 2023. Adaptive neural network force tracking control of flexible joint robot with an uncertain environment. *IEEE Transactions on Industrial Electronics*.

Zebardast, Omid, Hadi Moradi, and Farshid Najafi 2013. Safe joint mechanism using passive compliance method for collision safety. In *2013 First RSI/ISM International Conference on Robotics and Mechatronics (ICRoM)*, pp. 102–106. IEEE.

Zhang, Haochong, Rongyun Cao, Shlomo Zilberstein, Feng Wu, and Xiaoping Chen 2017. Toward effective soft robot control via reinforcement learning. In *Intelligent Robotics and Applications: 10th International Conference, ICIRA 2017, Wuhan, China, August 16–18, 2017, Proceedings, Part I 10*, pp. 173–184. Springer.

Zhang, Qi, Xiaofeng Liu, and Guoping Cai 2021. Dynamics and control of a flexible-link flexible-joint space robot with joint friction. *International Journal of Aeronautical and Space Sciences 22*, 415–432.

Zhang, Quan, James K Mills, William L Cleghorn, Jiamei Jin, and Zhijun Sun 2015. Dynamic model and input shaping control of a flexible link parallel manipulator considering the exact boundary conditions. *Robotica 33*(6), 1201–1230.

Zhao, Weihao, Junbei Liao, Wei Qian, Haoyong Yu, and Zhao Guo 2024. A novel design of series elastic actuator using tensile springs array. *Mechanism and Machine Theory 192*, 105541.

Zheng, Gang, Yuan Zhou, and Mingda Ju 2020. Robust control of a silicone soft robot using neural networks. *ISA transactions 100*, 38–45.

Zheng, Jia, Shuangyi Wang, James Housden, Zeng-Guang Hou, Davinder Singh, and Kawal Rhode 2021. A safety joint with passive compliant and manual override mechanisms for medical robotics. In *2021 IEEE International Conference on Intelligence and Safety for Robotics (ISR)*, pp. 1–4. IEEE.

Zhong, Haoran, Xinyu Li, Liang Gao, and Congbo Li 2021. Toward safe human–robot interaction: A fast-response admittance control method for series elastic actuator. *IEEE Transactions on Automation Science and Engineering 19*(2), 919–932.

# APPENDIX A

# STIFFNESS PARAMETERS AND SIMULATION RESULTS

Table A.1. Optimized modification matrix and virtual moment arms parameters. (N · m/m and N/rad units are simplified to N)

| | | | | | | | | |
|---|---|---|---|---|---|---|---|---|
| $k_1$ | $-682581.69$ N/m | $k_{18}$ | $-9860.23$ N | $k_{35}$ | $-133839.70$ N | $k_{52}$ | $-12712.36$ N · m/rad |
| $k_2$ | $-176694.31$ N/m | $k_{19}$ | 445958.51 N | $k_{36}$ | 455.36 N · m/rad | $k_{53}$ | $-1229.68$ N · m/rad |
| $k_3$ | 6931081.96 N/m | $k_{20}$ | 36396.56 N | $k_{37}$ | 297044.99 N | $k_{54}$ | 1353507.83 N/m |
| $k_4$ | 305814.59 N · m/rad | $k_{21}$ | 448089.83 N | $k_{38}$ | $-6789.15$ N | $k_{55}$ | 110128.52 N |
| $k_5$ | 319756.95 N · m/rad | $k_{22}$ | $-2013299.99$ N/m | $k_{39}$ | $-472.10$ N | $k_{56}$ | 118159.95 N |
| $k_6$ | $-614.58$ N · m/rad | $k_{23}$ | $-6392.84$ N/m | $k_{40}$ | $-412917.17$ N | $k_{57}$ | $-27232.35$ N · m/rad |
| $k_7$ | $-585347.64$ N/m | $k_{24}$ | 1166028.11 N/m | $k_{41}$ | $-192.70$ N | $k_{58}$ | $-10081.42$ N |
| $k_8$ | $-538600.05$ N/m | $k_{25}$ | 271346.39 N · m/rad | $k_{42}$ | $-10199.16$ N | $k_{59}$ | $-19382.79$ N |
| $k_9$ | $-38045.02$ N | $k_{26}$ | 367542.60 N · m/rad | $k_{43}$ | $-62556.25$ N/m | $k_{60}$ | 2427.17 N |
| $k_{10}$ | $-172485.58$ N · m/rad | $k_{27}$ | $-62.95$ N · m/rad | $k_{44}$ | $-28711.40$ N/m | $k_{61}$ | $-12128.66$ N |
| $k_{11}$ | 5288.43 N · m/rad | $k_{28}$ | $-23459.22$ N/m | $k_{45}$ | 48277184.32 N/m | $k_{62}$ | $-36977.22$ N |
| $k_{12}$ | $-2463245.79$ N/m | $k_{29}$ | $-16845.07$ N/m | $k_{46}$ | 262364.31 N · m/rad | $k_{63}$ | 1214.03 N |
| $k_{13}$ | $-19527.29$ N | $k_{30}$ | 89855.32 N | $k_{47}$ | 401376.50 N · m/rad | $h_1$ | 7.68 m |
| $k_{14}$ | 2021068.50 N | $k_{31}$ | 167530.02 N · m/rad | $k_{48}$ | 308.36 N · m/rad | $h_2$ | 3.54 m |
| $k_{15}$ | 1114.64 N · m/rad | $k_{32}$ | 605.51 N · m/rad | $k_{49}$ | $-2332.49$ N/m | | |
| $k_{16}$ | 326089.54 N | $k_{33}$ | 857749.02 N/m | $k_{50}$ | $-253469.03$ N/m | | |
| $k_{17}$ | 57396.59 N | $k_{34}$ | $-8392.46$ N | $k_{51}$ | $-161419.91$ N | | |

Table A.2. Finite Element Analysis (FEA) and Virtual Joint Method (VJM). The compliant deflection unit is $\mu m$. Sub-indices E, A, and B indicate the force is applied from the frames $\mathcal{F}(E)$, $\mathcal{F}(A)$, and $\mathcal{F}(B)$.

| Force Direction | Test Point 1 | | | | | | Test Point 2 | | | | | | Test Point 3 | | | | | |
|---|---|---|---|---|---|---|---|---|---|---|---|---|---|---|---|---|---|---|
| | $\mathbf{FEA_{EAB}}$ | | $\mathbf{VJM_E}$ | | $\mathbf{VJM_{EAB}}$ | | $\mathbf{FEA_{EAB}}$ | | $\mathbf{VJM_E}$ | | $\mathbf{VJM_{EAB}}$ | | $\mathbf{FEA_{EAB}}$ | | $\mathbf{VJM_E}$ | | $\mathbf{VJM_{EAB}}$ | |
| | $x$ | $y$ | $x$ | $y$ | $x$ | $y$ | $x$ | $y$ | $x$ | $y$ | $x$ | $y$ | $x$ | $y$ | $x$ | $y$ | $x$ | $y$ |
| **0°** | 1.7 | 0 | 1.7 | 0 | 1.9 | 0 | 2.6 | 0 | 2.5 | 0 | 2.9 | 0 | 4.4 | 0 | 4.3 | 0 | 4.9 | 0 |
| **30°** | 1.5 | 33.4 | 1.4 | 33.5 | 1.7 | 33.5 | 2.2 | 16.7 | 2.2 | 16.8 | 2.5 | 16.8 | 3.8 | 11.8 | 3.7 | 11.8 | 4.3 | 11.8 |
| **60°** | 0.8 | 57.9 | 0.8 | 58.1 | 1 | 58.1 | 1.3 | 29 | 1.2 | 29.1 | 1.4 | 29.1 | 2.2 | 20.5 | 2.1 | 20.5 | 2.5 | 20.5 |
| **90°** | 0 | 66.9 | 0 | 67.1 | 0 | 67.1 | 0 | 33.5 | 0 | 33.5 | 0 | 33.5 | 0 | 23.6 | 0 | 23.7 | 0 | 23.7 |
| **120°** | -0.9 | 58 | -0.8 | 58.1 | -1 | 58.1 | -1.3 | 29 | -1.2 | 29.1 | -1.4 | 29.1 | -2.2 | 20.5 | -2.1 | 20.5 | -2.5 | 20.5 |
| **150°** | -1.5 | 33.5 | -1.4 | 33.5 | -1.7 | 33.5 | -2.3 | 16.7 | -2.1 | 16.8 | -2.5 | 16.8 | -3.9 | 11.8 | -3.7 | 11.8 | -4.3 | 11.8 |

| Force Direction | Test Point 4 | | | | | | Test Point 5 | | | | | | Test Point 6 | | | | | |
|---|---|---|---|---|---|---|---|---|---|---|---|---|---|---|---|---|---|---|
| | $\mathbf{FEA_{EAB}}$ | | $\mathbf{VJM_E}$ | | $\mathbf{VJM_{EAB}}$ | | $\mathbf{FEA_{EAB}}$ | | $\mathbf{VJM_E}$ | | $\mathbf{VJM_{EAB}}$ | | $\mathbf{FEA_{EAB}}$ | | $\mathbf{VJM_E}$ | | $\mathbf{VJM_{EAB}}$ | |
| | $x$ | $y$ | $x$ | $y$ | $x$ | $y$ | $x$ | $y$ | $x$ | $y$ | $x$ | $y$ | $x$ | $y$ | $x$ | $y$ | $x$ | $y$ |
| **0°** | 16.9 | -16.3 | 17.8 | -17.7 | 17.4 | -16.4 | 5.7 | -9.9 | 5.8 | -10.5 | 6 | -9.9 | 3.9 | -12.6 | 3.9 | -12.9 | 4.1 | -12.6 |
| **30°** | 5.83 | -1.44 | 6.6 | -2.6 | 6.2 | -1.4 | -0.3 | 8.6 | -0.2 | 8.2 | 0 | 8.6 | -3.1 | 26.5 | -3.1 | 26.3 | -2.9 | 26.6 |
| **60°** | -6.84 | 13.9 | -6.4 | 13.2 | -6.6 | 13.9 | -6.2 | 24.8 | -6.2 | 24.6 | -6.1 | 24.9 | -9.2 | 58.5 | -9.2 | 58.5 | -9.1 | 58.6 |
| **90°** | -17.7 | 25.5 | -17.7 | 25.5 | -17.7 | 25.5 | -10.5 | 34.4 | -10.5 | 34.5 | -10.5 | 34.5 | -12.9 | 74.8 | -12.9 | 75 | -12.9 | 75 |
| **120°** | -23.9 | 30.3 | -24.3 | 31 | -24.1 | 30.3 | -12 | 34.8 | -12 | 35.1 | -12.1 | 34.8 | -13.1 | 71.1 | -13.1 | 71.4 | -13.2 | 71.2 |
| **150°** | -23.6 | 27 | -24.3 | 28.1 | -23.9 | 27 | -10.2 | 25.8 | -10.3 | 26.3 | -10.5 | 25.8 | -9.8 | 48.3 | -9.8 | 48.7 | -10 | 48.4 |

| Force Direction | Test Point 7 | | | | | | Test Point 8 | | | | | | Test Point 9 | | | | | |
|---|---|---|---|---|---|---|---|---|---|---|---|---|---|---|---|---|---|---|
| | $\mathbf{FEA_{EAB}}$ | | $\mathbf{VJM_E}$ | | $\mathbf{VJM_{EAB}}$ | | $\mathbf{FEA_{EAB}}$ | | $\mathbf{VJM_E}$ | | $\mathbf{VJM_{EAB}}$ | | $\mathbf{FEA_{EAB}}$ | | $\mathbf{VJM_E}$ | | $\mathbf{VJM_{EAB}}$ | |
| | $x$ | $y$ | $x$ | $y$ | $x$ | $y$ | $x$ | $y$ | $x$ | $y$ | $x$ | $y$ | $x$ | $y$ | $x$ | $y$ | $x$ | $y$ |
| **0°** | 11.6 | -29.6 | 11.8 | -30.2 | 11.8 | -29.7 | 16.1 | -21.4 | 16.7 | -22.5 | 16.4 | -21.4 | 97.6 | -48.1 | 101.9 | -50.5 | 96.7 | -47.6 |
| **30°** | -5 | 19.5 | -4.9 | 19.1 | -4.9 | 19.6 | 2.7 | 0 | 3.2 | -1 | 2.9 | 0 | 59.3 | -27.4 | 63.1 | -29.6 | 58.3 | -26.8 |
| **60°** | -20.3 | 63.4 | -20.3 | 63.3 | -20.2 | 63.6 | -11.4 | 21.3 | -11.1 | 20.8 | -11.3 | 21.4 | 4.7 | 0.7 | 7.2 | -0.6 | 4.3 | 1.1 |
| **90°** | -30.2 | 90.3 | -30.2 | 90.5 | -30.2 | 90.5 | -22.5 | 37 | -22.5 | 37.1 | -22.5 | 37 | -52.5 | 29.1 | -51.1 | 28.9 | -50.9 | 28.7 |
| **120°** | -32 | 93 | -32 | 93.5 | -32.1 | 93.2 | -27.6 | 42.7 | -27.9 | 43.4 | -27.7 | 42.8 | -96.8 | 50.1 | -96.1 | 50.7 | -92.4 | 48.7 |
| **150°** | -25.2 | 70.8 | -25.3 | 71.4 | -25.3 | 70.9 | -25.2 | 37 | -25.8 | 38 | -25.5 | 37.1 | -115.3 | 57.8 | -115.2 | 59 | -109.2 | 55.6 |

# VITA

İbrahimcan Görgülü received his BSc degree in Mechanical Eng. from Gediz University in 2015, graduating as the top student in his faculty. He received his MSc and PhD degrees in Mechanical Eng. from Izmir Institute of Technology in 2018 and 2024, respectively.

His research interests encompass robotics, haptics, stiffness and dynamics modeling, control, and optimal design. Since 2017, he has been working as a research assistant in the Mechanical Engineering department at the Izmir Institute of Technology. Additionally, he gained internship experience at CERN (The European Organization for Nuclear Research) in 2014.

**List of projects worked as researcher** (supported by the Scientific and Technological Research Council of Turkey):

- 'Design of an Inherently Balanced Robotic Manipulator with Remote Center of Motion to be used as an Endoscope Holder for Endonasal Skull Base Surgery (BalanScope)' with the grant number of 219M483.
- 'Methodologies for Increasing the Positioning Accuracy of High-Acceleration Parallel Robots Used in Industrial Applications' with the grant number of 116M272.
- 'HISS: design of a Haptic system with Improved performance via developing its new Sub-Systems' with the grant number of 117M405.

**List of selected publications**:

- Görgülü I., Dede M.I.C., Kiper G., "A New Safe Flexible Torsion Joint Design with Softening Stiffness Characteristics" (Under Review), Mechanism and Machine Theory, 2024.
- Görgülü I., Dede M.I.C., Kiper G., "Stiffness modeling of a 2-DoF over-constrained planar parallel mechanism", Mechanism and Machine Theory, Volume 185, 2023.
- Görgülü I., Dede M.I.C., Carbone G., "Experimental structural stiffness analysis of a surgical haptic master device manipulator", Journal of Medical Devices, Volume 15, 2021.
- Görgülü I., Carbone G., Dede M.I.C., "Time efficient stiffness model computation for a parallel haptic mechanism via the virtual joint method", Mechanism and Machine Theory, Volume 143, 2020.
- Görgülü I., Dede M.I.C., "A new stiffness performance index: volumetric isotropy index", Machines, Volume 7, 2019.
- Görgülü I., "Optimal design of a kinesthetic haptic device mechanism for enhancing its impedance characteristics", M.S. Thesis, Department of Mechanical Engineering, Izmir Institute of Technology, 2018.